Advanced Anode and Cathode Materials for Li-ion Batteries: Application to Printing Methodology

zur Erlangung des akademischen Grades einer

DOKTORIN DER INGENIEURWISSENSCHAFTEN

(Dr.-Ing.)

von der KIT-Fakultät für Chemieingenieurwesen und Verfahrenstechnik des

Karlsruher Instituts für Technologie (KIT)

genehmigte

DISSERTATION

von

Parvathy Anitha Sukkurji

aus

Kochi, Indien

Abstract

Batteries play an important role in energy storage applications spanning from electric vehicles, portable electronic devices to stationary storage grids. Basic structure of a lithium-ion battery (LIB) consists of two electrodes; the anode and the cathode separated by an ion-conductive electrolyte. With the advent of portable electronic products (such as internet of things, IoT), there is a growing need for rechargeable batteries with smaller size, smaller weight and higher energy densities. In recent years, inkjet printing has intrigued with the introduction of solution processed printed electronics (PE). PE and printed batteries have gained interest because they are inexpensive, easy to fabricate, up-scalable for large production and printing is possible on various kinds of substrates. Most research efforts strive for "better" batteries with high reversible capacities or the enhancement of the capacities of the state-of-the-art battery systems. Printing is a fast and inexpensive process and printed batteries with lower thickness values could be developed with the printing technique. The battery ink formulation can be tuned during printing procedure to achieve capacity and potential required for fully printed circuit. The demand for batteries that are thinner, and lighter with higher energy density has motivated the research into the next generation LIB electrodes, some of which will be explored in this work. The first focus of this dissertation is on the development of an alloying type anode material for the LIB, namely silicon (Si) and the assessment of its electrochemical and structural characteristics. The printability of Si/C anode inks and the effect of carbon coating on the improvement of the cycling process are analyzed. Later a full cell comprising of printed Si/C anode and NCM is fabricated. This full cell was used to deliver power to a printed electrolyte gated graphene transistor.

In the next part of this work, a new material class was developed, namely the high entropy fluorides (HEFs). To realize the printed full cell battery a printed cathode was needed, so a conversion cathode material composed of fluoride-based materials was formulated. Collectively, high entropy materials (HEMs) consist of the solid solution of various elements, homogenously distributed. HEF based materials were synthesized via a facile direct mechanochemistry route that can be used to incorporate multiple cations in a single-phase rutile structure. Due to high electronegativity of fluorine, transition metal fluorides are interesting candidates for cathode materials because of their high theoretical capacity (>571 mAh/g) in contrast to the conventional intercalation cathodes. The multi-cation substitution may provide a new path for tailorable electrochemical properties of the conversion electrodes via entropy effects. However, the underlying conversion reaction mechanisms in the HEFs are yet to be explored and this forms the second part of this study. The comprehensive examination shows that HEF cathodes follow a conversion reaction mechanism and the capacity loss occurs due to kinetically limiting factors affecting the cathode side. For investigating the performance of the batteries, various electrochemical methods such as galvanostatic cycling, cyclic voltammetry (CV), electrochemical impedance spectroscopy (EIS) are applied. A variety of structural characterization techniques were also employed to confirm the phase purities of electrode materials. Fabrication of batteries via printing was followed in this dissertation. Thickness of printed batteries are in millimeters range due to their reduced size and it can act as a power source for printed electronics. Finally, a full cell with carbon coated Si/C anode and HEF cathode is assembled and the viability of a completely printed full cell is demonstrated.

Zusammenfassung

Batterien spielen eine wichtige Rolle in der Anwendung als Energiespeichermedien. Dies reicht von Elektrofahrzeugen über tragbare elektronische Geräte bis hin zu stationären Speichern. Lithium-Ionen-Batterie (LIB) bestehen aus zwei Elektroden, einer Anode und einer Kathode, die durch einen elektrolytgetränken Separator voneinander getrennt sind. Mit dem zunehmenden Trend portabler elektronischer Produkte (z. B. Internet of Thinks, IoT) besteht ein wachsender Bedarf an wiederaufladbaren Batterien mit geringerer Größe, geringerem Gewicht und höherer Energiedichte. In den letzten Jahren hat der Tintenstrahldruck mit der Einführung von lösungsgefertigter gedruckter Elektronik (PE) immer mehr an Bedeutung gewonnen. PE und gedruckte Batterien haben an Interesse gewonnen, da sie kostengünstig und einfach herzustellen sind, für eine große Produktion hochskalierbar sind und das Drucken auf verschiedenen Arten von Substraten möglich ist. Die meisten Forschungsanstrengungen zielen auf "bessere" Batterien mit hohen reversiblen Kapazitäten oder auf die Steigerung der Kapazitäten der aktuellen Batteriesysteme. Das Drucken ist ein schneller und kostengünstiger Prozess und mit der Drucktechnik könnten gedruckte Batterien mit geringeren Dickenwerten entwickelt werden. Die Formulierung der Batterietinte kann während des Druckvorgangs abgestimmt werden, um die für den vollständig gedruckten Schaltkreis erforderliche Kapazität und das Potenzial zu erreichen. Die Nachfrage nach dünneren, leichteren Batterien mit einer höheren Energiedichte hat zu Forschungen auf dem Gebiet der nächste Generation von LIB-Elektroden geführt, von denen einige in dieser Arbeit untersucht werden. Im erste Teil dieser Dissertation geht es um die Entwicklung und die Bewertung der elektrochemischen und strukturellen Eigenschaften eines legierungsfähigen Anodenmaterials für LIBs, nämlich Silizium (Si). Die Druckbarkeit von Si/C-Anodentinten und der Effekt der Kohlenstoffbeschichtung zur Verbesserung des Zyklisierungsprozesses werden analysiert. Im Anschluss daran wird eine Vollzelle, bestehend aus gedruckter Si/C-Anode und NCM, hergestellt. Die Vollzelle wurde verwendet, um einen gedruckten elektrolytgesteuerten Graphen-Transistor mit Strom zu versorgen.

Im nächsten Teil dieser Arbeit wurde eine neue Materialklasse entwickelt, nämlich die Hochentropie-Fluoride (HEFs). Um die gedruckte Vollzellenbatterie zu realisieren, wird eine gedruckte Kathode benötigt, daher wurde ein Konversionskathodenmaterial entwickelt, das aus fluoridbasierten Materialien besteht. Generell bestehen Hochentropie-Keramiken (HEMs) aus einer festen Lösung verschiedener homogen verteilter Elemente. HEF-basierte Materialien wurden über eine einfache direkte mechanochemische Route synthetisiert. Dadruch ist es möglich mehrere Kationen in eine einphasige Rutilstruktur einzubauen. Aufgrund der hohen Elektronegativität von Fluor sind Übergangsmetallfluoride aufgrund ihrer hohen theoretischen Kapazität (> 571 mAh/g) im Gegensatz zu den herkömmlichen Interkalationskathoden interessante und vielversprechende Kandidaten für Kathodenmaterialien. Die Multi-Kationen-Substitution bietet möglicherweise einen neuen Weg zu maßgeschneiderte elektrochemische Eigenschaften von Konversionselektroden über den Entropieeffekte. Die zugrundeliegenden Konversionsreaktionsmechanismen in HEFs müssen jedoch zunächst noch erforscht werden. Dies bildet den zweiten Teil dieser Studie. Darüberhinaus wurde eine gründliche Untersuchung der HEFs als potentielle Kathodenmaterialen für LIB durchgeführt. Die umfassenden Untersuchungen zeigen, dass HEFs-Kathoden einem Konversionsreaktionsmechanismus

folgen und der Kapazitätsverlust auf kinetisch begrenzende Faktoren, die die Kathodenseite betreffen, zurückzuführen ist. Zur Untersuchung der Leistungsfähigkeit der Batterien werden unteranderem verschiedene elektrochemische Methoden wie galvanostatische Zyklen, zyklische Voltammetrie (CV) und elektrochemische Impedanzspektroskopie (EIS) angewendet. Darüberhinaus wurden verschiedene strukturellen Charakterisierungstechniken eingesetzt, um bspw. die Phasenreinheit der Elektrodenmaterialien zu bestätigen. In Rahmen dieser Dissertation wurde die Herstellung der Batterien durch Drucken wurde in dieser Dissertation verfolgt. Die Dicke der gedruckten Batterien liegt aufgrund der geringen Größe im Millimeterbereich weshalb die Batterie als Stromquelle für gedruckte Elektronik genutzt werden können. Abschließend wurde eine Vollzelle mit kohlenstoffbeschichteter Si/C-Anode und HEF-Kathode aufgebaut und die Funktionsfähigkeit einer komplett gedruckten Vollzelle demonstriert.

Table of Contents

Chapter 1 Introduction

1.1 Motivation

Batteries are defined as electrochemical devices that provide the conversion of chemical energy to electrical energy. This conversion process is facilitated by using two electrodes of anode and cathode, separator, and an ion-conducting electrolyte. Depending on its recharging cycles, batteries are classified as primary and secondary cells. Non-rechargeable cells or primary cells denote the type of cells in which oxidation/reduction reaction cannot be reversed. While, secondary cells are rechargeable batteries that can be replenished after discharging. Batteries are usually characterized in terms of capacity, reversibility, energy density, potential and shelf life [1]. Alessandro Volta invented for the first time the 'electric pile' as a proof of concept battery in 1800 and he demonstrated that electric current can be generated by an electrochemical reaction between two dissimilar metals kept in an acidic ionic solution [2]. Ever since, the foundation of modern-day batteries originated from the 'voltaic' pile concept.

The commonly used electrodes in the state-of-the-art electric vehicles are layered lithium transition metal oxides (with a general formula *LiMO$_2$*, where M: transition metal) with variant compositions of Ni, Co, Mn, or Al [3]. Usually, carbonaceous materials like graphite are employed as anode material. The first proof of concept of Lithium-ion batteries (LIB) employing metal chalcogenides as intercalation compound was put forward by Whittingham in the early 1970s [4]. LIB is characterized by their 'huge energy density', which denotes the maximum energy that a battery accommodates per unit volume [1]. Later, Goodenough introduced LiCoO$_2$ (LCO) as potential cathode material in the 1980s [5]. Padhi *et al.*, introduced phospho-olivine LiFePO$_4$ (LFP) in 1997 which exhibits excellent thermal, cycling stability and low toxicity [6]. Most of these standard cathodes have low electronic conductivities and hence for ensuring electronic conductivity, carbon additive during electrode slurry formulation is essential. Since the commercialization of LCO/graphite battery by Sony in 1991, LIB has attracted huge prospects in electronics and electric vehicle applications [7]. In recognition of this, in 2019, the Nobel Prize in chemistry was awarded to three scientists, Whittingham, Goodenough and Yoshino for their revolutionary inventions in LIB.

Considering the energy consumption at present, over 85 % of energy is produced from non-renewable resources (e.g., fossil fuels) [8,9]. During the industrial revolution in Europe, fossil fuels were mainly employed for energy needs. The constant fear of depletion of oil reserves and an alarming rise in CO$_2$ emission has led to increased awareness about our depleting non-renewable resources [10]. As the need of LIB are highly rising, the significant shortage of Li is

quite likely to happen in the future as compared to available Li resources in the earth crust. Henceforth, post-Li batteries based on sodium, magnesium, potassium or aluminium technology are gaining traction recently [11,12]. In accordance with the German government law of 'Energiewende' sanctioned in June 2011, there are continuous efforts in ruling out nuclear energy by the end of 2022. This law anticipates to increase the renewable energy utilization for grid electricity purposes [9,13]. In case of the automotive sector, electric mobility is being more critical as electric vehicles gain popularity. In the foreseeable future to achieve the dreams of a 400 to 500 km range for battery electric vehicles (BEV), there is a need for substantial progress to develop battery technology with high capacity and low cost [2,14]. Hence continued research efforts for finding novel battery materials are obligatory for a green world.

In recent years, inkjet printing has attained fascinating importance in scientific research and technology with the advent of printed electronics [15]. Major developments in the inkjet printing techniques gave promising links to bridge the gap between conventional thin-film polymer synthesis, polymer blends, and composites over conventional electronics process [16,17]. In a printed transistor, a gate insulator is used, giving rise to the electrolyte-gated transistor (EGT). Because of the higher capacitance values of the electric double layer (EDL) formation at the semiconductor and electrolyte interface, EGT can be operated at low voltage. Printing has gained immense interest over the past years due to its diverse applications in display, sensing, solar cells, lighting, batteries, RFID, etc [18]. For all the aforementioned printed applications, it is necessary to develop printed batteries for powering the printed circuits. Thus, we expect that the printed energy storage devices will gain more popularity due to the eco-friendly printing process, possible coverage over large areas, and better integration into internet of things (IoT)-based devices [19]. It is anticipated that the market demand for flexible organic and printed electronics market is expected to surpass 300$ billion by 2028 [17,20].

Printable electronics is an intriguing and challenging area that requires printable functional material ink development and device engineering. In foreseeable future printed electronics will complement rather than compete with silicon-electronics. Fabrication of batteries via printing is preferred in this study due to the following merits such as variable geometry, non-contact printing, low ink consumption, flexibility with inks, reduced size and most importantly as a power source for printed electronics.

For nearly three decades, lithium-ion batteries have transformed our daily lives powering the portable electronics. For many years, tweaks given to anode and cathode materials have improved the capacity and energy density of lithium-ion batteries, but the cost factor of LIB

still needs much improvement. To meet the market demands of LIBs, battery technologies which offer good safety, low cost of manufacturing, long lifetime etc needs to be fabricated on a large scale via roll-to-roll or solution-based printing processes [21].

Another difference between common LIB chemistries and printed electrolyte gated systems is the operating voltage. Due to the utilization of an electrolyte gating material, an operating voltage less than 2 V is only needed to operate an electrolyte gated field-effect transistor (EGFET) [22]. Higher potentials, as they are occurring in standard LIB (>3 V), would lead to a decomposition of the electrolyte and therefore are not suitable for a direct power supply of the device. Therefore, redox couples can be used for printed electronics, which otherwise would be insufficient regarding potential or reversibility. There are limited reports about printed batteries with next-generation LIB electrodes. Few reports detailing printed electrodes with graphene [23], LFP [24], SnO_2 [25], Si [26], LTO [27] etc are present. However, none of them have used composite Si (Si/C) or fluoride-based active materials for printing. Hence, an extensive study is necessary to understand the mechanism of ion transport in printed next-generation electrodes. Taking inspiration from these, in this dissertation, the main focus is on printed rechargeable batteries, which contain less amount of toxic elements and offer high capacities. The principal aim of this thesis is the integration of a fully printed thin-film battery (both anode and cathode) to meet the power requirements of printed electrolyte gated transistor (EGT) circuits. Initial investigations are focused on Si anode and Si is a promising candidate for next-generation anode material and abundantly available on earth crust. Si-Li follows alloying reaction and offers much more capacity than commonly used graphite [28–30]. First investigations for alloying FeS_2-based cells were reported as early in 1976 [31]. Later, the room temperature electrochemical performance of Si was shown in 1999, depicting reversible capacities of ~500 mAh/g [21].

One of the attractive candidates for high energy density LIBs is conversion based cathodes. Although the problem of low reversibility in conversion cathodes cannot be overcome by printing procedures, it is not necessary for printed cells in single-use devices to show high reversibility, rendering these materials as ideal candidates for printed batteries due to their exceptional first cycle capacities. The origin of high entropy materials (HEM) is based on the well-known entropy stabilized metallic high entropy alloys (HEAs), which consist of the solid solution of various metals. Similarly, the same concept of stabilization of a single-phase structure by utilizing high configurational entropy can be applied to ionic compounds wherein the multiple cations are occupying the same lattice, thereby increasing the configurational

entropy. Since their discovery in 2015, HEO compounds have attracted immense interest as a new class of crystalline solid solution materials[32]. High entropy fluorides (HEFs) represent an additional class of high entropy ceramics, which have recently attracted attention especially due to the development of HEO. A series of HEF was obtained by a simple mechanochemical process. Transition metal fluorides are promising conversion reaction cathode material with high theoretical capacity (>500 mAh/g) in comparison to the conventional intercalation cathodes. Fluoride based materials are interesting candidates for achieving high-capacity batteries [33]. However, the limitations faced by the conversion materials are the large volume expansion, voltage hysteresis and high irreversible capacity etc. [34]

1.2 Research Scope

Printed electronics is an emerging technique and they need energy storage devices, where printed batteries are most desirable option. This thesis provides an outline of the utilization of printing technology for fabricating next-generation Lithium-ion battery (LIB) cathodes and anodes, finally preparation of a printed full cell. Choice of materials for anodes and cathodes is done diligently. Si is considered primarily because of its large capacity and HEFs are the promising conversion material with high capacity. Since we are printing low power electronics, we only need 1 V to 2 V, so we can make use of high-capacity conversion cathode materials instead of a high potential intercalation material. The scope of this dissertation work is to find a methodology to power the printed electronics circuits. In order to streamline the respective energy storage device, the most suitable devices are printed batteries, as explained in the motivation section. Therefore, this thesis connects the areas of printed electronics and electrochemical energy storage with the development of next generation battery electrodes. The goal of the proposed study is to explore the alloying (Si) and conversion type (HEF) reaction mechanisms as printed LIB electrodes for powering printed electronics circuits.

In the anode section, anodes were printed using Si/C composites, and electrochemical testing was performed. To gain better understanding of the electrochemistry of alloying anode materials, variety of analytical techniques were implemented. In the first part of the study, composite carbon coated Si (Si/C) nanoparticles were prepared by simple pyrolysis. Si/C nanoparticles were printed by microplotting technique. Carbon coated composite Si anodes have immense potential to mitigate problems associated with capacity fading during charge-discharge cycles.

In the second part of the study, the development of a novel high entropy ceramics, the high entropy fluorides (HEFs) as a prospective cathode is described. Multicomponent rutile structured fluorides containing 4 to 7 transition metals (Co, Cu, Mg, Ni, Zn, Mn, Fe) in

equiatomic ratios were synthesized using a simple mechanochemical approach. Later, HEF was examined as a lithium battery cathode material, and their underlying mechanisms of conversion reaction are investigated. This paves the way for tuning the reaction mechanism and the tailoring of electrochemical behaviour by changing the elemental composition of the electrodes. Later, a full cell consisting of lithiated nickel cobalt manganese oxide (NCM) with the composition $LiNi_{1/3}Co_{1/3}Mn_{1/3}O_2$ (NCM111)//coated Si (Si/C) is used for powering printed electronic circuits. Finally, the application of HEF cathode in a full cell configuration with lithiated Si/C anode is also demonstrated.

1.3 Outline of this work

An outline of the thesis content is briefly presented in a chapter wise manner.

Chapter 2 gives an overview of fundamental concepts and basics of LIB, principles of different anodes and cathodes, the printing of battery electrodes. Fundamentals of printed electronics and fabrication of printed transistors are also dealt. In addition, the review of cathodes and anode materials are also introduced.

Chapter 3 deals with the basics of various analytical characterization techniques, and relevant equipment details are also summarized. Techniques, such as X-ray diffraction (XRD), Raman spectroscopy, thermogravimetric analysis (TGA), scanning electron microscopy (SEM), transmission electron microscopy (TEM) were used to identify the phase purity, crystal structure and morphology of as-synthesized electrode materials. The electrochemical performance characterization methods are detailed. Printing methodologies and its principles are also explained.

Chapter 4 deals with the synthesis of silicon-coated with carbon (Si/C) composite, printability of Si/C nanoparticles, and its electrochemical testing. Current unsolved issues for next-generation anode electrode materials will be discussed.

Chapter 5 primarily explains the experimental synthesis of HEF nanoparticles. Structural characteristics and investigation of functional properties are shown in this section.

Chapter 6, presents the electrochemical examination of HEF electroactive materials. Battery performance was evaluated by galvanostatic charge-discharge cycling, cyclic voltammetry (CV), and electrochemical impedance spectroscopy (EIS). Insights about conversion mechanism and affirmation by various ex-situ structural techniques are explored.

In Chapter 7, finally, the summary of the derived conclusions of this dissertation and suggestions for future scope are discussed.

Chapter 2 Fundamentals

2.1 Introduction

This chapter aims to introduce the fundamentals of lithium-ion batteries (LIBs), the individual components of LIB and printed electrolyte gated transistors (EGT). First part covers the basics of LIB, electrochemistry of each electrode material, energy storage principles and its applications. Further sections emphasize the classifications of printing technology, the application preview of printing in batteries and the electronics field. Operation principles of electrolyte gated transistors (EGT), mechanisms and their characterizations are also reviewed.

2.2 Lithium-Ion Batteries

As the name implies the working principle of Lithium-ion batteries (LIBs) relies on the repeated shuttling of lithium ions back and forth between the cathode and the anode. LIBs denote electrochemical device, which converts chemical energy into electrical energy. Owing to the light weight and lowest negative electrode potential of Li, LIBs are characterized by the highest energy density values as compared to the other conventional battery systems [35] and the advantages of LIBs are summarized in Table 2.1. Because of these qualities, LIBs continue to attract wide applications in portable electronics and electric vehicles. The first commercialization of LIBs was done in the 1991 by Sony. Batteries are essential for displays, sensors, RFID tags, solar cells, portable electronics etc [36]. In the 2019, three scientists were accoladed with the Nobel Prize in Chemistry for pioneering the innovations of LIBs. LIBs offer a unique combination of high power and energy densities in both gravimetric and volumetric terms, making it plausible for the portable electronics systems, electronic textiles, medical diagnostics, and hybrid electric vehicles [2]. High specific energy densities are highly desirable for portable electronics and e-mobility applications. The global market of LIBs is primarily for energy storage in portable devices and electric vehicles, with an estimated growth of more than $76 billion in 2020 [14]. This is possible due to the unique advantages of LIBs, specifically, negligible memory effect, low self-discharge, high energy density, etc [37]. Significant introduction of IoT devices and wearable electronics in our daily lives, printed electronics circuits became an attractive choice due to their low-cost and scalable technology. These printed electronics circuits require an energy storage device; namely "printed batteries". Printed batteries can be prepared by similar printing techniques and serve as a unitary integrated power source.

Table 2.1 Summary of the commercial battery chemistry systems and their properties (adapted from [38]). Following the choice of battery materials chemistry, the cell voltage, capacity, and energy density value of the whole battery are decided upon [37].

Type of battery chemistry	Specific Energy (Whkg^{-1})	Operating voltage (V)	Remarks/Attributes of battery systems
Lithium-ion	250	4.0 (depends on electrode chemistry)	Li is the lightest element, high capacity, negligible memory effect, good charge retention
Lead acid	30	1.9	Low cost, rechargeable, car battery, low energy density
Alkaline	120	1.5	Primary battery, suitable for low power devices
Ni-metal hydride	100	1.2	Suffers from memory effect, lower energy density values
Ni-Cd	50	1.2	Memory effect, cadmium pollutant, toxicity, low energy density

2.3 Working Principle of Lithium-Ion Battery

The main components of LIBs include: anode, cathode, electrolyte and separator. Anode and cathode denote the electrically conducting parts of LIBs. Conventionally, anode and cathode are called as negative and positive electrodes respectively. Among the electrodes side, anodes (negative electrode) are casted on the copper current collector and the cathode (positive electrode) on the aluminium current collector. The separator is a thin electronic insulating layer between two electrodes and usually wetted by a liquid electrolyte (Li-ion conducting). During the charging process, Li^+ ions are moving from the Li-containing anode and passing through the electrolyte-soaked separator and finally intercalating to the anode host structure. As a result, the electrons pass through the external circuit in the opposite direction. The reverse process occurs during discharging reaction thereby enabling current flow. Due to the shuttling of Li ions, LIBs are often denoted as "rocking chair batteries" (de/lithiation electrochemical reactions are listed in Equation 2.1 and 2.2). Enviably, electrode materials should possess high volumetric and gravimetric capacities, long cycling stabilities, inexpensive and environmentally benign. To obtain a high open circuit voltage, in the full cell, high and low values of redox potentials are necessary. Besides the active material, an electrode usually consists of conducting carbon

(additive) and a polymer binder. The binder is an important constituent of electrode material, which 'binds' the active material to the current collectors. Hence, the adhesion ability of the binder is critical for maintaining the stability of the electrode matrix [39]. A commonly used binder for non-polar solvents is polyvinylidene fluoride (PVDF) usually dispersed in NMP (N-Methyl-2-pyrrolidone). Water-based inks utilize binders such as sodium carboxy methyl cellulose (SCMC) and poly vinyl alcohol (PVA). Conducting polymers such as PEDOT: PSS can also be used as binders in electrode materials [40]. Carbon black is usually used to improve the electrical conductivity of the electrodes as conductive carbon. The typical structure of a rechargeable LIBs with LCO cathode and graphite anode is illustrated in Figure 2.1. The detailed description about the components of LIBs, crystal structures of various electrodes and their electrode performance is given in the next sections.

The half-cell reaction at the positive and negative electrode is given by Equations 2.1 and 2.2 (here, $LiMO_2$ denote the layered lithium transition metal oxides with mixtures of Ni, Co, and Mn as cathodes):

$$LiMO_2 \rightleftharpoons Li_{1-x}MO_2 + xe^- + xLi^+ \qquad \text{(Equation 2.1)}$$

The half-cell reaction at the positive electrode is given by (where x can range from 0 to 1):

$$C_6 + xLi^+ + xe^- \rightleftharpoons Li_xC_6 \qquad \text{(Equation 2.2)}$$

The specific capacity (gravimetric/volumetric) of a battery material is defined as the amount of charge stored per active mass or volume of the material. During higher amounts of delithiation, the maximum utilization of the theoretical specific capacity is not fully exploitable, as the crystal structure becomes unstable at a high degree of delithiation. State of charge (SOC) can be estimated by finding the ratio of the remaining capacity divided by the theoretical capacity. Another important parameter is coulombic efficiency (η_c) which is related to the current recovery or reversibility of the electrochemical reactions. Coulombic efficiency (ideal value is 100 %) is calculated by the ratio of amount of charge delivered at the discharge by the given amount of charge. Lower values of coulombic efficiency denote degradation, side reactions, electrolyte decomposition (irreversible capacity losses) etc. It should be noted that depending on the battery material, the state of the battery can be inferred from thermodynamics.
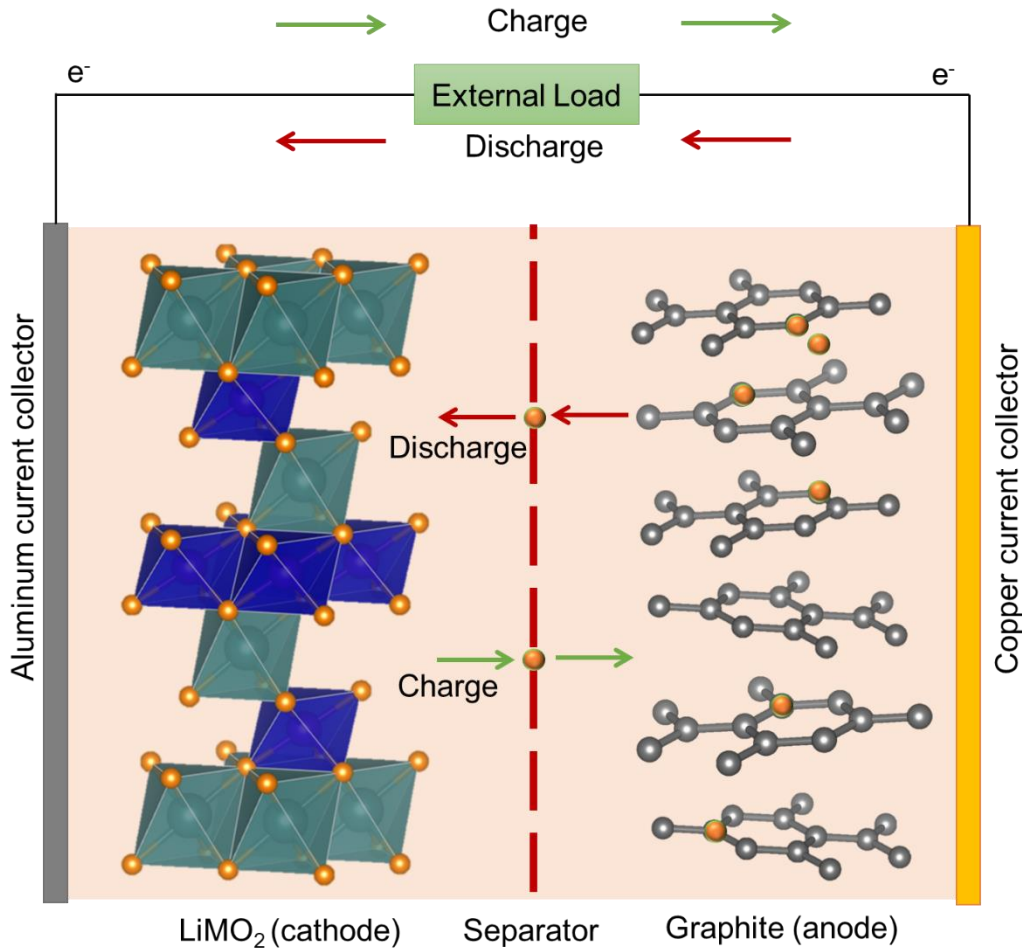
Figure 2.1. Schematic of a lithium-ion battery (LIB) with *LiMO₂* (LiCoO₂ as an example) as cathode and graphite (C) anode showing the charging and discharging modes (golden colored balls represent Li ions).

According to Gibbs free energy rule, the maximum effective work occurring in a chemical reaction is given by Gibbs free energy term. Gibb's free energy is the resultant of enthalpy (ΔH) of reaction deduced by the product of entropy change (ΔS) and absolute temperature (T) (refer Equation 2.3).

$$\Delta G = \Delta H - T\Delta S \hspace{5cm} \text{(Equation 2.3)}$$

In addition, ΔG term also corresponds to the maximum electrical work resulted from an electrochemical reaction (known as Nernst equation) (Equation 2.4) [41] as given below:

$$\Delta G = -nFE \hspace{6cm} \text{(Equation 2.4)}$$

where n is the number of transferred electrons, F the Faraday constant ($F \approx 96485$ C/mol) and E is the potential difference between the electrodes. Batteries are classified as primary and secondary batteries, depending on the possibility to recharge the system (secondary battery, accumulator) or on irreversible reactions that make it necessary to dispose of the battery after

use (primary battery). Therefore, the occurring redox reaction in these battery systems is either reversible or non-reversible [42].

2.4 Electrolyte

The standard electrolyte formulation includes a mixture of linear and cyclic carbonates (with ethylene carbonate, EC and dimethyl carbonate, DMC) along with lithium salt. Lithium hexafluorophosphate ($LiPF_6$) is a commonly used salt that forms the ion conducting part. Separator, serves as an electrical insulating part and is porous. It is primarily made of the polymeric membrane (polyethylene or polypropylene) or glass fiber composites [43].

2.5 Anodes

For the development of cells with higher energy density, specific capacity and working potential is quite critical. Prominent active anode materials for LIBs are: Si, graphite, $Li_4Ti_5O_{12}$ (LTO), TiO_2, Fe_3O_4, Co_3O_4, etc. [44–47]. Spinel type LTO has the highest redox potential among the other anodes and provides good thermal stability. Due to the "zero strain" effect material, LTO anodes possess a negligible amount of capacity loss during cycling [48]. LTO is an excellent choice for anode due to its virtuous Lithium-ion intercalation and de-intercalation reversibility with no structural change during charge-discharge cycling times [49]. During the early days of LIBs development, Li metal was used as a prominent anode material. For instance, Li offers the lowest redox potential (-3.04 V vs. H_2/H^+) and the highest specific capacity (3860 mAh/g), thereby providing high energy density. However, Li is a highly pyrophoric and light metal. The inherent limitations of elemental Li were needle like dendrite formation through the separator and resultant short circuiting of whole cell [50,51].

Since the commercialization of LIBs in the 1990s, graphite is still renowned as a state-of-the-art anode. Partly due to the low cost, graphite is still one of the extensively used anode material for the past 20 years. Table 2.2 shows the basic characteristics of available anode materials so far. Presently carbon containing materials are used for the commercially available anodes. During Li intercalation, the graphite electrodes expand up to 10 % and it possesses a specific capacity of 372 mAh/g [52]. The limitations of graphite include the unfavorable orientation for the current flow, resulting in low diffusion of Li ions [53]. Broadly, carbonaceous materials can be classified into two types: graphitic carbon and non-graphitic carbon. Graphitic type carbon is often regarded as "soft carbon" with better crystallinity. Non-graphitic counterpart is amorphous in nature and belongs to the "hard carbon" category. The structure of graphite can be described as a stacked pile of planar carbon and follows -A-B-A-B stacking sequence (A and B are carbon layers). Due to the weak interlayer bonds, Li ions can be inserted into or out of the host graphite structure. With the insertion of lithium, the stacking pattern can be shown

as -A-I-A-I- (where I is the guest Li layer). Typical lithium insertion/extraction reaction of carbon material anode can be given as Equation 2.5 (here the value of x can be between 6 to 12):

$$Li^+ + e^- + xC \rightleftharpoons LiC_x \qquad \text{(Equation 2.5)}$$

It is to be noted that one Li ion is intercalated to six carbon atoms (Li_xC_6), during the Li insertion process. This causes low energy density and inefficient carbon usage. Due to the lower redox potential, the irreversible capacity loss is caused due to the solid electrolyte interface layer (SEI) formation [54,55]. To circumvent these difficulties, different carbon based micro- and nanostructures are designed. These include 1D carbon nanostructures (nanotubes, nanofibers and nanorods), 2D carbon nanostructure (graphene) and 3D porous spherical structures (core-shell) [56,57]. In addition, mesocarbon microbeads (MCMB) are also utilized for good cyclability due to their low surface area, reduced side reactions and high packing density [58].

Table 2.2 Summary of characteristics of the commonly used anode materials [59–61].

Compound	Acronym/Common name	Materials structure	Practically achieved specific capacity (mAh/g)	Average potential vs Li/Li$^+$ (V)
Li_xC_6	Graphite	Layered	330-365	0.10
$Li_4Ti_5O_{12}$	LTO	Spinel	130	1.55
$Li_{22}Si_5$ (exists in many alloys forms)	Si	Alloying	4200	0.40

2.5.1 Alloying Electrodes

Alloying materials denote the elements which can electrochemically alloy with Li and attain compound phases with Li. As elaborated before, graphite suffers from limitations like safety issues (Li deposition) and low specific capacity. Alloying anodes are attractive due to higher magnitudes of theoretical specific capacities offered than graphite [28]. Alloying materials offer the possibility to achieve very high capacities to the cost of reversibility. Alloying anodes (for example, Sn, Sb, Mg, Si, Ag, etc.) can compensate lower capacity of graphite anodes. Alloying materials like Si is one of the prominent next generation anode material abundantly available on earth crust. Among these, Si has relatively low lithiation potential of ~0.4 V vs Li$^+$/Li (see Table 2.2). Lithiation of metal anodes is usually based on the insertion or chemical alloying

mechanism. Similar to the graphite intercalation reaction (LiC$_6$), Si active material forms Li_xM (*M* represents metal) during the reaction with lithium [63]. Since the *x* value ranges over 1 (*x* varies from 0 to 4.4), the alloying anodes are characterized by higher theoretical capacity. The lithiation stages occurring in Si anodes are demonstrated in Figure 2.2 and Equations 2.6 to 2.7. Here *x* denotes the molar ratio of Li to Si and ranges from 0 to 4.4.
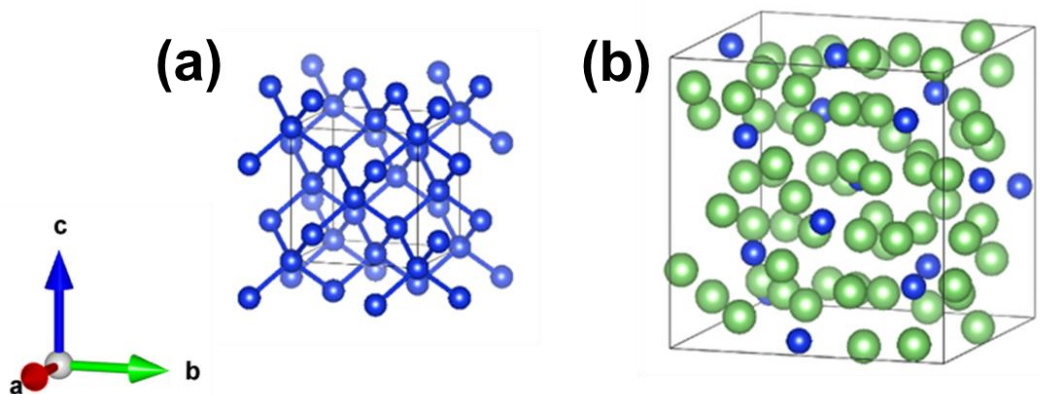
Figure 2.2 Schematic of the crystal structure of silicon anode material and illustration of different Si lithiation/delithiation stages is given, a) denotes the pristine starting Si crystal structure and b) lithiated Si phase (blue and green spheres denote Si and Li respectively) [62].

During lithiation/delithiation reaction:

$$Si\ (crystalline) + xLi^+ + xe^- \rightleftharpoons Li_xSi \qquad \text{(Equation 2.6)}$$

But practically during delithiation process, the crystallinity of Si is destroyed as given below:

$$Li_{15}Si_4(crystalline) \rightarrow Si(amorphous) + yLi^+ + ye^- + Li_{15}Si_4(residual)$$

$$\text{(Equation 2.7)}$$
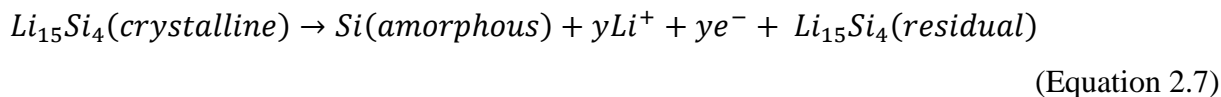
The compositions and crystal structures of the distinct Li-Si alloys during cycling process are given in Table 2.3.

Si during alloying reaction suffers from large volume expansion and low electrical conductivity which lead to capacity fading [64,65]. It is known that the alloying reaction of Li with Si is associated with volume expansion (up to ~300%) and pulverization effects [66]. This huge volume change can be accompanied by active material rupture, interparticle and carbon conductive network contact loss, as well as active Li consumption loss in the first cycles. One of the major disadvantages hindering the full cell usage of Si to reach commercial market maturity is the irreversible capacity loss in the first cycle. In general, the alloying reaction of Si with Li is a conversion reaction in which each Si atom can hold 4 Lithium atoms. To date, the highest Li rich phase reported is Li$_{22}$Si$_5$ (Li$_{4.4}$Si) and this composition provides lithium storage capacity of ~4200 mAh/g [66,67].

Considering the phase change during Li alloying reaction of Si in initial cycles, phase transition of Si occurs from crystalline to amorphous state. The presence of residual amorphous Si phase can reduce the stress induced during the reverse transition (from amorphous to crystalline phase) and it is favorable for overcoming the limitations of volume expansion. Furthermore, is also beneficial to use nanosized Si particles as active material instead of micron-sized active material, to counter fracturing of Si particle and Li trapping [68]. Hence, it is extremely important to overcome the inherent Si anode limitations via rational nanostructuring of the anode. One of the successful strategies to elude the huge volume variation of Si is to provide extra void space and introduction of inactive matrices (polymer matrices), to create composite structures. Perhaps, the most plausible approach is carbon composite structured Si, namely: Si-in-C (tubes), carbon coated Si and SiNPs@CNT (Si nanoparticles with CNT). Here, the carbon structure could effectively comply with the volume expansion, provide a continuous conductive network but at the cost of reduced battery capacity. Wu *et al.* elucidated a model structure for Si NP (Si nanoparticle) scattered on the porous carbon nanotube walls. This provided free expansion of Si nanoparticles using the empty space available in porous structure [69]. Li *et al.* reported a pomegranate structure of Si@C composite in which individual Si nanoparticle was impregnated with a porous carbon shell. Promising battery performance and 99.8 % of coulombic efficiency was reached at the end of 500th cycle [70]. Another issue for Si anode is the large consumption of Li over the first cycles and to alleviate this issue pre-lithiated Si electrodes can be employed [71–73]. Additional delimiting factor for Si is the presence of the native SiO_2 dielectric layer. This can be detrimental for battery performance due to the Li trapping, slow formation of various silicate species during cycling and blocking of Li to attain a fully lithiated Si phase [74,75]. Further, binders can also influence the long term cycling stability and loss of capacity [29]. The expansion/contraction of Si during lithiation/delithiation must also be catered by an elastic binder. Presumably, poly vinylidene fluoride (PVDF) is not the best choice due to the rigid properties. Water-based binders show excellent compatibility for Si anodes, for instance, poly vinyl alcohol (PVA) and poly acrylic acid (PAA) [74,76,77]. Regardless of all these efforts, the SEI layer is ruptured during cycling, fluorinated electrolytes (FEC additive) can be used for enhancing flexible SEI layer formation [78–81].

There are numerous ways reported in the literature for the synthesis of Si-carbon nanocomposites. These include pyrolysis, ball milling, mechanochemical milling etc. To ensure the adherence of active Si nanoparticles, structuring the current collector by using a conductive copper fiber network is also favorable for capacity retention [82]. In short, over 20 years of time

span, there were several improvements in Si anodes and more innovative research methods need to be implemented in the research of Si anodes to reach commercialization.

Table 2.3 Different alloy formation stages and their respective unit cell volumes along with specific capacity values (adapted from [83]).

Compound	x value in Li_xSi	Unit cell volume (Å^3)	Crystal structure
Si	0	160.2	Cubic
$Li_{12}Si_7$	1.71	243.6	Orthorhombic
$Li_{14}Si_6$	2.33	308.9	Rhombohedral
$Li_{13}Si_4$	3.25	538.4	Orthorhombic
$Li_{22}Si_5$	4.44	659.2	Cubic

2.6 Cathodes

Among the cathodes, active materials, such as intercalation [84], insertion [1] and conversion materials [85] are examined thoroughly by various research groups. Many cathode materials, e.g. $LiCoO_2$ (LCO), $Li(NiMnCo)O_2$ (NCM) or $Li(NiCoAl)O_2$ (NCA) contain toxic and heavy metals but exhibit very high reversibility during battery cycling. Nevertheless, the capacity of these materials is quite low (160 - 200 mAh/g) which is the result of a redox process, capable of transferring only one electron per formula unit while discharging [85]. With regards to the structure, $LiMn_2O_4$ spinel phase compounds provide a three-dimensional network, layered $LiCoO_2$ shows a two-dimensional network and polyanionic olivine, such as $LiFePO_4$ shows a one-dimensional network. Spinel $LiMn_2O_4$ (LMO) has advantages from the abundance of Mn and lower toxicity. LMO crystallizes in the general formula $A[B]_2O_4$ in a cubic closed packed structure. In an array of oxygen atoms, Li occupies tetrahedral sites and Mn locates in octahedral sites. This paves the way for a three-dimensional diffusion network. At lower voltages, LMO suffers from huge capacity fading due to Jahn Teller distortions and dissolution of Mn ions into the electrolyte [86,87].

Another new class of polyanionic cathode materials is phosphor-olivine type cathode material, $LiFePO_4$ (LFP) known for the good thermal and high-power capability. Li storage and reversible insertion properties were first shown by Goodenough *et al.* in 1997 [88]. Even though LFP offers environment safety, cheaper material costs [89] etc, one dimensional lithium paths result in sluggish Li^+ diffusion. To circumvent the low electronic conductivity, several carbon coating methodologies are used to increase the electrode conductivity [90,91]. Other reported olivine structures include $LiMnPO_4$ (LMP) and $LiFeSO_4F$ (LFSF) which offer higher cell

voltages and reasonable specific capacity (171 and 151 mAh/g respectively) than LFP [92,93]. Quite a few disordered intercalation compounds with Li rich phase have been reported, which include Li_3NbO_4 [94], $Li_{1.3}Ti_{0.4}Mn_{0.4}O_2$ [95], $Li_2Ni_{1/3}Ti_{1/3}Mo_{2/15}O_2$ [96], Li_2MnO_2F [97] etc. Typically, mechanochemical milling has been used for the inclusion of fluoride anions inside the disordered lattice, as it offers the direct synthesis. This partial substitution of O^{2-} by F^- could exploit the inclusion of oxygen as redox pair and increase the voltage of these materials [98]. Overall, as a summary, the important properties of the state of the art commercially available LIBs cathodes are given in Table 2.4. Despite the innocuous prologue of LIBs as a source for energy storage; the battery industry is still expediting a new range of electrode materials that could bring improvements in shelf life, cycles, energy density, cost, and safety boundaries.

Table 2.4 Characteristics of commercially used state of the art LIB cathodes [85,99–101].

Cathode compound	Acronym	Materials system	Practically achieved specific capacity (mAh/g)	Average potential vs Li/Li$^+$ (V)
$LiCoO_2$	LCO	Layered	140	3.9
$Li(Ni_{0.8}Co_{0.15}Al_{0.05})O_2$	NCA	Layered	200	3.8
$Li(Ni_xMn_yCo_{1-x-y})O2$	NCM	Layered	160*	3.8*
$LiMn_2O_4$	LMO	Spinel	120	4.1
$LiFePO_4$	LFP	Olivine	165	3.4
$LiNiO_2$	LNO	Layered	150	3.6
$LiNi_{0.5}Mn_{1.5}O_4$	LNMO	Spinel	140	4.8

*(for NCM-111)

2.6.1 Intercalation Cathodes

In the case of intercalation cathodes, the guest ions (Lithium ions) can be inserted in and out of the host network structure reversibly. The host structure may be based on transition metal oxides and polyanion compounds. These intercalation materials can be categorized as olivine, layered and spinel systems depending on their framework structure (Figure 2.3). The general layered transition metal oxides, include $LiNiO_2$ (LNO), $LiCoO_2$ (LCO) and $LiMnO_2$ (LMO). The layered LCO structure as a reversible LIB cathode active material was first reported by Goodenough. Even though LNO isostructural with LCO, it has a similar theoretical specific capacity (= 274 mAh/g), and suffers from crucial drawbacks. The challenges arise from difficult material synthesis, such as maintaining a stoichiometric Ni ionic state (Ni^{3+} is unstable above

250 °C) and phase transformation leading to dramatic capacity fading [102,103]. The first part of this dissertation work (chapter 4) deals with layered type cathodes for the preparation of full cell, hence more focus is laid on this type of system.
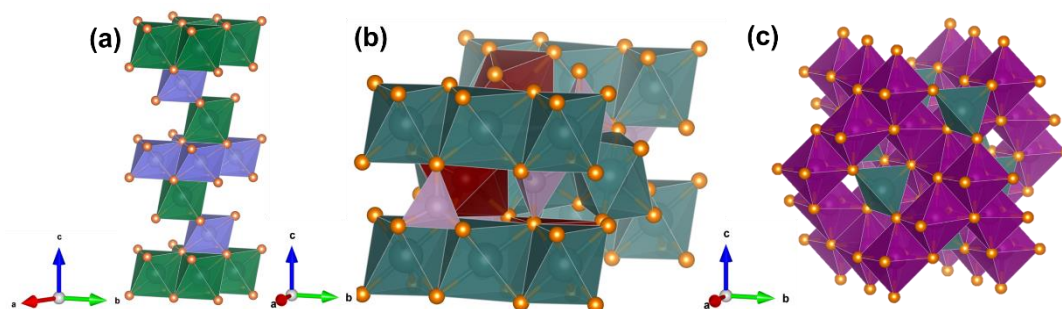
Figure 2.3 Crystal structure of the conventional cathode materials a) layered lithium transition metal oxide Li(NiCoMn)O_2 ($R\bar{3}m$), b) lithium ion phosphate LiFePO$_4$ (*Pnma*) and c) spinel lithium manganese oxide LiMn$_2$O$_4$ (*Fd-3m*).

Mixed transition metal oxides are increasingly used over the last decades arising from the benefits over single transition metal. Due to the demerits of LNO, most research works was focused on the effective replacement of Ni or Co with other transition metal cations. The determining factor for the best candidate may be good cyclability and high energy density [104]. As shown in the Figure 2.4, cobalt is used for maintaining the layered structural nature and to maintain charge neutrality [104,105]. With the inclusion of Co, Mn, Al replacing Ni, subsequent research led to LiNi$_{1-x-y}$Co$_x$Mn$_y$O$_2$ (NCM) and LiNi$_{1-x-y}$Co$_x$Al$_y$O$_2$ (NCA). From the previous reports (note, the electrodes are cycled in voltage range, 3.0 V - 4.3V) with differing Ni content, specific capacity increases from 150 mAh/g (in case of LiNi$_{0.33}$Co$_{0.33}$Mn$_{0.33}$O$_2$ (NCM111)) to ~200 mAh/g for LiNi$_{0.85}$Co$_{0.10}$Mn$_{0.05}$O$_2$ (NCM851005) [106,107]. In many cases, Mn and Al are not a key player in the redox process, rather beneficial in thermal and structural stability [108]. NCM cathodes take advantages (as shown in Figure 2.3) from high-rate capability of LCO, high capacity of LiNiO$_2$ and structural stability with Mn^{4+}. Added to that, due to the lower amount of Co, NCM is cheaper than LCO.

Regardless of the Ni content, the mixed transition metal cathode comprising of Ni, Co and Mn are isostructural to the layered α-NaFeO$_2$ type (space group $R\bar{3}m$), often denoted as NCM cathode. It consists of a layered ABC sequence of O along with alternating layers of Li and transition metals (M= Ni, Co, Mn) and this layering allows two-dimensional Li$^+$ transport paths. Recent research toils to get the maximum specific capacity with Ni-rich NCM type compounds [1]. The next potential candidates for the EV and HEV applications may be high voltage cathode (4.5 V-5.0 V limit) and high capacity LIB cathode (with Li-rich layered oxide cathodes) [109].
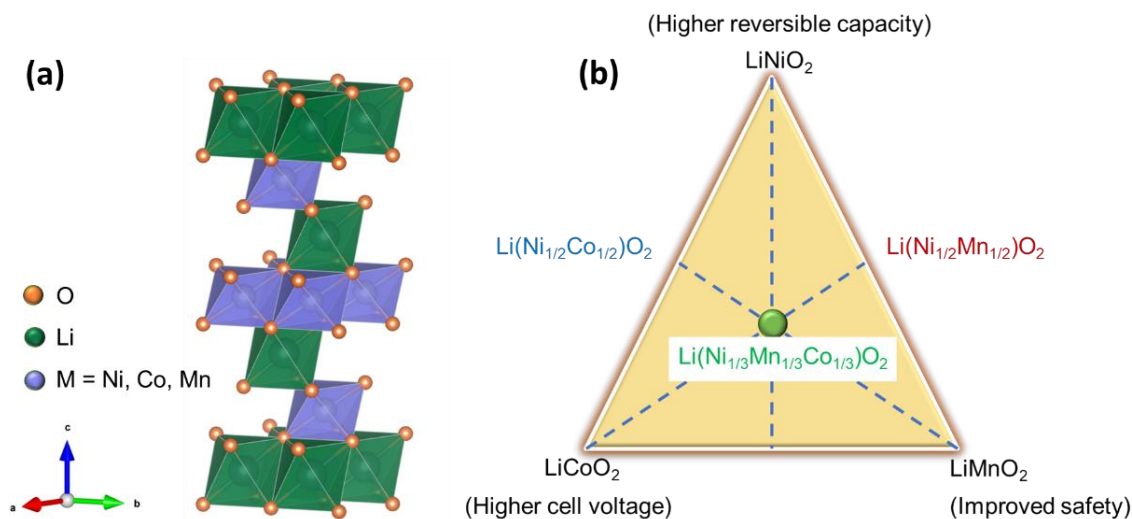
Figure 2.4 a) Unit cell of a quaternary layered lithium transition metal oxide *LiMO₂* (M= Ni, Co, Mn) and b) characteristic properties of Ni/Co/Mn concentrations in layered electrode performance (adapted from [110]).

2.6.2 Conversion Cathode Materials

Due to the limited capacity of insertion materials and huge volume changes in alloying materials, much attention has been gained for a new reaction concept namely, conversion mechanism. Arising from the features of reversible lithium uptake/release behaviour, low environmental impact and low cost, conversion cathodes are potential candidates. Over the past 15 years, conversion type electrode materials gained attraction due to their high capacity compared to conventional intercalation materials [111]. In comparison with the typical intercalation type materials, the majority of conversion materials constituents are less expensive and abundant in nature. Nevertheless, a commercial conversion type electrode is not yet reported, prominently due to the practical limitations which are yet to overcome. The low reversibility of the conversion reaction could be assigned to the complex phase changing steps occurring during the conversion [112].

Conversion materials research in recent years has evolved from transition metal (TM) oxides. Structural conversion occurs during lithiation process, the transition metal compound (MX) is reduced into fine metallic nanoparticle sizes (~1 to 10 nm), and LiX (X=halide ion) [113,114]. In the delithiation reaction, reactive metallic nanocomposites surrounded in LiX matrix decompose back to Li and MX respectively. Fundamental reaction in a conversion material is expressed in Equation 2.8. It is shown from reports that these nanocomposites are continuously formed during many charge/discharge cycles [111]. Subsequently, the reaction of TM compound with the Li is highly reversible and the above stated mechanism is collectively referred to as "conversion reaction".

$$M_xX_y + yLi \rightleftharpoons xM + yLiX \qquad\qquad \text{(Equation 2.8)}$$

where M= transition metal, X = anionic species like O, S, P, N, F. Even though it appears to be a single-step process, in reality, the process progresses through voltage plateaus with different intermediate stages and the active material traverses through various intermittent phase transformations during the lithiation/delithiation process. For instance, in the case of TM oxides as a conversion electrode, they reduce to the respective metallic nanograins embedded in the Li_2O oxide matrix during lithiation process. The conversion reaction is not only limited to TM oxides, but also exhibited by fluoride-based materials (as discussed in chapter 6). In general, it can be concluded that during the cycling process, the conversion electrodes consist of an agglomerated mixture of M_xX_y, M and LiX. Amongst the alloying-based anode electrodes which exhibit capacities well above 500 mAh/g (Si and Sn), not many cathodes have been identified with the matching capacities. Exceptional cases for this are conversion cathodes such as TM containing fluorides-based materials. The energy density of any cathode materials is determined by two factors namely: voltage and capacity. In a conversion reaction, the number of Li ions transferred during the conversion mechanism is normally higher than 1 and hence they are anticipated for having higher energy density. The overall electrode potential of conversion material is determined by the transition metal (M) and anion complex [115]. Hence by changing the constituent elements cell potential can be tuned as per the application requirement [115].

Among the TM fluorides, CuF_2 based material is attractive due to high cell potential (3.55 V) and specific capacity (~528 mAh/g). However, the application of CuF_2 is limited to primary batteries due to the poor electronic conductivity and irreversible redox reaction limit ($Cu^{2+/0}$). Alternative TM fluorides such as FeF_2 and FeF_3 are appealing due to the high reversibility, but lower voltages and capacity fading limits its performance. Nishijima *et al.* investigated cathodic performance of perovskite structured metal trifluoride (MF_3, where M= Fe, V, Ti, Mn, Co) electrodes for Li/Na based batteries. MF_3-C (metal trifluoride-carbon composite) were prepared by ball milling and exhibited over 200 mAh/g as first discharge capacity as LIB cathode [116]. Initial report of MF_3 type in 1997 by Arai *et al.* showed that (M= Fe, V, Ti, Mn, Co) these cathodes still possessed low reversible capacity (80 mAh/g) in comparison to FeF_3. This value accounted for only 34 % of the theoretical capacity offered by Fe^{3+}/Fe^{2+} redox couple [117]. Much more accomplishment was obtained by ball milling carbon with FeF_3 yielding FeF_3-C (composites with carbon). FeF_3-C presented reversible behaviour of 200 mAh/g and an average voltage of ~3 V [118–120]. Since then the group of Yushin *et al.* has examined various metal difluorides (MF_2) and their mixed phases (e.g., $CuFeF_2$) for their reversible Li storage and

conversion mechanism [121–123]. Wang *et al.* gave extensive insights about structural stability and electrochemical properties of ternary metal fluorides ($CuFeF_2$) by density functional theory calculations backed by experimental investigations. Authors found that the conversion reactions proceed through a two-step lithiation process, wherein the first process is Cu^{2+}/Cu^0 conversion, followed by disordered FeF_2 formation (Fe^{2+}/Fe^0) [115].

Despite the attractive features of conversion cathodes such as high voltage (wrt Li^+/Li), large capacity as explained before, the major issues faced by the conversion materials are: (1) low electronic conductivity, (2) lower cycle life, (3) large hysteresis voltage during lithiaion/delithiaton [115]. In due course of cycling, many side reactions namely, electrolyte decomposition, SEI layer formation etc. take place [111]. After repeated cycling, the loss of electrical contact due to pulverization and volume expansion of electrodes is observed [124]. Overall, there have been serious efforts to improve the conversion electrodes performance, however, finding a commercial alternative still is a daunting task. In this dissertation, the synthesis of multi-cationic difluorides (HEF) via a simple mechanochemical milling process and the usage of HEF as a conversion cathode is demonstrated (refer to chapter 5 and 6).

2.7 High Entropy Materials

For the completion of a printed full cell for powering printed electronics circuit, a novel cathode material is necessary. Stemming from entropy stabilized alloys, the utilization of high entropy fluorides (HEFs) and their functional properties are discussed in this section. In the quest for inventing new materials, more research efforts are directed to multiple-cation/anion incorporated compounds. Collectively, high entropy ceramics (HECs) or high entropy materials (HEMs) are equimolar, single phase compound with 5 or more principal cations or anions. The idea of HEMs stems from the high entropy alloy (HEA) materials. First reports of HEA describing structural properties of multicomponent alloys were done by Yeh *et al.* and Cantor *et al.* in 2004 [125,126]. Following the entropy stabilization concept in HEA, Murty *et al.* proposed that the entropy effect could also be anticipated for ceramics and polymeric materials [127]. Until to date, only a few numbers of high entropy ceramic structures are reported in the bulk state. With the innovative report by Rost *et al.* in 2015, a new class of materials namely high entropy oxides (HEO) was introduced extending the concept of HEA to ionically bonded oxides. Authors presented the synthesis of entropy stabilized equimolar solid solution with rock salt phase ((CuCoMgNiZn)O) via solid state reaction method followed by quenching [32]. Following this, developments for HEMs in diverse fields such as, high entropy diboride ceramics, high entropy perovskite ceramics, high entropy rare-earth oxides, high entropy fluoride ceramics, high entropy thermoelectrics, high entropy phosphides, high entropy oxyfluoride materials

were effectively synthesized in bulk form [128–134] [135]. A. Sarkar *et al.* reported the structural features of high entropy oxides (HEO) based on various materials classes [136–138]. HEO ceramics are the multi-cationic equiatomic oxide systems which include rock-salt type $((Cu_{0.2}Co_{0.2}Mg_{0.2}Ni_{0.2}Zn_{0.2})O)$, fluorite type $((Ce_{0.2}La_{0.2}Pr_{0.2}Sm_{0.2}Y_{0.2})O)$, perovskite based $((Gd_{0.2}La_{0.2}Nd_{0.2}Sm_{0.2}Y_{0.2})O)$ ceramic materials [139]. HEM based ceramics provide numerous applications spanning from thermoelectricity, hard coatings, electrocatalysis, hydrogen storage etc [140,141]. In recent years HEMs have also gained significant importance owing to their electrochemical properties [142]. There are few important core effects arising from high entropy effects namely lattice distortion, sluggish diffusion issues and cocktail effects [143].

HEMs can be classified based on the composition or configurational entropy values. Regarding composition, HEMs can be represented as compounds comprising of five or more elements and each constituent has atomic percentage values of 5% to 35 % [144]. Concerning to entropy classification, HEMs are designated as alloys with configurational entropy values greater than 1.5 R [145]. For a homogenous solid solution, ideal configurational entropy values (ΔS_{config}) can be expressed as in Equation 2.9:

$$\Delta S_{\text{config}} = -R\left\{\left(\sum_{i=1}^{n} C_i \log C_i\right)_{\text{cationic-site}} + \left(\sum_{j=1}^{n} C_j \log C_j\right)_{\text{anionic-site}}\right\} \quad \text{(Equation 2.9)}$$

Where R is the Universal gas contact; C_i and C_j denote the mole fraction of elements in cation and anion-site respectively. It has to be noted that configurational entropy primarily depends on a number of elements in the structure. Based on the Gibb's Helmholtz equation (Equation 2.10), this provides competition between the enthalpy of mixing various elements (ΔH_{mix}) and increased entropy (ΔS_{mix}), resulting in the Gibbs free energy ΔG_{mix}:

$$\Delta G_{\text{mix}} = \Delta H_{\text{mix}} - T\Delta S_{\text{mix}} \quad \text{(Equation 2.10)}$$

The selection criteria of the anions or cations in HEMs for attaining a solid solution are based on Hume-Rothery and Pauling's rules. These rules take into account the elements with similar ionic radii, charge neutrality, solubility and crystal structures. Hence the concept of entropy stabilized multi-element alloys were taken forward to oxides and other systems [146]. HEM compounds have also aroused interest in rechargeable battery fields. For example, Bérardan *et al.* formulated single phase $(CuCoMgNiZn)_{1-x-y}Ga_yA_xO$ (where A= Li, Na, K) electronically insulating compound as a solid-state Li conducting electrolyte. They found that when Li doping content in the A-site exceeds 20 mol %, the material exhibits superionic Li conductivity surpassing the commercially available LIPON (lithium phosphorous oxynitride). This attribute of Li-ion conductivity makes the HEO interesting for electrolyte applications [147]. In battery applications for the first time, HEO compounds were used as anodes which revealed entropy

stabilized conversion mechanism. In spite of micron sized electroactive material, the HEO anodes showed reversible long-term cycling with specific capacities of ~ 650 mAh/g (at 0.2 A/g) even after 900 cycles [142]. The practical demonstration of HEO anode and a standard NCM (111) cathode in a pouch cell configuration to drive series string of LED was conducted by Wang *et al.* [148]. In addition, intercalation cathodes with layered O3-type HEO structure showed the potential for reversible sodium or lithium-ion battery (SIB/LIB). Owing to the entropy stabilization, these novel compounds exhibited long term cycling stability [149–151].

Recently, Wang *et al.* extended the concept of enabling entropy contribution from multiple anionic sites along with cationic contribution, providing another class of high entropy ceramic namely, high entropy oxyhalides. These were devised by the incorporation of LiF and NaCl in the parent HEO structure ((CuCoMgNiZn)O) providing LiF-HEO and NaCl-HEO. With the inclusion of fluorine, the working potential of LiF-HEO shifted from 1.0 V to 3.4 V with regards to the parent HEO phase. Among the reports in high entropy fluorides (HEF), lately, Chen *et al.* synthesized for the first time a single phase transparent high-entropy fluoride (HEF) ceramic with composition $CeNdCaSrBaF_{12}$ (CNCSBF) and it exhibited a near-infrared range and visible-range photoluminescence emission [152]. Nevertheless, there are no reports about the examination of electrochemical properties of HEF compounds and its reversible Li storage mechanism. This aspect would be examined in detail in chapter 6 of this dissertation. So far, various synthesis approaches are available for the preparation of the HEM for instance, solid state reaction, wet chemical reaction and epitaxial thin film growth [153]. The prevalent synthesis route for HEM is mechanochemical milling wherein powders are mixed with high energy ball milling process. In some cases of high melting point precursors (e.g., oxides) ball milling is employed to mix the powders and followed by one more step of sintering [138]. The wet chemical methods include, FSP (flame spray pyrolysis) [154], NSP (nebulized spray pyrolysis) [138,155], RCP (reverse co-precipitation) [156], CP (co-precipitation) [157] etc. Most of the HEM shows the kinetic effect of metastability and undergoes phase separation while cooling down to room temperature. This shortcoming could be overcome by fast quenching from high temperature (1000 °C) to room temperature within minutes [138,158]. The last synthesis method is epitaxial thin film deposition techniques to attain heterostructures or superlattices [159,160].

2.8 Printed Electronics

Fundamental principles about prominent printing technologies and the basics of printed electronics are described in this section. Conventional inorganic semiconductors based on silicon technology are extensively used in smart phone or computers. These are manufactured via photolithography and etching methods on a Si wafer. Since these applications require ultra-

fast operating/switching speed and low leakage currents, high dielectric constant (k) materials such as SiO_2 are used. However, the Si-electronics fabrication process is complicated and owing to the rigid nature, these are not suitable for wearable devices. Remarkably, printing is a fascinating method used for the fabrication of transistors, which is an essential part of electronic circuits [161].

Over the past decades, portable electronic devices using printed electronics has gained momentum. The area of printing has continued to expand from conventional printing on paper to 'flexible' printed electronics circuits. Printed electronics can be achieved in diverse materials or substrate types such as polymers and textiles [15]. Advantages of printing are namely: fast prototyping, lesser fabrication steps, maskless (no lithography involvement), less expensive manufacturing and it can be scaled up for fabrication in various substrates (papers, polymer or rigid substrates) [16]. All of these advantages collectively can make the printing technologies very appealing for low-cost manufacturing [161,162]. Solution based printing is regarded as a promising method for the fabrication of printed electronics circuits, wearable electronics and devices suitable for internet of things (IoT) applications [20]. To operate the low power-IoT sensors and flexible electronics, rechargeable energy devices are ubiquitous (described in forthcoming sections).

Prominent solution-based technologies can be classified as inkjet printing, slot printing, screen printing, gravure printing, flexographic printing and offset printing [17]. There are distinct attributes for each printing technology, such as ink viscosity, speed of prototyping, thickness control etc. In most printing methods, colloidal solution or nanoparticle dispersion of functional material is deposited directly on the substrate. Broadly the printing methodologies can be classified into two types: contact (e.g., gravure) and non-contact based (e.g., inkjet) printing. A brief summary of the various printing methods and its attributes is shown in Table 2.5. For the fabrication of electronic devices mainly, screen printing, ink-jet printing and aerosol-jet printing (roll-to-roll (R2R)) are usually employed.

Typically, any printing process requires the transfer of functional ink onto the desired substrate. Screen printing is the mature and most prevalent technique based on a push-through process in which inks are passed through a metallic or polymer mesh screen. The screen plate contains the desirable pattern to be printed. The main advantages of screen printing are low cost, fast printing and diverse patterning possibilities [16,163]. Inkjet printing technology is a digital printing technology which provides maximum flexibility in terms of ink versatility, diverse substrate choice and slow to moderate printing speed. It is also denoted a drop-on-demand (DOD)

printing, which can be categorized as thermal and piezoelectric DOD printing. As the name implies, thermal energy is used for squeezing ink out of the nozzle. This is implemented by creating bubbles in the ink solvent. In the case of piezoelectric DOD printing, ink is discharged from the nozzle via the application of a voltage signal to a piezoelectric device. Inkjet printing enables to reduce the loss of material during the printing in comparison with screen printing. It is inexpensive, simple and provides wide flexibilities in ink and substrates [16]. In this thesis, chapter 4 describes the fabrication of electrolyte-gated transistors via inkjet DOD printing. In aerosol printing, an aerosol of ink solution is created with the help of high-pressure gas (e.g., N_2). This places limitations on aerosol printing as solvent parameters must be regulated. Hence aerosol printing has complexity in printing even though it offers high printing resolution. Roll-to-roll printing is suitable for high volume, continuous deposition and large-scale manufacturing. Here the important part is a rotating roll which transfer the print pattern to the substrate. This state-of-the-art contact printing can be categorized into gravure, flexographic, offset and rotary screen printing [164].

Another important DOD technique based on contact printing via a piezoelectric device is microplotting. The print patterns are transferred to the substrate similarly as the writing with a fountain pen. In this method, a fine tapered glass capillary tube is glued to a piezoelectric device. The resonant frequency of the hollow capillary tube changes due to ink inside the capillary. The resonant frequency of the capillary tube can be detected by vibrating it within a frequency range of 100 kHz to 700 kHz. For dispensing the ink to the substrate, this frequency is applied to the capillary as given in Equation 2.11:

$$f = nv/2L \qquad\qquad\qquad\qquad \text{(Equation 2.11)}$$

wherein velocity is given by $v = \sqrt{\gamma P/\rho}$, (γ denotes the Laplace correction for resonant frequency of a hollow tube), L is the capillary length, P is the applied pressure and ρ is the mass density of the capillary, which depends on the ink contained in the capillary.

To assist the printing process, the capillary tube is contacted on the substrate and a suitable voltage is applied to the piezoelectric material for the ejection of ink. Microplotting is very helpful to print inks with variant viscosities, surface tension values and particle sizes. The final resolution of the print pattern can be adjusted by changing the capillary tube diameter.

Table 2.5 Summary of the features among various printing techniques [15,165].

Printing technique	Printing principle	Layer thickness range (µm)	Resolution (µm)	Viscosity range (mPa s)	Throughput (m^2/s)	Material wastage; need of controlled environment
Gravure	Ink splitting	0.8 - 8	75	50 – 200	60	Yes; Yes
Flexographic	Ink splitting	0.8 - 2.5	80	50 – 500	10	Yes; Yes
Offset	Ink splitting	0.5 - 2	20 - 50	30000-100000	5 - 30	Yes; Yes
Inkjet	Pressure or thermal impulse	0.3 - 20	20 - 50	1 - 30	0.01 – 0.05	No; No
Screen	Pressing ink	3 - 100	20 – 100	500 – 50000	2 – 3	Yes; No

2.8.1 Field-Effect Transistors

One of the key components present in most of the electronic devices available today is the transistor. It is a three-terminal device in which current flow between two electrodes is modelled by a current or an electric field applied to the third terminal. The basic architecture of a transistor consists of: a semiconducting channel, a gate dielectric, drain, source, and gate electrodes. FETs are unipolar devices, where electrons or holes can be the charge carriers [166]. Among the different classes of FET, metal oxide semiconductor field-effect transistors (MOSFETs) are the particularly sought ones for electronic applications. First report of the early MOSFET structure by Lilienfeld, consisted of copper sulfide as a semiconductor layer, aluminium (as source, gate and drain electrodes) fabricated on a glass substrate [167]. Today, the important constituent in any available electronic devices is MOSFET. In general, MOSFET is equivalent to an electrical switch constituted by three parts namely: dielectric (which block the electron flow), conductor (offers electron conduction) and semiconductor (which allows electronic conduction under certain applied bias). As the name implies, semiconductor has tuneable properties and its resistance value can be changed the application of voltage on a conducting plate, which is separated by an insulating layer. The advantages of MOSFET include fast switching speed and higher impedance, low leakage currentsas compared to ipolar junction transistors [166]. Many

architectures of MOSFET were established in the recent past and this stemmed the development of modern transistors.

The working principle of MOSEFT is based on the charge carrier flow from one drive electrode (source) to the other (drain) electrode. This charge carrier flow is controlled by a field applied at the gate electrode. Here, the source and drain electrodes connected to the external circuit. Generally, the gate electrode is insulated from the channel via an oxide or dielectric layer. Figure 2.5 shows the typical structure of a electrolyte gated transistor (EGT) and its double layer formation principle. With the application of voltage V_{GS} (gate voltage w.r.t grounded source) across metal (gate) electrode and semiconductor contact, an electric field is established. With the electric field formation, charges accumulate in the channel at the semiconductor/dielectric interface layer. To maintain charge neutrality, opposite polarity charges are formed at the metal gate electrode. As the semiconductor layer is smaller, the charges are distributed over a small thickness at the semiconductor/dielectric interface. Hence the voltage applied to the gate terminal controls the current carrier density of the semiconducting channel, which can regulate the source-drain current. In this dissertation, to understand the characteristics of MOSFET devices, two types of measurements were performed: (1) sweeping of V_{GS} with constant value of V_{DS} (drain voltage w.r.t grounded source), this results in transfer characteristics and (2) by varying V_{DS} with constant V_{GS} voltage will give us output characteristics. The output characteristics can be divided into three distinct regions viz., linear, nonlinear and saturation regions. With the lower drain voltage values, FET channel behaves like an ohmic resistor (linear relationship of voltage with the current). At higher drain voltages, channel potential builds up at the drain electrode end and channel differs from a linear resistive behaviour. Note that, at this point the channel begins to deplete towards the drain end. When V_{DS} increases, at certain point the channel is pinched off. In the event of pinch off, gate loses control of charge flow between source and drain. Finally, the drain voltage saturate as a result of the negligible inversion layer at drain terminal and this value of V_{DS} is called saturation voltage [167]. This particular value of the drain voltage at which the drain current saturates is named as pinch off voltage. The relationship of the drain current with varying gate voltage is quadratic in nature and can be described in simplified form as, $I_D \propto (V_G - V_T)^2$. The detailed derivation of drain current I_D can be found in [168,169].

2.8.2 Electrolyte-Gated Transistors

In this subsection, the principles of electrolyte gated transistors (EGTs) are discussed. Electrolyte gated transistors (EGTs) were invented in 1950s, but the concept of using EGTs is gaining prevalent attention since past decades [170]. There is great surge of interest in EGT due

to the low voltage operation and easy printing steps. Typical structure of EGT and its interfacial double layer formation is shown in Figure 2.5. The basic difference between MOSFET compared to FET is the presence of gate insulator layer. In the case of MOSFET, high dielectric constant materials (SiO_2) are employed as gate dielectrics, which generate capacitance by dielectric polarization. Conversely, electrolytes are used in EGTs for the effective capacitance via the formation of electric double layers (EDLs). EDLs are produced by the accumulation of ionic charges at the interface of electrode and electrolyte. With the application of electric field, ions will accumulate at the interface and polarization of these ions result in EDLs formation [170]. The first model of electrode polarization and EDLs formation was proposed by Hermann von Helmholtz *et al.* in 1853 [171]. Due to serious shortcomings of this model, numerous models were developed by Stern *et al.* and Grahame *et al.* along with many other groups. Inner and outer Helmholtz plane formation corrugated by Grahame model is commonly used for modelling of EDLs. Many configurations of FET such as in-plane gate geometry FET and porous channel FET can broadly employ electrolyte gating mechanism [18,170,172].
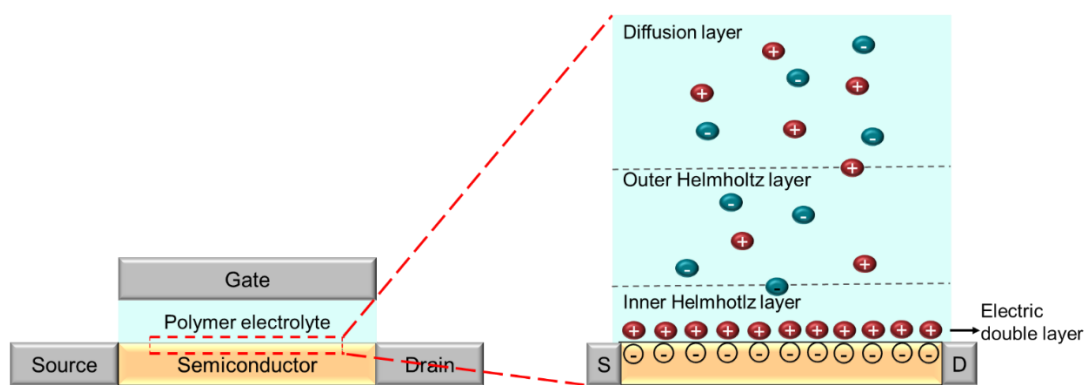
Figure 2.5 Schematic illustration of an electrolyte gated transistor and the electric double layer formation at the interface of semiconductor/electrolyte (adapted from [173]).

EDLs formation arising from polarization of accumulated ions at interface usually exhibits capacitance values of ~10 µF cm^{-2} [174]. This is far higher than those offered by inorganic dielectrics. Due to this higher capacitance values in EGT, they typically require low gate voltages, V_g (< 2V) and hence there is surge of interest of EGT in low voltage electronic circuits. A printed graphene electrode based EGT is implemented in the current thesis (detailed in chapter 4). Inorganic based dielectrics often are not viable for flexible electronics as it suffers cracks during the substrate bending. On the contrary, the polymer electrolyte in EGT delivers flexibility and elasticity, enabling application in wearable electronics [164]. The inkjet printing process be effectively used for the fabrication of EGT based devices quite easily.

It has to be noted that one of the demerits of EGT is the slow switching speed. This arises from the slow ionic movement and formation of the EDLs. For critical switching speed demanding applications MOSFET devices are more competitive than EGT. Hence future research efforts should be dedicated to enhance the ionic conductivity values and accelerate EDLs formation process.

Finally, in this section, a brief overview of printed electronics studies in the fabrication of circuit components reported so far is detailed. Marques *et al.* pointed out the advantages of printed electronics over Si based component fabrication counterparts [18]. Electrodes of an EGT transistor were patterned via electron beam lithography and inkjet printing was used for the top-gate electrodes, along with an electrolyte gated oxide layer. The authors found that an extremely low voltage supply is necessary for powering inkjet fabricated transistors. This might be beneficial for lower operating voltages applications such as smart sensors and wearable electronics [175]. Marques *et al.* also reported about the electrolyte-based FET from organic oxide semiconductors and proposed that high mobility and electrical characteristics can be modelled by PSPICE simulators [176]. Nasr *et al.* prepared an electrolyte gated ZnO nanowire FET with solid polymer electrolyte. This study provides a perspective on the fabrication of inkjet printed transistors at room temperature [177]. Liu *et al.* reported the fabrication of inkjet printed thin film transistor with ZnO and PVP as the active device and gate dielectric respectively [178]. The implementation of inkjet printing for passive components like resistors, capacitors and inductors on polyimide substrates was shown by Kang *et al.* [179]. It has to be noted that inkjet printing cause uneven and less uniform morphologies with partial coverage of channel [180]. Recently, Singaraju *et al.* showed the potential application of printing technique by the fabrication of graphene thin film transistor with electrolyte gating. Furthermore, contrasting of top gated devices with PEDOT: PSS and their in-plane counterparts with merits in device switching speed and current values were illustrated [164].

2.9 Printed Batteries

For all the applications of printed electronic devices as described above, the primary requirement is the power supply unit. In recent years, there is high demand for compact batteries due to the smaller size of the portable electronics devices. Most cases, the size of the electronic device is determined by the battery, as battery size cannot be reduced at the cost of capacity. The terminology 'printed battery' denotes the combination of printing and battery technologies, wherein at least one component must be printed. It is challenging to develop printed battery which meets the space constraint laid by the electronic circuits. On the other hand, to reach the ultimate goal of "all-printed batteries", more studies must be devoted to the development of

printed separators and printed electrolytes along with printed electrodes. Printing process is a facile and fast prototyping technology that can be carried out at room temperature. Amidst the printed batteries field, Li and Zn based (Zn/MnO_2 or Zn/Ag) batteries are the commonly used ones and they differ mainly in the constituents [181]. In any printing process, the print pattern is achieved by the application of specified ink on an appropriate substrate. Batteries belonging to flexible or stretchable types can also be regarded as printed batteries if one or more components are fabricated by printing techniques. Moreover, the support structure such as copper or aluminium current collectors are mostly non-printed constituents.

First step for the development of printed batteries is tailored electrode ink/slurry preparation as needed for the type of printing technique [182]. Prerequisite for any printed electrode slurry includes: (1) rheological properties (apt viscosity range tuned as per the printing method), (2) dispersivity of the electrode powders, (3) structural stability (adhesion with substrate, agglomeration) [182,183]. One of the crucial factors for printed batteries is high active material loading for better battery performance. When electrode thickness increases, it leads to mass transport limitation of Li^+ ions of electrolyte; overall this will lead to the reduction in battery capacity [184,185]. The porosity of the printed electrodes also is important, as it can directly influence the electronic and ionic conductivity values [186]. Next, to render electronic conductivity in electrodes, conductive additives such as carbon nanotubes (CNT), carbon black (C65/C45) are often added. Another important part of LIB which provides conductive path to external circuit is current collectors, available in the form of foams, meshes, foils etc. Usually, metallic Al and Cu foils are widely used as cathode and anode current collectors respectively. Only a few reports exist for the printed current collector due to the metallic nature and rigidy for structural support. A spray coated CNT current collector was described by Singh *et al.*, which showed sheet resistance value as low as ~10 Ω sq^{-1} [187].This finding indicates the applicability of printing by using versatile metallic inks. A printed UV-cured separator membrane consisting of crosslinked polyacrylic acid and polyethylene oxide fillers exhibiting mechanical robustness are also reported [188]. Printed flexible solid-state electrolyte consisting of UV cross-linked ETPTA polymer network (mechanical framework), EC/PC solvent (high boiling point solvents) and alumina nanoparticles (nano spacers) was demonstrated by Lee *et al*. Stencil printing technique was used to print the tuned electrolyte paste onto substrates and later it was subjected to UV curing process for solidification [188]. Additionally, one of the emerging fields useful for fabricating different form factors of micro-nano structured electrodes is 3D printing methods [189]. Detailed description about the electrode and printable ink formulation can be found in Chapter 3 (experimental section).

Among the printed battery anodes, different inks based on anodes like tin oxide (SnO_2) [25], silicon (Si) [26], lithium titanium oxide (LTO) [190], graphene [23], carbon nanotubes (CNT) [191] were reported. The major attributes of printed batteries along with their advantages are listed in Figure 2.6.

Table 2.6 Overview of different printed battery chemistries and its components.

Components	Battery constituents	Attributes/Functions	Examples	Ref.
Current collector	Metallic foils for positive and negative electrodes	Possess high electronic conductivity; transmits or conducts current in/out of electrode	Cu and Al	[192]
Separator	Polymer membrane	Prevent short circuit, enable ionic conductivity	Silica based ionogels with ionic liquid for LIBs; KOH gel electrolyte in PAA for Zn/MnO_2 type	[193–195]
Electrodes	Anodes	Absorption of Li ions	LIBs: SnO_2, $Li_4Ti_5O_{12}$(LTO) or graphite; other battery types: Zn or Ni	[196–198]

Electrodes	Cathodes	Source for Li ions, determining factor for cell capacity	LIBs: LiCoO$_2$ (LCO), LiMn$_2$O$_4$ (LMO), LiFePO$_4$ (LFP); other battery types: Ag$_2$O and MnO$_2$	[193,198,199]
Electrode additive	Conductive material	Provide electrical conductivity of electrode	Conductive carbon black	[200]
Binders	Polymer binders	Important for adhesion of electrodes to the current collector and provide mechanical strength	CMC, PMMA, PVDF, PEO	[201–203]
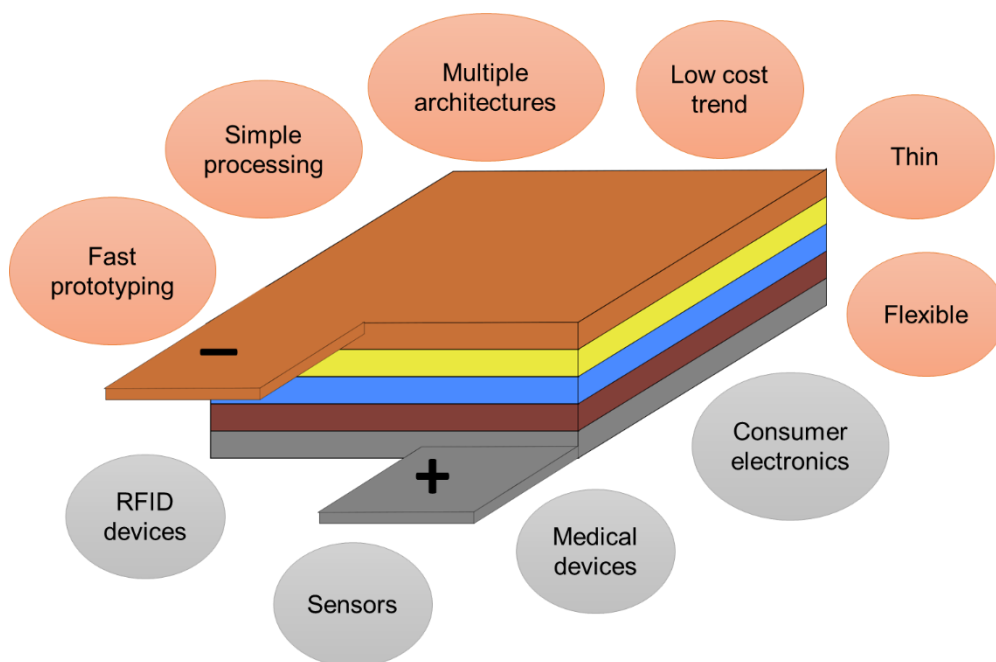
Figure 2.6 Schematic of a printed battery, overview of the main applications (grey colour in bottom) and main features (red colour on top) of the printed batteries (adapted from [19,204]).

On the cathode side, LiCoO$_2$ (LCO) [200], LiFePO$_4$ (LFP) [205] were also realized as printed cathodes. On the organic battery side, Gaikwad *et al.* demonstrated the fabrication of printed batteries for driving ink-jet printed circuits. They showed that a flexible printed battery can be used to power an ink-jet printed 5-stage complimentary ring oscillator based on organic

semiconductors [206]. R. Kumar *et al.,* in their radical report, showed a printed stretchable zinc: silver oxide rechargeable battery, which might pave way for wearable electronics regime [207]. These low-temperature printed components are quite interesting in the industrial perspective and are widely viewed as the "next generation" printable storage devices. A brief overview of the literature reports about the printed battery components are given in Table 2.6. In this dissertation, the focus is mainly on printable secondary batteries which were prepared by microplotting method. Later these printed cathode and anode electrodes were integrated to make a fully printed battery to meet the power requirements of printed electronic circuits (explained in Chapters 4 and 6).

Chapter 3 Experimental Section

3.1 Introduction

This chapter explains the experimental characterization techniques, sample preparation and printing methodologies involved. A brief description of each experimental technique and the sample preparation methods are given in the following section, therefore the morphological (scanning and transmission electron microscopy) and structural techniques (such as X-ray diffraction, Raman spectroscopy) are explained. Finally, galvanostatic cell cycling, cyclic voltammetry (CV) and electrochemical impedance spectroscopy (EIS) are discussed. Emphasis is laid on the battery cycling and printed cell fabrication section, which forms the essential part for the anode and cathode section. In addition, battery electrode ink and transistor ink preparation and printing methods are also discussed.

3.2 X-ray Diffraction

With the discovery of X-rays in 1895 by Röntgen and the first observation of diffractions of X-rays in 1913 by Bragg (W. H. Bragg and W. L. Bragg), the science of X-ray crystallography was born [208]. X-ray diffraction (XRD) is a standard technique used for determining the sample structure or composition. XRD normally employs X-ray beams as the wavelength is quite similar to the spacing of the atoms in sample. In this thesis, XRD was mainly employed to identify the crystallinity and phase purity of the electrode materials. The planes at which scattering of X-rays occurs is called lattice planes. The notation of lattice planes is given by the *hkl* values known as the Miller indices. When X-ray beams are scattered by a periodic array of atoms in a crystal, they interact with the electrons, creating a diffraction pattern. With constructive interference of elastically scattered X-rays (shown in Figure 3.1), it follows the Bragg's law [208] stated in Equation 3.1.

$$n\lambda = 2d \sin \theta \qquad \text{(Equation 3.1)}$$

Where *n* represents a positive integer, λ is the incident X-ray wavelength, *d* is the interplanar spacing and θ denotes the incident angle.

When the path difference of the monochromatic X-rays (upon reflection on lattice planes) matches with an integer (*n*) multiple of the wavelength, constructive interference is resulted. Intensity of each Bragg peak at a given crystallographic plane (*hkl*) depends on the scattering power of atoms. The relationship between atomic position and intensity I_{hkl} is given by the structure factor F_{hkl}. Equation 3.2 provide the intensity which is proportional to the square of the structure factor [209]:

$$I_{hkl} = |F_{hkl}|^2 \qquad\qquad \text{(Equation 3.2)}$$

In turn, the structure factor can be evaluated by the Equation 3.3 [208]:

$$F_{hkl} = \sum_n f_n \cdot e^{i\Phi_n} = \sum_n f_n \cdot e^{i2\pi(hx_n+ky_n+lz_n)} \qquad\qquad \text{(Equation 3.3)}$$

Where f denotes the atomic form factor of the atom 'n', Φ is the phase shift of the atom n and x_n, y_n and z_n are the fractional coordinates of the nth atom in the elementary cell.

Peak identification and background corrections were performed with the HighScore suite (PANalytical B.V, version 2.2). The results of XRD are usually plotted as a function of signal intensity for various angles of diffraction corresponding to the two theta angles. More the intensity of a peak, one can infer that large amounts of crystals are present with that distinct spacing. The width of individual peaks is inversely related to the crystal size of the particles. In powder samples, due to the random orientation of the grains, the diffraction condition of individual crystallites is met for various sets of lattice planes. This results in diffraction pattern with multiple peaks, collectively called Debye-Scherrer cones.

XRD measurements of Si, Si/C (anode) and pristine high entropy fluorides (HEF) based nanoparticles (cathode) were conducted using Bruker D8 Advance diffractometer with a Cu-Kα radiation source (λ=1.54 Å) and equipped with a LYNXEYE detector of fixed divergence slit (0.3°). XRD patterns were collected in the range from 10° to 90º (2θ) and with a step size of 0.02º and 4 s time per step at a source voltage and current of 30 kV and 40 mA, respectively. Rietveld refinements were performed by using the TOPAS software (TOPAS 5, Bruker) to identify phase composition and lattice parameters. LaB_6 (NIST 660a) was used as reference material to determine the instrumental intensity distribution for the refinement of XRD data. Structural model for pristine HEF nanoparticle (HEF7, explained in chapter 5) was created using 3D visualization software, VESTA (Visualization for Electronic and Structural Analysis). In cathode section, X-ray diffraction (XRD) measurements were conducted on the HEF7/CNT battery electrodes at different states of charge (SoC) during cycling to probe the reaction mechanism. XRD patterns of all HEF based electrodes and pristine powders were measured with STOE Stadi P diffractometer, equipped with a Ga jet-Kβ radiation source (λ=1.208 Å). For the different cycled electrode samples, the sample powder was collected from the respective electrodes after collecting the residue inside Ar filled glovebox. XRD sample preparation, measurements and phase analysis were done by author.
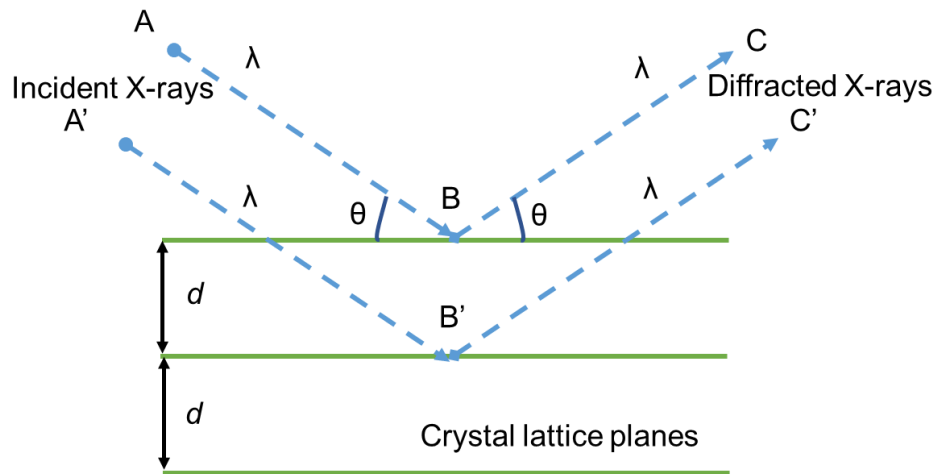
Figure 3.1 Schematic of incident X-rays strikes on a set of planes (with interplanar spacing *d*) and angle of diffraction (*θ*).

3.3 Electron Microscopy

Electron microscopes utilize electron matter interactions to evaluate the structural, morphological, compositional and chemical features of the samples. The electron microscope is constituted by electron gun, vacuum pumps, sets of electromagnetic lenses, secondary and back scattered electron detectors etc.

3.3.1 Scanning Electron Microscopy

Scanning electron microscopy (SEM) uses a focused electron beam (typically acceleration voltages upto 30 kV) which is raster scanned over the sample surface. As shown in Figure 3.2 the electron beam interacts with the sample surface and produces backscattered electrons, Auger electrons, secondary electrons and characteristic X-rays (refer Figure 3.2). The interaction volume over the sample surface varies depending upon the incident acceleration voltages. Focusing of the beam of electrons is done by using a set of electromagnetic coils. The detector gathers the electrons reflected from the sample surface and with further signal processing, micrographs are obtained. SEM can be performed on all types of solid samples. As shown in Figure 3.2, the incoming electron beam interacts with the atoms of sample at different depths to yield backscattered electrons, secondary electrons and characteristic X-rays. Each of the signal shown in Figure 3.2 has a dedicated detector in SEM. The back scattered electrons originate from the elastic scattering interactions of the electrons that are reflected from the sample. Back scattered electrons have higher energies, hence characteristics about deeper regions of the sample can be studied. In addition, the backscattered electron intensity is dependent on the atomic number (Z), thus it can also provide insights about the distribution of elements in sample, such as allowing differentiation between heavier and lighter elements based on Z-contrast. Secondary electrons arise from the inelastic scattering from beam electrons and

have low energy electrons. Hence, secondary electrons get heavily absorbed and only the ones close to the surface are detected, providing topological information of the sample.

Characteristic X-rays are emitted when the incoming electron beam ejects an inner shell electron. This results in a higher energy electron filling this hole and extra energy arising from the transition is released as X-Ray. The wavelength or energy of these emitted characteristic X-rays can be measured to identify the elemental distribution in the sample. Energy-dispersive X-ray spectroscopy (EDS) [210] detector attached to SEM can be used for elemental analysis. EDS is a quantitative chemical analysis technique, wherein the characteristic X-rays will be detected by a semiconductor detector and the incoming X-ray energy is translated to electric current. The drawback of EDS is the limitation for light element detection. The microstructure of the pristine nanoparticles and cycled electrodes were examined via a scanning electron microscope (SEM) Leo 1530 operated at 5 kV acceleration voltage with 4 mm as working distance value. In this thesis, all samples were coated with thin gold layer (~7 nm thickness) by sputtering technique to avoid the artifacts due to charging effects. SEM powder/thin film sample preparation, measurements and data analysis were done by author.
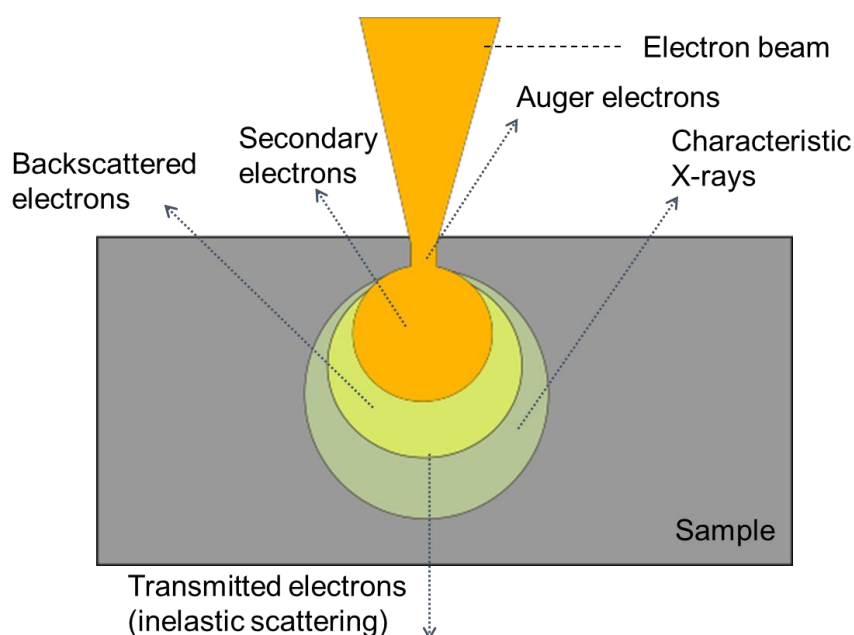
Figure 3.2 Schematic of the electron beam interacting with the sample (adapted from [211]).

3.3.2 Transmission Electron Microscopy

Transmission electron microscope (TEM) is a powerful analytical technique that provides information about morphology, composition and crystal structure of the material. During the TEM experiment, the material is irradiated with high energy electron beam, the resultant interaction can be used to learn about the material characteristics. These include the crystal structure, grain boundaries, lattice dislocations etc.

TEM provides higher magnification than a normal optical microscope or SEM due to the higher electron beam energy [212]. The basic principle of TEM relies on investigating the electrons, which are transmitted through the sample. With the help of high energy electron beam and resulting lower electron wavelength, it is possible to attain higher magnification and atomic resolution. For this criterion to be satisfied, the samples for TEM need to be thin (typically <100 nm). The penetrating electron beam interacts with the atoms of the thin sample via elastic and inelastic scattering processes. The transmitted beam is then detected to which will provide the information about crystal structure, composition, defects etc. In addition, *in-situ* experiments such as *in-situ* battery cycling can also be explored with TEM [213].

Different modes are offered for the TEM characterization, namely imaging and electron diffraction modes [211]. In imaging mode (refer Figure 3.3 a), electrons are focused on the sample by set of the condenser lens. During illumination with the electron beam, some are transmitted through the sample and the transmitted signal is detected by a charge coupled device (CCD). In accordance with mass-thickness contrast, the areas of the sample where more electrons are transmitted exhibit lighter contrast than the less transmitted areas with darker contrast. In diffraction mode (shown in Figure 3.3 b), when electrons traverse through the sample, electrons are scattered by the sample. The scattered light is focused to one point in the image plane using an electromagnetic lens objective. As the electrons are scattered in the same direction, they are collected together in one point. This diffraction pattern namely selected area electron diffraction (SAED) gives information about the crystal structure, space group, and orientation of the sample.

In scanning transmission electron microscopy (STEM) a fine beam of electrons is faster scanned across the sample, then the scattering from each of the points may be measured separately and continuously. Hence, this method requires no extra lenses placed after the specimen. In STEM, we can illuminate a small segment of the sample at one time and magnitude of electron scattering is captured rapidly. In the case of high angle annular dark field detector (HAADF), instead of lenses after the specimen, a set of the annular detector are used. This enables the detection of electrons scattered through large angles, typically > 50 mrad. STEM-HAADF imaging along with other analytical detectors, it is possible to quantitatively access the elemental components of the specimen (upto atomic scale). STEM-HAADF generally allows for better imaging contrast, especially in materials with lower atomic weight compared to conventional TEM imaging. The chemical analysis and quantification of constituents can be performed by Electron Energy Loss Spectrometry (EELS). In EELS, the

kinetic energy change of the electrons after the inelastic scattering process is measured. The change in energy gives the structural and chemical information of the sample. EELS offers the possibility to detect and quantify all elements including the lighter elements unlike EDS.

TEM (HR-TEM, SAED, STEM-EDS and EELS) were used in this study to investigate the crystallinity and local elemental distribution of pristine nanoparticles (Si/C or HEF) and cycled electrodes. All imaging studies was conducted on Si, Si/C powder samples (Chapter 4) and pristine HEF nanoparticles (Chapters 5 and 6) with a Titan 80-300 (FEI) equipped with CEOS image spherical aberration corrector, a HAADF-STEM detector (Fischione model 3000), EDS detector and a Tridiem Gatan image filter.

All imaging of described samples was operated at an accelerating voltage of 300 kV. To avoid the exposure of the samples to air, the samples were loaded into a Gatan vacuum-transfer holder in Ar-filled glovebox and transferred to the TEM instrument. Elemental maps were constructed using energy dispersive X-ray spectroscopy (EDS) for case studies. The as-synthesized HEF nanoparticles and Si/C nanoparticles were dispersed on a holey carbon-coated gold grid inside Ar filled glovebox to avoid any air exposure during TEM sample preparation. HR-TEM, SAED and STEM-EDX analysis were similarly performed on HEF battery samples. TEM electrode sample preparations were carried out inside Ar filled glovebox. These electrodes were washed with EMC solvent and powder samples were collected, which was later dispersed on a lacey gold grid and loaded onto a FEI double tilt holder. TEM sample preparation was done by author. TEM measurements were performed in close collaboration with Kai Wang, at Institute of Nanotechnology, KIT.
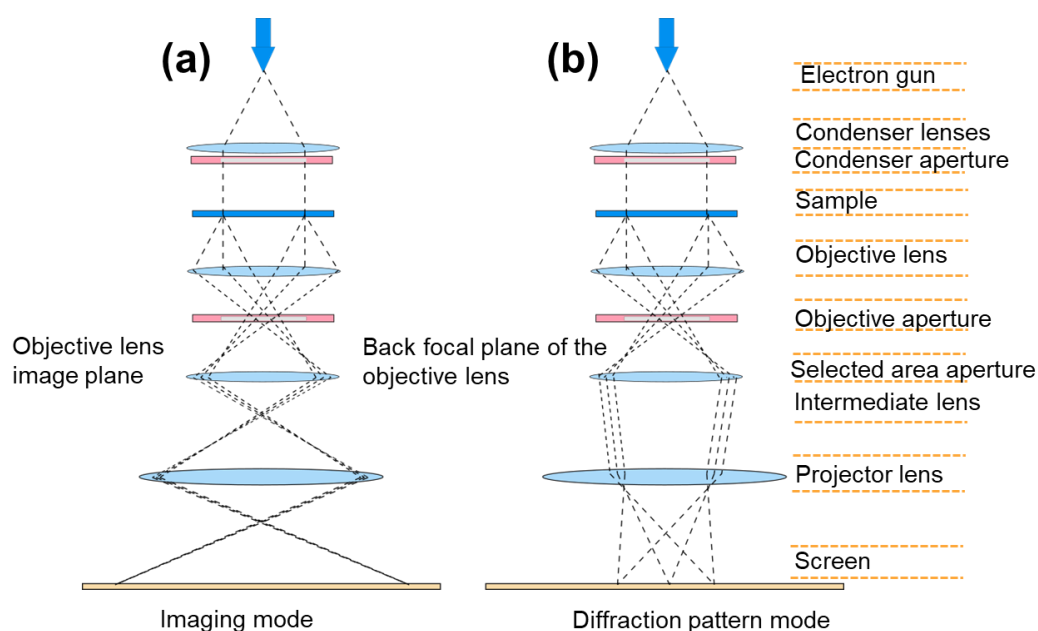
Figure 3.3 Schematic depiction of transmission electron microscope (TEM), in a) TEM sample imaging configuration and b) diffraction configuration modes (adapted from [214]).

3.4 Raman Spectroscopy

Raman spectroscopy is a non-destructive analysis tool for probing the chemistry and structure of the material that originates from the characteristic "finger print" region. Raman scattering is named after the C. V. Raman who discovered this effect in 1928. It is based on the inelastic scattering of the monochromatic light from a laser source. It is highly informative for understanding the type of carbon material and the amount of defects prevalent in the sample [215]. In the first part of chapter 4, Raman spectra of Si/C pristine nanoparticles were acquired to find evidence about the type of carbon coating. Besides, it is a non-destructive method without any complex sample preparation steps and can be used directly on the sample surface.
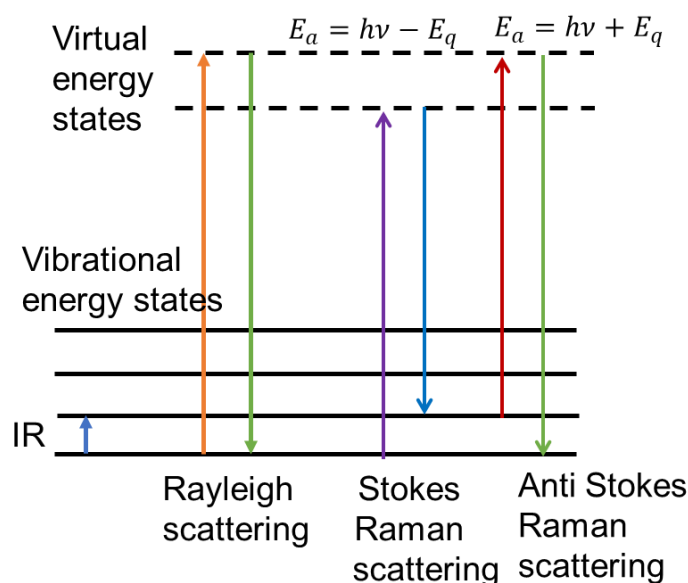
Figure 3.4 Schematic of Raman scattering mechanisms: Rayleigh, Stokes, anti-Stokes scattering, involving two-photon scattering process (adapted from [216]).

Figure 3.4 shows the basic principles of Stokes, anti-Stokes and Rayleigh scattering. When a focused light (mostly from a laser) interacts with matter, photons may be scattered, absorbed or reflected. For the inelastic scattering process, when laser light (E_{laser}) with a definite energy, $E_{laser}(= h\nu)$ is incident on the sample, it undergoes scattering, thereby producing a photon with altered energy (lower/higher). In accordance with the conservation of energy rules, scattered photons follow the form as in Equation 3.2:

$$E_s = h\nu \pm E_q \qquad \text{(Equation 3.2)}$$

Here, *Es* denote scattered photon energy and E_q represents the created or annihilated photon energy during the scattering. Probing of this change gives information about vibrational, rotational and other low energy transitions in materials [215]. Raman effect emerges from the molecular deformations caused by the incident laser beam (oscillating electromagnetic wave)

on the sample. Raman effect is based on two photon scattering process, conversely to one photon process in infrared spectroscopy (IR). According to the scattering mechanism, three different processes can occur in Raman spectroscopy as shown in Figure 3.4.

1. In the first category, a material with no Raman active modes absorb an incoming photon with energy hν from a specific vibrational energy state. After de-excitation, molecule return back to the same vibrational state with no energy change and this is termed as Rayleigh scattering.

2. In the second case, the excitation photon with energy hν is absorbed by Raman active material at a certain vibration state. After a certain amount of energy transfer, the photon comes back to a vibration state with lower energy. When the resultant radiation is scattered with frequency lower than the frequency of incident laser energy ($E_s = h\nu - E_q$) is called Stokes radiation.

3. In the third case, an incoming photon with energy hν is absorbed y the Raman active molecule and the excess energy of the Raman mode is released; while returning to the basic vibration state. The scattered radiation has increased frequency than the incident photon ($E_s = h\nu + E_q$) and is termed as Anti-Stokes radiation.

Raman spectroscopy in this work was performed with a confocal Raman instrument (Renishaw, Wire 4.0, excitation wavelength 532 nm, exposure time 30 s) using the 10x magnifier lens. The spot size of the laser beam was ~ 1 μm and the spectra were taken in the range of 100–3000 cm^{-1}. By deconvoluting the Raman spectra peaks in Wire 4.0 software with two Gaussian wave peaks, the carbon defect band intensities and peak positions were analysed. Raman sample preparation, measurements and data analysis were done by author.

3.5 X-ray Photoelectron Spectroscopy

X-ray Photoelectron Spectroscopy (XPS) is one of the widely used surface analysis techniques to comprehend the surface chemistry, chemical composition and electronic structure of solid sample. With the help of XPS technique, elemental composition and electronic structure of the material sample can be determined. XPS is based on the photoelectric effect first described by Heinrich Hertz in 1887. Later, in 1905, Albert Einstein described the photoelectric effect in detail and was awarded the Nobel Prize in physics in 1921 [217,218]. During XPS measurements, the sample is irradiated with a monochromatic X-ray beam (with Al Kα or Mg Kα) and detected emission electrons are analyzed [219]. As per the photoelectric effect, during the irradiation with X-rays, it triggers the emission of electrons on the surface of sample. The emitted photoelectrons possess kinetic energy (*KE*) and follow Equation 3.3.

$$KE = hv - BE - \phi_s \qquad \text{(Equation 3.3)}$$

where the terms hv, BE and ϕ_s denote the incident energy of photon, binding energy of the electron and the spectrometer work function. Binding energy is unique to each electron in a specific atomic shell and it represents how tightly the electrons are bounded to the atom/orbital [220]. Hence, the binding energy is independent of the type of X-ray source used for ejecting it and it is a material property [217]. Excluding the light elements like hydrogen and helium, XPS technique can be used to identify the rest of the elements in the periodic table. Due to the low penetration volume, XPS is mostly regarded as a surface sensitive technique (< 10 nm), and therefore the detection level is limited to the top layer of sample surface.

In the anode section (chapter 4), XPS measurements of Si/C nanoparticles were conducted using Specs Phoibos 150 electron spectrometer equipped with Al Kα X-ray radiation source. XPS sample scans were performed on the Si/C nanoparticles with spot size of 200 µm. In the cathode section of the thesis (chapter 5), XPS measurements on HEF pristine nanoparticles and cycled cathodes were performed on a K-Alpha+ instrument (Thermo Fisher Scientific) with a monochromatic Al-Kα X-ray source (1486.6 eV) and 400 µm spot size. The K-Alpha+ charge compensation system was applied to prevent localized charge build-up during analysis using 8 eV electrons and low-energy Ar ions. Data acquisition and processing were carried out using the Thermo Avantage software [221,222]. The spectra were fitted with one or more Voigt profiles. The binding energies are reported for the C 1s peak of hydrocarbons at 285.0 eV. The analyzer transmission function, Scofield sensitivity factors[222] and effective attenuation lengths (EALs) for photoelectrons were applied for quantification. EALs were calculated using the standard TPP-2M formalism [223]. XPS sample preparation and data analysis were done by author. XPS measurements for HEF sections were carried out via collaboration with Dr. Azmi Raheleh, and Dr. Julia Maibach from the Institute of Applied Materials (IAM-KIT).

3.6 Nuclear Magnetic Resonance Spectroscopy

Nuclear Magnetic Resonance (NMR) is a well-established technique for examination of structures and dynamics of molecules [224]. In general, NMR spectroscopy can probe atoms with non-zero nuclear spin ($I{\neq}0$) and inherent magnetic moment values. NMR is based on the principle of nuclear magnetic moment interactions within an electromagnetic field in the radio frequency range, while a strong magnetic field (B_0) is applied. During the application of a strong external magnetic field, energy transfer occurs from base energy level to higher energy level, at a wavelength corresponding to radio frequencies. This detected signal is processed further to obtain the NMR spectrum of the nucleus in the specimen. With the help of NMR local defects, atomic disorder, dynamic processes etc., could be detected [224]. Room temperature ^{19}F-MAS-

NMR (magic-angle spinning) data were acquired with a Bruker 200 MHz spectrometer at a field of 4.7 T, corresponding to a Larmor frequency of 188.3 MHz. Spinning was performed at 25 kHz in 2.5 mm rotors NMR spectra were acquired with a Hahn-Echo experiment ($\pi/2$ pulse of 0.5 μs duration). Liquid $CFCl_3$ was used as the reference for the chemical shift calibration. NMR sample preparation, measurements and data analysis were achieved by collaboration Dr. Slyvio Indris at IAM-ESS, KIT.

3.7 Thermogravimetric Analysis

Commonly used thermal analysis methods are thermogravimetric analysis (TGA) and differential scanning calorimetry (DSC). TGA is a method to understand the thermal stability of the sample via heating or cooling the sample at specific temperature. The variation of the sample mass is recorded as a function of temperature (heating up or cooling down) by applying a specific temperature scanning rate (K/min or °C/min). The sample environment is usually controlled by purge gas. Inert gases such as argon or nitrogen indicates the sample decomposition at elevated temperature. Air or oxygen are mostly used to promote the burning of sample for trace material/impurities, quantification of carbon residue or oxidative mass loss/gain etc. In this work, the amount of carbon content (Chapter 4) was estimated from TGA. TGA measurements were carried out on a TG 209 F1 Libra (NETZSCH) at a heating rate of 5 °C/min at the BELLA laboratories, KIT with instrumental support from David Kitsche. Rest data analysis and measurements were done by author.

3.8 Electrochemical Characterization

The prominent methods for the characterization and assessing performance of Lithium-ion batteries are galvanostatic charge-discharge cycling measurements, cyclic voltammetry (CV) and electrochemical impedance spectroscopy (EIS).

3.8.1 Galvanostatic Battery Cycling

The galvanostatic cycling is a widely used technique to estimate battery specific capacity and cycling stability. For this, the cells (whether in half or full-cell configuration) are charged and discharged with a constant current. Each cell is characterized by the current rate or C-rate factor which defines the charging and discharging rates. For example, 1C denotes the amount of current the battery utilizes to charge/discharge the cell in an hour [225]. C-rate was calculated for Si and Si/C anodes as the product of active material loading of absolute Si content (in grams) and theoretical capacity of Si (in mAh/g). C-rate is defined for all HEF cathode electrodes as the product of active material loading of absolute HEF type content (in grams) and the theoretical capacity of HEF (579 mAh/g). The areal loading was maintained in the range of 0.5

to 1 g/cm^2. The voltage charge-discharge profile, rate capabilities and long-term performance of electrodes were examined by galvanostatic cycling. In the present thesis, CR-2032 or coin type cells were prepared and electrochemically examined with Arbin BT-2000 system. Constant current is applied for a definite time interval and resulting cell voltages were recorded accordingly. In typical coin cells, two electrode systems are used quite prevalently, wherein two sides are constituted by sample (either anode or cathode) and Li metal (reference electrode). In some cases, constant voltage step is also included for maintaining Li de/insertion process. Depending on the electrode type, it is usually achieved after reaching a cut off voltage (at a certain constant current).

Figure 3.5 shows the typical charge/discharge profiles of HEF7/CNT composite used as a cathode electrode. From these profiles, charge/discharge capacity and average reaction potentials can be inferred. To understand power and energy density capabilities, C-rate test with different current rates for charge/discharge can be applied. The theoretical capacity (Q) of any active electrode material can be defined as per the Equation 3.4:

$$Q = \frac{nF}{M}$$
(Equation 3.4)

where n denotes the number of transferred electrons (during the redox process), F is the Faraday's constant and M is the molecular weight of the active material. Depending upon the active material, cells were cycled at variant current and cycling rates, which are detailed in the forthcoming chapters.
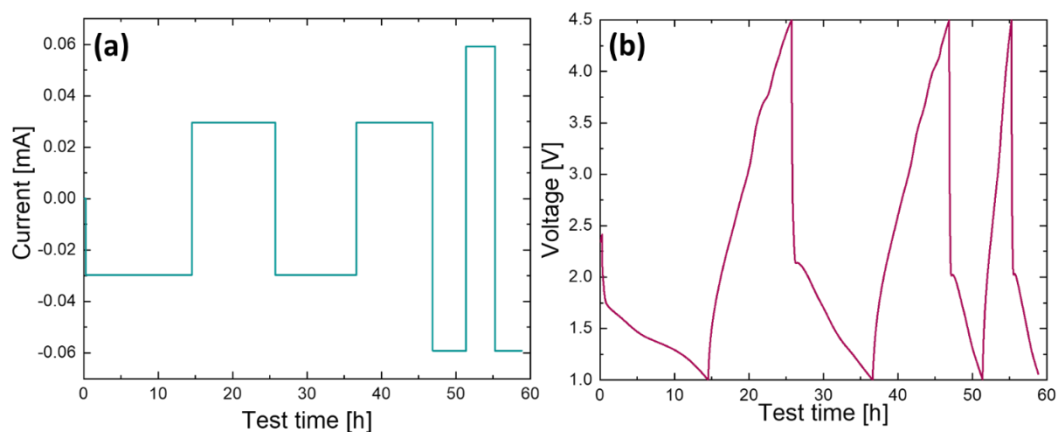
Figure 3.5 a) Schematic depiction of a galvanostatic charge/discharge test carried on a HEF based electrode (described in chapter 6) and b) typical voltage discharge-charge profile of HEF based electrode wrt time in hours.

Figure 3.6 Photograph of Arbin BT-2000 battery test cycler and Binder climate chamber test systems used in this study.

The battery cycling performance of the Si/C anodes (chapter 4) and HEF/CNT nanocomposite cathodes (chapter 6) were measured using Arbin BT 2000 battery cycler kept inside a Binder climate chamber set to room temperature (25 °C). A photograph of Arbin 2000 battery cycler and battery test chamber is given in Figure 3.6. After drying the printed Si/C samples at 80 °C at vacuum, coin type cells (using 13 mm circular Si/C anodes) were assembled in an Ar filled glovebox (O_2 and Ar level below 0.5 ppm), with Li foil (0.3 mm thick, Gelon LIB Co., Ltd, China) as the counter electrode. 1 M $LiPF_6$ in a 1:1 (w/w) mixture of fluoroethylene carbonate (FEC) and ethyl methyl carbonate (EMC) was used as electrolyte. Two pieces of glass microfiber filter (type GF/C, Whatman, 0.26 mm) was used as a separator.

In the cathode discussion part of this thesis, the half-cells (wrt Li counter) were tested with standard liquid electrolyte composed of 1 M $LiPF_6$ in 1:1 (w/w) mixture of ethylene carbonate (EC) and ethyl methyl carbonate (EMC). To identify the influence of the electrolyte, HEF7/CNT type composite electrodes were also tested with 1 M $LiPF_6$ in a mixture of fluoroethylene carbonate (FEC) and ethyl methyl carbonate (EMC) (1:1 w/w) solvents. This electrolyte is a well-known standard for alloying reaction-based materials. Glass fiber separator (GF/C, Whatmann, 0.26 mm) was used as a separation layer. All battery electrode preparation, measurements and data analysis were done by author.

3.8.2 Cyclic Voltammetry

Cyclic voltammetry (CV) is an extensively used potentiodynamic method to probe the redox reaction process inside an electrochemical cell [226]. CV is measured by recording the resulting current while sweeping the voltage input to the working electrode at a constant rate (given in mV/s). It can be employed to find the electrochemical reaction process, voltage window of redox process, the formation and stabilization of the solid-electrolyte interface (SEI) etc [227]. Additionally, CV is a qualitative technique that is quite useful to find the equivalent double

layer capacitance, reaction rate constants and redox reactions of electroactive materials [226]. It can also be used for examining reversible, irreversible and quasi-irreversible systems of electroactive species. In this work, CV measurements of HEF/CNT composite cathodes (at 0.1mV/s within 1.0 V to 4.5 V range) and Si/C anodes (at 0.1 mV/s spanning from 0.1 V to 1 V) were performed using a BioLogic VSP-300 potentiostat device (in two probe configuration). All CV electrode preparation, measurements and data analysis were done by author.

3.9 Electrochemical Impedance Spectroscopy

Electrochemical impedance spectroscopy (EIS) is an important method for identifying the impedance properties of battery cells [228]. With EIS technique, the identification of charge transfer resistance and Warburg impedance can be achieved. This will give evidence for interfacial kinetics at the electrode-electrolyte interface and Li-ion diffusion properties. Assuming a linear relationship, a sinusoidal alternating potential is applied to the sample and the resulting response of phase-shifted current is recorded [229] (as shown in Figure 3.7). The applied AC voltages and recorded currents can be expressed as sinusoidal functions as given in equations (3.5 and 3.6) and by applying Ohm's law (U=IR, equation 3.7), the impedance can be expressed as (pictorial representation is given in Figure 3.6):

$$E_i = E_0 \sin(\omega t) \hspace{4cm} \text{(Equation 3.5)}$$

$$I_i = I_0 \sin(\omega t + \phi) \hspace{4cm} \text{(Equation 3.6)}$$

$$Z(\omega) = \frac{E_i}{I_i} = \frac{E_0 \sin(\omega t)}{I_0 \sin(\omega t+\phi)} = Z_0 \frac{\sin(\omega t)}{\sin(\omega t+\phi)} \hspace{2cm} \text{(Equation 3.7)}$$

where the terms, ω is radial frequency, ϕ denote phase angle shift, I_0 and E_0 are absolute amplitudes.
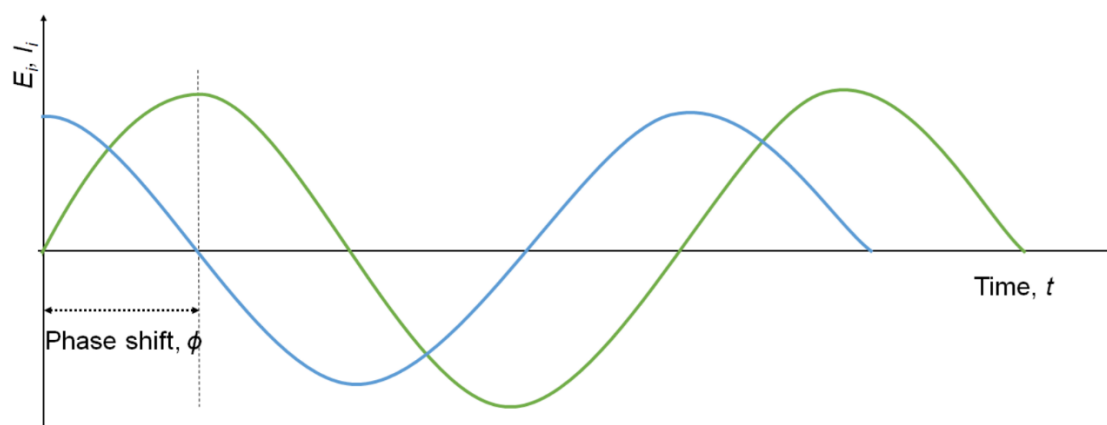
Figure 3.7 Applied voltage input (E_i) and phase shifted current (I_i) response in EIS.

Impedance (Z) properties of a LIB cell can be measured by applying a known voltage at a particular frequency and thereby estimating the resultant current (also frequency dependent)

and phase shift. Parameters that can be derived from EIS are classified into two categories. The primary parameter is correlated to material properties, such as mobility, conductivity, dielectric constant etc. The second property is allied to electrode-electrolyte interfaces namely, interfacial capacitance, effective diffusion coefficients, reaction rate constants etc. [210,230] These phenomena can be identified according to the capacitance values determined for each response. The frequency dependent impedance behaviour of EIS could be delivered in Nyquist and Bode plots. In the Nyquist plot, the real part of impedance (Z_{real}) is given in abscissa while the imaginary part (Z_{imag}) is presented in the ordinate. Typical Nyquist plots consist of a set of semicircles and each point corresponds to a particular frequency. The absolute value of frequency is not evident in the Nyquist plot. To understand the frequency dependent behaviour of LIB electrodes the Bode plot can be used (analysis explained in Chapter 4). In the Bode plot, the magnitude of Z (usually $log|Z|$, defined in Equation 3.8) and phase angle are plotted as a function of frequency. In application specific cases, such as for polymer gels and LIB, the Bode plot is more preferred to examine frequency-dependent behaviour.

$$|Z| = \sqrt{Z_{real}^2 + Z_{imag}^2}$$
(Equation 3.8)

Typically, EIS is measured by fitting the experimentally acquired data with an equivalent circuit model. The commonly used electrical circuit elements are: resistor *R*, capacitor *C*, constant phase element representing a non-ideal capacitor *CPE* and inductor *L*. Inductive components are rarely included as they are observed at very high frequencies (> 1 MHz), which is often the resolution limit of the instruments. To model the mass transfer process, a special Warburg element is typically utilized. In summary, impedance *Z(ω)* is constituted by real and imaginary parts. This value can be experimentally measured and with the help of an equivalent circuit the impedance and capacitance values can be obtained. The commonly used circuit elements in EIS are given in Table 3.1. In the resultant equivalent circuits, these circuit elements are combined in series or parallel accordingly to the EIS measurement data and the experimental cell configuration.

All impedance spectroscopy measurements in this dissertation were carried out using a BioLogic VSP-300 potentiostat device in two-probe configuration. Impedance spectra were acquired by applying 50 mV amplitude signal over a frequency range of 1 MHz to 1 Hz (20 points/decade). The separating layer namely, glass fibre separators (GF/C) was usually wetted with 200 μL standard electrolyte (LP57). For the construction of anode symmetric cell, two printed electrodes (Si or Si/C) were placed towards each other separated by two sheets of glass fibre separator. The electrolyte solution was poured to fill the space between the electrodes to

complete an anode symmetric cell. Symmetric cells of cathode part were constructed in a similar manner sandwiching two HEF/CNT electrodes separated by two sheets of GF/C.All EIS tests were done at room temperature. All EIS sample preparation, measurements and data analysis were done by author.

3.9.1 Equivalent Circuit Analysis for LIB Electrodes

With the help of theoretical electrical equivalent circuit, the EIS analysis can be carried out accurately. Herein the experimental data can be translated to its corresponding electrical equivalent circuit as shown in Table 3.1. Therefore, the crucial part of EIS analysis is fitting the data to the appropriate equivalent circuit. Once equivalent circuit model is selected, the calculated equivalent circuit parameters can postulate more information about the physical and electrochemical phenomena within the cell [231]. EIS experimental plots in this work were fitted by using Zview software (Scribner Associates, Southern Pines, NC). Different algorithms are available for fitting the experimental values with equivalent circuits. Before the fitting process, a randomization step is added to obtain an estimate of starting values.

Table 3.1 The constituent elements in the EIS equivalent circuits (where, j is the imaginary number).

Equivalent circuit elements	Impedance	Admittance
Resistor	R	$\dfrac{1}{R}$
Capacitor	$\dfrac{1}{j\omega C}$	$j\omega C$
Inductor	$j\omega L$	$\dfrac{1}{j\omega L}$
Warburg element (W)	$\dfrac{1}{Y_0\sqrt{(j\omega)}}$	$Y_0\sqrt{(j\omega)}$
Constant phase element (CPE)	$\dfrac{1}{Y_0(j\omega)^a}$	$Y_0(j\omega)^a$

3.10 Inductively Coupled Plasma Optical Emission Spectroscopy

Inductively coupled plasma optical emission spectrometry (ICP-OES) employs a plasma, which is ionized gas [232]. This plasma is created with an induction coil electromagnetically. The specimen under examination is subjected to this plasma and all chemical bonds are dissociated at this high temperature. The plasma conditions stimulate light emission and the produced wavelengths can serve as characteristic identifiers for individual elements. The concentration of the elements is determined the emitted light intensity. Simultaneous emission of light from

various elemental constituents is possible providing a shorter measurement time [233,234]. The elemental analysis of all HEF based powders was determined by ICP-OES (iCAP 7600DUO from ThermoFisher Scientific). About 5 - 10 mg of the samples (weighing accuracy $\pm$ 0.05 mg) were dissolved in 6 mL hydrochloric acid and 2 mL nitric acid at 353 K for four hours in a graphite oven. The analysis of the elements was accomplished with four different calibration solutions and an internal standard (Sc). The range of the calibration solutions did not exceed a decade. Two or three wavelengths of each element have been used for calculation. The amount of fluorine was estimated using an ion-selective electrode (perfectION, Mettler Toledo). The obtained residue was diluted and pH was leveled between 5 and 8 using both 5 M NaOH solution and TISAB (total ionic strength adjustment buffer) solution. The concentration of fluorine was found by the method of standard addition. ICP measurements were obtained through collaboration with Dr. Thomas Bergfeldt (IAM-AWP, KIT). ICP data analysis was done by author under the supervision of Dr. Ben Breitung (INT-KIT).

3.11 Printable Ink and Slurry Formulation

Printable battery ink is formulated from three components: active material, conductive agent (carbon) and polymer binder (water or organic solvent based). In this thesis, commercially procured silicon nanoparticles (~50 nm diameter) and HEF composites with CNT was employed as electroactive constituents. Carbon black (C65) was used as the conductive agent. The synthesis strategy of anode and cathode ink/slurry along with electrode preparation will be elaborated in the next sections.

3.11.1 Si/C Composites Synthesis Methodology

For preparing the carbon coated Si composites (Si/C) in the anode side of LIB, a standard pyrolysis with a carbonaceous precursor was used [235]. In a typical experiment, 0.5 g of Si nanoparticles (99.95%; Alfa Aesar) were dispersed in 50 mL of ethanol (99.5%; Sigma Aldrich). After stirring the suspension, an additional 0.25 g of glucose (99.9%; Sigma Aldrich), dissolved in 10 mL of deionized water were added. Afterward the solution was stirred at 90 °C for 2 h. After solvent evaporation, the particles were calcined in Ar/H$_2$ atmosphere at 600 °C for 4 h. The Si/C composite was used without further treatment for electrode preparation. Si/C composites were prepared with synthesis support from Dr. Ibrahim Issac (INT-KIT). The anode electrode slurry was prepared via thorough mixing of Si or Si/C composite nanoparticles (63 wt.%), carbon (C65, 22 wt.% in water; Timical USA) and PVA (polyvinyl alcohol, 15 wt.%; Solvay 425) by using a high energy dispersion Thinky mixer (ARE 500, Japan). The composition ratio of active material, carbon additive and binder were adapted based on the

previous works stated by C. Erk *et al.* [74] and I. Kovalenko *et al.* [236]. Viscosity of the slurry was adjusted for printability with microplotter by varying the solvent content (water). Later, these printed electrodes on a copper foil were dried in a vacuum oven at 80 °C overnight inside an Ar-filled glove box (O_2 and Ar < 0.5 ppm) under reduced pressure (2mB). For cathode preparation, NCM 111 (BASF SE, Ludwigshafen), carbon (C65) and PVDF (Solef 5130, Solvay) were mixed in 8:1:1 ratio (wt %) with an adequate amount of NMP (N-methyl-2-pyrrolidone, Sigma Aldrich). The prepared electrode slurries were tape casted by using 200 μm doctor blade on Al foil (Gelon LIB Co., Ltd, China) and electrode sheets were dried overnight at 80 °C under reduced pressure. The cathode active material loading was fixed at 1.5 mg/cm^2. Electrode disc dimensions of 13 mm were fixed for both cathode and anode samples. For full cell preparation, printed anode electrode was prepared by mixing Si/C nanoparticles (50 wt%), carbon (C65, 40 wt%) and PVA (10 wt% in water) and tape-casted NCM as a cathode. All battery electrode preparation, measurements and data analysis were done by author.

3.11.2 HEF Synthesis Methodology

Commercially available analytical grade transition metal difluorides with purity >99 % (such as MnF_2, FeF_2, CoF_2, NiF_2, CuF_2, ZnF_2, MgF_2; Alfa Aesar) in equimolar ratios were used for this work. All the chemicals were used for the synthesis without any further purification steps. These HEF materials were prepared by a long-term high energy milling process carried out at 500 rpm for 48 h in a WC jar with a ball to powder weight ratio of 20:1. Using this synthesis route, HEF samples containing 4, 5, 6 and 7 constituent elements were produced. All samples were prepared in Ar atmosphere (H_2O < 0.5 ppm, O_2 < 0.5 ppm). To encounter the low electronic conductivity of fluoride materials, composite structures with MWCNT (multiwalled carbon nano-tubes, Sigma Aldrich, 7.5% MWCNT basis, outer diameter 7 to 15 nm, length 0.5 to 10 μm) were prepared via ball milling carried out for 3 h at 500 rpm. Cathode electrode slurry was prepared by mixing weighted ratio of the composite electrode (HEF/CNT, 85 wt%), carbon black (C65, 15 wt%) and polyvinylidene fluoride (PVDF, Solef 5130, Solvay) homogeneously mixed in N-methyly-2-pyrrolidone as solvent. The mixed slurry was tape casted with 200 μm thick doctor blade onto an Al foil and left for overnight drying. All electrodes tapes were prepared in an Ar filled glovebox to avoid contamination from air. In case of printable ink, the solution was sonicated prior to the printing process to ensure less particle agglomerations and uniform ink distribution. Printed electrodes were prepared under ambient atmospheric conditions. The electrodes were cut using a precision electrode cutter to 13 mm diameter circular discs. As an illustration, the steps followed during the electrode testing process are

given in Figure 3.8. The respective slurry of required viscosity is firstly prepared, which is transformed into printed or tape casted counterparts. The first step is sample printing, then drying the electrodes in a vacuum, followed by cell fabrication inside a glovebox, and it is subsequently tested for battery performance. All battery electrode preparation, measurements and data analysis were done by author and Yanyan Cui, with equal contribution.
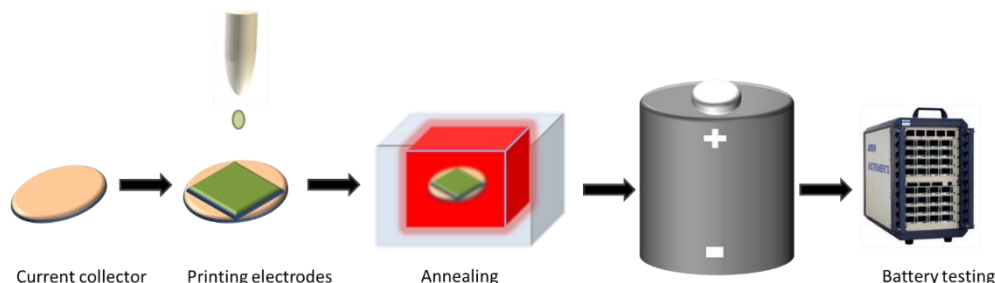
Figure 3.8 Process flow chart for the preparation of battery electrode slurry preparation and coin-cell testing.

3.12 Coin-Cell assembly

The typical coin type cell configuration was extensively employed in this dissertation for galvanostatic testing of half or full cells. The individual elements in a typical coin-cell assembly is shown in Figure 3.9. The components inside a coin type cell consist of stainless-steel bottom casing, a positive or negative electrode (working electrode [WE]/sample on Cu or Al foil), glass fiber separator, counter or reference electrode (CE, Li foil), wave separator, stainless steel spacer, stainless steel top casing. All coin cell casing parts were dried at 120 ℃ overnight to avoid moisture contamination. Since the amount of electrolyte is crucial for the cell performance, each fabricated cell contained either 90 µL (CR 2032 type) or 200 µL (TC2-coin type) of standard liquid electrolyte. All coin cell preparation and measurements were done by author.

3.13 Drop on Demand Printing

3.13.1 Inkjet Printing for Transistor Fabrication

Printing technique is a cost-effective technique, which offers large area coverage and can be applied on flexible substrates. Even though, there exists several low-cost methods such as spin coating, doctor blading, spray coating etc, the printing method offers more advantages [164]. Printing is a mask-less, non-contact process, no vacuum requirements, room temperature deposition and possesses high scalability for large scale manufacturing [237]. The terminology printed electronics represent the transfer of printable functional materials inks into desirable electronic patterns on substrates [15]. Depending on the application perspective, different printing techniques can be adopted namely, gravure, offset, flexography, screen and inkjet printing.
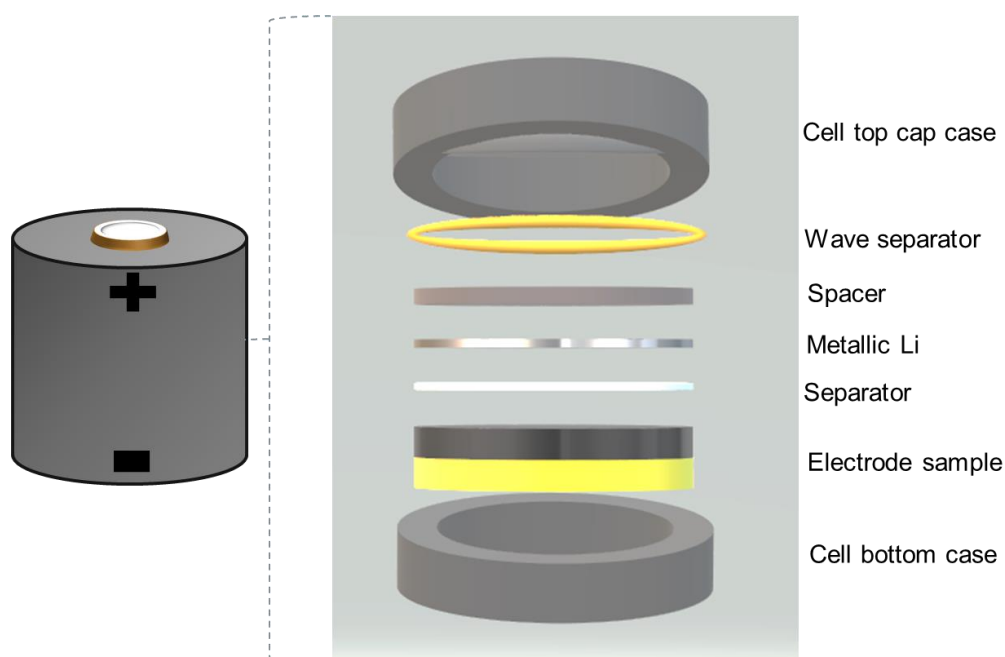
Figure 3.9 Schematic diagram of the coin type cell configuration showing the individual components.

Among all of these, inkjet printing is preferred obliging to the digital print pattern and ink versatility, with moderate resolutions. In accordance with the process of droplet generation, three classifications are present, namely: thermal (ejection of ink due to thermal effect), piezoelectric (electronic voltage pulse for mechanical pressuring of ink ejection or via applying constant pressure) [238,239]. Most of the available inkjet printers use piezoelectric transducer principle because of the high reliability offered by this method. This dissertation used piezo driven inkjet printer for the fabrication of transistor components. When the voltage input is given to piezoelectric actuator, it causes pressure waves to be circulated in the capillary. In case of a positive pressure wave, the fluid is ejected outwards. A successful droplet is formed when the transferred kinetic energy is greater than the droplet surface energy formation [240]. A fruitful droplet ejection from the nozzle as shown in Figure 3.9 hinges on several instrumental parameters like applied voltage pulse, nozzle diameter, frequency as well as the ink characteristics like surface tension, viscosity etc. To enhance the printing process, usually surface of the substrate is plasma treated to enhance the surface energy and adherence of the ink droplets. In many instances, the droplets deposited on the surface of the substrate may show the coffee ring effect, wherein the solute particles are deposited on the pattern boundary, resulting in a thick circumference and a thin centre [241]. Printing of semiconductor channel materials and CSPE is performed using a commercial Dimatix (2831) desktop inkjet printer (see the printer nozzle schematic in Figure 3.10). To ensure the printing process conformity, a constant distance between the print head and the substrate is maintained (400 μm). The ink

jetting frequency was kept constant at 5 kHz and jetting voltages was varied (between 25 V to 40 V) to account for the viscosity and complexity of the printing pattern.
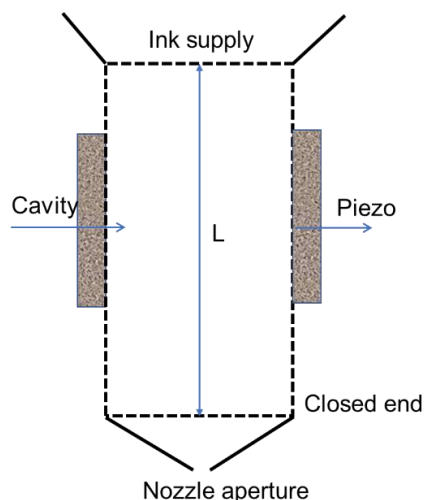
Figure 3.10 Illustration of an inkjet printer nozzle. The print head consists of the ink supply tank, ink cavity, piezo electric transducer and tiny nozzle aperture (which serves as a release point for ink) (adapted from [238]).

3.13.2 Microplotting Technique for Battery Electrode Printing
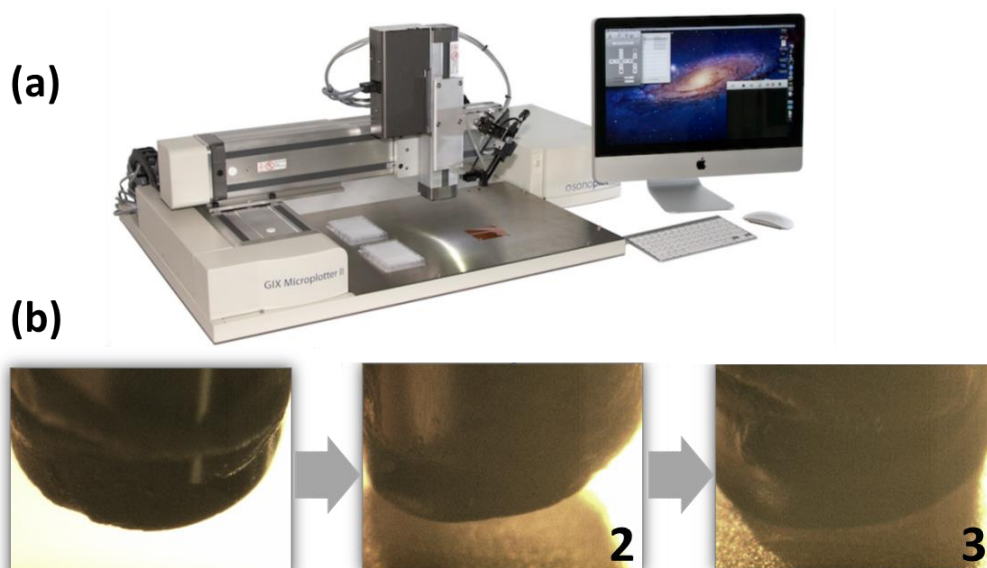
Figure 3.11 a) Microplotter II along with its allied positioning system, b) meniscus formation process on the substrate surface (copper foil) with a capillary tube filled with electrode ink.

The principle of microplotter relies on the fluid ejection based on ultrasonic pumping controlled by a precise robotic dispensing system. For maintaining uniformity, terminology microplotter will be used in this dissertation. The microplotter can disperse the precise amount of solutions to any planar surface with variant patterns. The main part of microplotter is the movable robotic

arm with hollow glass capillary dispenser attached with a piezoelectric element (refer to Figure 3.11 a). With the input of certain frequencies, resonant vibrations occur and ink is pumped down from the needle or sprayed out from the end of the capillary. For starting the printing process, desirable ink is loaded via dipping in the fluid tank. The tapered end of the capillary tip is brought to the substrate surface (in this case Cu/Al current collector) as shown in Figure 3.11 b). The printing of the patterns is viable with manual control mode by the user or can be automated by a preset drawn pattern (using Sonodraw option). The meniscus droplet is created by pumping the fluid from the dispenser tip. Once the meniscus is formed on the surface, the tip is retracted to a certain height from the substrate surface. Several patterns can be achieved by microplotter system depending on the end application requirement. The robotic dispenser system relies on a proximity sensor and an electronic feedback system to perform the height determination. Any dispenser before filling the ink must be calibrated for its inherent resonant frequency. Depending upon the viscosity and application needs, the amount of fluid injection can be controlled by varying the dispensing and spraying voltages (1 V to 20 V). Empty capillary after several rounds of printing can be replenished by dipping in an ink well.

Microplotting technique was utilized to print the graphene electrodes of printed transistor and the battery electrodes. In the anode part (chapter 4) the as-prepared Si/C slurry was printed on Cu foils (MTI Corp., USA) by using a robotic dispensing system (Sonoplot Microplotter II, USA). Square patterns with 9 mm were printed on a circular copper metal foil of 13 mm diameter with sonoplotting technique. Microplotting system makes use of a glass capillary, which was in our case filled with the Si or Si/C based inks. Similar settings were utilized for the cathode electrode printing (HEF compounds in chapter 6) on Al foil. During printing, a vibration of the capillary can be applied, deriving from a piezo-element. A resonance vibration was applied to the piezo electric in order to achieve the best printing results. The capillaries with a tip diameter ~ 400 μm were used for microplotting. The resonant dispensing frequency and voltage of 424 kHz and 20 V were employed, respectively. All printed battery electrode preparation and measurements were done by author.

3.14 Ink Preparation of Electrolyte-Gated Transistors Components

This section describes the ink formulations employed in the preparation of the EGT components such as the semiconductor channel, top-gate electrode and graphene electrodes. The transistor part is realized from a combination of i) indium oxide precursor ink, ii) graphene ink iii) composite electrolyte, and iv) PEDOT: PSS (poly(3,4-ethylenedioxythiophene) polystyrene sulfonate) conductive ink.

3.14.1 Indium Oxide Precursor Ink Preparation

There are many methods for fabrication of solution processed EGT, namely with nanoparticulate ink or chemical precursors and in this thesis, precursor route was followed (further details on precursor route can be found in [242]). The semiconducting channel material was formulated by dissolving 0.05 M indium nitrate hydrate [$In(NO_3)_3 \cdot xH_2O$] in 5 mL of solvent. The solvent consists of 4 mL D.I water and 1 mL glycerol. Glycerol served the purpose of controlling the viscosity. To exclude the larger particles, polyvinylidene fluoride (PVDF) filter of 0.45 μm pore size was used. As-synthesized solution could be printed. Further heat treatment and conversion to In_2O_3 was facilitated by heat treatment at 400°C for 2 h.

3.14.2 Ink Preparation of Composite Solid Polymer Electrolyte

The ink of composite solid polymer electrolyte (CSPE) preparation was carried out for creating the electrolyte layer. Here, 0.3 g of PVA was mixed in 6 g of dimethyl sulfoxide (DMSO, anhydrous 99.9 %, Sigma Aldrich) in a solvent. For the dissolution of PVA, this resultant mixture was heated at 60-80 °C for a couple of hours. Afterward, 0.07 g of lithium perchlorate (LiClO$_4$, 99.99 %, Sigma Aldrich) and 0.63 g of propylene carbonate (PC, anhydrous 99.7 %, Sigma Aldrich) were added and stirred overnight until a transparent solution was obtained. Again, before inkjet printing process to remove larger agglomerates, the final CSPE was filtered by a poly(tetrafluoroethylene) (PTFE) filter of pore size 0.2 μm.
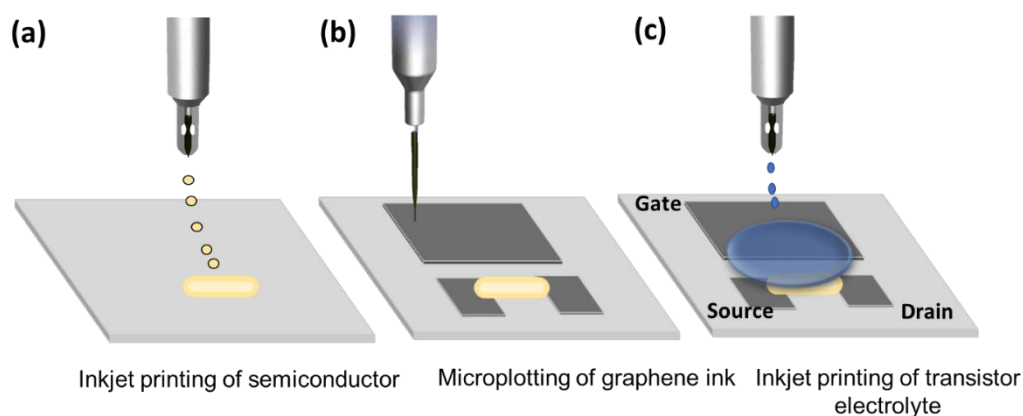
Figure 3.11 Schematic illustration of a printed EGT and the consequent printing steps, a) inkjet printing of semiconductor precursor on the glass substrate, b) microplotting of graphene electrodes and c) inkjet-printing of CSPE layer across the gate and semiconductor electrode (adapted from [243,244]).

3.14.3 Ink Preparation of Conductive Ink (PEDOT: PSS)

Poly(3,4-ethylenedioxythiophene)-poly(styrenesulfonate) (PEDOT:PSS) is commercially available conductive polyelectrolyte polymer complex [245]. PEDOT: PSS polymer is used as a

top gate electrode due to its intrinsic conductivity. PEDOT: PSS and de-ionised (D.I.) water was combined in 70:30 ratio. To avoid the inkjet printed nozzle blockage, as prepared ink was filtered with a PVDF filter of 0.45 µm pore size. After the printing process, the water content was removed by evaporation and further solidification of the top gate electrode.

As the first step in transistor fabrication, indium oxide precursor was printed by the ink-jet printer (Dimatix 2831, Fujifilm, USA). Due to a mandatory heat treatment step at 400 °C to obtain semiconducting Indium oxide nanoparticles, the precursor was printed first. This step helped to avoid the decomposition of graphene precursor ink in the next stage. Passive graphene electrodes (source and drain) were printed using sonoplotter (Microplotter II, USA). As a gate insulator, CSPE was later printed via inkjet printing technique. Top gated transistor device was realized by printing PEDOT: PSS. All the electrical measurements (two-probe output characteristics) were measured using a precision probe station (SUSS MicroTec MLC-150C) with a semiconductor parameter analyser (Agilent 4156C). For operation, the gate voltage was fixed at the battery voltage (full cell Si/C anode/NCM cathode) and the drain voltage swept from 0 V to 1 V. The source terminal was kept as common ground. Printed transistor fabrication was implemented in close collaboration with Dr.Surya Abhishek Singaraju (INT-KIT) and rest data analysis was carried out by author.

Chapter 4 Tailored Silicon/Carbon Compounds for Printed Lithium-ion Anodes

Selected parts of this chapter are published in [244] within the framework of this thesis. The respective paragraphs – with minor adjustments included – are indicated by a vertical gray bar at inner page margin. The experimental work was carried out by Parvathy Anitha Sukkurji under the supervision of Dr. Ben Breitung. The manuscript was organized and written by Parvathy under the guidance of Dr. Breitung and all other co-authors. Co-authors contributed by supporting with pyrolysis reaction, certain characterization methods, providing valuable discussions, and reviewing the article draft.

Silicon (Si) is a potential candidate for next-generation anodes. One prominent method to improve the electrochemical performance of Si anodes is ensuring a conductive network during cycling via a carbon coating the surface of active nanoparticles. In this chapter, investigation of printability of Si anodes and the impact of carbon coating in their electrochemical behavior as printed Si anodes is investigated. For electrical conductivity, surface coating was provided with low-cost and environmentally-friendly precursor material such as glucose. To characterize the effective carbon coating content, thermogravimmetric and Raman spectroscopy methods are employed. Last part of chapter deals with possible applicability of Si anodes for powering the low-voltage printed electronic applications. Furthermore, the fabricated printed Si anode is tested in a full cell configuration with $Li(Ni_{1/3}Co_{1/3}Mn_{1/3})O_2$ (NCM) as cathode. Additionally, the direct applicability of the printed Si anodes is shown by successfully powering an ink-jet printed transistor.

4.1 Background

Si is one of the most promising electrode material with a very high theoretical capacity (~4008 mAh/g) [78,246]. Nevertheless, the limitations known of Si as electrode material (pulverization effects, volume change etc), are impeding the development of Si anodes to market maturity. These result in pulverization of the Si particles, which leads to a degradation of the electrode integrity and therefore to a drastic capacity loss while cycling [247]. Many different investigations on the improvement of the capacity retention were conducted, leading to the conclusion that nanosized and nanostructured Si structures are necessary to counteract the volume expansion effects [247–249].

Another issue hampering the implementation of pure Si anodes in applications is the comparatively low C-rate compatibility [250]. Intercalation-based materials offer the possibility to provide very high specific current densities, if needed, which is not possible for a Si anode because of different reaction mechanism [247]. Therefore, Si, as anode material, is an ideal

candidate for low-power electronics applications with less necessity of high current rates. A growing area of such applications for low power electronics is the field of printed electronics (PE). In the research field of PE, electronic components are printed with cost-effective and up-scalable techniques [164]. The PE technology can be used to create various circuit designs, with suitable solution processed inks, on the surface of any possible material, including flexible substrates, dielectrics, etc [15,251]. Active PE applications usually need a power source for independent operation. Different types of power sources have been considered, e.g. energy harvesting devices, or flexible printed batteries [252]. Desirably, the lifetime of these power supply units should fit to the lifetime of the printed application and they should be reusable or disposable [253]. In this scenario, flexible batteries with non-toxic active materials are attractive choices, e.g., Si as a potential anode material due to its nontoxicity, high theoretical specific capacity of 4008 mAh/g and natural abundance [254].

4.2 X-ray Diffraction and Thermal Characterization of Si and Si/C Nanoparticles

The tailoring of the carbon coating on Si was conducted for two reasons. Literature reports reveal the enhanced electrochemical performance of carbon-coated Si and the printability of the prepared ink is increased [248,255,256]. Two different Si compounds were used namely, Si nanoparticles (Si) and carbon-coated Si nanoparticles (Si/C). The carbon coating process was based on a pyrolysis reaction, using a decomposition of glucose as carbon source, as explained in the experimental section. Figure 4.1 a) represents the X-ray diffraction (XRD) pattern of Si and Si/C (JCPDS no. 27-1402), which indicate that crystalline Si phases exist in both Si and Si/C composites [256].
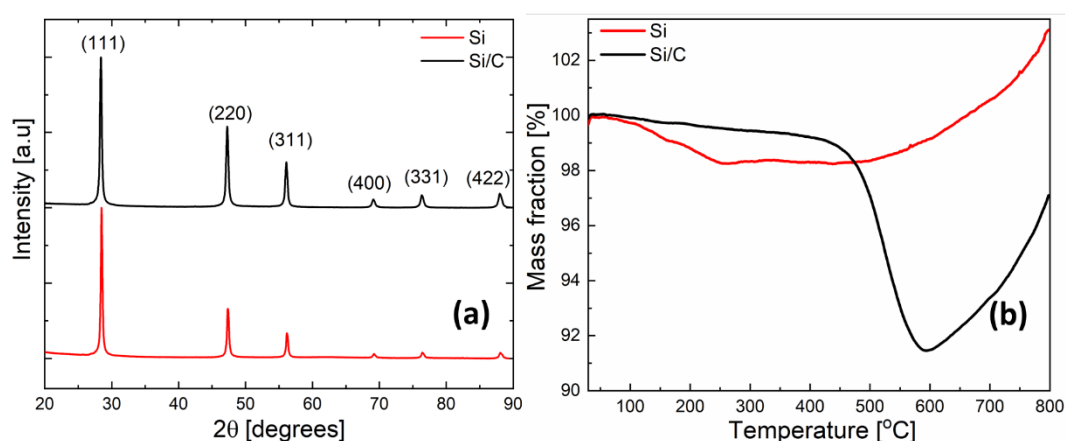
Figure 4.1 a) XRD patterns of Si and Si/C show crystalline Si (JCPDS no. 27-1402), and **b)** thermogravimetrical measurements of Si/C reveal a carbon content of ca. 10 wt %.

The amount of carbon incorporated in the coating was determined by thermogravimetric analysis (TGA). Figure 4.1 b) shows the thermogravimetrical analysis (TGA) data of Si and

Si/C composites. The nanopowders were heated to 800 °C in ambient air and the mass change detected. The mass decrease in Si, around 200-300 °C, can be attributed to the decomposition of surface groups, which were formed during the industrial Si synthesis. The mass increase, starting between 500 and 600 °C can be assigned to SiO_x formation in case of Si nanoparticles [235]. Since this SiO_x formation appears in the case of Si/C composites after decomposition of the carbon shell, the mass difference at 800 °C between both measurements is related to the total amount of carbon burnt in Si/C composite sample. The TGA measurement comparison of both nanopowders results in a carbon content of ~10 wt %, which is in good agreement with performed elemental analysis and XPS measurements (see Figure 4.3 a), b) and Figure 4.5 c)).

4.3 Raman Spectroscopy Analysis of Si and Si/C Nanoparticles

Raman Spectroscopy was used to identify the structure of the carbon coating, by measuring the characteristic defect band spectrum of the carbonaceous coating material based on the vibrational modes [257]. The Raman spectrum of Si/C (Figure 4.2 b) exhibits two distinctive peaks at 1350 cm^{-1} and 1595 cm^{-1}, corresponding to the D and G bands, respectively [257]. The intensity ratio of the D band to G band (I_D/I_G) was calculated to be 0.67 (as given in Figure 4.2 b), therefore, the carbon layer can be presumed to be a mixture of nanocrystalline graphite and amorphous carbon with a low sp^3/sp^2 hybridization ratio [258]. The two typical peaks of Si at 520 cm^{-1} and SiO_2 at 1000 cm^{-1} (indicated in Figure 4.2 a) could be detected in both samples.
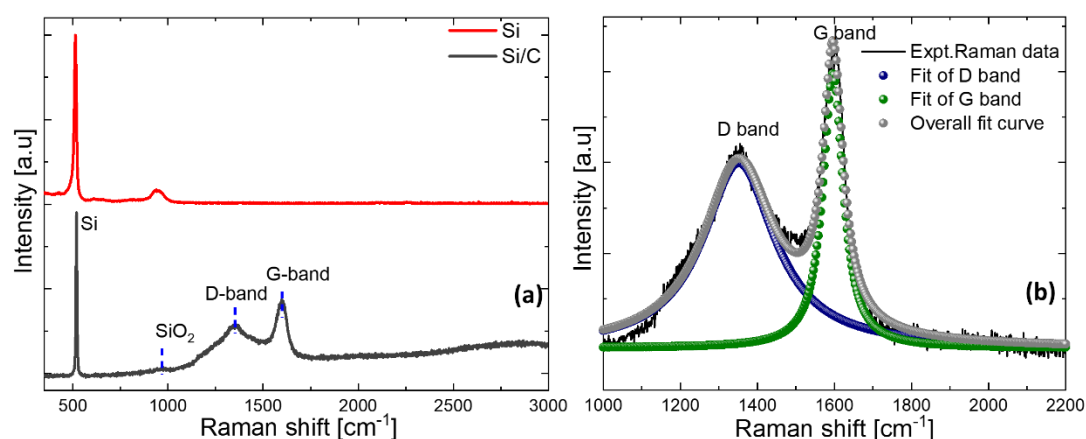
Figure 4.2 a) Raman spectra of the Si and Si/C indicate the presence of carbon coating in the latter case and b) Raman spectra fitting of the Si/C composite nanoparticles.

Raman spectroscopy was employed to identify the composite electrode morphology and carbon defect peaks (D band and G band) as depicted in Figure 4.2 b). The Raman spectra were fitted (gray curve), and the contributions of the D (blue curve) and G bands (green curve) were determined.

4.4 X-ray Photoelectron Spectroscopy Analysis of Si/C Nanoparticles
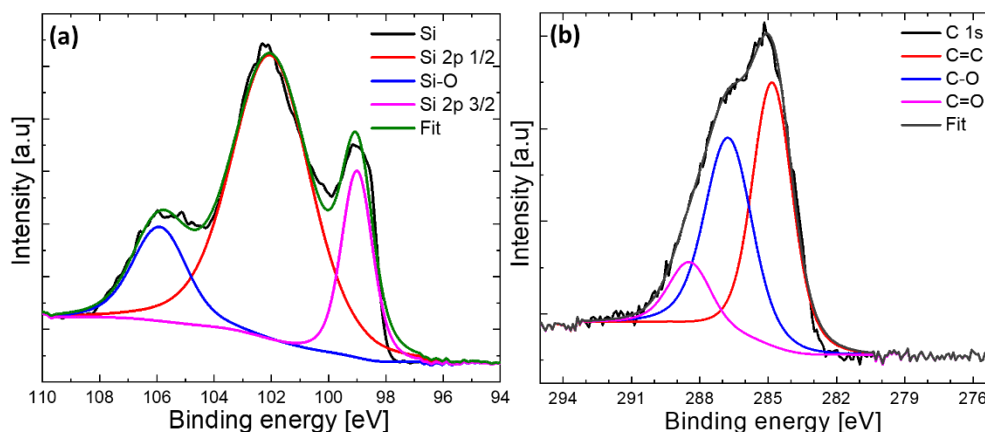
Figure 4.3 XPS spectra of a) Si 2p and b) C 1s peaks of Si/C composite nanoparticles.

Figure 4.3 a) shows the XPS analysis of Si 2p spectrum of carbon-coated composite Si/C nanoparticles. XPS analysis of the composite samples were carried out to investigate the Si-C interactions in the electrode. Si-O_x species are also present which arises due to the native oxide layer shell [74]. By the deconvolution of Si 2p spectrum, three distinct bonding states correlating to Si^0 (2p 1/2), Si^0 (2p 3/2) and Si-O at the positions 102.05 eV, 99.05 eV and 105.95 eV can be identified. Figure 4.3 b) shows the XPS spectrum of the C 1s original and fitted curves of Si/C nanoparticles. The spectra consist of three major peaks with positions at 288.5 eV, 286.8 eV and 284.8 eV; which can be attributed to C=O, C-O, C=C species respectively [259]. These peaks indicates the presence of carbon coating effectively incorporated in the Si/C nanoparticles.

4.5 Morphological Analysis of Si and Si/C Nanoparticles

TEM and SEM measurements were performed to gain further insights into the structure of the Si and the Si/C nanoparticles (for SEM, refer Figure 4.4). The comparison of the morphologies of the respective electrode starting nanopowders morphologies are shown in Figure 4.4. Both, the Si and the Si/C compound indicate particle sizes around 50 nm, but appear in agglomerates with irregular morphologies.

Overview of TEM investigations on the as-received Si and pristine carbon coated Si/C nanoparticles (~50 nm diameter) were carried out (Figure 4.5). The TEM micrograph of Si/C nanoparticles (Figure 4.5 b) shows agglomerates with the existence of irregular spherical and oval shaped nanoparticles. Figure 4.6 a) shows a high resolution TEM (HR-TEM) micrograph of Si nanoparticles, along with a magnified image denoting the clear lattice fringes of ~0.32 nm, corresponding to the Si (111) plane. The selected area electron diffraction (SAED) pattern is displayed as inset of the image to confirm the crystallinity of the Si observed by XRD. TEM

micrographs of Si nanoparticles show particle sizes of ~50 nm and exhibit a thin (~10 nm) SiO_2 shell (see Figure 4.5 a)). Figure 4.6 b) shows similar findings for the Si/C compound. Lattice fringes of around 0.32 nm and Si nanoparticles with ~50 nm diameter (Figure 4.5 b)) could be found. Additionally, a carbon shell could be detected, as further displayed in Figure 4.5 c). Here, for the Si/C compound, STEM-EDS mapping (energy dispersive X-ray spectroscopy) is utilized to confirm the presence of the coated carbon layer (few nanometers). The elemental composition mapping results of Si and C along with its representative STEM image are displayed, the results are in accordance with the outcome of the XPS measurements shown in Figure 4.3 a) and b).
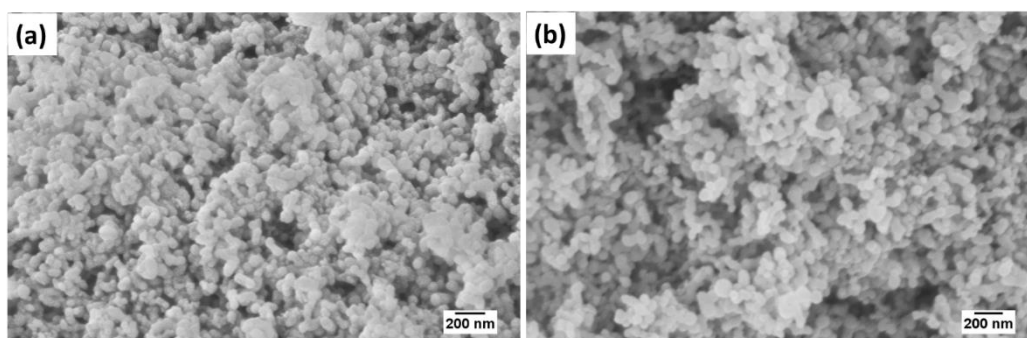
Figure 4.4 SEM analysis of a) Si/C composite and b) Si nanoparticles.
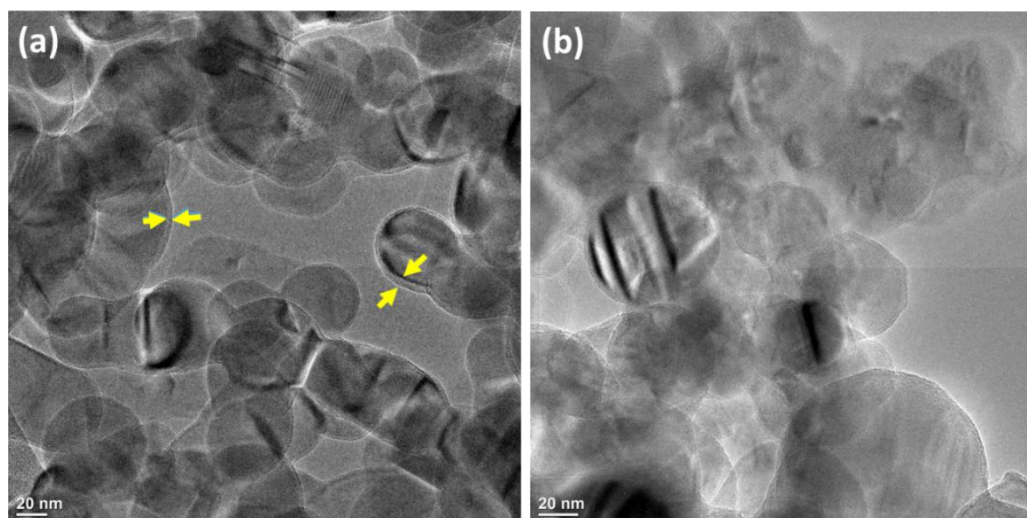
Figure 4.5 TEM micrographs showing the overview of a) pristine Si nanoparticles with arrows illustrating the presence of native SiO_2 shell and b) Si/C nanoparticles.

The printability of an ink is usually connected to different material properties, ink fluidity behaviour as well as on the chosen printing procedure. Two inks were prepared using Si or Si/C as active materials, Polyvinyl alcohol (PVA) as binder and conductive carbon (C65) as additive to render the slurry conductive. Depending on the agglomeration/segregation of particles and the viscosity of the ink, the adhesion properties on the current collector surface and the printability of the ink changes. The pure Si ink showed severe segregation and agglomeration

of Si, leading to clogged printing nozzles, impeding the storage and reuse of the ink. The particle size distribution and the agglomeration behaviour over time was investigated using dynamic light scattering (DLS). A visible colour difference of the two inks was observable directly after preparation and is demonstrated in Figure 4.7 a).
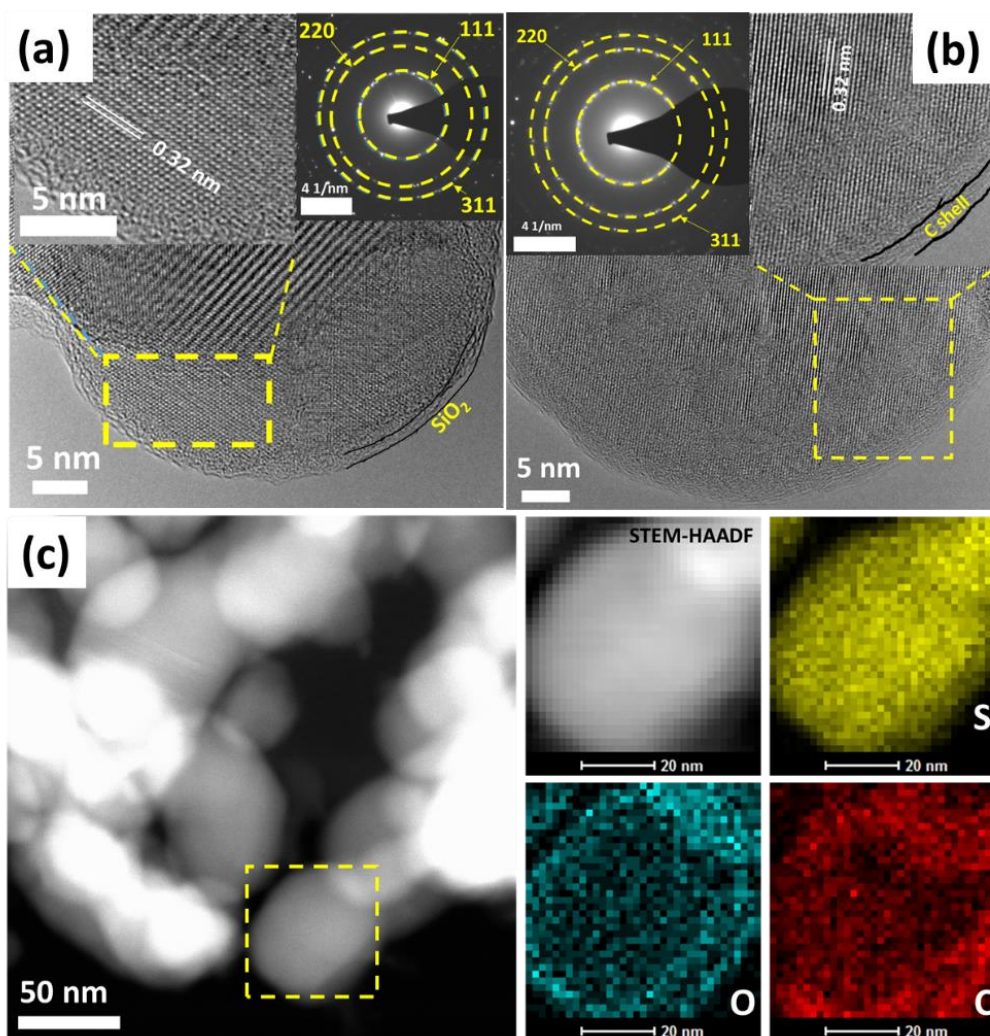
Figure 4.6 HR-TEM micrographs of a) pristine Si with SiO_x amorphous layer b) Si/C nanoparticles possessing an amorphous non continuous carbon shell. SAED patterns of both samples confirm the crystallinity of Si and Si/C nanoparticles. c) STEM-EDS elemental mapping of a Si/C nanoparticle.

The size distribution of the nanoparticles with respect to residence time in water are depicted in Figure 4.7 b) (concentration of both dispersions was kept constant at 40 mg/L). It shows the broad and narrow size distributions in case of Si and Si/C composite nanoparticles respectively. Si particles were found to form large agglomerates, with a maximum around 520 - 540 nm and precipitating faster than the Si/C compound. The Si/C compound can be easily dispersed in water without forming large fractions of bigger agglomerates. Here, the major volume fraction is represented by aggregates with diameters between 290 - 320 nm. Possibly, the increased

amount of polar groups attached to the carbon shell (resulting from the pyrolysis process of glucose) leads to a higher hydrophilic character compared to pure Si, and therefore to a better dispersivity in polar solvents.
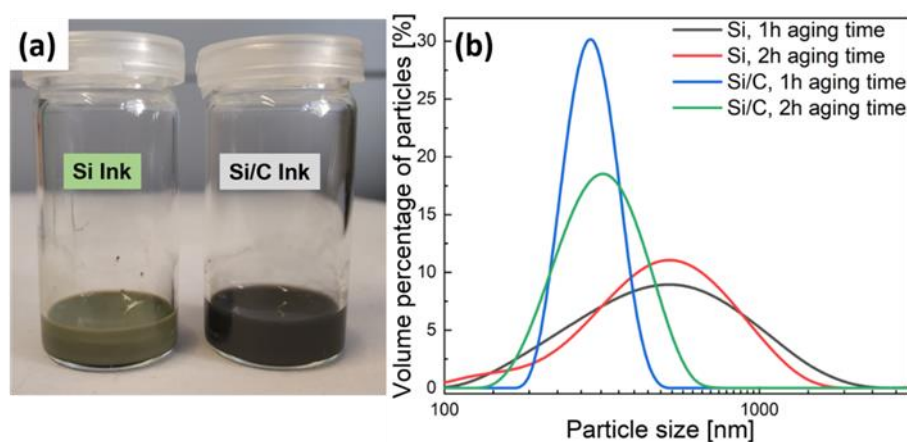
Figure 4.7 a) Photograph showing a visible color difference of the inks and **b)** DLS studies of the aggregation of the Si and Si/C composite ink dispersion with respect to time.

4.6 Electrochemical Characterization of Si and Si/C Electrodes

To examine the effect of carbon coating on the electrochemical performance of Si anodes, a comparative study between Si and Si/C electrodes was conducted. Both, Si and Si/C inks were printed, using a micro-plotting technique, and the electrochemical performance compared. The printing process allows precise deposition of the slurry, so that electrodes with the same loading ($\sim$0.3 mg$_{Si}$/cm^2) could be compared. Cyclic voltammetry (CV) measurements were performed to compare the redox reaction peaks of both electrodes. The printed electrodes were tested in coin-type cells, using 1 M LiPF$_6$ with FEC/EMC (1:1 wt %) as electrolyte and lithium foil as counter electrode. Cycling was performed using cut-off potentials of 10 mV and 1 V at different C-rates (where 1 C = $\sim$4000 mA/g$_{Si}$) with included constant voltage step with a C/10 cut-off current. Figure 4.8 shows the comparative electrochemical characterization of the Si and the Si/C composite materials. Clearly, the sharp cathodic peaks represent the phase transformation, which can be attributed to the formation of Li-Si alloy during the charging process. In the anodic regime, two distinct anodic peaks represent the delithiation process of amorphous phase of Li-Si alloy [256]. High degree of coincidence after first cycle is found from the CV curves of over a number of cycles, indicating the notable reversibility of the Si/C composites.
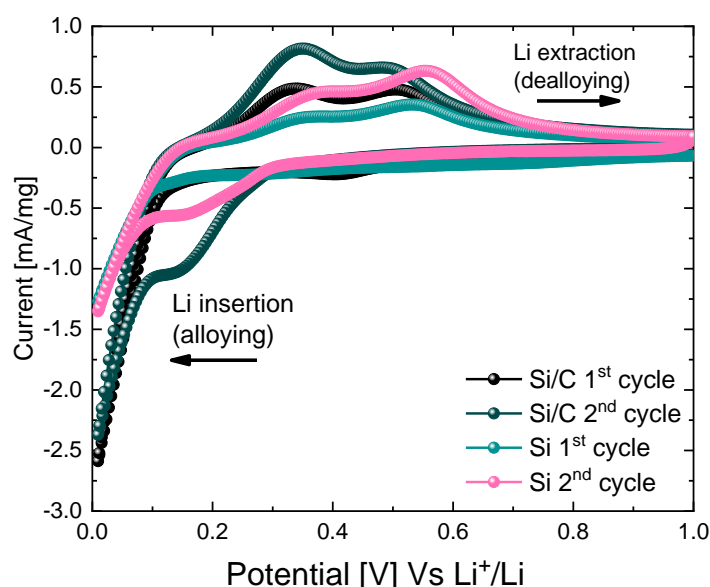
Figure 4.8 Cyclic voltammograms of printed Si and Si/C electrodes from 0.01 V to 1V (versus Li/Li$^+$) at 0.1 mV/s scan rate.

Figure 4.9 a) depicts galvanostatic testing using different specific current densities (with constant voltage holding step as described in Table 4.1). The specific capacities are calculated based on the weight of active material (Si). Over the first 20 cycles, the specific current densities are set to 0.2 A/g, 0.4 A/g, 0.8 A/g, 2 A/g, 4 A/g, and 2 A/g, respectively. The initial discharge capacities for Si and Si/C amount to 4135 and 4240 mAh/g$_{Si}$. The high first discharge capacities (above the theoretical value) can be attributed to irreversible reactions deriving from reductions of the functional groups at the carbon coating, or the silicon surface. While the Si electrode shows a decay of the capacity over the first 100 cycles and a strong impact of the C-rate, the Si/C electrodes show much less capacity degradation and a better electrochemical performance at higher C-rates.

Table 4.1 Stepwise cycling protocol used for testing of Si anode with respect to Li counter (half-cell) with constant voltage holding step [where 1C = active material loading (in grams) * theoretical capacity of Si (in mAh/g$_{Si}$)]

Steps	Process	Cut off voltage	C rate	Mode	Number of Cycles
1	Lithiation	0.01 V	C/20	CC/CV	2
2	Delithiation	1 V	C/20	CC/CV	
3	Lithiation	0.01 V	C/10	CC/CV	2
4	Delithiation	1 V	C/10	CC/CV	
5	Lithiation	0.01 V	C/5	CC/CV	5
6	Delithiation	1 V	C/5	CC/CV	

7	Lithiation	0.01 V	C/2	CC/CV	5
8	Delithiation	1 V	C/2	CC/CV	
9	Lithiation	0.01 V	1 C	CC/CV	2
10	Delithiation	1 V	1 C	CC/CV	
11	Lithiation	0.01 V	C/2	CC/CV	100
12	Delithiation	1 V	C/2	CC/CV	
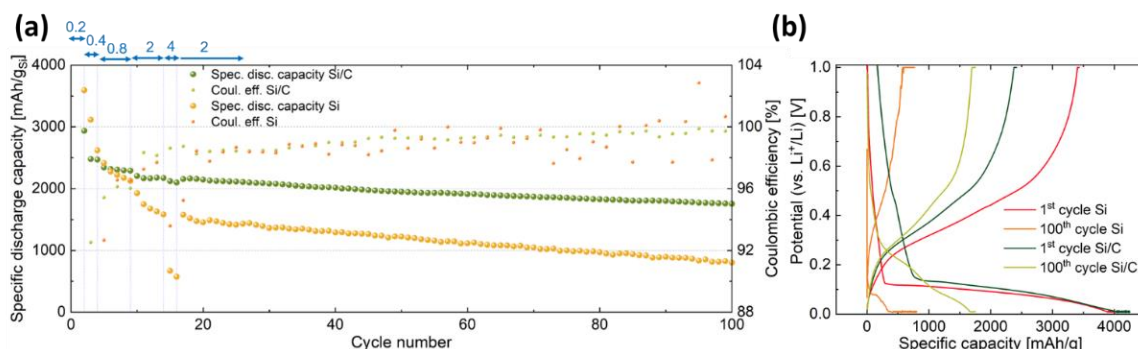
Figure 4.9 a) Galvanostatic cycling performance of printed Si electrode cycled at various current rates versus cycle number. The current steps are implemented during the first 20 cycles and amount to 0.2 A/g, 0.4 A/g, 0.8 A/g, 2 A/g, 4 A/g, and 2 A/g, respectively. **b)** 1st and 100th charge/discharge profiles of Si and Si/C electrodes respectively. The testing protocol is explained in detail in **Table 4.1**. The current densities in a) are given in units of A/g.

Table 4.2 Summary of electrochemical performances of Si and Si/C electrodes tested at different current densities in constant current rates (CC).

Cycle no.	Current density (A/g)	Discharge capacity Si electrode (mAh/g$_{Si}$)	Discharge capacity Si/C electrode (mAh/g$_{Si}$)
2	0.2	3592	2937
4	0.4	2619	2471
9	0.8	2125	2292
14	2	1583	2174
16	4	574	2099
100	2	803	1753

The capacity of the Si decayed after 100 cycles at 2 A/g to 800 mAh/g$_{Si}$, while the Si/C showed a greatly enhanced capacity retention, with 1754 mAh/g$_{Si}$ after 100 cycles using the same specific current density values. Additionally, the coulombic efficiency for the Si/C electrodes is stabilized compared to the Si electrodes. Figure 4.9 b) shows the typical discharge/charge

profiles of the 1st and 100th cycle for the two types of electrodes. These results indicate an improved electrochemical performance of the Si/C electrodes compared to Si. This improved performance can be ascribed to the conductive carbon coating resulting in a higher specific capacity and cycling stability of the electrode [256,260]. The areal capacities of the Si and Si/C electrodes amount to 0.5 mAh/cm² and 0.65 mAh/cm² at the 17th cycle (first cycle in the long-term cycling at 2 A/g), respectively. Furthermore, the electrochemical performances (specific discharge capacity) of both electrodes at different current densities are presented in Table 4.2. These results imply that the functional C coating layer in the Si-based composite electrodes will provide an effective pathway for better cyclability [235]. Hence, synergetic approach of using carbon coating and an aqueous binder is demonstrated to improve the anode performance.

4.7 Morphological Characterization of Printed Electrodes

Cross section SEM micrographs (Figure 4.10 a) and b)) were taken from printed Si and Si/C electrodes. The micrographs show the interface between the substrate and the printed thin film layer and indicate a homogenous mixture of active particles, carbon and binder. Printed Si/C electrodes with lower thickness values were found to have better adhesion to copper substrate, and hence, contributing to the better electrical performance. As illustrated in Figure 4.10 c), homogenous distribution of the nanoparticles and a presence of smooth interfaces between substrate and the printed thin films could be found.

In order to examine the structural stability of the Si/C electrodes, the surface morphology of the Si/C electrodes before battery cycling, and after 100 cycles were investigated by SEM. The micrographs of the printed electrodes are shown in Figure 4.11. The pristine electrode before cycling showed homogenous distribution of Si/C composite. By comparing the morphologies between the Si/C electrode before/after 100 cycles (Figure 4.10 b)), a significant amount of cracks on the electrode surface due to volume expansion process can be observed. The morphology of the cycled electrode did not return to the pristine state due to the SEI layer, pulverization and crack formation, resulting in initial irreversible capacity loss.
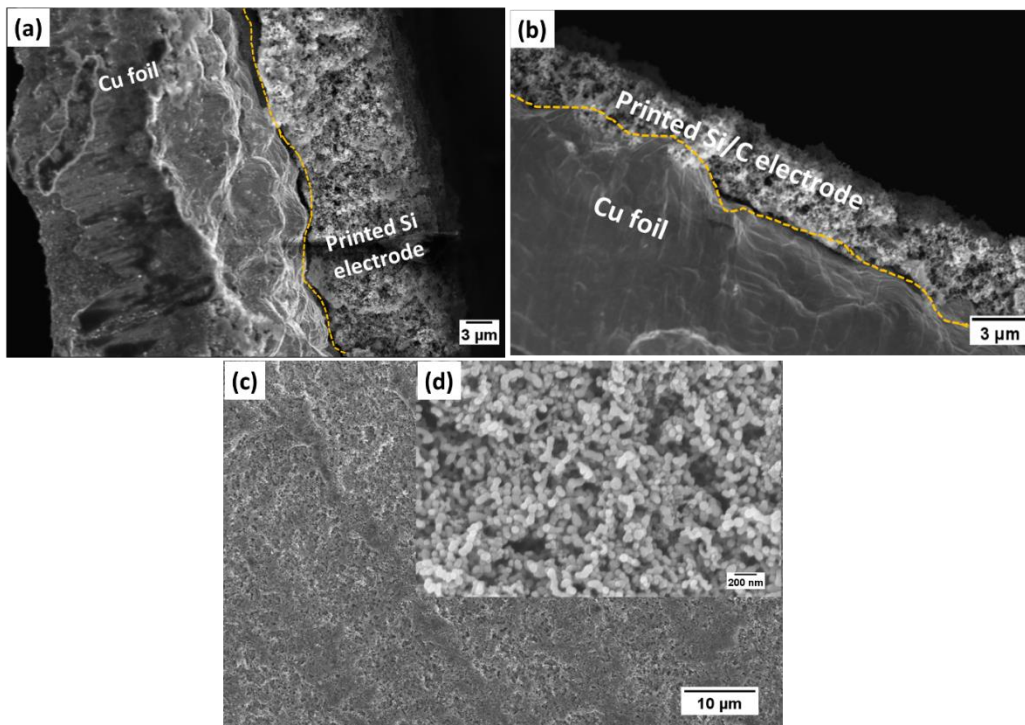
Figure 4.10 Cross section SEM micrographs of **a)** printed Si electrode, **b)** the printed Si/C electrode, **c)** top view of printed Si/C anode electrode with visible overlap of the printed profile and **d)** its magnified view.
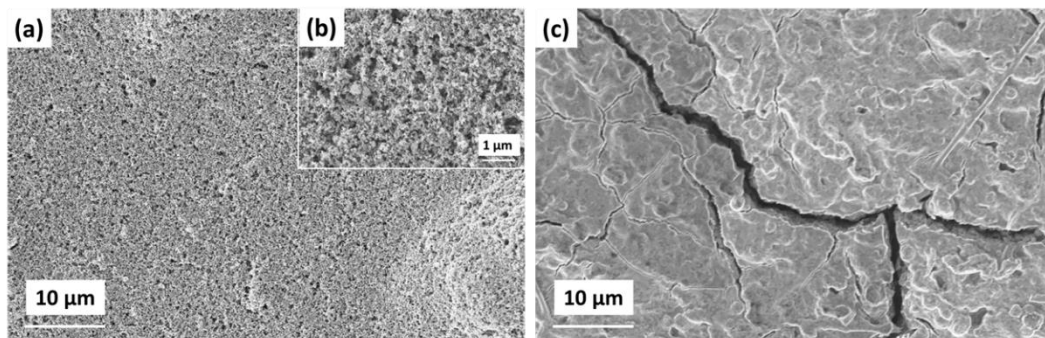
Figure 4.11 Top-view SEM micrographs of printed Si/C electrode **a)** before, **b)** its enlarged view and c) after 100 cycles of electrode testing.

4.8 Electrochemical Impedance Analysis of Symmetric Cells

The conductivity properties of the Si/C and the Si electrodes were analysed using electrochemical alternating current impedance spectroscopy (EIS). In order to identify the individual processes contributing to the EIS response, two-electrode cells in symmetric cell configuration (either two printed Si electrodes or two printed Si/C electrodes) were fabricated and measured. The electrolyte composition for both cells was 1 M LiPF$_6$ salt in FEC: EMC solution. Figure 4.12 a) shows the Nyquist plot of the two symmetric cells. The experimental spectra of both electrodes (denoted by dots) are dominated by a low-frequency blocking feature

and further consist of two flattened higher-frequency semicircles as well as a high-frequency Z_{real}-intercept [261,262].

In order to get a further insight into the EIS features, the data were fitted using the equivalent circuit shown in Figure 4.12 b), and the Zview software (Scribner Associates, Southern Pines, NC). This equivalent circuit comprises a series connection between a contact resistance (R_s), two parallel connections, consisting of a resistor (R) and a constant phase element (CPE)(R_1, R_2 with Q_1, Q_2), and a constant phase element (Q_3) [263,264]. The fits are added as solid lines to Figure 4.12 a), showing very good agreement with the experimental data. The high-frequency resistance values (R_s) of the Si/C and Si electrodes were found to be 22.6 Ω and 28.5 Ω, respectively. The series resistances can be attributed to the ohmic resistance of the electrolyte and the current collection system. The lower value of the Si/C electrode may be due to better electronic contact of the electrode with the current collectors, resulting from the presence of carbon.

Figure 4.12 c) and d) show a deconvolution of the imaginary part of the impedance of the Si and Si/C cells, respectively, into the circuit subcomponents, allowing to visualize their individual contributions. Both spectra show two RQ-features, a small one at ca. 40 kHz and a larger one at ca. 12 Hz, as well as a dominating Q feature. The latter can be assigned to the blocking nature of the electrodes (note that none of the electrodes was pre-lithiated, therefore a large resistance towards delithiation is expected). Tentatively the larger of the two RQ features, $(RQ)_2$, can be assigned to the charge transfer. The charge-transfer resistances of Si/C electrodes (R_2) were found to be approximately 15.4 Ω, which is much lower than the value of Si electrodes (74.9 Ω). The lower value of Si/C electrodes may be obliged to a wide network of conductive carbon, resulting from the carbon coating. The origin of the high-frequency feature $(RQ)_1$, which is much smaller, is unclear. In conclusion, due to the presence of carbon coating, the EIS analyses indicate that Si/C electrodes exhibit enhanced electrical conductivities and improved charge-transfer kinetics. The supplementing Bode plot is depicted in Figure 4.13. The fitted parameter values of the equivalent circuit are summarized in Table 4.3.
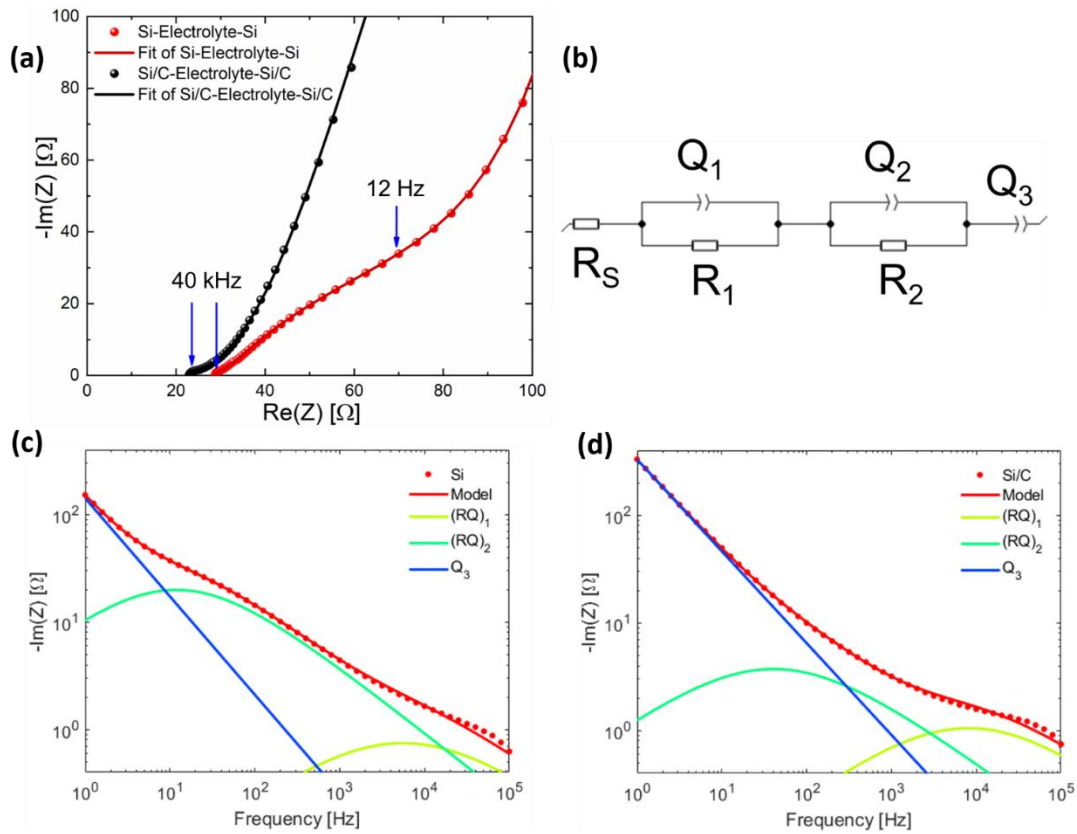
Figure 4.12 a) Electrochemical impedance spectra of symmetrical cells with Si and Si/C electrodes along with fitted curves in a frequency range of 1 MHz -1 Hz (fitting performed with Zview), **b)** equivalent circuit for fitting the experimental data (where R_S, R_1, R_2 denote the resistances, Q_1, Q_2, Q_3 designate constant phase elements), **c)** and **d)** deconvolution of the imaginary part into the three equivalent subcircuits $(RQ)_1$, $(RQ)_2$ and Q_3. A Bode plot of the same data is shown in Figure 4.16.

4.8.1 Bode Plot of Symmetrical Printed Si and Si/C Electrodes

Figure 4.13 shows the Bode plot results (discrete points) and its fitted curves (solid lines) of printed Si and Si/C electrodes (tested in symmetric cell configuration with 1M LiPF$_6$ salt in FEC: EMC electrolyte). In the lower frequency range, two linear features with receding slopes could be identified, whereas in higher frequency region (> 40 kHz) a plateau region of log (|Z|) can be seen.
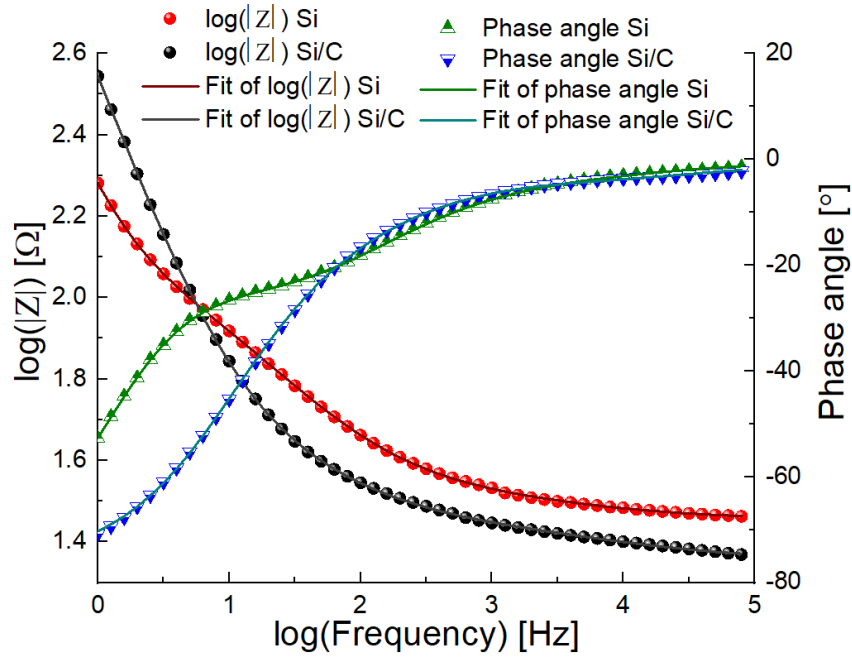
Figure 4.13 Bode plots of Si and Si/C printed electrodes assembled in a symmetric cell configuration.

Table 4.3. Numerical values of the equivalent circuit components obtained by fitting the impedance data of printed Si and Si/C electrodes given in **Figure 4.13 b)**.

Parameters	Si electrode	Si/C electrode
R_S (Ω)	28.45	22.63
R_1 (Ω)	3.12	4.28
Q_1 (F.s$^{(n-1)}$)	8.33×10^{-4}	4.31×10^{-4}
n_1	0.569	0.581
R_2 (Ω)	74.85	15.38
Q_2 (F.s$^{(n-1)}$)	9.11×10^{-4}	2.70×10^{-3}
n_2	0.623	0.574
Q_3 (F.s$^{(n-1)}$)	13.04×10^{-4}	6.17×10^{-4}
n_3	0.914	0.853

4.9 Printed Si/C Anodes for Printed Electronic Applications

To demonstrate the applicability of the printed battery electrode for printed electronic devices, a full cell in coin-type cell geometry was constructed. As testing device, an electrolyte-gated ink-jet printed transistor was chosen to analyse the battery/transistor compatibility. For printing the electrolyte-gated transistor, a technique reported by Singaraju *et al.* was adapted [243]. A unique feature of the electrolyte-gated transistors is the possibility to operate at low voltages, enabling a direct potential supply from a battery without power converter. The printed graphene transistor was prepared by inkjet printing indium oxide (In_2O_3) semiconductor precursor ink on a clean glass substrate. The substrate and the printed layer were annealed to form a uniform

oxide film. Subsequently, passive graphene electrodes (source and drain) were printed on both sides of the semiconductor and a gate electrode in an in-plane geometry [243] (Figure 4.14 a) and b)). As gating material, a composite solid polymer electrolyte (described in detail in [243]) was inkjet printed across the semiconductor and gate electrode [176,251]. The semiconductor channel length, width and thickness were 50 μm, 60 μm and 200 nm, respectively. Figure 4.14 a) and b) depict a schematic view and an optical image of the printed graphene transistor used for this study. The prepared cell utilized NCM ($LiNi_{1/3}Co_{1/3}Mn_{1/3}O_2$) as cathode material and the printed Si/C as anode. The battery construction followed the above-described half-cell arrangements. Prelithiation of Si/C anode was carried out electrochemically by cycling the anode part for 5 cycles in a half-cell configuration. After prelithiation, the counter electrode was replaced by NCM cathode. The electrochemical performance of printed Si/C//tape-casted NCM full cell is studied by cyclic voltammograms for first three cycles with an operational voltage ranging from 2.0 V to 4.3 V at a sweep rate of 0.1 mV/s as shown in cyclic voltammogram (refer Figure 4.15). Later, this full cell was connected to the printed graphene transistor in a two-probe configuration. Before the full cell was attached to the printed transistor, the cell was charged to 3 V (vs. Li^+/Li) and afterwards directly connected to provide the necessary gate potential (V_G) for transistor operation. Figure 4.14 c) illustrates the output curves of the single printed transistor with the printed battery connected to supply the gating potential (OCV of the cell after connection to the transistor: OCV = V_G = 2.1 V, slightly changing over operation) and without any gate potential (V_G = 0). It can be inferred that the battery is capable of switching a printed transistor on and off for more than 10 minutes, therefore indicating that printed electronic circuits can be successfully powered by printed Si// tape-casted NCM batteries with loadings in the low mg/cm² range and without requiring an external power converter.
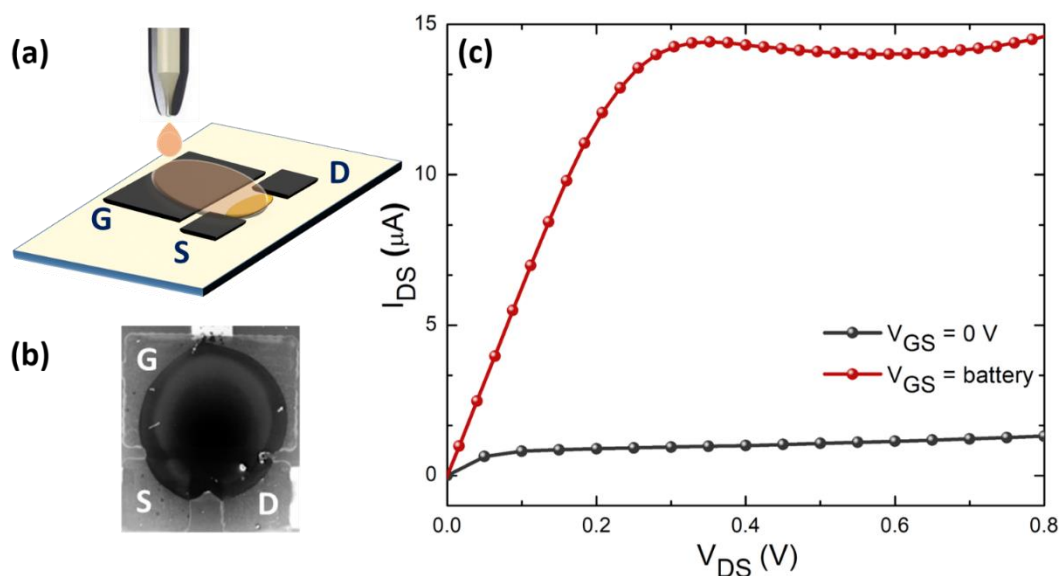
Figure 4.14 a) Schematic view of printed graphene transistor, b) optical microscope image of the printed transistor with gate (G), source (S), drain (D) terminals and c) electrical characterization of transistor powered with and without battery at the gate terminal.
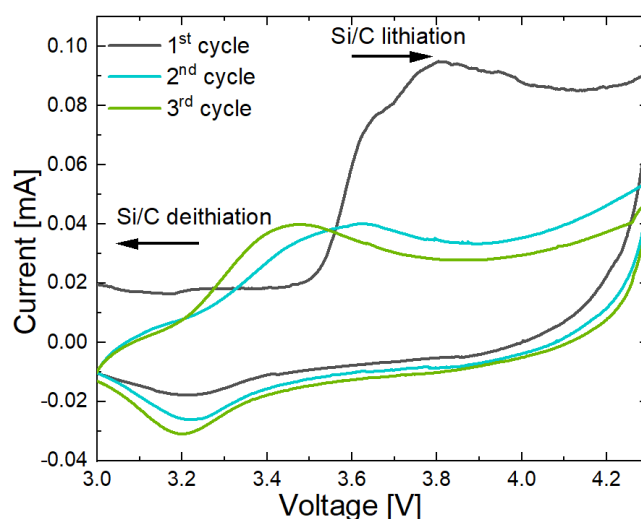
Figure 4.15. Cyclic voltammogram of a full cell with precycled printed Si/C anode// tape casted NCM cathode from 2.0 V to 4.3 V. Voltage sweep rate was kept at 0.1 mV/s.

4.10 Summary

Nano silicon (Si) is an attractive candidate for LIB anode, since it delivers 10 times more capacity than commercial graphite electrodes. However, drawbacks found for Si based materials are reactions with large volume change during lithium alloying/dealloying. Among the nanostructured Si electrodes, composite carbon coating provides high electrical conductivity paths and plays a role for improved electrochemical performance of alloying anodes. Herein, a partial carbon coating was used to decrease particle agglomeration in the ink and to simultaneously enhance the cycling performance. Composite carbon coated Si (Si/C) anodes were fabricated via printing techniques and optimized regarding the printability and

battery performance. The printed Si/C electrodes showed compatibility with water-based binder, PVA. Specific capacities around 1754 mAh/g_{Si} could be shown for printed Si/C anodes after 100 cycles, with C-rates up to 1C. By evaluating the electrochemical performance of printed electrodes prepared with pristine Si and Si/C composites, it can be concluded that the carbon coating effectively prevented the degradation of electrodes and improved the long-term cycling stability. In contrast with carbon coated Si anodes, Si anode without C coating showed huge capacity fading effect over long term cycling. This enhanced rate performance may be ascribed to carbon shell coating, which moderates the pulverization and rupture of electrical conduction path. In order to show the compatibility of the printed Si/C anodes with printed electric circuits, a full cell, using a printed Si/C anode and commercially available NCM as cathode, was constructed, and a printed transistor successfully switched on and off. This demonstrates that printed Si/C anodes can be used directly without power converter for electrolyte-gated transistors, paving the way for Si/C anode utilization in future printed applications.

Chapter 5 Mechanochemical Synthesis of Novel Rutile-Type High Entropy Fluorides

Selected parts of this chapter are published in [265] within the framework of this thesis. The respective paragraphs – with minor adjustments included – are indicated by a vertical gray bar at inner page margin. The experimental work was carried out jointly by Parvathy Anitha Sukkurji and Yanyan Cui under the supervision of Dr. Ben Breitung. The manuscript was organized and written by Parvathy and Yanyan together under the guidance of Dr. Breitung and all other co-authors. Co-authors contributed by helping with synthesis, certain characterization methods, providing valuable discussions, and reviewing the article draft for the peer-reviewed publication process.

The chapter describes the synthesis of high entropy fluorides (HEF) and their comprehensive analysis using different characterization techniques. For printed cathode materials, the main focus is laid on conversion materials, which serve as a potential cathode for printed electronics devices. In the next chapter, HEF as possible conversion electrode material is examined. These novel compounds were prepared by a straightforward and simple synthesis process. With the introduction of the novel high entropy fluorides, noticeable interest could be generated due to the diverse applications (such as lithium-ion battery electrode and electrocatalyst for water splitting) stemming from fluoride-based materials. This chapter introduces multicomponent rutile-type ($P4_2/mnm$) structured fluorides, containing 4 to 7 transition metals (Co, Cu, Mg, Ni, Zn, Mn, Fe) in equiatomic ratios, which were synthesized using a simple mechanochemical approach. The high entropy fluorides were characterized using different techniques, which all indicate that the high entropy fluorides tend to crystallize in a homogeneously mixed solid solution and single-phase structure.

5.1 Background: High Entropy Materials

In recent years, materials with high entropy (HEMs) and their remarkable and often unexpected properties have aroused increasing interest. Sometimes unexpected properties make it possible that a whole class of promising HEMs can be used for future applications[266,267]. The high entropy concept is based on the incorporation of different elements into a single-phase crystal structure, increasing the configurational entropy and sometimes even to stabilize the crystal structure according to the Gibbs-Helmholtz equation[142]. In addition, these materials offer great versatility and the possibility to adjust the properties by replacing a single element or by varying the stoichiometry. All inter-elemental interactions and the associated properties can be modified accordingly. The origin of the HEMs is based on the well-known high entropy alloys (HEAs), which consist of a solid solution of a large number of metals[145,268]. Similarly, this concept of

using a high configurational entropy to obtain desired properties (controversial discussions if many high entropy materials are really entropy-stabilized or "just" showing a high configurational entropy are ongoing) can be applied to ceramic compounds, wherein the multiple cations or anions are occupying the same sublattice, thereby giving rise to the configurational entropy.[136,269] In 2015, Rost *et al.* reported about entropy stabilized oxides ($(CoCuMgNiZn)_1O_1$) as a special group of high entropy ceramics, which led to an increase in related activities.[32] This material crystallizes in a rock-salt structure and shows a reversible mixing/demixing behavior upon heating and cooling, respectively, which indicates entropy stabilization. Bérardan *et al.* investigated the electrical properties of $(CoCuMgNiZn)_1O_1$ and the effect of dopants like Li^+, In^{3+}, $Ga^{3+,}$ and Ti^{4+}.[270] Additionally, co-doping with Li^+ and Ga^{3+} led to phase pure solid solutions $(CoCuMgNiZn)_{1-2x}Li_xGa_xO$.[147] Numerous reports describe such ceramic compounds in detail, including silicides,[271] borides,[133] nitrides,[272] carbides [273] etc. These materials exhibit a wide range of applications, including thermoelectric, dielectric, and optic purposes.[138,152,274]

One important materials class in materials science are metal fluorides, due to their special properties and manifold applications, which will be discussed in detail as follow. Inorganic metal fluorides are used in catalysis, as electrode active materials, superconducting components, and corrosion protection.[275–278] Non-binary compounds, such as Co-doped MgF_2, exhibit additional properties, like in the mentioned case above, the modification of surface acidity properties while retaining the rutile phase.[279] Ternary metal fluorides , e.g. $AgCuF_3$,[280] $Cu_xFe_{1-x}F_2$ or Li_3MF_6 (M=V, Cr, Mn, Co, Fe) show reversible conversion reactions with Lithium-ions,[33,281,282] rendering them as potential energy storage materials. Taken together, the application of the high entropy concept to transition metal fluorides in general, seems to be a promising approach for the development of novel catalytic and electrochemical materials.[115,283] First reports about rare-earth-based fluorite and perovskite structured high entropy fluorides and rock-salt structured oxyfluorides have shown promising properties for energy storage, optical and catalytic properties.[136,152,275] Wang *et al.* reported that the existence of weak bonds between transition metal (TM)-fluoride species, intrinsic structural defects and a distortion of the HEM lattice due to different TM constituents, can provide enhanced oxygen evolution reaction (OER) activity.[275] Due to their special electronic configuration and surface complexity, HEMs are in general expected to provide desirable electrocatalytic properties.[284,285]

In the present chapter, the synthesis and an in-depth characterization of multi-cationic (with 4 to 7 cations) composed rutile-type ($P4_2/mnm$) structured medium- (4 cations) and high-entropy (5-7 cations) fluorides (MEF and HEFs, respectively) are described in detail. Considering a

solid solution state, the configurational entropy for a 7-cation containing compound can be calculated to be $1.95R$ (based on equation 5.1, where R is the universal gas constant). Configurational entropy values were calculated based on the following equation (Equation 5.1):

$$S_{\text{config}} = -R \left[\left\{ \sum_{i=1}^{N} x_i \ln x_i \right\}_{\text{cation-site}} + \left\{ \sum_{j=1}^{N} x_j \ln x_j \right\}_{\text{anion-site}} \right] \qquad \text{(Equation 5.1)}$$

These compounds were synthesized using a straightforward and scalable mechanochemical ball milling process, therefore avoiding more complex synthesis procedures as reported in previous publications about HEFs.[275] The characterization of the HEFs is demonstrated to support the assumption of a solid solution structure of the compounds, which is imperative for confirming the high configurational entropy. By using various measurement techniques, stretching of M-F bonds at the surface of the nanocrystalline particles was detected, resulting in different chemical environments, as similarly described for nanosized FeF_2 particles by Ramansamy *et al.* [286] Additionally, the compounds were tested regarding their electrocatalytic performance for OER. These results show the promising catalytic features of these easily synthesized high entropy fluorides, thereby avoiding the need of expensive rare earth metals.

5.2 Synthesis and Structural Characterization of HEF Based Compounds

5.2.1 Synthesis of HEF Based Compounds

Commercially available transition metal difluorides such as MnF_2, FeF_2, CoF_2, NiF_2, CuF_2, ZnF_2, MgF_2 (analytical grade >99 %, Alfa Aeser) were used for this work. All chemicals were used without any further purification steps. The following compounds $(CuNiFeZn)F_2$, $(CuNiFeCoZn)F_2$, $(CuNiFeCoMn)F_2$, $(CuNiFeCoZnMn)F_2$ and $(CuNiFeCoZnMnMg)F_2$ were synthesized and characterized, hereinafter referred to as MEF4, HEF5_A, HEF5_B, HEF6, and HEF7, respectively, based on the number of incorporated cations. The HEF materials were prepared by long-term high energy ball milling process carried out at 500 rpm for 48 h in WC jar with a 40:1 WC ball-to-powder weight ratio. All samples were prepared in Ar atmosphere (H_2O < 0.5 ppm, O_2 < 0.5 ppm). Using this simple route, HEF samples containing 4, 5, 6 and 7 elements in equimolar ratios were produced.

Configurational entropy calculations are provided in **Table 5.1**. The entropy values range from $1.38R$ for the 4-cation system to a maximum of $1.95R$ in case of the 7-cation HEF system. All materials crystallized in a rutile-type ($P4_2/mnm$) structure.

Table 5.1 Configurational entropy values (S_{config}) of the synthesized HEF (where R is the universal gas constant)

Synthesized fluoride type	Compound	S_{config}
MEF4	$(Cu_{1/4}Ni_{1/4}Fe_{1/4}Zn_{1/4})F_2$	$1.39R$
HEF5_A	$(Cu_{1/5}Ni_{1/5}Fe_{1/5}Co_{1/5}Mn_{1/5})F_2$	$1.61R$
HEF5_B	$(Cu_{1/5}Ni_{1/5}Fe_{1/5}Co_{1/5}Zn_{1/5})F_2$	$1.61R$
HEF6	$(Cu_{1/6}Ni_{1/6}Fe_{1/6}Co_{1/6}Zn_{1/6}Mn_{1/6})F_2$	$1.79R$
HEF7	$(Cu_{1/7}Ni_{1/7}Fe_{1/7}Co_{1/7}Zn_{1/7}Mn_{1/7}Mg_{1/7})F_2$	$1.95R$

HEF similar to ZnF_2 crystallizes in a rutile, tetragonal structure (space group: $P4_2/mnm$, refer Figure 5.1 a). The transition metals (TM) form a tetragonal lattice. TM cations are surrounded by six fluorine atoms in a slightly distorted octahedron. This result in almost hexagonal close packed structure in which the TM cations occupy half of the octahedron gaps. The crystal structure can therefore be better described as a tetragonal packing of strands of edge-linked $[TMF_6]$ octahedrons parallel to the crystallographic c-axis. These chains are connected by the corners of the octahedra, the rutile structure is commonly known from oxide and fluoride compounds, e.g. TiO_2, FeF_2, ZnF_2, etc. The respective cations for the MF_2 HEF (M= Co, Cu, Mg, Ni, Zn, Mn, Fe) are selected by adhering to the Hume-Rothery and Pauling's rules, which propose similarity in ionic radii, coordination numbers and crystal structures to successfully achieve a solid solution.[287] Table 5.2 shows the space group and lattice constant values of the starting binary fluorides precursors utilized for this study. A similar range of lattice constant values is exhibited by all binary fluorides, ZnF_2 ($a=b=$ 4.705 Å and $c=$ 3.134 Å, as given by ICSD#9169) was used as the reference for refining the X-ray diffraction (XRD) patterns of the HEF. A representative Rietveld refinement result of the HEF7 is presented in Figure 5.1 b). Single phase rutile structure is confirmed with lattice parameters values, $a = b = 4.7134 (1)$ Å, $c = 3.1726(0)$ Å and average crystallite sizes of 8.7(5) nm.[288,289] Figure 5.1 c) indicates that all materials show a single-phase rutile structure, the Miller indices hkl are labeled at the top diffractogram of HEF7. Since different sized ions are incorporated into the one single-phase crystal structure, the shift of the (110) reflection, as shown in Figure 5.1 d, can be explained as follows. In MEF4 an average metal ion radius of 0.74 Å is calculated based on the assumption of equimolar proportions of the metal ions and the ionic radius values given by Shannon.[290] Additionally, the high-spin configuration of the metal ions (where applicable) was assumed, since F^- as ligand leads to only a small splitting (weak ligand in the spectrochemical series for octahedral coordinated ions) of the d-orbitals into t_{2g} and e_g states, therefore favoring high-spin configuration of the ions. Incorporating Mn^{2+} (HEF5_A, Mn^{2+} ion radius 0.83 Å) leads to an expansion of the MEF4 unit cell, indicated by peak shift to lower 2θ values. When Mn^{2+} is replaced by Zn^{2+} (HEF5_B, radius Zn^{2+} 0.74 Å), a larger unit cell than MEF4 but a smaller unit

cell than HEF5_A is expected, but the XRD reflections show similar unit cell sizes as for HEF5_A. Zn^{2+} seem to widen the unit cell more than expected, since adding both Mn^{2+} and Zn^{2+} in HEF6 leads to a further increased unit cell volume compared to the HEF5 compounds. Adding the smaller Mg^{2+} (HEF7, radius Mg^{2+} 0.72 Å) reduces the size of the unit cell again, as shown in the respective pattern.

Table 5.2 Crystal structure, cation coordination number and cation radius of the precursor binary fluorides.

Binary fluorides	Crystal system	Lattice constant (Å)	Ionic radius, with/without spin config. (Å)	References
CuF$_2$	Monoclinic	a= 3.2973; b=4.5624; c=4.6157	7.7	ICSD#71833
NiF$_2$	Rutile	a= b= 4.6498 c=0.3.0838	6.3	ICSD#9168
FeF$_2$	Rutile	a= b= 4.6945; c=3.3097	7.8 (H), 6.1(L)	ICSD#9166
CoF$_2$	Rutile	a= b= 4.6941; c=3.1698	7.45(H), 6.5(L)	ICSD#9167
ZnF$_2$	Rutile	a= b= 4.7048; c=3.1338	6.8	ICSD#9169
MnF$_2$	Rutile	a= b= 4.877; c=3.311	8.3(H), 6.7(L)	ICSD#9165
MgF$_2$	Rutile	a= b= 4.621; c=3.0519	7.2	ICSD#397
HEF7	Rutile	a= b= 4.7134; c=3.1726	-	Calculated (TOPAS)

*L= low spin, H= high spin, adapted from [290]

5.3 Morphological Characterization of HEF compounds

SEM images (in Figure 5.2 a to e) reveals agglomerated pristine HEF based nanoparticles. All the HEF compounds exhibited random morphology with fine nanoparticle nature. Transmission electron microscopy (TEM) analysis was carried out using HEF7 as an example, since it contains the highest number of different incorporated cations. The morphology of the as-synthesized HEF7 indicated very fine polycrystalline nanoparticles with crystallite sizes around 10 nm. This is in accordance with the Rietveld results (crystallite size, D=8.7(5) nm). The sizes of the particles, composed of many crystallites, range up to hundreds of nm (Figure 5.3 a)**.** The inset in Figure 5.3 a show the results of selected-area electron diffraction (SAED) taken on a small area at the edge of a HEF7 nanoparticle. The nanoparticles possess high crystallinity with rutile-structure and the SAED annular pattern confirms that the material is obtained without any secondary phases or impurities. Figure 5.3 b illustrates a high-resolution TEM micrograph of the lattice planes from HEF7, with a d-spacing corresponding to the 110 planes (as confirmed from the XRD pattern).
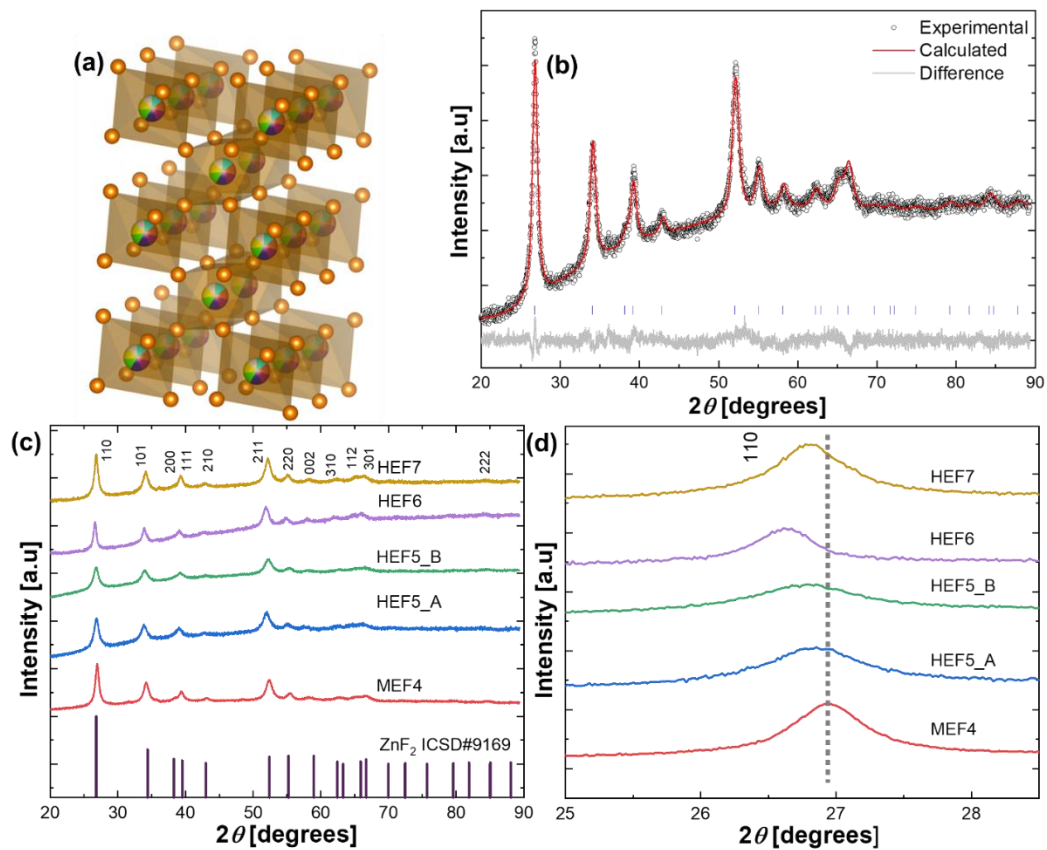
Figure 5.1 a) Crystal structural of HEF7. The colored spheres are corresponding to the different incorporated metals, the orange balls spheres to F **b)** Rietveld refinement of the XRD pattern of HEF7 confirming its phase purity **c)** XRD patterns of 4, 5, 6, 7 cations containing MEF and HEF samples and **d)** evolution of the 110 reflection due to multiple cation incorporation into the crystal structure.
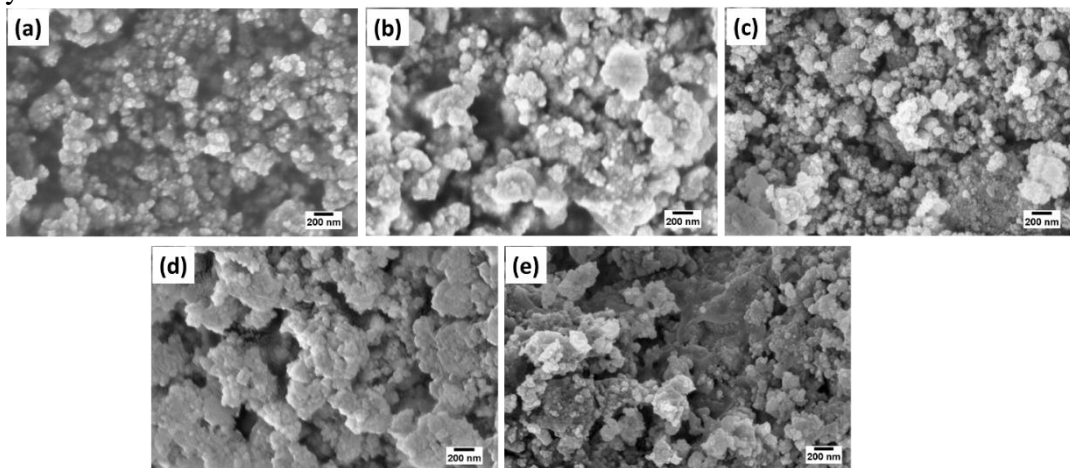
Figure 5.2 SEM images of a) HEF4, b) HEF5_A, c) HEF5_B, d) HEF6 and e) HEF7 pristine nanoparticles.
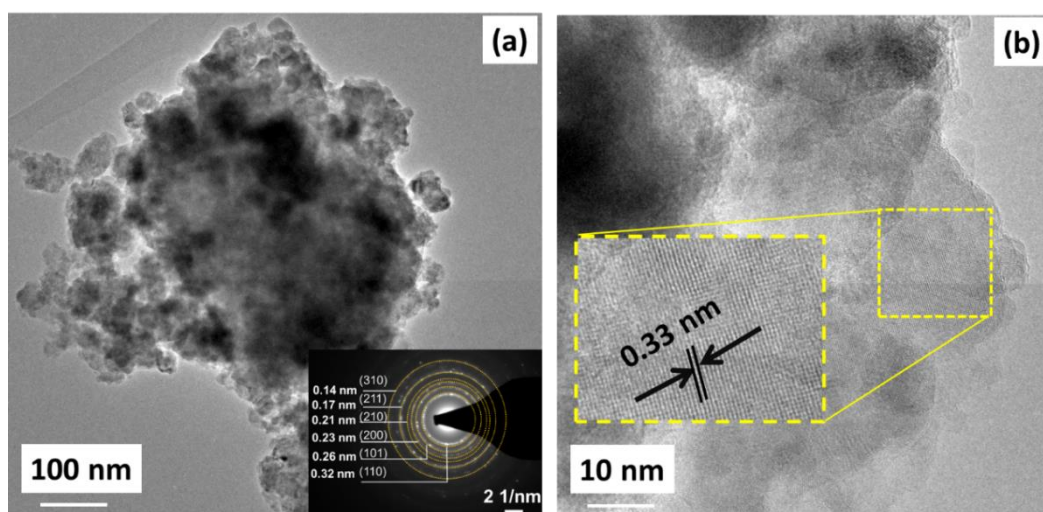
Figure 5.3 a) TEM images of HEF7 and the corresponding SAED pattern (inset). These SAED indices correspond to ZnF$_2$ (rutile-type structure, *P*4$_2$/*mnm*, 136) b) HR-TEM image showing lattice planes (inset depicting a magnified area) with a d-spacing value corresponding to the (110) plane of ZnF$_2$.

Figure 5.4 shows the results from energy-dispersive X-ray spectroscopy (EDS) analysis of HEF7 nanopowders. The mapping indicates a solid solution with all 7 metallic cations and fluorine being homogeneously distributed at the nanometer level. From the elemental distribution in EDS mapping, the TEM and the XRD results, it is assumed that the synthesized powders were homogeneous single-phase solid solution materials. The stoichiometry of all the HEF based compounds with chemical formula MF$_2$ were calculated based on inductively coupled plasma-optical emission spectroscopy (ICP-OES). ICP-OES allows for the precise quantification of the elements contained in the sample. Figure 5.5 shows the corresponding stoichiometries of all of HEF compounds based on ICP-OES analysis. The theoretical value of metal to fluorine ratio (M: F) is 0.5 for the rutile-type MF$_2$ based HEF materials. The relative cationic species concentration were normalized based on the fluorine content.
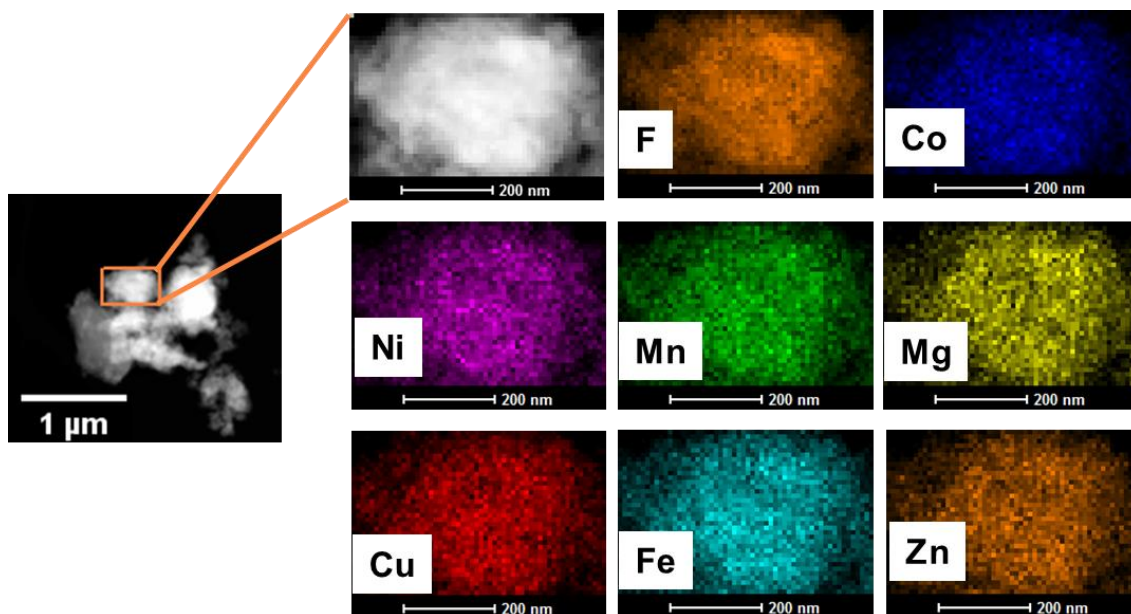
Figure 5.4 STEM-EDX mapping of HEF7. All incorporated elements show homogenous distribution.
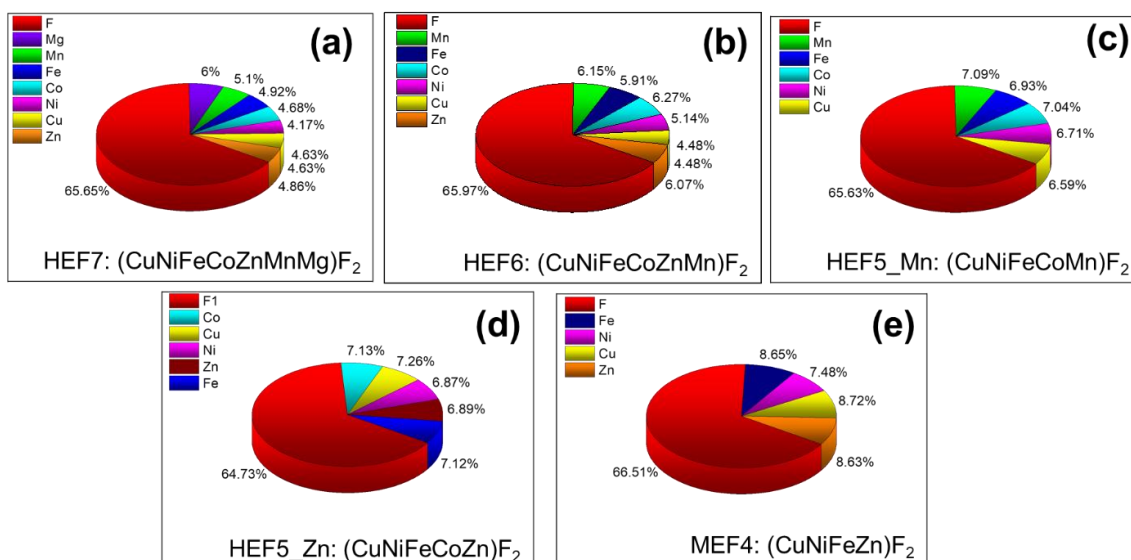
Figure 5.5 a) to e) ICP-OES results of HEF based compounds with variant incorporation transition metal cations (HEF7, HEF6, HEF5_B, HEF5_A, and MEF4, respectively). All values are expressed in atomic %.

5.4 Mössbauer and Electron Energy Loss Spectroscopy of HEF Nanoparticles

In order to further confirm the solid solution state of HEF7, ^{57}Fe Mössbauer spectroscopy (MS) investigation was carried out to identify the chemical environment and the oxidation state of Fe in HEF7. 57Fe Mössbauer spectroscopy data was gathered in transmission geometry using a spectrometer with a moving source of 57Co in a Rh matrix and a triangular velocity variation. All reported isomer shifts of samples are reported relative to bcc phase-Fe measured at room temperature. Figure 5.6 shows the Mössbauer spectrum of HEF7 pristine nanoparticles. The

spectrum was fitted using two quadrupole doublets sub-spectra, both corresponding to Fe^{2+} environments (doublet I and II) with nearly identical isomer shifts (IS, I = 1.34 mm/s, II = 1.30 mm/s) but distinct quadrupole splits (QS, I = 2.67 mm/s, II = 1.96 mm/s). In addition, a small fraction of Fe^{3+} was evident (IS = 0.40 mm/s, QS = 0.48 mm/s). The quantification, based on the relative area fraction, yielded the values of Fe^{3+}, Fe^{2+} (doublet I) and Fe^{2+} (doublet II) as 19 %, 50 % and 31 %, respectively. However, this result is in contrast to the other obtained results from SAED, XRD, TEM mapping and NMR, since it suggests a different chemical environment and even a mixed-valence state of the incorporated Fe. Nevertheless, this contrasting behavior is coherent with the conclusions drawn from the Mössbauer studies of FeF_2 nanoparticles, reported by Ramasamy S. *et al.*[286] They reported a similar finding, wherein MS peak splitting arose from local defects due to a large amounts of grain boundaries. Additionally, they referred to a slightly different Fe-F bond stretching at the surface (due to minor topological hydration), which could lead to a different chemical environment and therefore requires different fitting parameters than bulk FeF_2. Hence, we presume that the origin of broadening in MS spectrum HEF7 might be due to the ball milling procedure and the vast amount of local defects and grain boundaries formed during this procedure.[291]
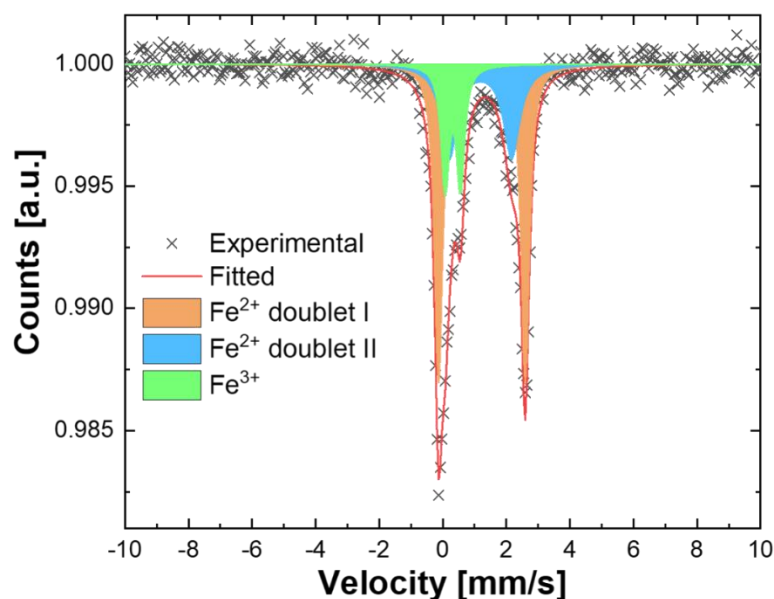
Figure 5.6. Mössbauer spectrum of pristine HEF7 nanoparticles showing two different oxidation states and two different chemical environments.

To elucidate the presence of $Fe^{2+/3+}$ at the surface of the particles, electron energy loss spectroscopy (EELS) mapping was performed on the particle edges to identify the oxidation states of Fe, Co, Ni, Cu and Mn. Zn and Mg were assumed to be in the 2+ oxidation state. The sample was transported in a vacuum transfer TEM holder to exclude oxidation. Figure 5.7 shows the EELS investigation of HEF7 with five different areas on the edges of different

particles being measured. Co, Cu, and Ni could only be found in the 2+ state and did not show any indications that point towards a mixture of different valence states. Figure 5.7 a show the L_3- and L_2-edges of Mn, exhibiting a maximum peak shift between the different areas of about 0.6 eV. The L_3/L_2 ratio shows some minor differences between the areas, but the ratios for Mn^{3+} and Mn^{4+} would be much lower, so Mn in 3+ and 4+ states can be excluded (see Figure 5.8 a)). Therefore, Mn in all areas is measured to be in the state of 2+. The Fe L_3- and L_2-edge positions are displayed in Figure 5.7 b. Two different L_3-edges are detected, which can be indexed into Fe^{2+} and Fe^{3+} as indicated by Mössbauer spectroscopy results (more details in Figure 5.8 b). Different measured areas show different valence states, which implies that an inhomogeneous change in the oxidation state takes place. We attribute this to the local defects resulting from ball-milling, as explained in the Mössbauer section of this article. Figure 5.7 c shows one of the measured areas and an EELS mapping, depicting that Fe^{2+} and Fe^{3+} appear mixed, and not separated into areas with only Fe^{2+} or Fe^{3+}. However, it should be noted that no secondary phases were observed, either from XRD or HR-TEM, which indicates that these differences in the charge states are intrinsic features of single phase HEF7.

5.5 X-ray Spectroscopy Analysis of HEF Nanoparticles

Further, the surface chemical state of the HEF7 sample was probed with X-ray photoelectron spectroscopy (XPS). The relevant spectra of the constituent elements are shown in Figure 5.9 and the corresponding reference spectra in Figures 5.10 to 5.19. In the Zn 2p spectrum (Figure 5.9 a), a single doublet with the $2p_{3/2}$ component at 1023.1 eV binding energy and the full width at half maximum (FWHM) intensity of 2.3 eV is observed. As determining the Zn oxidation state purely from the Zn 2p peak is difficult, the Zn LMM Auger line is also considered (see Figure 5.9 b). The Zn LMM Auger line is observed at a kinetic energy of 985.4 eV and thus Zn can be attributed to the Zn^{2+} state.[292] This agrees with our measurements on pure ZnF_2 (see Figure 5.10) as a reference that shows similar values as Zn $2p_{3/2}$ is identified at 1022.9 eV with a FWHM intensity of 1.9 eV and a Zn LMM line at 985.2 eV.
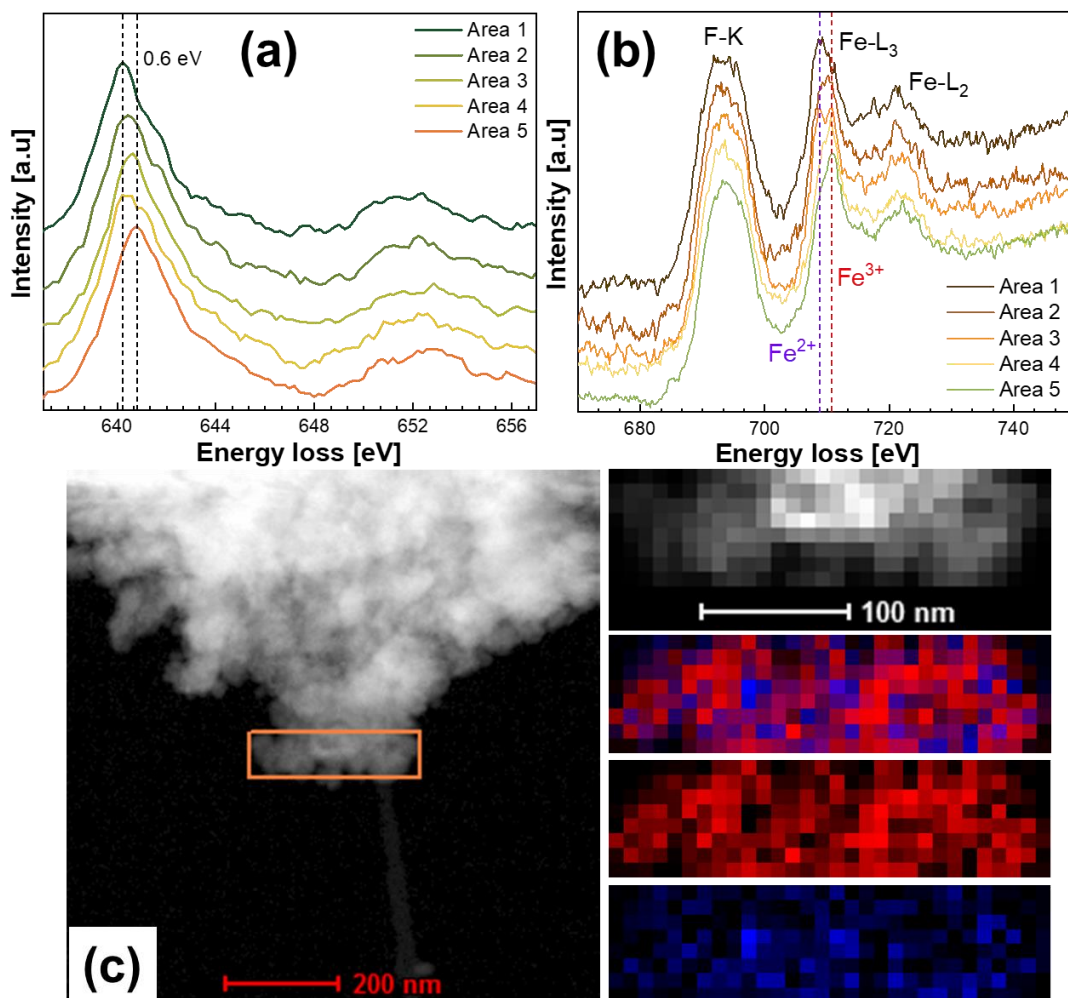
Figure 5.7 Valence state characterization of HEF7 pristine nanoparticles. EELS spectra of a) Mn $L_{2,3}$-edge b) Fe $L_{2,3}$-edge c) EELS mapping results on the marked area denoting the presence of Fe^{2+} (red) and Fe^{3+} (blue).

In the Cu 2p region (Figure 5.9 c), Cu ions in HEF7 show a spectrum with 2 main peaks at 933.4 and 937.3eV. The peak at 937.3 eV with FWHM intensity of 3.5 eV is analogous to Cu $2p_{3/2}$ of pure CuF_2 measurements shown in Figure 5.11. Additionally, satellites of the Cu^{2+} state appear at 942-945 eV in the spectrum. However, the additional peak at 933.4 eV (FWHM: 2.3 eV) in the Cu $2p_{3/2}$ spectrum of HEF7 could be attributed to a reduced state of Cu ions or possibly CuO or $Cu(OH)_2$ state.[293] According to this peak assignment, the majority of Cu ions at the surface of HEF7 (64 % of total Cu ions) are attributed to Cu^{2+}.[293]
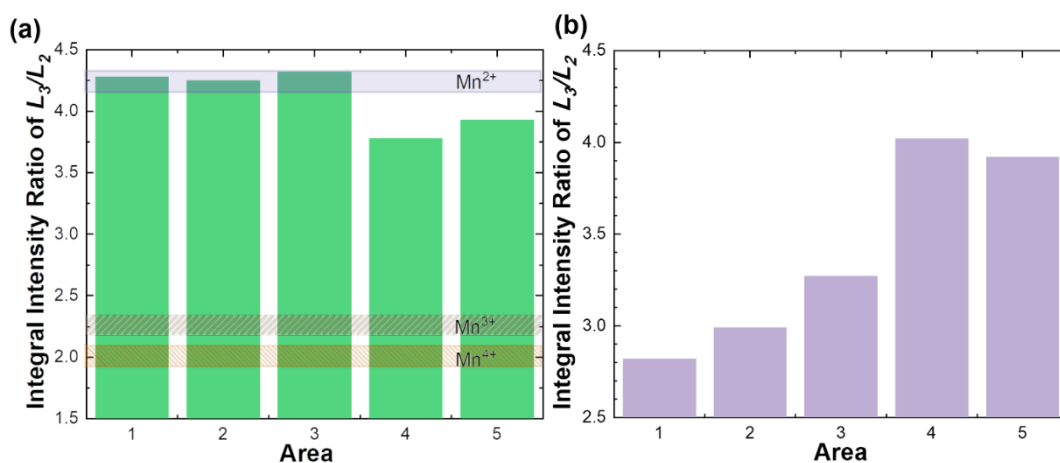
Figure 5.8 Intensity ratios of L_3/L_2 values of a) Mn and b) Fe calculated from the spectra obtained from HEF7 nanoparticle as a function of the areal mapping values acquired at different points.
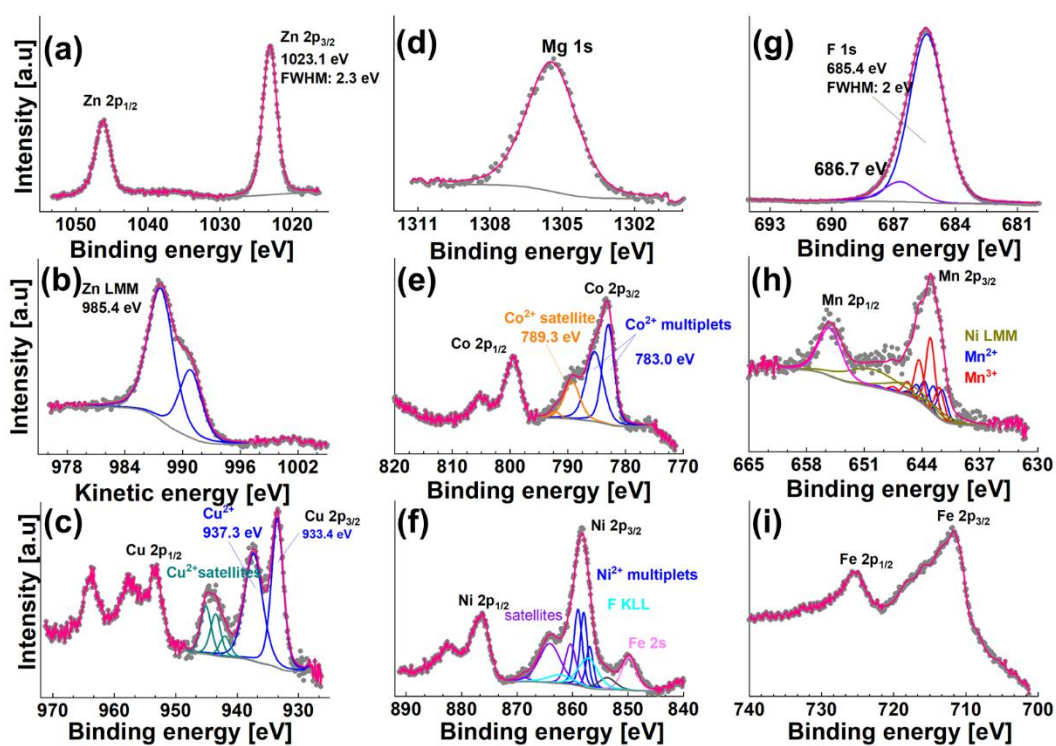
Figure 5.9 XPS spectra of a) Zn 2p, b) Cu 2p, d) Mg 1s c) Zn Auger LMM kinetic energy spectra, e) Co 2p, f) Ni 2p, g) F 1s, h) Mn 2p and i) Fe 2p of HEF7 nanoparticles.
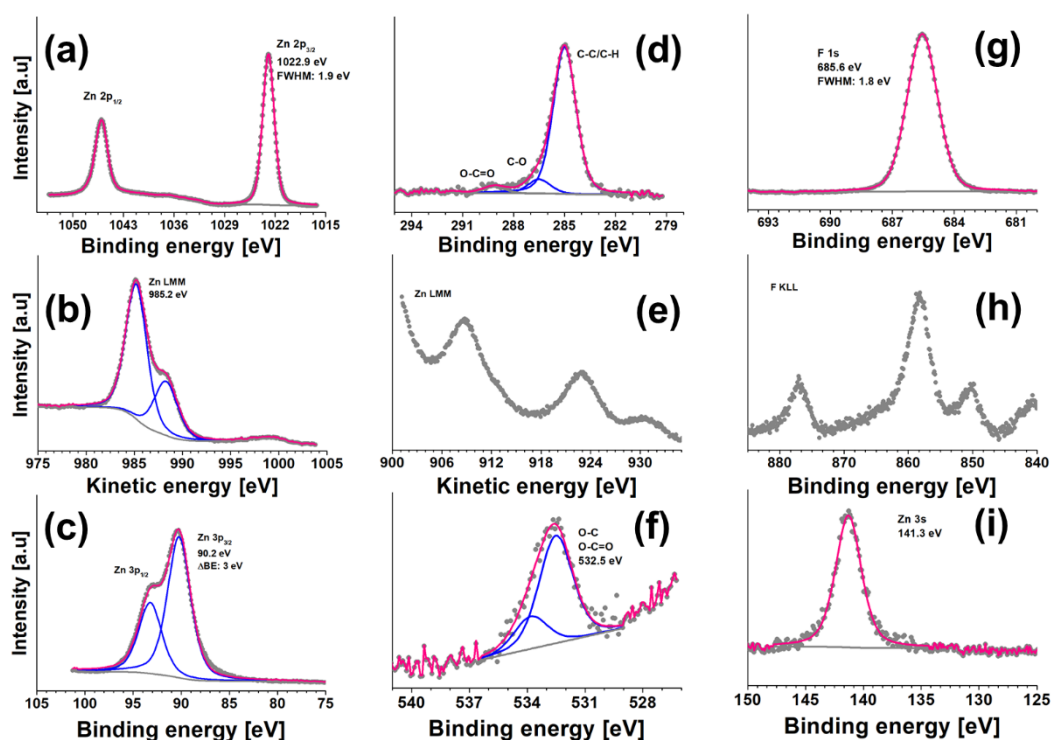
Figure 5.10. XPS spectra of a) Zn 2p, b) Zn LMM (kinetic energy), c) Zn 3p, d) C 1s, e) Zn LMM (kinetic energy), f) O 1s, g) F 1s, h) F KLL, and i) Zn 3s of ZnF_2 powder.

In Figure 5.9 d, Mg 1s peak in the HEF7 sample is assigned to Mg^{2+} ions in a Mg-F bond at 1305.4 eV with FWHM intensity of 2.5 eV [294,295] (pure MgF_2 XPS spectrum is given in Figure 5.12). To interpret the Ni $2p_{3/2}$ spectrum (Figure 5.9) in HEF7, it is compared to the Ni $2p_{3/2}$ spectrum of pure NiF_2 powder sample. The overlap of the Ni LMM and Fe LMM line on Co 2p spectra is ignored, because of the low intensity of the Auger peaks. The peak overlay in Figure 5.14 shows a similar binding energy and FWHM intensity of the main peak. Therefore, the Ni $2p_{3/2}$ spectrum of HEF7 was fitted with the multiplet parameters of Ni $2p_{3/2}$ in NiF_2 and can be attributed to Ni^{2+} state. However with this method the existence of a minor contribution of Ni^{3+} ions cannot be fully excluded, since the binding energies of Ni^{2+} and Ni^{3+} ions are very close to each other, at least in oxide samples.[149,296–299] In the peak fitting of the Ni spectrum, overlapping F KLL, Mn LMM, and Fe 2s peaks are taken into consideration. The majority of F ions (Figure 5.9 g) at 685.4 eV with a FWHM of 2 eV are attributed to the F ions in the crystal structure and have a binding energy similar to the binary fluorides (shown in Figures 5.10 to 5.18).The low-intensity peak 686.7 eV might probably occur through the ball milling process by forming C-F contaminations on the surface.[300] In the Mn 2p spectra (Figure 5.9 h), a broad doublet can be observed. The Mn $2p_{3/2}$ peak can be fitted with two sets of multiplets and including the overlapping Ni LMM Auger peaks that indicates approximately 60% Mn^{3+} and

40% Mn^{2+} on the surface of HEF7. The multiplet sets of Mn^{2+} and Mn^{3+} are taken from the MnF_2 and MnF_3 reference measurements shown in Figures 5.15 and 5.16, respectively.
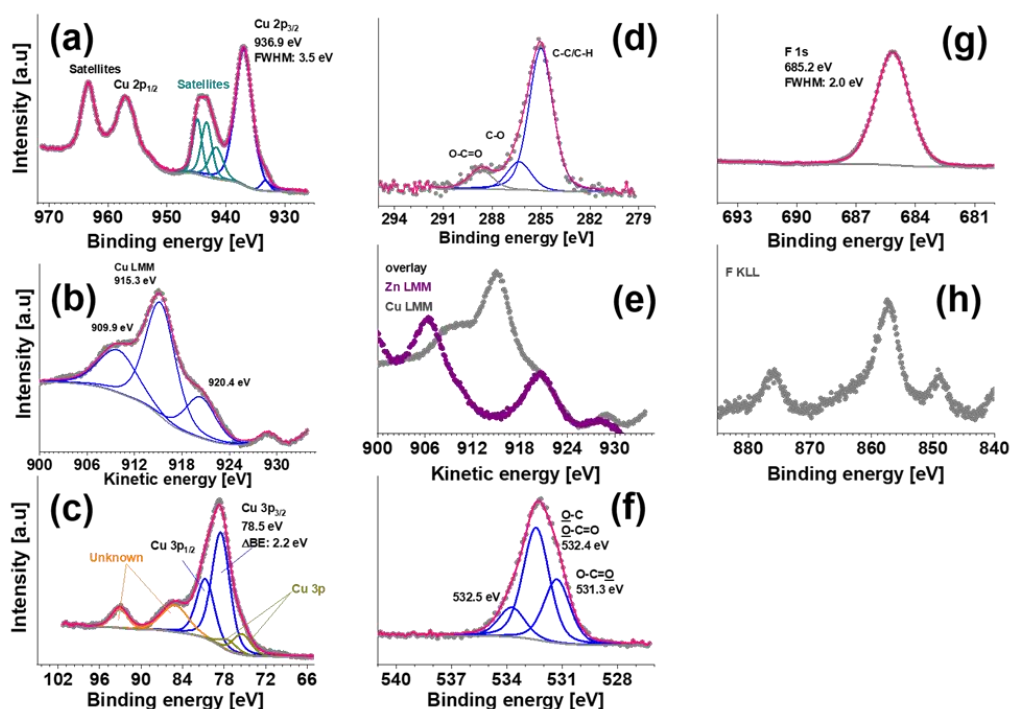
Figure 5.11. XPS spectra of a) Cu 2p, b) Cu Auger LMM kinetic energy spectra, c) Cu 3p, d) C 1s, e) overlay plot of Zn LMM and Cu LMM kinetic energy spectra f) O 1s g) F 1s and h) F KLL, of CuF_2 powder (In pure CuF_2 powder, the Cu $2p_{3/2}$ spectrum has a pronounced peak at 936.9 eV with FWHM of 3.5 eV).

The Co 2p spectrum (Figure 5.9 e) of HEF7 shows one doublet with multiplet structure and a characteristic satellite. The main peak position at 783 eV as well as the satellites at 6.3 eV higher than the main peak indicate that the Co ions in HEF7 appear as Co^{2+} in a Co-F bonding situation. Additionally, the fitting parameters of the HEF7 match with the pure CoF_2 precursors as presented in Figure 5.13.
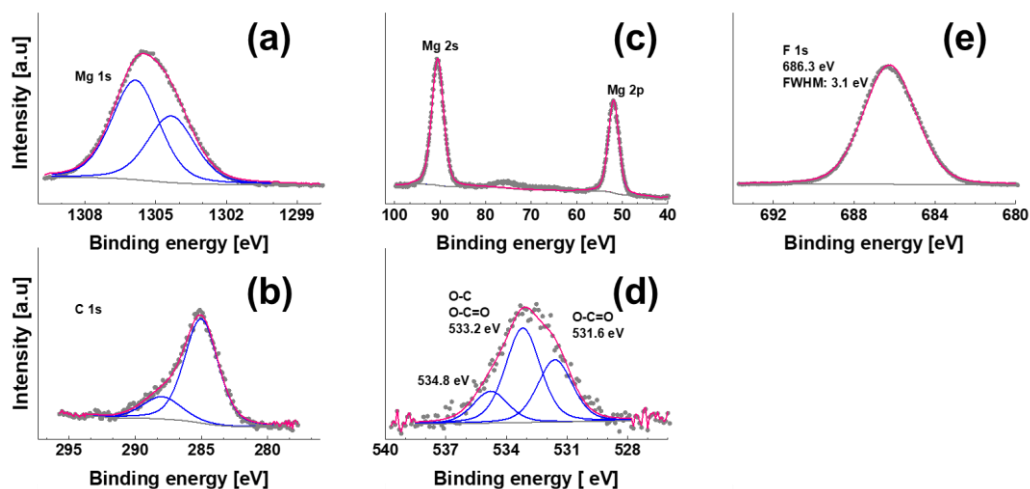
Figure 5.12 XPS spectra of a) Mg 1s, b) C 1s, c) Mg 2p, Mg 2s, d) O 1s and e) F 1s of MgF_2. The broadening of C 1s and Mg 1s spectra is because of difficulties of charge compensation.
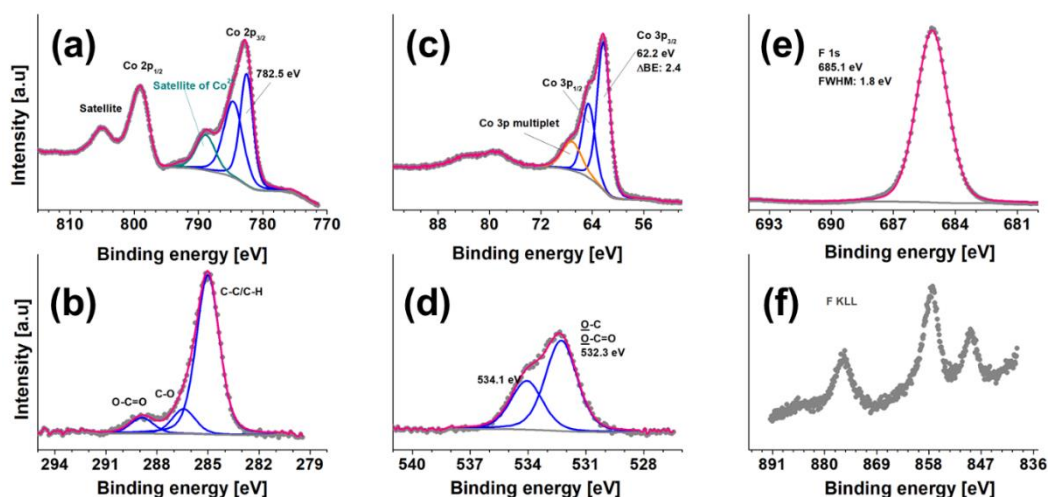
Figure 5.13 XPS spectra of a) Co 2p, b) C 1s, c) Co 3p, d) O 1s e) F 1s, and f) F KLL of CoF_2 powder.
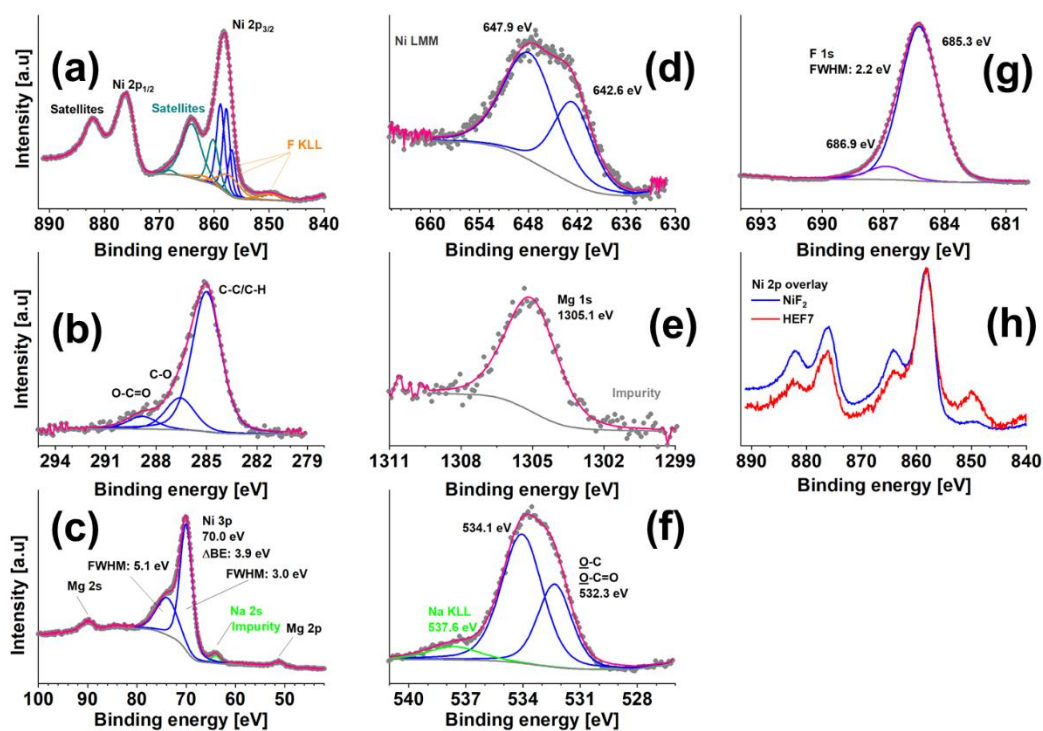
Figure 5.14 XPS spectra of a) Ni 2p, b) C 1s, c) Ni 3p (Mg 1s, Na 2s as impurity), d) Ni LMM, e) Mg 1s, f) O 1s, g) F 1s of NiF_2 powder and h) overlay data of NiF_2 power (with HEF7).
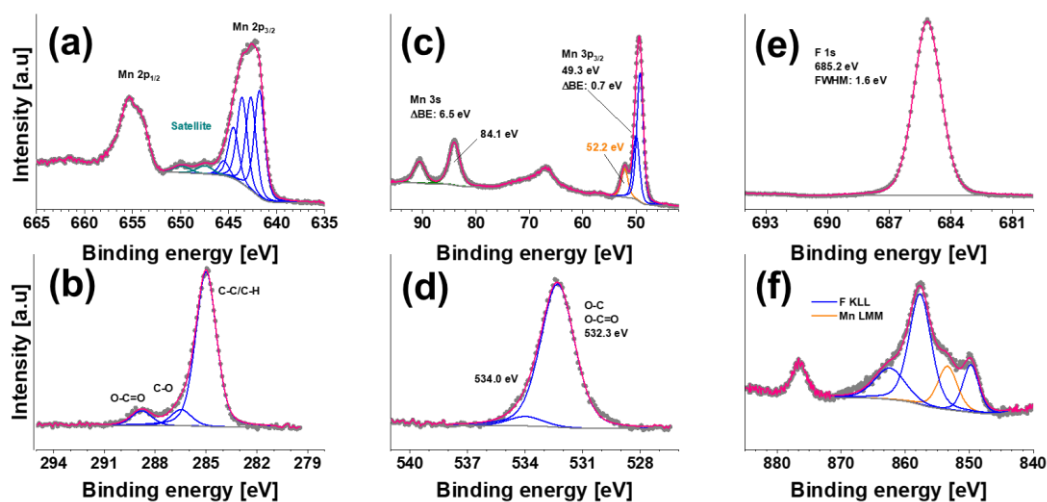
Figure 5.15 a) Mn 2p, b) C 1s c) Mn 3p, Mn 3s, d) O 1s e) F 1s and f) F KLL XPS spectra of MnF$_2$ powder.
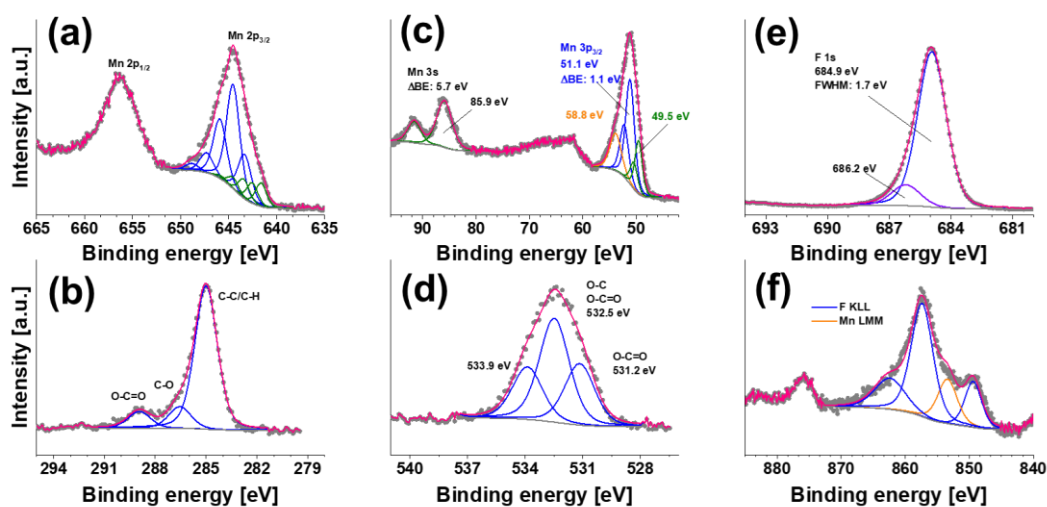
Figure 5.16 a) Mn 2p, b) C 1s c) Mn 3p, Mn 3s, d) O 1s e) F 1s and f) F KLL XPS spectra of MnF$_3$ powder.

Identification of the chemical state of Fe ions in HEF7 using XPS is challenging. In HEF7, the Fe 2p (Figure 5.9 i) overlaps with low intensity F plasmons and the Co LMM Auger line. Both increase the background intensity and hamper reliable peak and background positioning. Furthermore, the overlapping Co Auger line hinders direct comparison to the FeF$_2$ reference. Therefore, oxidation state analysis of the Fe ions in HEF7 from XPS was not possible.
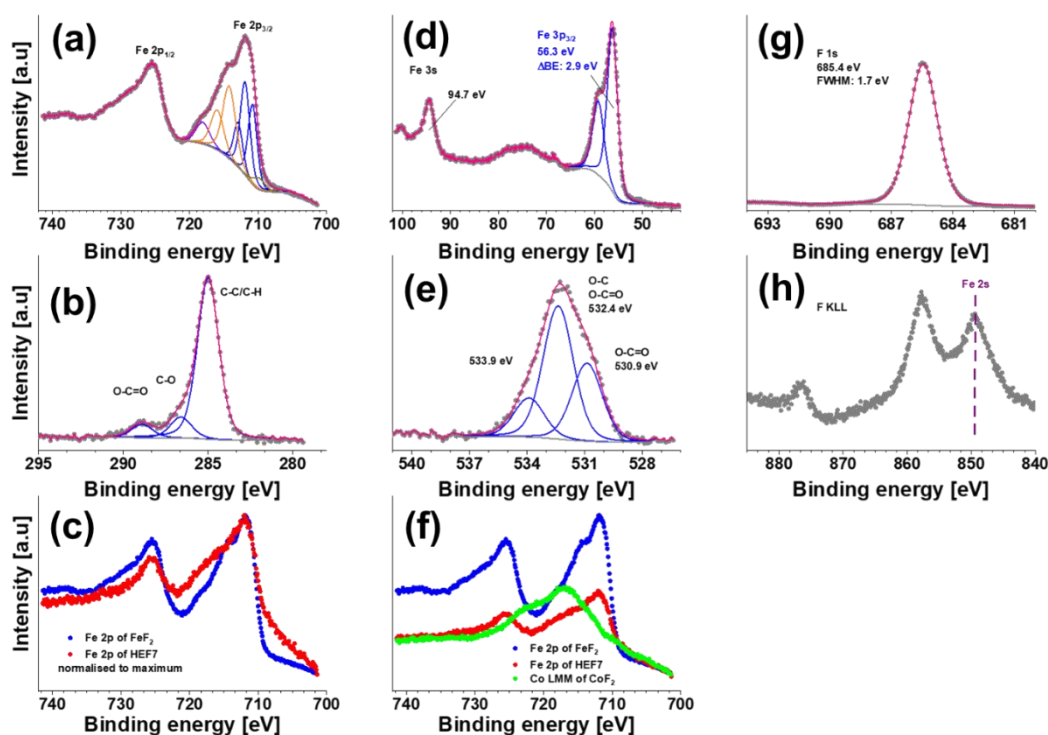
Figure 5.17 XPS spectra of a) Fe 2p, b) C 1s, c) overlay comparison of FeF$_2$, HEF7 d) Fe 3p, Fe 3s e) O 1s, f) overlay comparison of FeF$_2$, HEF7, Co LMM of CoF$_2$, g) F 1s and h) F KLL of FeF$_2$ powder.

In summary, XPS confirms that Mg, Zn, and Co ions are present in the 2+ state, even at the outer surface of the HEF particles. For Cu and Mn, mixed valence states were found at the surface, including around 64 % of Cu ions and 40 % of Mn ions in the 2+ state. Also, the majority of Ni ions can be considered as Ni^{2+}. The Fe oxidation state could not be analyzed from XPS because of intense peak overlap. We assume that the discrepancy between XPS and EELS results regarding the oxidation state of Cu and Mn is surface related, since EELS refers to the bulk material while XPS only to the surface. Indications of a different surface condition compared to the bulk material were confirmed by MS measurements. As already mentioned, the differences can probably be traced back to the ball grinding effect.
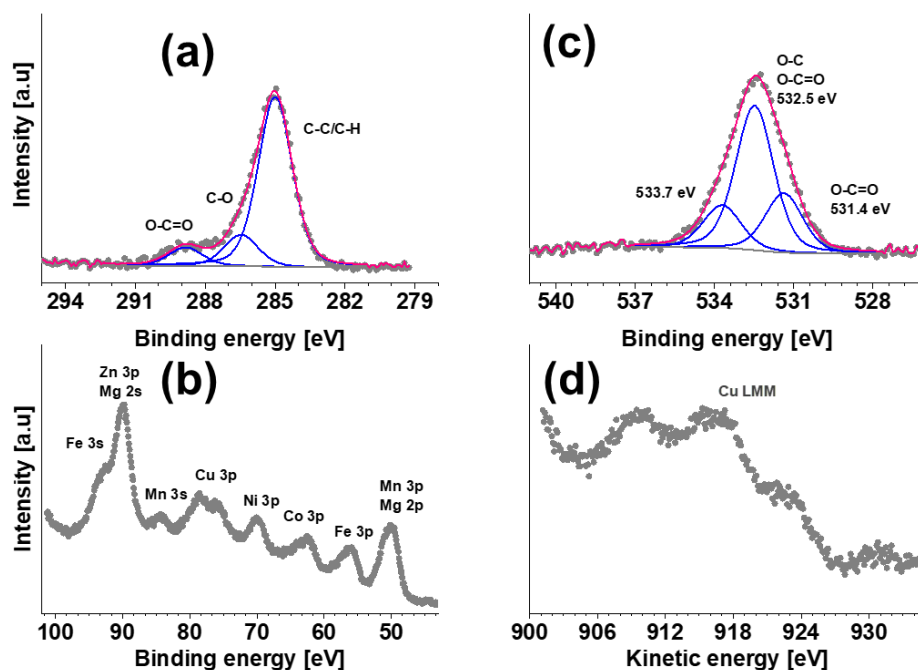
Figure 5.18. XPS spectra of a) C 1s, b) overlapping spectra hamper evaluation of Mn 3p and Mn 3s for elucidation of Mn oxidation state c) O 1s and d) Cu LMM of HEF7 nanoparticles.

5.6 Nuclear Magnetic Resonance Spectroscopy of HEF Nanoparticles

Finally, ^{9}F solid state nuclear magnetic resonance (NMR) spectroscopy was performed on pure HEF7 and MEF4 nanoparticles to analyze the anionic site and to identify the presence of F$^-$ in the complex crystal structure. Exact probing of fluorine, which is a direct neighbor of the transition metal elements, is quite challenging due to often unpaired electronic spins. Among the binary fluoride precursors (described in detail in the experimental section) MgF_2, ZnF_2, and NiF_2 shows distinct resonance peaks in the NMR spectra (refer Figure 5.19 b). Other binary fluorides exhibited no signals as the unpaired electronic spin density at the F$^-$ sites leads to strong line broadening and very fast nuclear spin relaxation as F$^-$ sites are bounded directly to paramagnetic ions.[301–304] Figure 5.19 a shows the ^{9}F-NMR spectra of 4- and 7- element containing fluoride powders (MEF4 and HEF7). It should be noted that the overall intensity for both samples is extremely low, compared to the spectra of the binary samples (Figure 5.19 b), since all contributions are strongly broadened. MEF4, (CuNiFeZn)F_2, still shows some residual peaks in the region between 0 and -400 ppm, which might indicate residual clustering of some of the metals (comparable NMR data of binary fluorides can be found in Figure 5.19 b). In the NMR spectrum of HEF7, (CuNiFeCoZnMnMg)F_2, however, no more signals appear.

This indicates that the electronic situation and the relaxation time in HEF7 materials has changed compared to the initial compounds (MgF_2, ZnF_2, and NiF_2) as well as MEF4. This is remarkable because the cations of binary fluorides showing a signal in ^{19}F-MAS-NMR and

those do not show a signal are mixed with similar ratios in MEF4 (2:2) and HEF7 (3:4). Whether this is a direct result of the high entropy cannot be confirmed with certainty from the data available here.
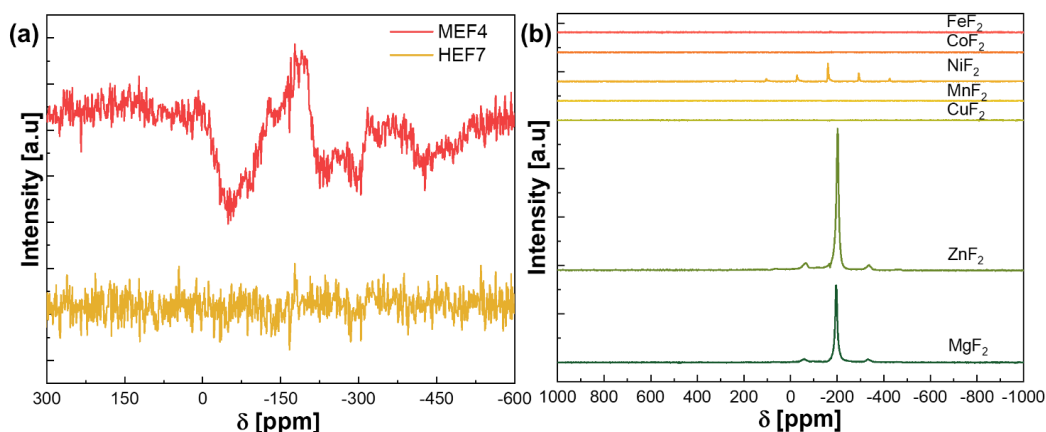
Figure 5.19 a) ^{19}F-MAS-NMR comparative spectra of MEF4 and HEF7. Due to the high degree of cation mixing, peak-absence is noted in the HEF7 and b) ^{19}F-NMR spectra of the reference binary fluorides used as the precursors for HEF based materials synthesis.

5.7 Summary

In summary, this chapter shows the preparation of novel transition-metal-based high entropy fluorides by a cost-effective mechanochemical synthesis route and their characterization by XRD, SEM, TEM, XPS and NMR. Synthesis by simple ball milling avoids the need for a cost intensive high temperature preparation and quenching process. Based on the combined investigations from XRD, ICP-OES, TEM, NMR and EDX-EELS studies, it is shown that all pristine HEF samples crystallized in a phase-pure rutile structure with the presence of agglomerated fine nanoparticles. The identification of the local structure of the HEF compounds was probed by ^{9}F-NMR and XPS. The local structural disruption of HEF compounds can most likely be attributed to the synthesis process and the resulting variation of the oxidation states of Fe as demonstrated by Mössbauer spectroscopy. As reported for high entropy oxides, multi-cation substitution in HEF materials may provide as well an interesting route for tailor-made electrochemical properties of conversion electrodes for energy storage applications. In addition, oxygen evolution activity with tailored HEF material was validated for electrocatalysis applications and the HEF exhibited a lower overpotential and Tafel slope in comparison to a reference IrO_2 (not included in this dissertation, this part is published in [265]).

Chapter 6 Tailored High Entropy Fluorides as High-Capacity Lithium-Ion Batteries Cathodes: Insight into the Conversion Mechanism

Selected parts of this chapter will be submitted for peer-reviewed publication review process within the framework of this thesis. The experimental work was carried out jointly by Parvathy Anitha Sukkurji and Yanyan Cui under the supervision of Dr. Ben Breitung. The manuscript was organized and written by Parvathy and Yanyan combinedly under the guidance of Dr. Breitung and all other co-authors. Co-authors contributed by helping with synthesis, certain characterization methods, providing valuable discussions, and reviewing the article draft for the peer-reviewed publication process.

The synthesis of high entropy fluorides (HEF) nanoparticles possessing single phase microstructure was explained in the last chapter. Owing to the high theoretical specific capacity, metal fluorides are attractive cathode materials. Therefore, in the current chapter, the use of HEFs as a lithium battery cathode material and their underlying mechanisms of reversible lithium storage properties are investigated. Primary, the attention is focused on HEF based cathodes prepared via tape-casting method. Following that, galvanostatic cycling and insights into the conversion reaction mechanism are described. The battery performance is quantitatively analyzed with variety of techniques including cyclic voltammetry (CV), galvanostatic cycling and *ex-situ* TEM methods. Eventually, the conversion reaction hypothesis is validated with the experimental results. In addition, it is demonstrated that the concept of entropy stabilization can greatly improve the cycling stability. These findings offer new guidelines for the material design and the controllability for high-performance lithium-ion batteries. This chapter also covers the illustration of printed HEF as conversion cathodes, its electrochemical optimization as well as their application preview with a full cell prepared with an alloying anode (printed Si), adapted from the initial part of this dissertation. This printed full cell can be employed for powering the low power printed electronic circuits.

6.1 Background

With the rapid development of high-capacity anodes such as silicon, lithium metal and conversion-based materials, the commercial intercalation-type transition metal oxide cathode materials (i.e., $LiCoO_2$ (LCO), $LiNiMnCoO_2$ (NCM), and $LiFePO_4$ (LFP)) encounter the challenges to deliver high energy density batteries. This limits the further development of LIB [305], hence, it is highly necessary to investigate high capacity cathode materials for catering the need of high energy density LIB. Recently, conversion-based electrode materials with

potentially higher energy densities than conventional intercalation-based electrode materials have drawn attention [122]. The conversion reaction can be expressed as (Equation 6.1):

$$MX_m + nLi = nLiX_{m/n} + M \qquad \text{(Equation 6.1)}$$

where M denotes the transition metals and X depicts the halides such as F, Cl, O, S, P or N [306].

Due to the advantage of multiple electrons transfers per metal center during the heterogenous conversion reaction process, these electrode materials could deliver a capacity three to five times greater than conventional cathode materials, which could offer a possibility to match the high capacity anode [115]. Among the conversion materials reported so far, metal fluorides (MFs) have the highest electromotive force compared to nitrites, hydroxide, oxides, and sulfides. MFs are an alternative to conventional intercalation compounds and have a high capacity, 3 times higher than the state of the art intercalation materials [115,33]. As fluorine has the highest electronegativity, MFs have a high reaction potential rendering it suitable as cathodes materials [307].

In tune with the reported conversion materials [307], MFs electrodes have large volumetric expansions during cycling that will pulverize the electrode leading to large capacity losses, and side reactions resulting in extremely poor performance at elevated temperatures. Moreover, the large voltage hysteresis is also a critical limitation for MFs [122,308]. The actual reaction potential in the practical case is much lower than the value of the electromotive force calculated in theory, which affects the rate of charge exchange [309]. In order to circumvent these issues, doping or increasing electronic conductivity via carbonaceous materials are best to improve the properties of MFs [310]. Wang [115] *et al.* prepared $Cu_{0.5}Fe_{0.5}F_2$ via simple mechanochemical synthesis and this ternary material revealed hysteresis values of less than 150 mV at slow cycling rate. Following that, Gordon [121] *et al.* synthesized combinations of binary fluorides such as FeF_2-MnF_2, FeF_2-CoF_2, FeF_2-NiF_2. These composites demonstrated that the cathode stability strongly depends on the ability of the solid electrolyte interphase (SEI) on the cathode, which in turn strongly depends on the metal composition. From these reports, it is evident that multiple cationic substitutions provides us a new avenue for tailoring key electrochemical properties of MF based electrodes.

In Chapter 5, it is already shown that high entropy materials (HEMs) concept can be employed to develop advanced materials with tailorable properties [137]. Many HEMs have been evolved into different compounds including oxides [132,159,270,311], carbides [312], borides, nitrides [272,313], fluorides [275] and sulfides [314], shows unique properties and broad potential applications in variant areas. Motivation for the examination of HEF as a prospective conversion cathode material

arises from Li-storage properties of high entropy oxides (HEO) and high entropy oxyhalides [134,142,148]. However, to date, there are no reports into the entropy stabilization effect on electrochemical properties of HEFs. In the present section, we reported a series of HEF based materials as cathode materials for Lithium-ion battery applications, namely: $(CuNiFeCoZn)F_2$, $(CuNiFeCoMn)F_2$, $(CuNiFeCoZnMn)F_2$ and $(CuNiFeCoZnMnMg)F_2$. Structural and morphological identities of the cycled HEF electrodes were investigated to substantiate the electrochemical properties of HEF cathodes. It is also observed that the electrochemical behavior of the high entropy fluorides depends on individual metal element contribution, therefore electrochemical properties can be tailored by tuning the elemental composition. In addition, we demonstrate that the concept of entropy stabilization can greatly improve the cycling constancy. In this following, various HEF based compounds are extensively examined in the context of battery application, along with additives such as multiwalled carbon nanotubes (MWCNT) to improve the electrical conductivity of the electrodes.

6.2 Synthesis of HEF/CNT Composites

Herein the simple facile synthesis of the multi-cation incorporated HEFs via ball milling process is described. Solid solutions of 4, 5, 6, 7- element containing HEF nanopowders were synthesized via high energy mechanochemical milling process as described in chapter 5. Equimolar weighted ratio of the respective binary fluorides (CuF_2, NiF_2, FeF_2, CoF_2, ZnF_2, MnF_2 and MgF_2, Alfa Aesar, >98% purity) were mixed using Retsch PM100 planetary ball mill with 50 mL WC ball mill jar for 48h at 500 rpm (WC balls of 10 mm diameter). Figure 6.1 a) illustrates the process of composite preparation. For the mixing process, a WC vial and a ball to powder ratio of 40:1 was utilized. The composite formation with carbon nanotubes (MWCNT, Sigma Aldrich, 7.5 % MWCNT basis, an outer diameter of 7 to 15 nm, length 0.5 to 10 μm) was carried out by mechanochemical milling (3 h) with 15 wt % (either of the carbon types) and 85 wt% of HEF powder (active material). The nanotube fibre structure of the MWCNT used for inducing conductivity and HEF/CNT composite preparation is given in Figure 6.1. In a similar manner, for the comparison of electrochemical properties, medium entropy fluorides (MEFs) labelled as MEF3 [$(FeNiCu)F_2$] and MEF4 [$(FeNiCuZn)F_2$] were also prepared by ball milling with MWCNT for 3h at 500 rpm.

For *ex-situ* XRD and TEM measurements active material (HEF) to CNT ratio of 9:1 wt % were utilized to probe better HEF signals from electrode samples. After the milling, the HEF and the HEF/CNT nanocomposites were collected in an Ar filled glovebox to avoid contact with air. The high entropy fluorides of $(CuNiFeCoZn)F_2$, $(CuNiFeCoMn)F_2$ $(CuNiFeCoZnMn)F_2$ and $(CuNiFeCoZnMnMg)F_2$ are marked as HEF5_A, HEF5_B, HEF6, and HEF7, respectively in

the following sections. All the starting precursors were analytical grade purity and used without further purification process.
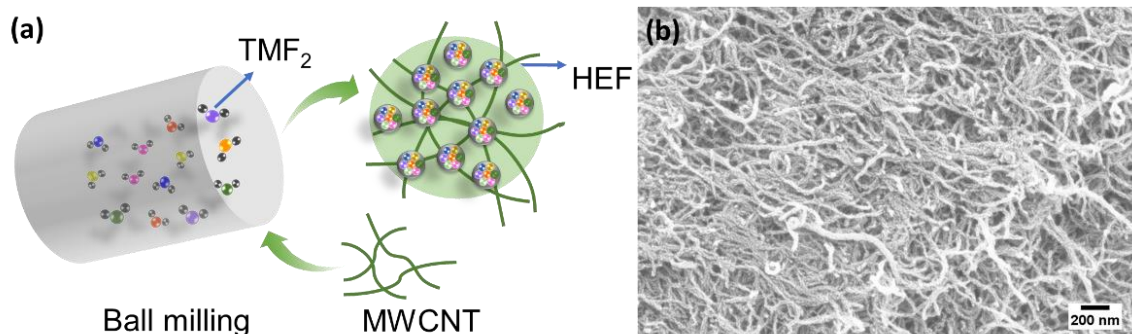
Figure 6.1 a) Illustration of experimental process flow showing the synthesis process adopted for the preparation of HEF/CNT composites, where MF_2 denotes the equimolar ratio of the binary fluorides such as CuF_2, NiF_2, FeF_2, CoF_2, ZnF_2, MnF_2 and MgF_2 and b) SEM image of multiwalled CNT used for composite structure preparation.

6.3 Structural Characterization of HEF/CNT Composites

In this section, scanning electron microscopy (SEM) analysis of pristine HEF/CNT nanocomposites, which were prepared via ball milling method, are presented. Due to the low electronic conductivity of fluorides, MWCNT were utilized to fabricate the composites with HEF powder. This helped to provide rapid pathways for electron flow and interconnectivity between HEF nanoparticles. SEM images of HEF/CNT composites with various sizes and morphology are presented in Figure 6.2 a) to e). Overall, the SEM images revealed irregular and spherical morphology of HEF/CNT nanoparticles. Morphological characterization of HEF/CNT in Figure 6.2 shows that all nanoparticles are agglomerated agglomerates of nanocrystallites with connected particle domains of CNT. Detailed descriptions of structural characterization are given in chapter 5.

6.4 Electrochemical Characterization of HEF Compounds

Electrodes were prepared by slurry coating of of 80 wt.% cathode material (HEF/MWCNT), 10 wt.% carbon black (C65), and 10 wt.% polyvinylidene fluoride (PVDF, Solef 5130, Solvay) in N-methyly-2-pyrrolidone onto aluminium foil. The electrodes were dried over night at 100 °C. All electrode tapes with an areal loading of around 0.5-1 g/cm^2 were prepared in Ar-filled glovebox to avoid contamination with air. Electrochemical testing was done with CR2032 type coin cells. All cells were assembled inside an Ar-filled glovebox and comprised an HEF7 composite cathode, a GF/D glass microfiber separator (GE Healthcare Life Science, Whatman) and a lithium anode (China Energy Lithium Co., Ltd) of diameters 13 mm, respectively. LP57

[1 M LiPF6 in 3:7 (w/w) mixture of ethylene carbonate (EC) and ethyl methyl carbonate (EMC)] was used as electrolyte.

Cyclic voltammetry (CV) were performed using a BioLogic VSP-300 potentiostat device. To investigate the electrochemical properties, cyclic voltammetry (CV) measurements were performed. For comparison of electrochemical properties in the following sections, all individual MF were also ball milled for 24 h and then combined with MWCNT (ball milling for 3 h). CV curves of the HEF based compounds and binary fluorides (MF_2) electrodes given in Figure 6.3 and Figure 6.4. Figure 6.3 a) to d) provide the CV profiles of HEF7, HEF6, HEF5_A, HEF5_B respectively. For better identification of redox peaks contributing the electrochemistry, medium entropy fluorides (MEFs) with labels MEF3 and MEF4 are implying $(FeNiCu)F_2$ and $(CuNiFeZn)F_2$ respectively. Herein, MEFs represent the compounds with configurational entropy values of 1.39R (<1.5R limit, R= Universal gas constant).
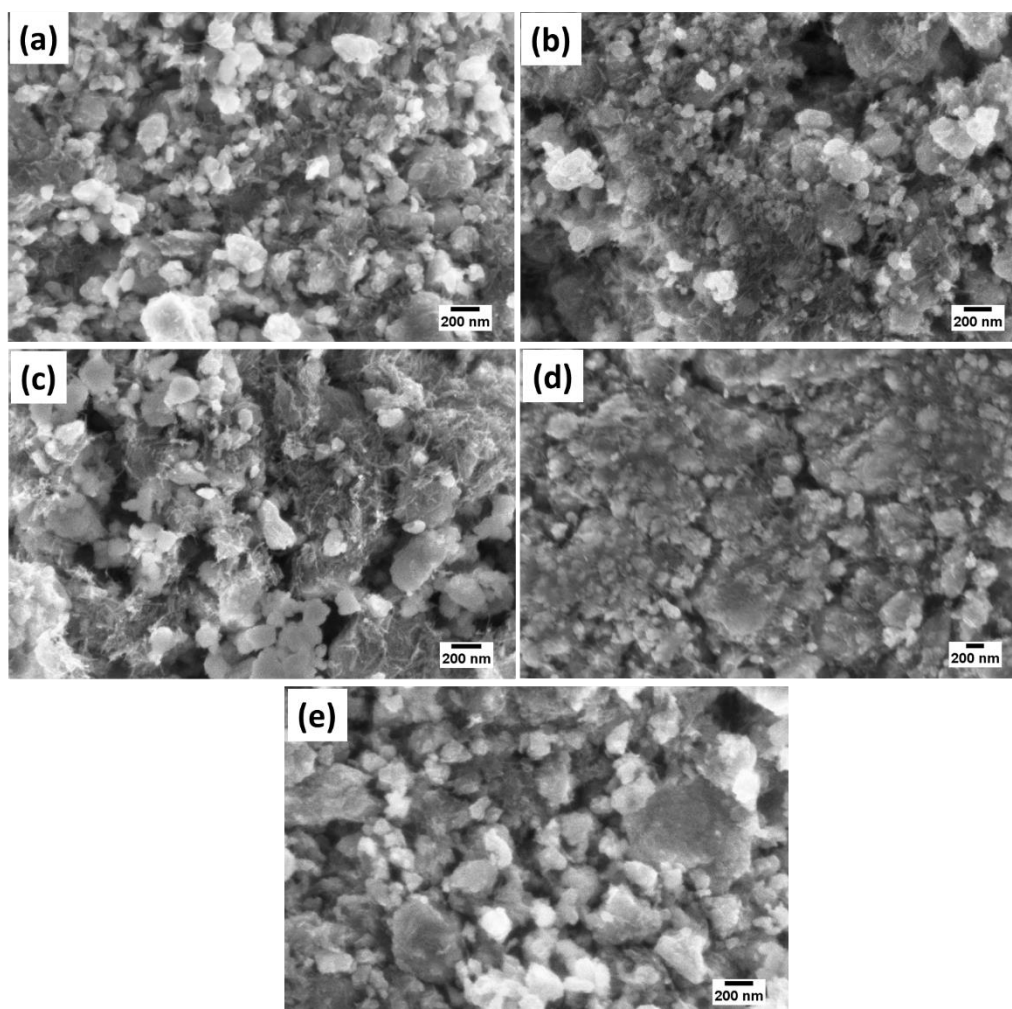
Figure 6.2 SEM images of various HEF/CNT composites: a) MEF4/CNT, b) HEF5_A/CNT c) HEF5_B/CNT, d) HEF6/CNT and e) HEF7/CNT after 3 h of high energy ball-milling process.
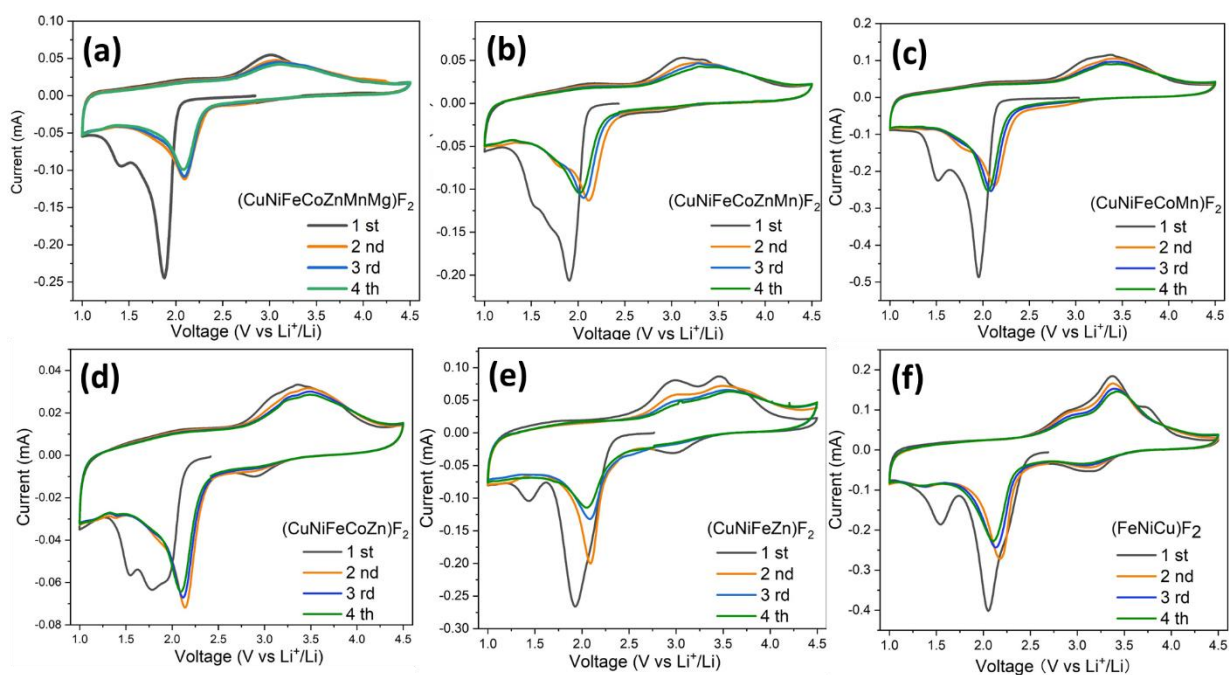
Figure 6.3 Cyclic Voltammetry (CV) curves for each HEF/CNT composite namely a) HEF7, b) HEF6, c) HEF5_A, d) HEF5_B, e) MEF4 and f) MEF3 based compounds measured in the voltage range of 1.0-4.5V with a scan rate of 0.1 mVs^{-1}.

Apparently, during the first lithiation and delithiation process, a prominent redox couple (behaving symmetrical in both directions) were observed in all HEF based electrodes. More noticeable delithiation peaks were found at 3.5 V, 3.3 V, 3.25 V and 3.0 V (refer Figure 6.3 a to e) while the corresponding lithiation peaks showed ~2.0 V respectively for HEF5_A, HEF5_B, HEF6, and HEF7. However, two distinct anodic plateaus at 2.7 V and 3.4 V appeared on MEF4 during the delithiation process (shown in figure 6.3 e). This might be due to the lowered amount of entropy and structural stability contained in MEF4 system. On subsequent cycles, the voltage profiles have similar cathodic and anodic peak potentials, indicating a high cycling reversibility for all HEF materials. In comparison to the redox peaks of MEF4, the oxidation peak at 2.7 V gradually diminishes and the delithiation peak at 3.5 V shifts to 3.7 V in the subsequent cycles, implying increase of overpotential. Even though the oxidation peak of HEF5_A, HEF5_B and HEF6 resonates with the two-oxidation peaks of MEF4, interestingly, its overpotential is lower than that of MEF4. Remarkably, for HEF7 compound with 7 incorporated elements, the oxidation peak is located at ~ 3.0 V and the reduction peak at around 2.2 V. This accounts that HEF7 has the lowest overpotential among other HEF compounds. In the case of MEF4 and MEF3 compounds (Figure 6.3 e and f), the presence of two or more redox peaks denote the unstable solid solution in contrast to the HEF (which contains a single phase solid solution).
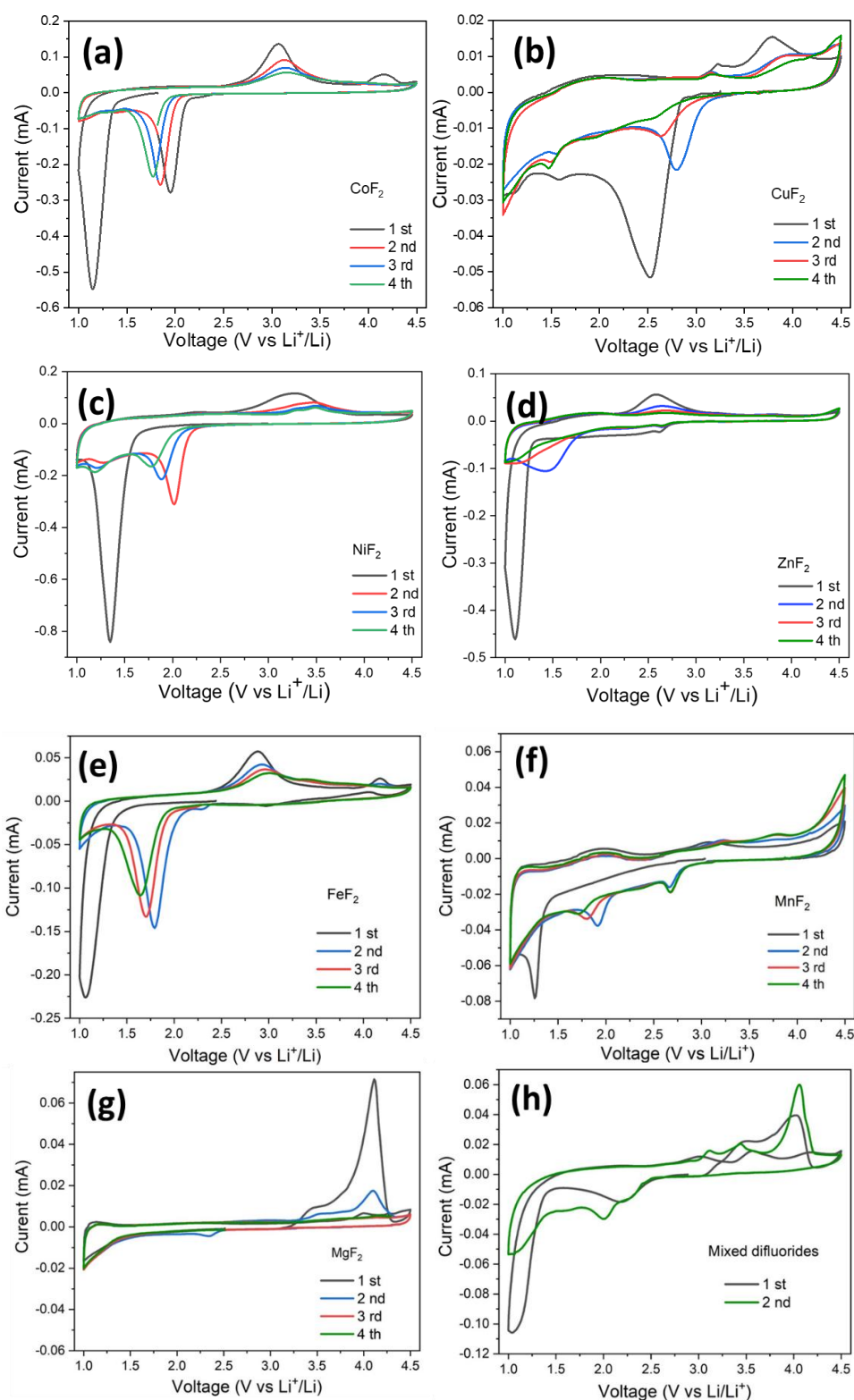
Figure 6.4. CV curves of the a) to g) binary fluorides and MWCNT composite which were utilized as the starting precursors in this study and h) CV data obtained from the physical mixture of all difluorides/CNT contained in HEF7 sample.

A similar phenomenon was also observed in medium entropy oxide anode $((Co_{0.25}Cu_{0.25}Mg_{0.25}Ni_{0.25})O)$ [142], a two-step oxidation process exhibited rather than a single peak in HEO of $((Co_{0.2}Cu_{0.2}Mg_{0.2}Ni_{0.2}Zn_{0.2})O)$. For instance, the removal of Zn (subsequently

other constituent elements as well) from the parent HEO [(CuCoMgNiZn)O] structure, which ascribed the entropy stabilization of the crystal structure as well as indicated the reaction mechanism and the electrochemical behavior, can be tailored by changing the elemental composition [142]. Interestingly, in ternary difluorides ($Ni_{0.5}Fe_{0.5}F2$, $Co_{0.5}Fe_{0.5}F_2$ or $Mn_{0.5}Fe_{0.5}F_2$), it is reported that reduction occurs in a single step with a reduction potential between the two binary difluorides [315]. While two reaction steps corresponding to the transition of Cu^{2+}/Cu metal and Fe^{2+}/Fe metal in the $Fe_{0.5}Cu_{0.5}F_2$ system can be observed [33]. That because the binding energy difference between Fe-F and Cu-F is much larger than that between Fe-F, Ni-F and Mn- F [315276316]. It is worth to note that for MEF3 and MEF4, only the oxidation occurs in two separate processes (two peaks), while the reduction process occurs exclusively in a single process (one peak). However, when the metal species is increased from 5 to 7, both lithiation and delithiation reactions tend to occur within a single step. In addition, a prominent electrolyte reduction peak at ~1.2 V appeared for all HEF based electrodes in the first cycle, indicating the decomposition of electrolyte with the formation of the solid electrolyte interface (SEI) layer formation in the HEF samples [317]. In the subsequent lithiation processes, only one reduction peak around 2.1 V was observed for all materials. This indication of the reduction peak completely disappears after two cycles, which then may be attributed to the conversion mechanism. In contrast to the lithiation process, there were significant differences in the delithiation process between the HEFs and MEFs. For the HEFs, an oxidation peak was observed at 3.3 V, 3.25 V, and 3.1 V for HEF5, HEF6, and HEF7, respectively. In the case of the MEF4, two distinct peaks occurred around 2.9 V and 3.5 V during delithiation (see Figure 6.3 e and Figure 6.3 f.

As shown in Figure 6.4 a to g for the CV of binary fluorides, the lithiation of CoF_2, FeF_2, MnF_2 and ZnF_2 initially occurs at a potential around 1.2 V for the first process, and lower than 2.0 V in the subsequent cycles. Besides, the first lithiation voltage for CuF_2 and NiF_2 are 2.5 V and 1.6 V, and second peak are at 2.7 V and 2.1 V, respectively, while MgF_2 is inactive in the given potential range [318–320]. The voltage hysteresis between the first and second cycle for very promising cathode materials of CoF_2, NiF_2 and FeF_2 are around 0.7 V, but for HEF system, it reduced below 0.5 V. For all HEF materials of subsequent cycles, the voltage profiles have similar cathodic and anodic peak potentials, indicating high cycling reversibility. In comparison to the redox peaks of MEF4, the oxidation peak of HEFs at ~2.7 V gradually diminishes and the delithiation peak at 3.5 V shifts to 3.7 V in the subsequent cycles, implying an increase of overpotential. Even though the oxidation peak width of HEF5 and HEF6 is overlaying the two-oxidation peaks of MEF4, interestingly, its overpotential is smaller than that of MEF4. Intriguingly, even Mg is not active, for HEF7 with 7 incorporated elements, the oxidation peak

of HEF7 is at approximately 3.1 V while the potential for HEF6 is at 3.25 V. This accounts that HEF7 has the lowest overpotential among all HEF compounds. From the different elemental incorporation, it is evident that the addition or elimination of an element has a significant effect on the redox potentials. This paves way for tuning the reaction potential and tailoring the electrochemical behavior by changing the elemental composition of the electrode active material. Figure 6.4 h) illustrates the CV profiles from the physical mixture of all 7 transition metal difluorides. The physical mixture was prepared by combining the difluorides (CuF_2, NiF_2, FeF_2, CoF_2, ZnF_2, MnF_2 and MgF_2) respectively using mortar and pestle inside Ar filled glovebox. This mixture was later mechanochemically milled with CNT to obtain composite structures. In the mixed difluorides system (Figure 6.4 h), several redox peaks were observed during the de/lithiation process, which indicates the reactions tend to occur independently for each difluoride compound. For the multi-element fluorides (HEFs and MEFs), a comparable behavior could be observed in the case of the lithiation processes for all materials.

From the different elemental incorporation, it is evident that the addition or deduction of an element will affect the redox potentials and can reduce voltage hysteresis in HEF electrodes. As reported in the binary difluorides [115], the reduction of FeF_2-NiF_2 occurs at an intermediate potential between the two mixed MFs within a single reduction peak. In the mixed difluorides system (Figure 6.4 h), several redox peaks were observed during the de/lithiation process which indicate the reactions tend to occur independently for each difluoride. From Figure 6.3 g) it may be inferred that MgF_2 contributes to the stability of HEF electrochemical performance as a part of HEF7 compound (further explanations are given in section 6.7).

6.5 Galvanostatic Cycling Performance of HEF Compounds

Table 6.1 shows the overview of the specific theoretic capacities and the entropy values for all of the HEF compounds. The galvanostatic cycling performance of MEF4, HEF5, HEF6, and HEF7 at different currents is given in Figure 6.5 a. At the rate performance test, HEF6, HEF7 and MEF4 initially show better or comparable discharge capacities compared to HEF7 at currents of 25 mA/g and 50 mA/g. However, as the current increases (100 mA/g), HEF7 shows increasingly better performance and even after returning to 50 mA/g, exhibits the highest discharge capacities (~300 mAh/g). The same situation also occurred in the cycling performance at 25 mA/g and 50 mA/g (Figure 6.5c). Each HEF electrode sample could yield discharge capacity more than 400 mAh/g before the first 5 cycles at a small current of 25 mA/g and retain about more than 100 mAh/g after 80 cycles, which show markedly better performance than CoF_2, NiF_2, CuF_2, MgF_2, MnF_2, and ZnF_2 (Figure 6.6). At the first 10 cycles,

HEF7 shows the lower capacity among HEFs and MEF4. However, it could provide the capacity 190 mAh/g after 80 cycles, exhibiting the best stability. Notably, the huge capacity fading of MEF4 in comparison with HEFs indicating the stability of HEFs, possibly arising from entropy effects.

Since HEF7 shows the highest stability, it will be discussed in the following. The voltage profiles at different rates were presented 6.5 b, HEF7 exhibits superior rate performance with reversible discharge capacities of 460, 350, 300, 230, and 180 mAh/g while testing at 25, 50, 100, 250, and 500 mA/g respectively. The high specific capacity explains that the HEF-based electrodes presumably undergo conversion mechanisms [321]. Moreover HEF7 electrode maintains a discharge capacity of 125 mAh/g after 100 cycles and a high coulombic efficiency of ~99% (Figure 6.5 d) under large current of 500 mA/g. However, the long-term cycling performance at a large current of 500 mA/g is quite comparable with that at the current of 50 mA/g (Figure 6.5 d). During the long term cycling at a small current density, it lead to depleted active materials. This can be inferred from the EDX-mapping of cycled lithium plate in Figure 6.7, wherein several transition metal species were found after 100 cycles. In addition, it is noted that HEF7 show better performance compared with HEF6, even though Mg is inactive in the given potential range. This could be because the presence of Mg^{2+} plays a role as a matrix in maintaining the rutile structure, which in turn proves the effect of high entropy stabilization on the cycling stability of materials [142,322].

Table 6.1 Summary of theoretical specific capacity and entropy values of the HEF based compounds (where R is the Universal gas constant).

Fluoride type	Compound	Theoretical specific capacity (mAh/g)	ΔS value
HEF4	$(CuNiFeZn)F_2$	787	1.39R
HEF5_A	$(CuNiFeCoMn)F_2$	693	1.61R
HEF5_B	$(CuNiFeCoZn)F_2$	687	1.61R
HEF6	$(CuNiFeCoZnMn)F_2$	588	1.79R
HEF7	$(CuNiFeCoZnMnMg)F_2$	579	1.95R
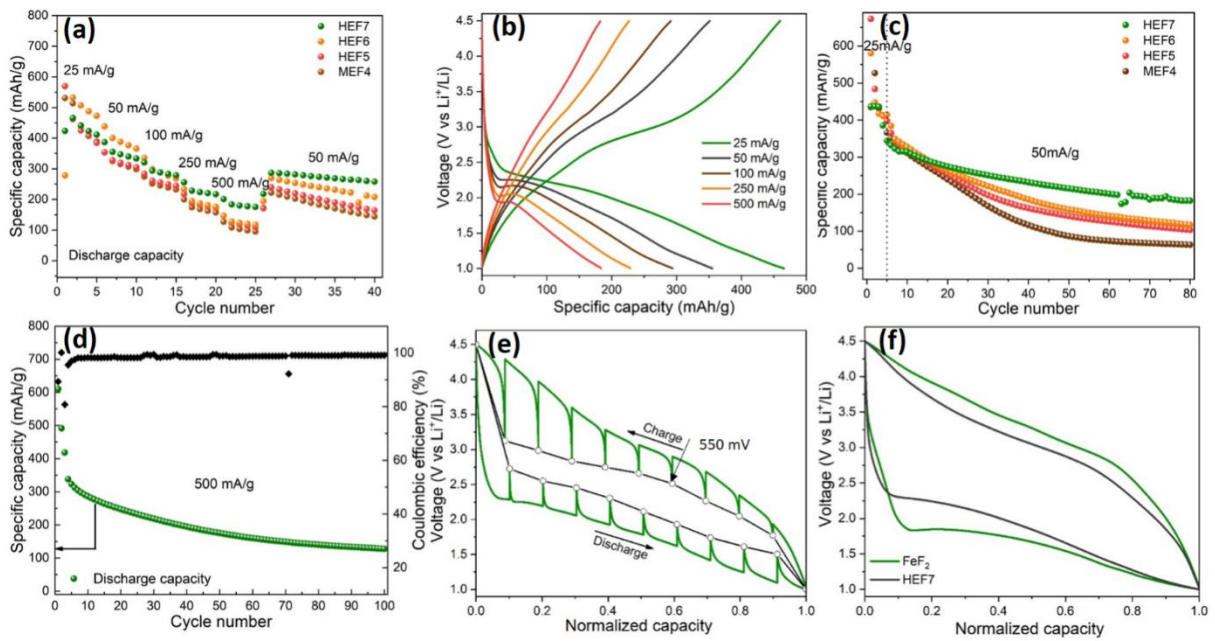
Figure 6.5 a) Galvanostatic rate capability performance of MEF4, HEF5, HEF6 and HEF7 at different currents and b) cycling profiles at different currents for HEF7, (c) cycling capacity at 25 mA/g and 50 mA/g measured in the voltage range of 1.0-4.5 V, d) cycling performance of HEF7 at 500 mA/g. (e) Quasi-equilibrium voltage profile of HEF7 obtained from galvanostatic intermittent titration technique measurements, GITT (cycling at 50 mA/g for 2 h followed by a 10 h equilibration step). Dotted lines depict the open circuit potential (OCV) values and f) Voltage profiles of HEF7 and FeF$_2$. All galvanostatic testing were carried out at room temperature.
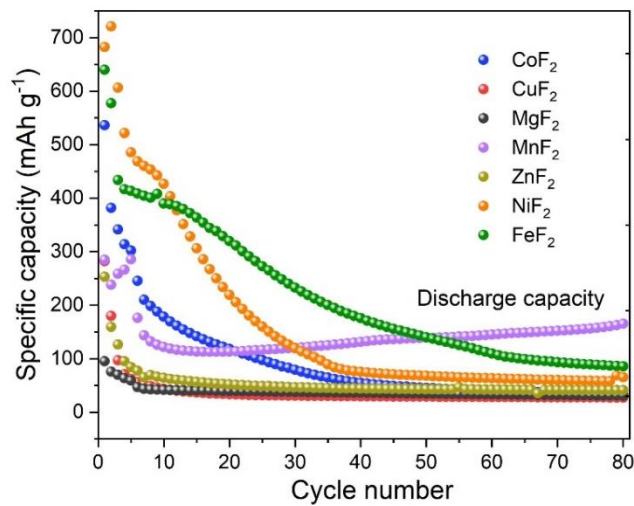
Figure 6.6 Galvanostatic cycling performance of individual binary fluorides (with CNT composites) used in this study. The current steps are implemented during the first 2 cycles accounts to C/20 and later C/10 constant current rates.
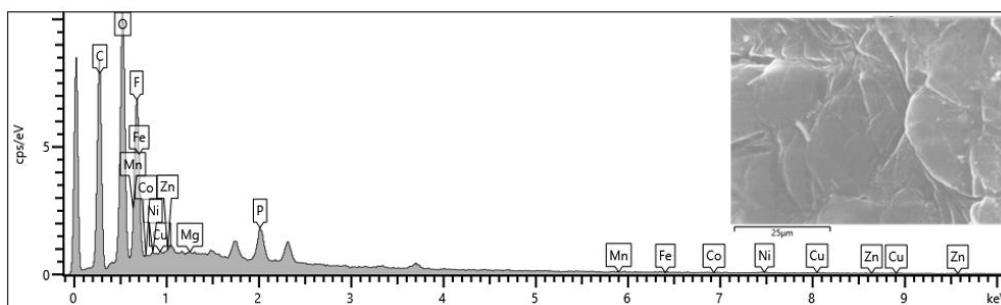
Figure 6.7 SEM of lithium (inset image) after 100 cycles and corresponding EDX analysis.

To better understand the hysteresis arising from HEF7 during the lithiation/delithiation process, the galvanostatic intermittent titration technique (GITT) was further performed after the 1st activation cycling process at 25 mA/g. HEF7 electrode was subjected to charging/discharging process (de/lithiation) with a pulse current of 50 mA/g for 2 h followed by a relaxation of 10 h to approach equilibrium potential value. Figure 6.5 e shows the voltage profile of the GITT measurement with the corresponding degree of lithiation. The dashed line shows the equilibrium voltage after each relaxation step. In GITT profile, the potential suddenly changes during the relaxation due to charge transfer and ohmic resistance which results from the kinetically driven ion diffusion. The gradual potential change can be attributed to the thermodynamically driven sluggish ion diffusion [32334]. As shown in Figure 6.5 e, the voltage hysteresis reaches a steep rise when the charging voltage reaches 2.3 V and discharge voltage reach to 1.9 V at the beginning of charge and discharge and slowdown in the following subsequent which indicate the lithiation/delithiation process start. The barrier of ion transport pathway because of volume shrinkage and the resulting high reaction over potentials contribute to the high voltage hysteresis. Note that the thermodynamic voltage hysteresis at the reaction voltage dominated by M/M^{x+} redox is ∼530 mV, it is lower than in pure FeF_2 (700 mV) [309]. It can be seen that in the voltage profiles of FeF_2 and HEF7 (Figure 3f), HEF7 exhibits the lower overpotential between charge and discharge process. Moreover, HEF7 shows a higher discharge voltage than FeF_2, which would benefit energy density of the battery.

Figure 6.7 presents the enlargements of open-circuit relaxation curves at the beginning and end of discharge and charge, the ion diffusion resistance is minor at the beginning of lithiation and delithiation process, but gradually increases upon charging and discharging process and reach a maximum near the end of each process. This suggests that the diffusion length of ions and phase change reaction resistance increase as conversion reaction proceeds. The thermodynamic potential hysteresis for HEF7 electrode is found to be around 0.2-0.3 V, while the kinetic overpotential is 0.05-0.1 V during the lithiation process between 1.8-2.3 V. However, during the intercalation process between the voltage range 2.8-3.7 V, the thermodynamic potential

hysteresis is 0.35 V to 0.60 V and the kinetic overpotential is more than 0.3 V. Notably, the thermodynamic open-circuit potential appears slightly flat with the Li transfer number reach around 0.8 in charge process, this suggests a phase transformation process. As reported in the two-phase mechanism, metal ions diffusion is blocked by the interface resistance between two phases[34324325]. As the Li transfer number is close to 1.6, it can be presumed that some of the redox pairs, such as Mg/Mg^{2+}, to be inactive in this HEM system. As shown in the SEM micrographs, the HEF/MWCNT composite electrode is highly agglomerated in nature. In addition, microstructural shrinkage which lead to poor contact of carbon matrix and active HEF compound can also contribute to the irreversible lithium ion insertion/extraction [326].
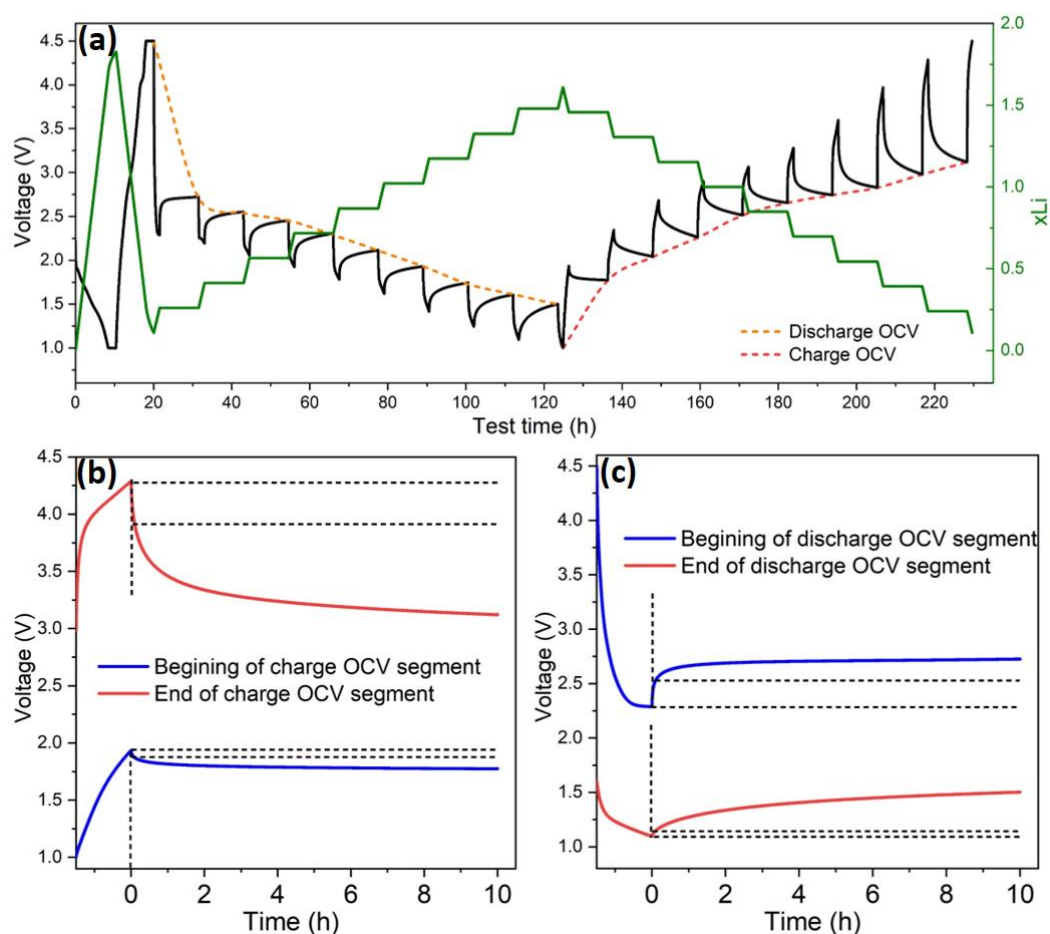
Figure 6.8 a) GITT profiles and with the corresponding degree of lithiation and b) the enlargement of initial and last charge segments for open-circuit voltage change profiles.

Notably, the huge capacity fading of MEF4 in comparison with the other HEF indicates the stability of the HEF structure, possibly arising from entropy effects (Figure 6.5 a, b and c). While examining the HEF based cathodes, HEF7 electrode shows the best cycling performance, providing 190 mAh/g at 50 mAh/g after 80 cycles and 125 mAh/g at 0.5 A/g after 100 cycles. The high temperature cycling performance of HEF7 was also examined at 40 °C, and HEF7

could deliver more than 100 mAh/g after 40 cycles (Figure 6.9 a and b). HEF based electrodes follow the conversion mechanism stemming from the constituent difluorides, exhibiting high specific capacity. This hypothesis will be elucidated in the next sections.
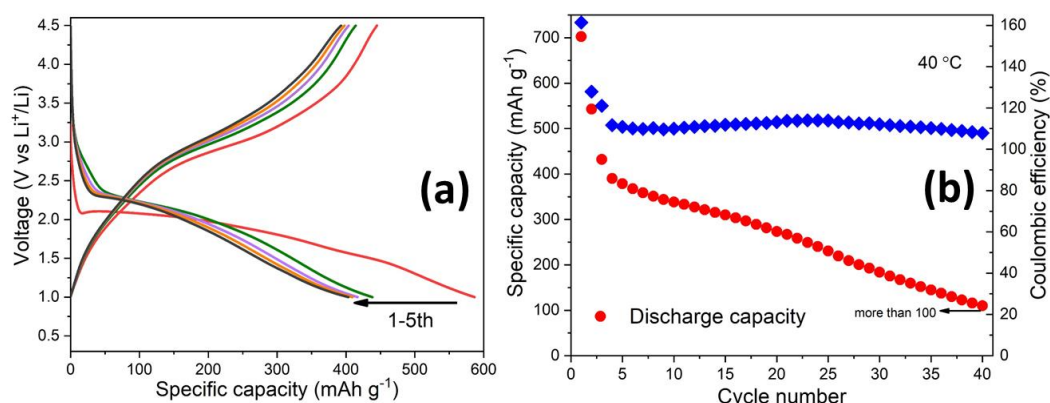
Figure 6.9 Galvanostatic cycling performance of HEF7/CNT composite electrode a) voltage profile for 5 cycles, b) specific discharge capacity wrt cycle number at 40°C.

SEM investigation of the HEF7 electrodes before and after the cycling process was carried out. Figure 6.10 a) shows the surface of HEF7/CNT composite electrode. Electrode cracking could be found in the cycled electrode after 100 charge-discharge cycles (see Figure 6.10 b). The cracks and pulverization can be attributed to the significant capacity fading observed upon cycling of the HEF compounds.
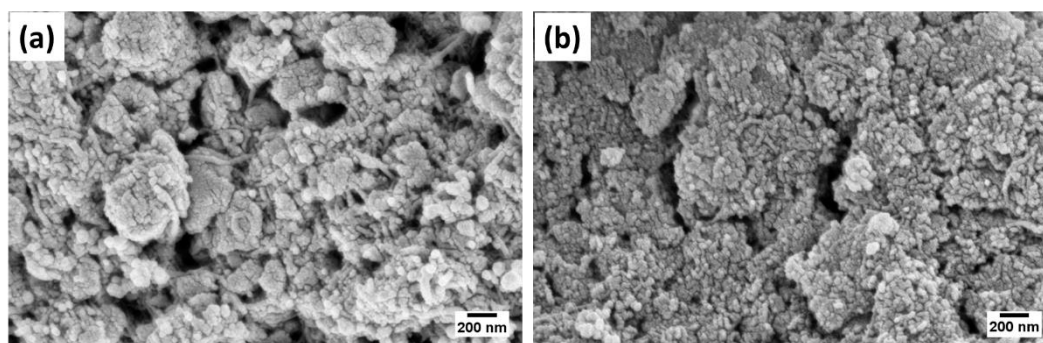
Figure 6.10 Surface SEM images of a) pristine HEF7/CNT electrode and b) electrode after 100 charge-discharge cycles.

6.6 Electrochemical Impedance Spectroscopy (EIS)

EIS (Electrochemical impedance spectroscopy) is a fundamental technique to define the diffusion process, the charge transfer kinetics, and the electrolyte-electrode resistance [327]. To gain more information about the conductivity properties of the HEF7 electrodes, EIS was performed. To recognize the individual processes contributing to the EIS response, first, two-electrode cells in symmetric cell configuration (identical HEF7CNT composite electrodes) were prepared. Standard electrolyte composition (LP57) was utilized for all the EIS tests. Additionally, reasons responsible for capacity fading have been drawn from the EIS results of

the cycled HEF7/CNT electrodes. Electrochemical impedance spectroscopy measurements (EIS) were performed using a BioLogic VSP-300 potentiostat device. The impedance data was acquired by applying 10 mV AC perturbation signal over frequency range of 1 MHz to 1 Hz (20 points/decade). Symmetric cells were constructed by sandwiching two HEF/MWCNT electrodes separated by two sheets of GF/C separators in a coin type cell. GF/C was wetted with 200 µLof standard liquid electrolyte (LP57). EIS experimental plots were fitted by using Z-view software (Scribner Associates, Southern Pines, NC).
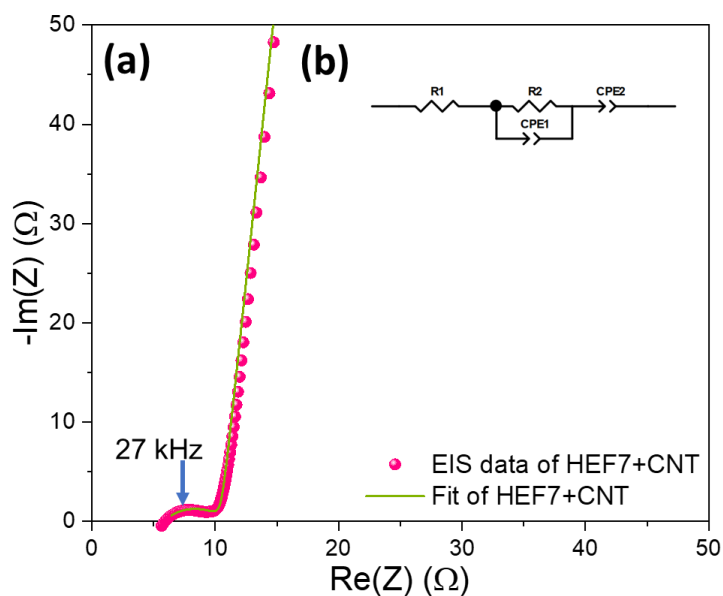
Figure 6.11 a) Electrochemical impedance spectra of symmetrical cells with HEF7 electrodes and inset b) equivalent circuit for fitting the experimental data (where R_1, R_2 denote the resistances, CPE1, CPE2 denote the constant phase elements).
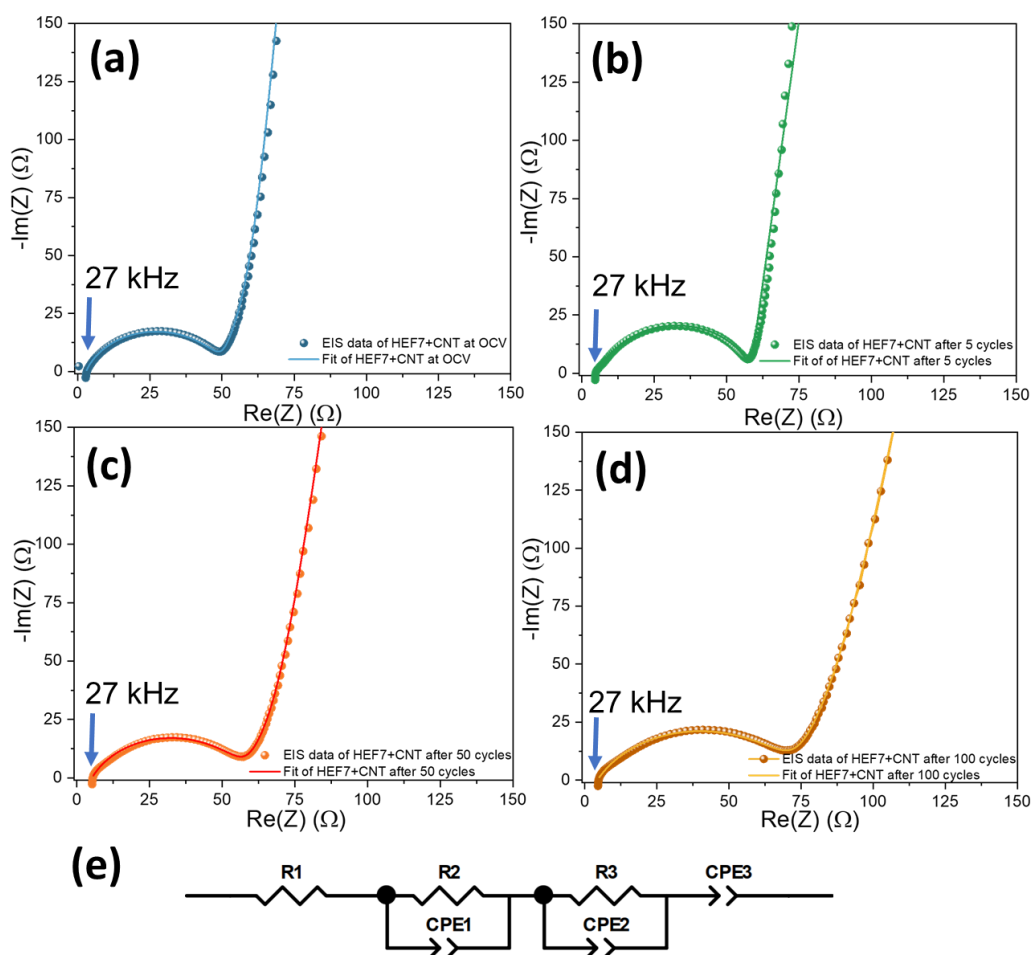
Figure 6.12 Nyquist plots for the HEF7 at a) OCV, b) after 5 cycles, c) 10 cycles and d) 100 cycles, (e) equivalent circuit model used to fit the experimental data (where R_1, R_2, R_3 are the resistances, CPE1, CPE2, CPE3 denote the constant phase elements). Table S2 shows the equivalent circuit values of the fitting components obtained from the equivalent circuit models.

Figure 6.11 depicts the Nyquist plot of the HEF7/MWCNT composite electrode in a symmetric cell configuration along with the inset (Figure 6.11 b) showing the equivalent circuit utilized for fitting. In all the EIS spectra presented here continuous lines show the fitting curves and dots represent the experimental data acquired. The EIS spectra of the symmetrical cell of HEF7 (Figure 6.11 a) is composed of a depressed semicircle in the higher frequency region and a sloping straight line feature in the lower frequency region. The real part of the impedance is denoted by R_1 in the equivalent circuit, which may arise from the connector resistances. The first semicircle in the high frequency region may be attributed to the charge transfer resistance between cathode and electrolyte (R_{ct}) [264]. The straight line shown in the low-frequency region can be represented by a constant phase element (CPE), which shows the blocking of Li^+ diffusion in the cathode side.

Figure 6.12 shows the EIS data from HEF7/MWCNT composite electrode with a Li counter electrode in a half-cell configuration. From these EIS spectra, the experimental data of

electrodes (denoted by points) show a prominent blocking feature (at low frequencies) and two flattened high and medium frequency semicircles. The first high-frequency region semicircles in the cycled EIS electrode can be caused by the SEI layer formation in the cathode surface. These semicircles of the half-cell configuration in Figure 6.12 a to d are similar to the counterpart present in symmetrical cell spectrum (shown in Figure 6.11, f_{max} = 27 kHz) with an additional influence from the SEI formation during cycling. The medium frequency region second semicircle can be ascribed to the charge transfer resistance at the anode/electrolyte interface. In the composite structure, better interfacial contact between the active material and MWCNT in comparison with carbon block (C65) could be anticipated due to the porous structure of MWCNT. The derived parameters from the equivalent circuit model fitting performed with the Zview software can be found in Table 6.2. Due to the overlap of the high and medium frequency semicircles of the half-cell measured at OCV, the absolute quantification of the equivalent circuit components was quite cumbersome. On the other hand, with progressing cycle numbers from 5 up to 100 cycles it is evident that the SEI formation plays a significant role in increasing the charge transfer resistance on the cathode side. A more notable resistance increase is observed for the medium frequency semicircle, attributed to the charge transfer to the Li anode.

Table 6.2. Numerical values of the equivalent circuit components were obtained by fitting the impedance data from symmetrical configuration cells and cycled HEF7 electrodes.

Electrode type	R_1 (Ω)	CPE1 ($Fs^{(n-1)}$)	n1	R_2 (Ω)	CPE2 ($Fs^{(n-1)}$)	n2	R_3 (Ω)	CPE3 ($Fs^{(n-1)}$)	n3
Symmetric cell of HEF7	5.89	0.274×10^{-3}	0.62	4.63	0.952×10^{-3}	0.95	-	-	-
HEF7 at OCV	2.90	9.49×10^{-3}	0.79	9.70	3.405×10^{-5}	0.79	47.26	2.1189×10^{-3}	0.96
HEF7 after 5 cycles	4.94	5.66×10^{-6}	1.0	2.05	1.842×10^{-5}	0.85	51.40	3.899×10^{-3}	0.93
HEF7 after 50 cycles	5.14	0.013	0.64	14.40	4.758×10^{-5}	0.72	52.35	0.003	0.94
HEF7 after 100 cycles	4.33	0.012	0.64	18.98	5.362×10^{-5}	0.69	68.17	2.348×10^{-5}	0.91

6.7 Structural Evolution during cycling: *In situ* XRD, *Ex-situ* TEM and XPS Analysis of Cycled Electrodes

In order to have a better understanding of the reaction mechanism present in the HEF and the structural changes during the reversible de/lithiation process, a comprehensive characterization implementing transmission electron microscopy (TEM), X-ray photoelectron spectroscopy (XPS) and ex-situ XRD (X-ray diffraction) methods were performed.
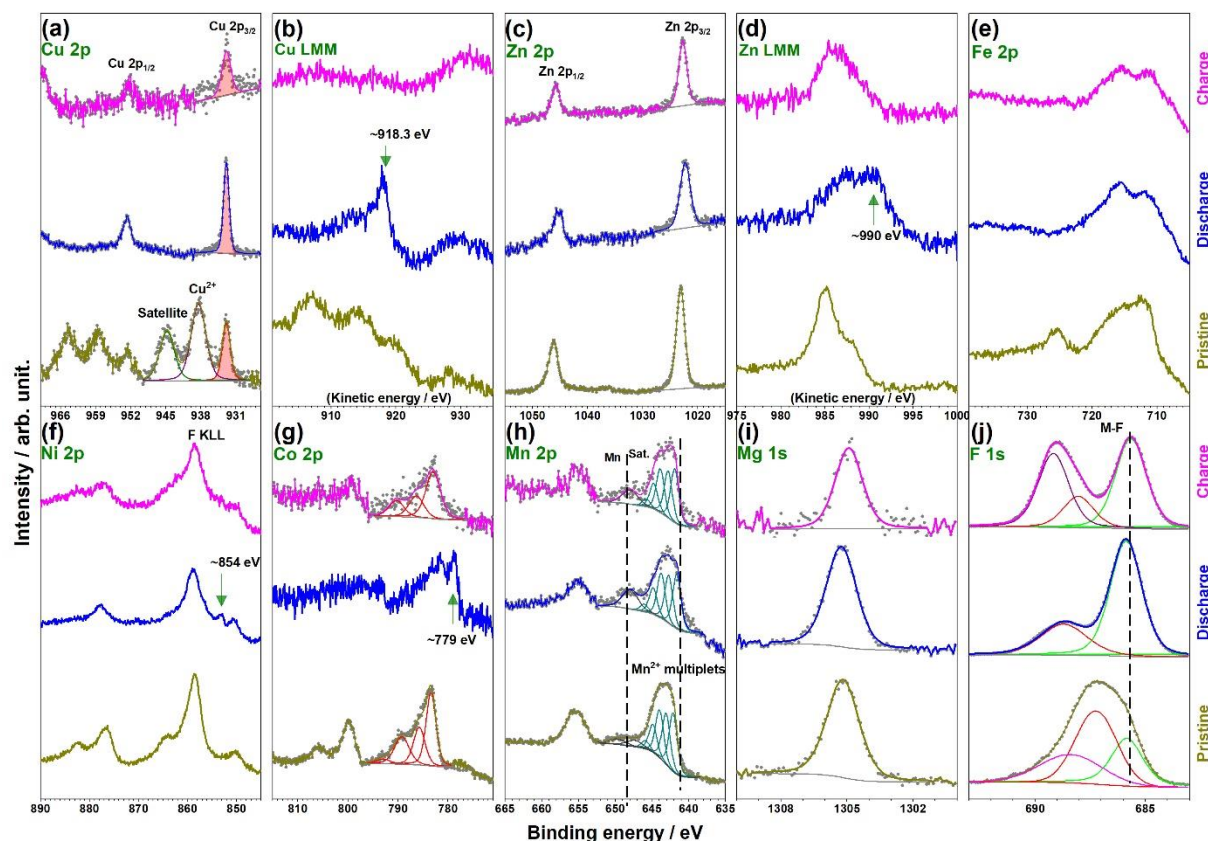
Figure 6.13 XPS spectra of a) Cu 2p, b) Cu LMM, c) Zn 2p, d) Zn LMM, e) Fe 2p, f) Ni 2p, g) Co 2p, h) Mn 2p, i) Mg 1s and j) F 1s of pristine electrode (green), first lithiation (blue) and first delithiation electrode (pink).

XPS analysis on HEF7 pristine and first discharged/charged electrodes are shown in Figure 6.13. Cu ions in the pristine electrode show two peaks at around 937 eV and 944 eV which could be attributed to Cu $2p_{2/3}$ main peak and satellite of Cu^{2+}, respectively (refer to Figure 6.13 a). The third peak at lower binding energy (~ 933 eV) can be attributed to either Cu^{1+} or Cu^{0}. Cu peak is no more Cu^{2+} and stays in the reduced state at the binding energy of around 933 eV after discharge. Although the Cu LMM peak of HEF7 is overlapped with Zn LMM and has low intensity. Nevertheless, it can be inferred from the spectra of charged and discharged electrodes (Figure 6.13 a and b) that Cu is involved in the reaction. Narrow Zn $2p_{3/2}$ peak consistently appears at around 1023 eV, however, the binding energy of Zn^{2+} and Zn^{0} are very close to each other and the analysis of Zn *LMM* auger peak (Figure 6.13 d) is required. The Zn LMM peak

at 990 eV at the lithiated electrode indicates the emergence of metallic Zn, then the peak shifts mainly back to 985 eV at the delithiated electrode and can be attributed to the Zn^{2+} regenerate. The analysis of Fe 2p ions (Figure 6.13 e) are hampered due to the overlap of Ni and Co auger peaks resulting in high background intensity of Fe 2p region. The Ni ions also overlap intensively with F *KLL* auger peaks, which makes their analysis difficult. However, the comparison of the spectra in Ni 2p region (Figure 6.13 f) shows the emergence of a small shoulder at around 853 eV in the discharged (lithiated) electrode that could probably be attributed to metallic Ni. This small shoulder is indicated by an arrow and disappears again after de-lithiation (charging), therefore might suggest also reversibility for Ni^{2+} formation by delithiation [328][329]. The Mn ions in the pristine electrode can be attributed to the Mn^{2+} ions according to the provided peak deconvolution in Figure 6.13 h that shows the multiplet splitting of Mn^{2+}. The metallic Mn $2p_{3/2}$ and Mn $2p_{1/2}$ peak appears normally at low binding energies at around 639 eV and 648 eV [330]. The peak positions show some slight negative shifts for the discharged states in comparison with the pristine electrode with a peaks at 647 eV and a small shoulder at 660 eV appearance, indicating the reduction Mn^{2+} into Mn metals phases during the discharging processes [331,332]. The spectra of Co ions in pristine and charged electrodes (Figure 6.13 g) show characteristic satellite of Co^{2+} ions at around 6 eV higher than the main peak (indicated by an arrow in Figure 6.13 g), however, their low intensity mainly in the cycled electrodes makes peak assignment difficult. The emergence of a small shoulder at around 778.5 eV in the discharged (lithiated) Co $2p_{3/2}$ spectra might indicate the reduction of Co ions to metallic Co upon lithiation [333]. Mg 1s peak (Figure 6.13 i) appears at around 1305 eV and remains consistent in all of the electrodes, and its binding energy can be attributed to Mg^{2+} ions, whereas the metallic Mg normally appears at around 1303 eV. Therefore, Mg is not involved in the reduction or oxidation process. Fluoride ions in the structure of HEF7 appear at around 685.5 eV (Figure 6.13 j), whereas the PVDF peak appears at around 688 eV. In F 1s spectra, also the contribution of electrolyte degradation products can be found. However, the binding energy difference between Li-F and M-F is too tiny to distinguish. Therefore, the plateau in F 1s between discharged and charged sample is observed slightly change. Nevertheless, we can infer that LiF and M-F generate after discharge and charge, respectively.
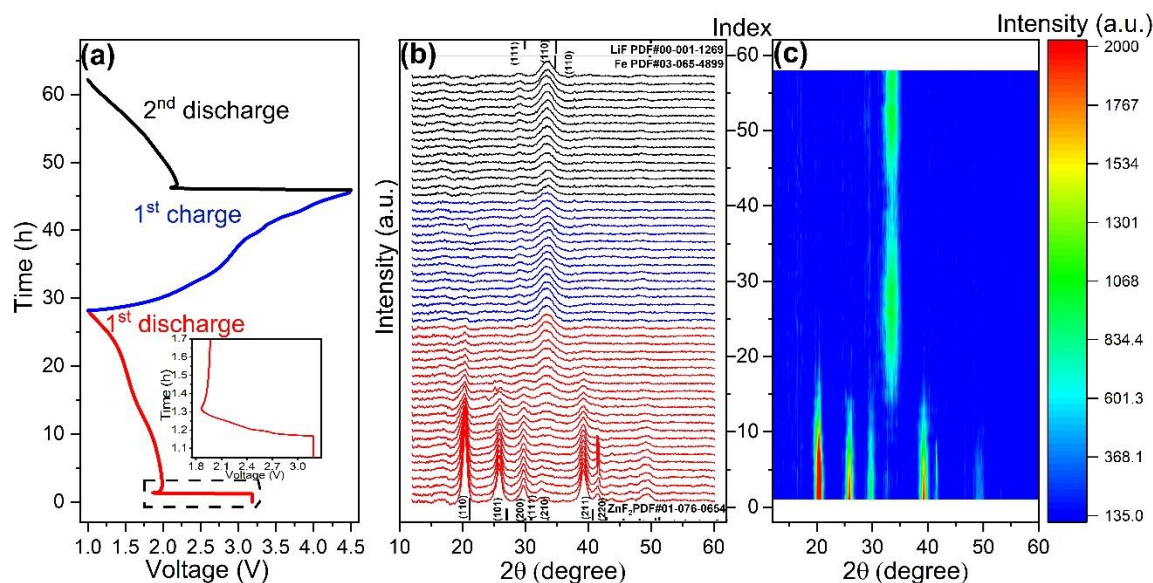
Figure 6.14 *Operando* XRD patterns a) lithiation/delithiation profiles, b) collected during the first discharge and charge process at a current density of 50 mA/g and d) corresponding contour map.

Figure 6.14 shows the *operando* XRD patterns of HEF7 during the discharge and charge process and their corresponding contour map. XRD patterns and associated profiles from 1st discharge, 1st charge and 2nd discharge are marked with red, blue and black, respectively. As shown in Figure 6.14 a, the discharge reaction begins at an equilibrium discharge voltage of 3.1 V and with a rapid drop voltage to 1.86 V (inset image of Figure 6.14 a), yields a small specific current of 40 mA/g. Given that existence of Fe^{3+} and Mn^{3+} species in HEF7 structure (as shown in XPS results), this can be ascribed to the Li^+ insertion into the structure to form Li_xHEF species [334][335]. Afterwards, an obvious recovery of the voltag e occurring before the flat operating voltage at ~1.95 V, which usually caused by the faster Li transportation than the metal diffusion and along with the formation of a new phase, indicate the onset of the conversion reaction [336]. Therefore, the intensity of (220) at 2θ angle of 40° is observed to increase could be explained by the structure distortion with more Li^+ introduced. Subsequently, a peak at 34° might originate from the nano sized metal particle and LiF formation are presented with the the peaks from rutile structure are disappeared, which are consistent with metal FCC (110) and LiF (110) planes, indicating solid solution metals generated. Besides, along with presence of small peak at 29° which might be from LiF (111), and (200) is overlapped by the reflection of FCC (200) [336]. Then the reflections from metal/LiF become stronger with continuing of discharge and get weaker with occurring state of charge, indicating that the conversion reaction is reversible. However, no crystalline phases of parent rutile are observed in subsequent of charged samples, therefore, TEM is used for further characterization.

Figure 6.15 shows the *ex-situ* TEM images of electrochemically lithiated HEF7 electrode (Figure 6.15 a) sample (1.0 V) and delithiated to 4.5 V (Figure 6.15 d). SAED pattern (6.15 b) reveals that after lithiation process (carried out until 1.0 V), HEF7 electrode was electrochemically reduced to individual transition metals and LiF. SAED pattern in Figure 6.15 b demonstrated a solid solution of transition metals contained in HEF7 sample with LiF being homogeneously distributed at the nanometer level. The diffused ring pattern observed in Figure 6.15 (lithiated HEF7), can be indexed to (200) and (110) planes of solid solution of metals and HEF (111). After delithiation of the HEF7 electrode to 4.5 V, the majority of marked areas in HR-TEM image (given in Figure 6.15 c) show lattice spacing of ~ 0.33 nm. This gives a clear indication that d-spacing corresponds to the (110) plane of the parent rutile phase. HR-TEM patterns in Figure 6.15 c show the homogeneous distribution of elements in the structure after lithiation without the presence of any agglomeration or segregations. Since the HEF powder is extremely fine and beam sensitive, unfortunately, the EDX-mapping images were not collected from delithiated samples. From the SAED after delithiation, the rutile structure is reformed. However, a small broad peak appeared at 4.05 1/nm in the profile of SAED pattern (Figure 6.16), which is ascribed to metal metallic solid solution. This indicates that the metal does not fully convert to fluoride in the delithiation reaction that could be ascribed to the low electrical conductivity nature of fluorides as well as the poor contact resulting from the volumetric change during the conversion process. During delithiation process, the reformation of high entropy compounds breaks the conductive network formed by metals, which impedes the reaction leading to capacity fading. Besides, the diffraction rings and lattice d-spacing of monoclinic CuF_2 phase could not be detected, which means that CuF_2 cannot be formed. It can be inferred from CV and XPS results that HEFs solid-solution phase has been reformed after F^- transfer from LiF to the solid solution of transition metals. This evidence combined with the *operando* XRD pattern (see figure 6.14) shows the evidence of conversion reaction mechanism present in the HEF based materials. The occurrence of the continuous networks of metallic nano domains can be beneficial as an internal conductive network. This can facilitate the conversion kinetics and voltage polarization, thereby improve the overall electrode cycling performance.
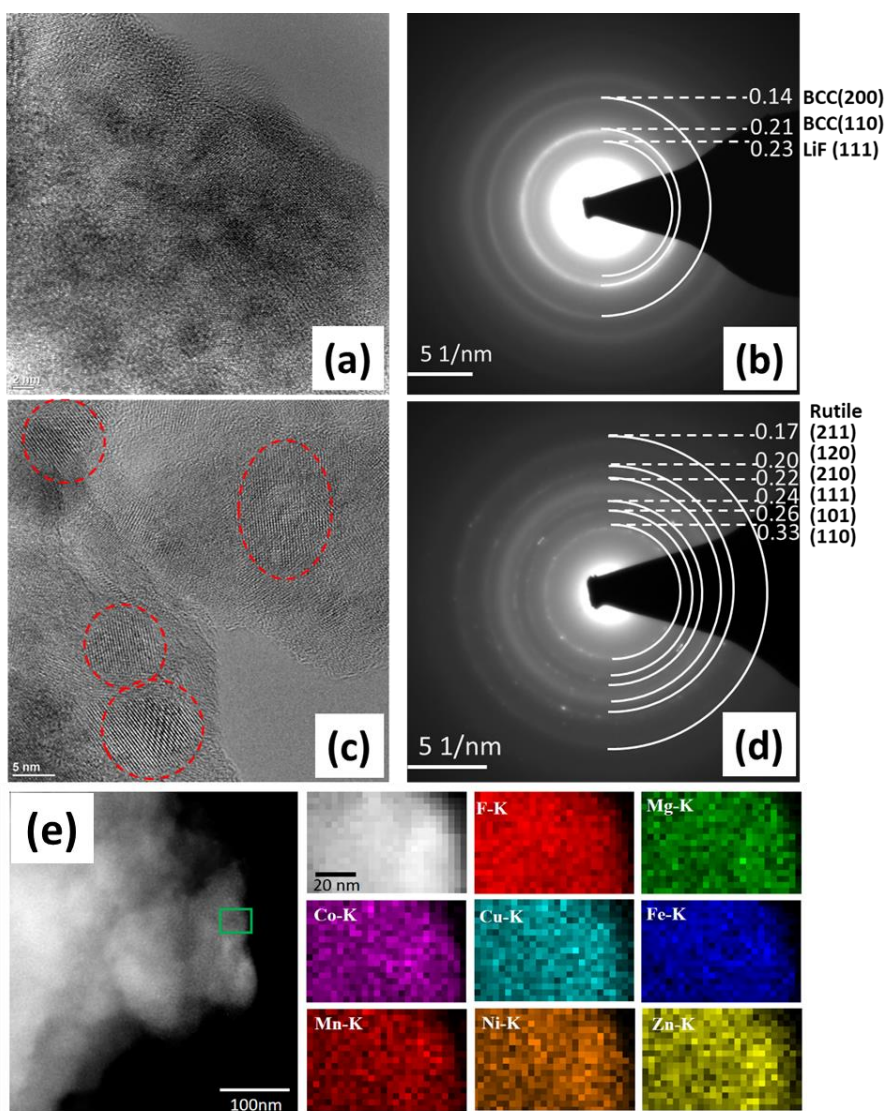
Figure 6.15 HR-TEM images of various cycled HEF7 electrodes after a) lithiation to 1.0 V, c) delithiated to 4.5 V, and their corresponding SAED patterns in panels b) and d), respectively (all values of d spacing illustrated in SAED images are given in nm and all TEM images were acquired in 1st cycle). e) EDX-mapping after 1st discharge.
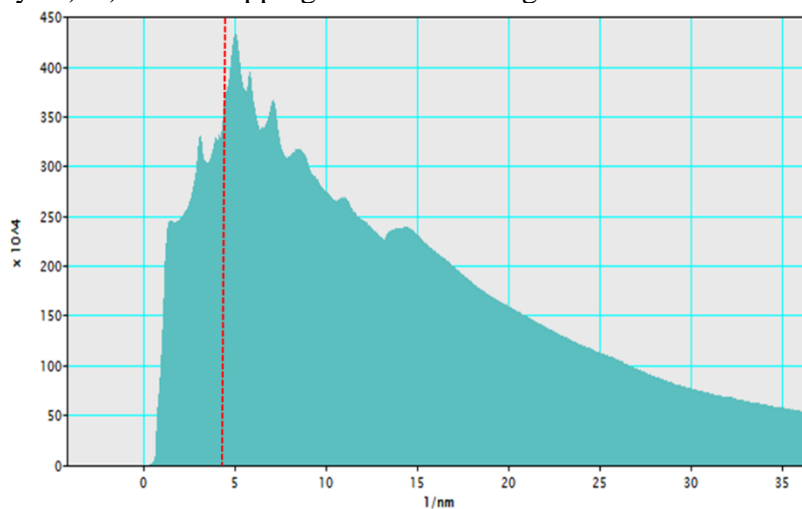
Figure 6.16 SAED profiles of delithiated HEF7 electrodes (1st cycle).

6.8 Printed HEF/CNT Composite Electrodes

This section describes the electrochemical properties of the printed HEF electrodes as a cathode for LIBs. Similarly, as discussed at the beginning of this chapter, the HEF7/CNT composites were prepared via mechanochemical milling with HEF7 and MWCNT powders. Later, this was used as an active material for the printing process. The HEF7/CNT electrode discs were made via the printing technique carried out at ambient conditions. The electrochemical behaviour of the printed cathodes was probed by cyclic voltammetry (CV) and other cycling methods. The highly reversible conversion reaction peaks occur at 3.0 V- 4.3 V. However, followed by the conversion reaction peak at 1.5 V for the HEF7/CNT, the latter reduction peaks present were shifted to a high potential (>2.0 V). The peak current was significantly reduced. The CV profiles of the printed electrodes follow the same pattern as that of the tape casted electrodes discussed in section 6.4. Figure 6.17 b) shows the battery capacity profiles of the printed electrodes tested at a rate of 0.1 C (where 1 C = ~580 mAh/g) between the voltage range of 1.0 V to 4.5 V. The capacity at the first discharge (lithiation) and the charge (delithiation) are at 318 mAh/g and 475mAh/g, respectively. The coulombic efficiency of the HEF7/CNT cathode at the first cycle was accounted for 66.9 %. Figure 6.17 b shows the typical cycling behaviour of the printed HEF7/CNT cathode, which exhibited good cycling capacities at higher discharge rates. The rapid capacity loss that undermines the performance of the battery can be inferred from the printable ink preparation and the conversion reaction process of HEF cathodes [24].

The typical specific capacity of the printed HEF7/CNT electrode measured at different current rates as a function of the cycle number is shown in Figure 6.18. The HEF7 active material yields a discharge capacity of 414 mAh/g in the first cycle and degrades to 133 mAh/g after 30 cycles.
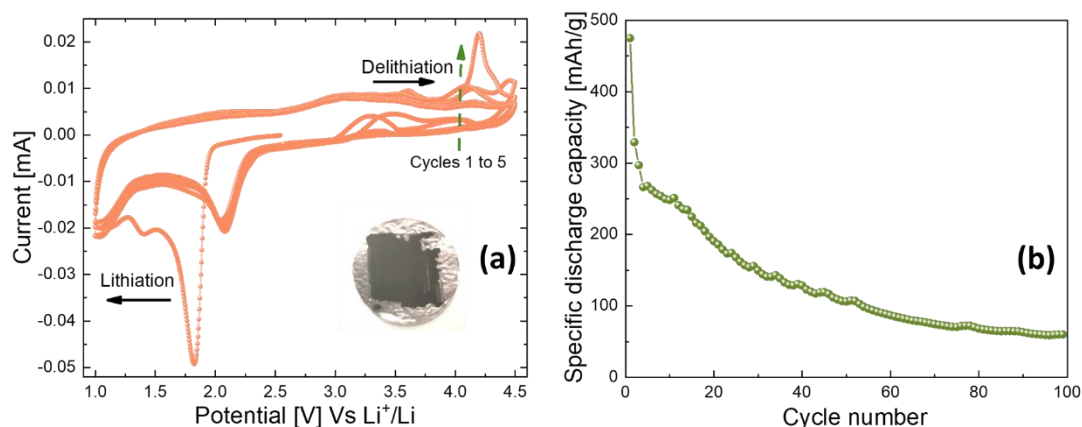
Figure 6.17 a) Cyclic voltammetry (CV) curves of HEF7/CNT cathode measured at a scanning rate of 0.1 mV s $^{-1}$ (inset shows the printed HEF7/CNT electrode prototype), b) Cycling behaviour of battery prepared via printing cycled at 0.1 C (50 mA/g) current rates after initial cycling at 0.05 C (25 mA/g) current rates, measured in the range of 1.0 V to 4.5 V.
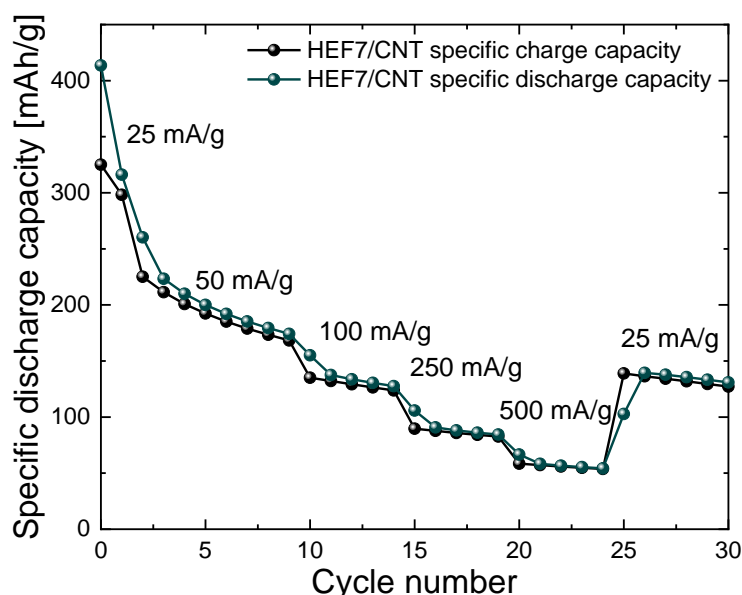
Figure 6.18 Rate testing behaviour of printed electrodes at various discharge current rates measured in the voltage range of 1.0 V to 4.5 V. The current rates used are denoted in the rate steps.

6.9 Effect of water-based binders in printed HEF/CNT electrodes performance

Presently, organic solvents-based binders are usually used in the commercial LIBs Among these, PVDF is known to be less flexible during the expansion and contraction process prone during the cycling process [337]. During the testing of electrochemical performance of electrodes, binder plays a crucial role. There are no studies reported for the suitability of the type of binder for HEF based cathodes. Prepared in a similar fashion as in the previous sections, printed electrodes of the HEF7/CNT composites were prepared with the water-based PVA binder and carbon addictive (C65). Figure 6.19 a depicts the CV profiles of the HEF7/CNT electrodes with the water based PVA binder measured at a scanning rate of 0.1 mVs^{-1}. Multiple pairs of oxidation and reduction peaks corresponding to the transition metals in the HEF7 are present. In the galvanostatic cycling, as anticipated for the conversion mechanism, the capacity degrades during the long-term cycling performance of these printed electrodes (Figure 6.19 b). The capacity is reduced to ~100 mAh/g after 50 cycles at a constant current rate of 50 mA/g. Furthermore, this binder effect study of HEF compounds emphasizes the importance of optimizing the ink rheological properties and the best formulation of the ink with a specific binder type according to the end application requirement.
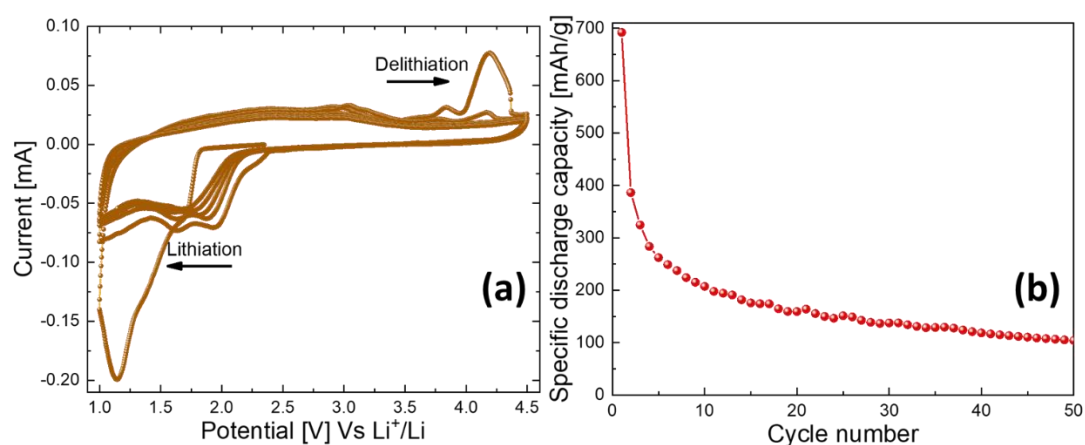
Figure 6.19 a) Cyclic voltammetry curves and b) galvanostatic cycling performance of printed HEF7/CNT composite electrode prepared with water-based PVA binder.

6.10 Printed Full Cell: HEF/CNT Cathode and Prelithiated Si/C Anode

From the previous chapters, we know that fully printed batteries are essential as a powering source for fully-printed electronic circuits. This section details the main goal of the dissertation namely the demonstration of fully printed electrodes from next-generation anodes and cathodes. To summarize, the printed anodes and printed cathodes (described in Chapter 4 and 5) are utilized to form a printed full cell. This full-cell could be beneficial as a powering source for low-power printed electronics. The cathode part was derived from conversion type fluoride material which is relatively new. The full cell was fabricated in a layerwise stacking model in a coin-type cell case combining a printed Si/C anode and a printed HEF7/CNT composite cathode. To cater the need of a lithium source for the HEF7/CNT cathode, a prelithiated Si/C electrode was utilized. The construction of full-cell in a coin type cell configuration is given schematically in Figure 6.20 a. 200 μL of standard electrolyte solution containing 1 M LiPF$_6$ in FEC:EMC (1:1 w/w) was used for battery preparation. Prelithiation of Si/C anode at slow rate (C/20, where 1C= 4000 mAh/g) implemented electrochemically for 3 cycles with Li counter in a half-cell configuration. After the prelithiation of Si/C anode, the counter Li electrode was substituted by HEF7/CNT cathode. The electrochemical performance of printed HEF7/CNT cathode // prelithiated Si/C anode full cell is probed by cyclic voltammograms for first five cycles with an operational voltage window spanning to 0.8V to 4.3 V at a sweep rate of 0.1 mV/s as shown in Figure 4.20 b. Explicitly it has to be noted from Figure 6.20 that the first electrochemical lithiation cycle is different from the subsequent cycling. In the subsequent cycles, a large broad peak present at ~3.0 V smeared out after the 2nd cycling. Other than the strong peak at 1.1 V in the first cycle and the new broad peak arising at ~2 V, this behavior is similar to the lithiation of the HEF/CNT half cells.
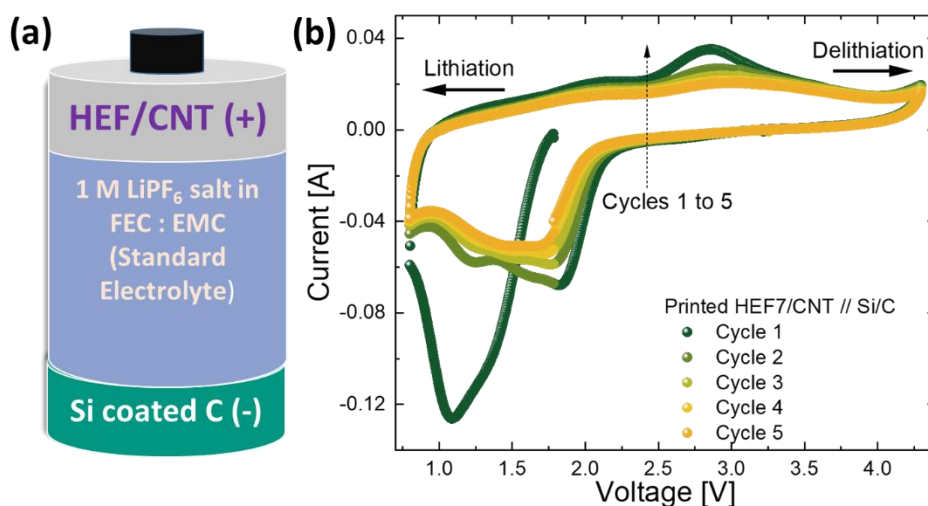
Figure 6.20 a) Schematic of full cell configuration and b) cyclic voltammetry curves of the full cell employing prelithiated Si/C anode and HEF7/CNT cathode measured between 0.8V and 4.3 V at a voltage rate 0.1 mVs^{-1}.

6.11 Summary

In this chapter, high entropy fluorides (HEF) are introduced as a high-capacity cathode material for lithium ion batteries. The electrochemical activity of the HEF based materials could be tailored by simply changing the constituent elements needed for a prospective application. The in-depth characterization of the electrodes with HR-TEM and XRD techniques revealed that the solid solution of the transition metals is present in the lithiated phase, whilst the rutile HEFs phase could be restructured after the transfer of fluorine from LiF. During the electrochemical redox reactions, the HEF exhibited a single step reduction process, wherein only one solid state metal reduction potential intermediate was present. The single redox peak signifies the solid solution present in HEFs. This effect is in contrast to the step wise reduction into a single metal as in the case of the binary fluorides. To counteract the inherent poor electrical conductivity of the fluorides, a composite structured electrode was created with MWCNT. The HEF with 7 metal elements maintained good cycling performance with a capacity of more than 125 mAh/g after 100 cycles at a high current of 0.5 A /g. It is also observed that the electrochemical behaviour of the high entropy fluorides depends on the individual elemental incorporation, therefore the electrochemical properties can be tailored by the tuning of the elemental composition. As a prospective outlook, the potential advantages of the high entropy fluorides can be further improved through coating with a conducting agent (carbon) to inhibit the dissolution of certain metals in the electrolyte and forming of a composite structured cathode by combination with the conductive carbonaceous materials.

Summarizing, this chapter covers the introduction of HEF as conversion cathodes, its electrochemical optimization as well as a preview of the application as a full cell prepared with an alloying anode (Si/C). It was also observed that the electrochemical behavior of the HEFs depends on each individually incorporated element. HEFs with 7 metal elements incorporated, showing a single-phase rutile-type structure, exhibited better cycle stability than metal difluorides and lower hysteresis voltage. This study shows an important step for the tailorable electrochemical properties in accordance with the application.

Chapter 7 Outlook and Conclusion

7.1 Conclusion

This thesis shows the development of novel electrode materials for Lithium-ion batteries (LIB). The major aim of this doctoral dissertation is focused on the printability and optimization of the alloying-based anodes (silicon, Si), conversion-based cathodes (high entropy fluorides, HEF), and especially its electrochemical optimization. Later the possibility of full cell preparation was demonstrated using the printed cathode and anode electrodes. As detailed in Chapters 4, development of printed electrodes was done, and a partially printed full cell was prepared, which powered an electrolyte-gated transistor (EGT). Chapter 5 and 6 demonstrated the development of HEF material and its tailorable electrochemical properties. The summary of the derived conclusions from this dissertation are given below:

1. **Development of Si coated with carbon (Si/C) alloying anodes:**

   In recent years, Si is considered as an alternative high-capacity anode for LIB. The main highlight of the thesis among the anode side is the synthesis of carbon-coated Si (Si/C) via simple pyrolysis reaction. The important aspect of this method was to provide a carbon coating over high-capacity alloying anode. This helped alleviate the volume expansion effects or loss of electronic conductivity. Herein the first-time report about printed Si coated with carbon for electrochemical properties has been shown in this thesis. For battery cycling FEC–containing electrolyte was used to further enhance the capacity retention. Additionally, a full cell comprising of Si/C anode and NCM(111) state-of-the-art cathode was optimized to power the printed electrolyte gated graphene transistor (EGT). In contrast to the physical mixture of Si with carbon additive, the Si/C composite showed good battery performance.

2. **Development of multi-cation doped rutile structured fluoride-based conversion cathodes and development of full cell assembly with next-generation LIB electrodes:**

   In the cathode section, preparation of entropy stabilized multi-component fluoride systems is another emphasis of this thesis. In this study, multiple cations based high entropy fluoride (HEF) was successfully developed, by simple and facile mechanochemical milling. This remarkable achievement was carried forward to identify the electrochemical properties of HEF compounds. HEF ceramics possessing single phase rutile structure provide distinct Wyckoff sites and has great prospects in tailoring of electrochemical properties. The nanocomposite structured HEF was prepared by ball

milling with CNT yielding HEF/CNT. This nanocomposite showed evident improvement in comparison with binary or ternary fluoride battery performance. However, HEF conversion-based cathodes experience certain limitations due to volume expansion and irreversible capacity loss.

The third focus of this dissertation is the fabrication of full cell battery. The experimental full cell fabrication pairing Si/C anode and novel HEF cathode was effectively demonstrated. These anode and cathode in printed forms give the applicability of printing technologies for LIB fabrication. Printed full cell with Si/C//HEF could be used as a power source for printed electronics circuits due to the potential range below 3 V.

7.2 Outlook

From the previous chapters, it is known that printing techniques are more suited integrating small battery systems for consumer electronics. To attain the commercial efficacy of printing technique which is relatively new method, more work must be devoted for their development. Even though printed electrodes have the limelight to potentially achieve the aim of "all-printed batteries", efforts must be devoted to realizing printed separator membranes and printed electrolytes. The potential challenge to tackle the clogging of nozzles may be synthesis nanoparticles with apt size (less than 1 μm) for inkjet printing.

For Si/C anodes, the perception of carbon coating is an effective method to minimize electronic conductivity loss incurred during the alloying reaction of Si-Li system. One of the promising methods to ensure conductivity during the alloying reaction is to create yoke-shell structure with Si@carbon shell (Si inside a hard carbon shell). This might be helpful to preserve the stability of coated Si during long term battery cycling. Another method for boosting the specific capacity of Si anode is by scavenging the surface of Si with HF acid to remove the native SiO_2 layer. Porous Si structures with voids will also be beneficial to overcome the volume expansion issues. A controlled, highly porous structure will promote adequate mass transport across the electrode.

For overcoming the aforementioned issues of conversion reaction of HEF cathodes, a well-designed conductive coating (carbon) can be considered. This is an effective approach to reduce the rising impedance values with long term cycles. Future projects could focus on improvement of HEF-based conversion cathodes, for example, by making use of passivation layers. This passivating layer could reduce the formation of unstable SEI layer and unwanted parasitic side

reactions with the electrolyte. For instance, previous reports show that a thin passivating layer of porous Al_2O_3 on NCM based cathode could reduce the dissolution of metal ions in the electrolyte during cycling. To account for the low electronic conductivity of transition metal fluoride-materials, carbon coating would also be beneficial. Another possibility for obtaining high performance cathodes would be the development of lithiated HEF phase (Li-HEF). Inherent Li present in Li-HEF structure will be helpful for diminishing the volume change of the cathode during the first lithiation/delithiation process and provide maximum Li insertion into the crystal structure in the first cycling process. Furthermore, innovative LIB redox couples with novel HEM concept could be designed with tailor-made voltage as necessary for powering the printed electronics circuits.

A. List of Abbreviations

2D	Two-dimension
C rate	Current rate
CMOS	Complementary-Metal-Oxide- Semiconductor
CP	Co-precipitaton
CV	Cyclic voltammetry
DLS	Dynamic laser scattering
DOD	Drop on demand
DOD	Drop on demand
E_0	Standard potential
EELS	Electron energy loss spectroscopy
EGT	Electrolyte gated transistor
F	Faraday constant (= 96,487 A s/mol)
FEC	fluoroethylene carbonate
HAADF	high-angle annular dark-field
HEC	High entropy ceramic
HEF	High entropy fluoride
HEM	High entropy material
HEO	High entropy oxide
ITO	Indium-doped tin oxide
IoT	Internet of things
LIB	Lithium-ion batteries
LP57	1M LiPF6 in EC: EMC 3:7 (wt:wt)
MWCNT	Multi walled carbon nanotube
NCM	Lithiated nickel cobalt manganese oxide
NMR	Nuclear Magnetic resonance
NSP	Nebulized spray pyrolysis
PE	Printed electronics
R	Gas constant
R2R	Roll to roll
RCP	Reverse co-precipitation
SEI	solid electrolyte interphase
SEM	Scanning electron microscopy
Si	Silicon
Si/C	Silicon coated with carbon
T	Temperature
TEM	Transmission electron microscopy
TM	Transition metal
V	Potential
XPS	X ray spectroscopy
XRD	X ray diffraction
a.u	Arbitrary units
e-	Electron
ppm	Parts per million
z	Number of electrons
°C	Degree Celsius

B. Acknowledgements

C. Publication List

Publications (* = published during Ph.D)

- Structure and Conductivity of epitaxial thin films of barium ferrite and its hydrated form $BaFeO_{2.5-x+\delta}$ $(OH)_{2x}$, <u>Parvathy. A.S</u>, Alan Molinari, Alexander Benes, Christoph Loho, Venkata Sai Kiran Chakravadhanula, Suresh Kumar Garlapati, Robert Kruk and Oliver Clemens, Journal of Physics D: Applied Physics 2017, 50, DOI: https://doi.org/10.1088/1361-6463/aa5718

- Anion Doping of Ferromagnetic Thin Films of $La_{0.74}Sr_{0.26}MnO_{3-\delta}$ via Topochemical Fluorination, <u>Parvathy Anitha Sukkurji</u>, Alan Molinari, Christian Reitz, Ralf Witte, Christian Kübel, Venkata Sai Kiran Chakravadhanula, Robert Kruk and Oliver Clemens, MDPI Materials 2018, 11(7), DOI: https://doi.org/10.3390/ma11071204

- *Spinel to Rock-Salt Transformation in High Entropy Oxides with Li Incorporation, Junbo Wang, David Stenzel, Raheleh Azmi, Saleem Najib, Kai Wang, Jaehoon Jeong, Abhishek Sarkar, Qingsong Wang, <u>Parvathy Anitha Sukkurji</u>, Thomas Bergfeldt, Miriam Botros, Julia Maibach, Horst Hahn, Torsten Brezesinski, Ben Breitung, Electrochem 2020, 1(1), 60-74, https://doi.org/10.3390/electrochem1010007

- *Printing Technologies for Integration of Electronic Devices and Sensors, T.T Baby, G. C. Marques, F. Neuper, S.A Singaraju, S.K Garlapati, F. Seggern, R. Kruk, S. Dasgupta, B. Sykora, B. Breitung, <u>P. A Sukkurji</u>, U. Bog, R. Kumar, H. Fuchs, T. Reinheimer, M. Mikolajek, J R. Binder, M. Hirtz, M. Ungerer, L. Koker, U. Gengenbach, N. Mishra, P. Gruber, M. Tahoori, J. A. Hagmann, H. von Seggern, H. Hahn, Functional Nanostructures and Sensors for CBRN Defence and Environmental Safety and Security. NATO Science for Peace and Security Series C: Environmental Security. Springer, https://doi.org/10.1007/978-94-024-1909-2_1

- *Tailored silicon/carbon compounds for printed Lithium-ion anodes, <u>Parvathy Anitha Sukkurji</u>, Ibrahim Issac, Surya Abhishek Singaraju, Leonardo Velasco Estrada, Jasmin Aghassi Hagmann, Wolfgang Bessler, Horst Hahn, Miriam Botros, Ben Breitung (https://doi.org/10.1002/batt.202000052, 2020, Batteries and Supercaps, Wiley Gmbh)

- * Mechanochemical Synthesis of Novel Rutile-Type High Entropy Fluorides for Electrocatalysis, <u>Parvathy Anitha Sukkurji</u>, Yanyan Cui, Seunghwa Lee, Kai Wang, Raheleh Azmi, Abhishek Sarkar, Sylvio Indris, Subramshu Shekar Bhattacharya, Robert Kruk, Horst Hahn, Qingsong Wang, Miriam Botros and Ben Breitung, 2021, Journal of Materials Chemistry A, RSC (https://doi.org/10.1039/D0TA10209A)

- Tailored High Entropy Fluorides as High-Capacity Lithium-Ion Battery Cathodes: An Insight into the Conversion Mechanism, Yanyan Cui, <u>Parvathy Anitha Sukkurji</u>, Simon Schweidler, Kai Wang, Raheleh Azmi, Junbo Wang, Alexandra Nunn, Wolfgang Bessler, Horst Hahn, Qingsong Wang, Ben Breitung and Miriam Botros (manuscript under preparation)

D. Bibliography

(1)   Manthiram, A. A Reflection on Lithium-Ion Battery Cathode Chemistry. *Nat. Commun.* **2020**, *11* (1), 1–9 DOI: 10.1038/s41467-020-15355-0.

(2)   Thackeray, M. M.; Wolverton, C.; Isaacs, E. D. Electrical Energy Storage for Transportation - Approaching the Limits of, and Going beyond, Lithium-Ion Batteries. *Energy Environ. Sci.* **2012**, *5* (7), 7854–7863 DOI: 10.1039/c2ee21892e.

(3)   Myung, S. T.; Maglia, F.; Park, K. J.; Yoon, C. S.; Lamp, P.; Kim, S. J.; Sun, Y. K. Nickel-Rich Layered Cathode Materials for Automotive Lithium-Ion Batteries: Achievements and Perspectives. *ACS Energy Lett.* **2017**, *2* (1), 196–223 DOI: 10.1021/acsenergylett.6b00594.

(4)   Whittingham, M. S.; Thompson, A. H. Intercalation and Lattice Expansion in Titanium Disulfide. *J. Chem. Phys.* **1975**, *62* (4), 1588 DOI: 10.1063/1.430581.

(5)   Mizushima, K.; Jones, P. C.; Wiseman, P. J.; Goodenough, J. B. LixCoO2 (0<x<1): A New Cathode Material for Batteries for High Energy Density. *Solid State Ionics* **1981**, *3–4*, 171–174.

(6)   Padhi, A. .; Nanjundaswamy, K. B.; Goodenough, J. B. Phospho-olivines as Positive-Electrode Materials for Rechargeable Lithium Batteries. *J. Electrochem. Soc.* **1997**, *144* (4), 1188–1194.

(7)   Ozawa, K. Lithium-Ion Rechargeable Batteries with LiCoO2 and Carbon Electrodes: The LiCoO2/C System. *Solid State Ionics* **1994**, *69* (3–4), 212–221 DOI: 10.1016/0167-2738(94)90411-1.

(8)   Gielen, D.; Boshell, F.; Saygin, D.; Bazilian, M. D.; Wagner, N.; Gorini, R. The Role of Renewable Energy in the Global Energy Transformation. *Energy Strateg. Rev.* **2019**, *24*, 38–50 DOI: 10.1016/j.esr.2019.01.006.

(9)   Ortner, A.; Totschnig, G. The Future Relevance of Electricity Balancing Markets in Europe - A 2030 Case Study. *Energy Strateg. Rev.* **2019**, *24*, 111–120 DOI: 10.1016/j.esr.2019.01.003.

(10) Martins, F.; Felgueiras, C.; Smitkova, M.; Caetano, N. Analysis of Fossil Fuel Energy Consumption and Environmental Impacts in European Countries. *Energies* **2019**, *12* (6), 1–11 DOI: 10.3390/en12060964.

(11) Walter, M.; Kovalenko, M. V.; Kravchyk, K. V. Challenges and Benefits of Post-Lithium-Ion Batteries. *New J. Chem.* **2020**, *44* (5), 1677–1683 DOI: 10.1039/c9nj05682c.

(12) Durmus, Y. E.; Zhang, H.; Baakes, F.; Desmaizieres, G.; Hayun, H.; Yang, L.; Kolek, M.; Küpers, V.; Janek, J.; Mandler, D.; Passerini, S.; Ein-Eli, Y. Side by Side Battery Technologies with Lithium-Ion Based Batteries. *Adv. Energy Mater.* **2020**, *10* (24), 1–21 DOI: 10.1002/aenm.202000089.

(13) Kim, Y. J.; Wilson, C. Analysing Future Change in the EU's Energy Innovation System. *Energy Strateg. Rev.* **2019**, *24*, 279–299 DOI: 10.1016/j.esr.2019.04.012.

(14) Dai, Q.; Kelly, J. C.; Gaines, L.; Wang, M. Life Cycle Analysis of Lithium-Ion Batteries for Automotive Applications. *Batteries* **2019**, *5* (48), 1–15 DOI: 10.3390/batteries5020048.

(15) Raut, N. C.; Al-Shamery, K. Inkjet Printing Metals on Flexible Materials for Plastic and Paper Electronics. *J. Mater. Chem. C* **2018**, *6* (7), 1618–1641 DOI: 10.1039/c7tc04804a.

(16) Wu, W. Inorganic Nanomaterials for Printed Electronics: A Review. *Nanoscale* **2017**, *9* (22), 7342–7372 DOI: 10.1039/c7nr01604b.

(17) Eugenio Cantator. *Applications of Organic and Printed Electronics*; Cantatore, E., Ed.; Integrated Circuits and Systems; Springer US: Boston, MA, 2013.

(18) Cadilha Marques, G.; Weller, D.; Erozan, A. T.; Feng, X.; Tahoori, M.; Aghassi-Hagmann, J. Progress Report on "From Printed Electrolyte-Gated Metal-Oxide Devices to Circuits." *Adv. Mater.* **2019**, *31* (26) DOI: 10.1002/adma.201806483.

(19) Costa, C. M.; Lanceros-Méndez, S. *Printed Batteries*; 2018.

(20) Clemens, W.; Krumm, J.; Blache, R. Printed RFID and Smart Objects for New High Volume Applications. In *Applications of Organic and Printed Electronics*; Springer US, 2013; pp 115–132.

(21) Weydanz, W. J.; Wohlfahrt-Mehrens, M.; Huggins, R. A. A Room Temperature Study of

the Binary Lithium-Silicon and the Ternary Lithium-Chromium-Silicon System for Use in Rechargeable Lithium Batteries. *J. Power Sources* **1999**, *81–82*, 237–242 DOI: 10.1016/S0378-7753(99)00139-1.

(22)   Adam, R.; Lepple, M.; Mayer, N. A.; Cupid, D. M.; Qian, Y.; Niehoff, P.; Schappacher, F. M.; Wadewitz, D.; Balachandran, G.; Bhaskar, A.; Bramnik, N.; Klemm, V.; Ahrens, E.; Giebeler, L.; Fauth, F.; Popescuh, C. A.; Seifert, H. J.; Winter, M.; Ehrenberg, H.; Rafaja, D. Coexistence of Conversion and Intercalation Mechanisms in Lithium Ion Batteries: Consequences for Microstructure and Interaction between the Active Material and Electrolyte. *Int. J. Mater. Res.* **2017**, *108* (11), 971–983 DOI: 10.3139/146.111509.

(23)   Hassoun, J.; Bonaccorso, F.; Agostini, M.; Angelucci, M.; Betti, M. G.; Cingolani, R.; Gemmi, M.; Mariani, C.; Panero, S.; Pellegrini, V.; Scrosati, B. An Advanced Lithium-Ion Battery Based on a Graphene Anode and a Lithium Iron Phosphate Cathode. *Nano Lett.* **2014**, *14* (8), 4901–4906 DOI: 10.1021/nl502429m.

(24)   Gu, Y.; Wu, A.; Sohn, H.; Nicoletti, C.; Iqbal, Z.; Federici, J. F. Fabrication of Rechargeable Lithium Ion Batteries Using Water-Based Inkjet Printed Cathodes. *J. Manuf. Process.* **2015**, *20*, 198–205 DOI: 10.1016/j.jmapro.2015.08.003.

(25)   Zhao, Y.; Zhou, Q.; Liu, L.; Xu, J.; Yan, M.; Jiang, Z. A Novel and Facile Route of Ink-Jet Printing to Thin Film SnO2anode for Rechargeable Lithium Ion Batteries. *Electrochim. Acta* **2006**, *51* (13), 2639–2645 DOI: 10.1016/j.electacta.2005.07.050.

(26)   Lawes, S.; Sun, Q.; Lushington, A.; Xiao, B.; Liu, Y.; Sun, X. Inkjet-Printed Silicon as High Performance Anodes for Li-Ion Batteries. *Nano Energy* **2017**, *36* (March), 313–321 DOI: 10.1016/j.nanoen.2017.04.041.

(27)   Zhao, Y.; Liu, G.; Liu, L.; Jiang, Z. High-Performance Thin-Film Li4Ti5O12 Electrodes Fabricated by Using Ink-Jet Printing Technique and Their Electrochemical Properties. *J. Solid State Electrochem.* **2009**, *13* (5), 705–711 DOI: 10.1007/s10008-008-0575-6.

(28)   Feng, K.; Li, M.; Liu, W.; Kashkooli, A. G.; Xiao, X.; Cai, M.; Chen, Z. Silicon-Based Anodes for Lithium-Ion Batteries: From Fundamentals to Practical Applications. *Small* **2018**, *14* (8) DOI: 10.1002/smll.201702737.

(29)   Zhang, W. J. A Review of the Electrochemical Performance of Alloy Anodes for Lithium-

Ion Batteries. *J. Power Sources* **2011**, *196* (1), 13–24 DOI: 10.1016/j.jpowsour.2010.07.020.

(30) Terranova, M. L.; Orlanducci, S.; Tamburri, E.; Guglielmotti, V.; Rossi, M. Si/C Hybrid Nanostructures for Li-Ion Anodes: An Overview. *J. Power Sources* **2014**, *246*, 167–177 DOI: 10.1016/j.jpowsour.2013.07.065.

(31) Ram A. Sharma and Randall N. Seefurth. Thermodynamic Properties of the Lithium-Silicon System. *J. Electrochem. Soc.* **1976**, *123* (12), 1763–1710.

(32) Rost, C. M.; Sachet, E.; Borman, T.; Moballegh, A.; Dickey, E. C.; Hou, D.; Jones, J. L.; Curtarolo, S.; Maria, J. P. Entropy-Stabilized Oxides. *Nat. Commun.* **2015**, *6*, 1–8 DOI: 10.1038/ncomms9485.

(33) Wang, F.; Kim, S. W.; Seo, D. H.; Kang, K.; Wang, L.; Su, D.; Vajo, J. J.; Wang, J.; Graetz, J. Ternary Metal Fluorides as High-Energy Cathodes with Low Cycling Hysteresis. *Nat. Commun.* **2015**, *6*, 1–9 DOI: 10.1038/ncomms7668.

(34) Li, L.; Jacobs, R.; Gao, P.; Gan, L.; Wang, F.; Morgan, D.; Jin, S. Origins of Large Voltage Hysteresis in High-Energy-Density Metal Fluoride Lithium-Ion Battery Conversion Electrodes. *J. Am. Chem. Soc.* **2016**, *138* (8), 2838–2848 DOI: 10.1021/jacs.6b00061.

(35) Etacheri, V.; Marom, R.; Elazari, R.; Salitra, G.; Aurbach, D. Challenges in the Development of Advanced Li-Ion Batteries: A Review. *Energy Environ. Sci.* **2011**, *4* (9), 3243–3262 DOI: 10.1039/c1ee01598b.

(36) Wang, Y.; Liu, B.; Li, Q.; Cartmell, S.; Ferrara, S.; Deng, Z. D.; Xiao, J. Lithium and Lithium Ion Batteries for Applications in Microelectronic Devices: A Review. *J. Power Sources* **2015**, *286*, 330–345 DOI: 10.1016/j.jpowsour.2015.03.164.

(37) M. Armand and J.-M. Tarascon. Building Better Batteries. *Nature* **2008**, *451* (7), 652–657.

(38) Winter, M.; Brodd, R. J. What Are Batteries, Fuel Cells, and Supercapacitors? *Chem. Rev.* **2004**, *104* (10), 4245–4269 DOI: 10.1021/cr020730k.

(39) Wang, R.; Feng, L.; Yang, W.; Zhang, Y.; Zhang, Y.; Bai, W.; Liu, B.; Zhang, W.; Chuan, Y.; Zheng, Z.; Guan, H. Effect of Different Binders on the Electrochemical Performance

of Metal Oxide Anode for Lithium-Ion Batteries. *Nanoscale Res. Lett.* **2017**, *12* DOI: 10.1186/s11671-017-2348-6.

(40) Das, P. R.; Komsiyska, L.; Osters, O.; Wittstock, G. PEDOT: PSS as a Functional Binder for Cathodes in Lithium Ion Batteries. *J. Electrochem. Soc.* **2015**, *162* (4), A674–A678 DOI: 10.1149/2.0581504jes.

(41) Huggins, R. A. *Advanced Batteries: Materials Science Aspects*; Springer Science + Business Media, 2009.

(42) Tian, X.; Jin, J.; Yuan, S.; Chua, C. K.; Tor, S. B.; Zhou, K. Emerging 3D-Printed Electrochemical Energy Storage Devices: A Critical Review. *Adv. Energy Mater.* **2017**, *7* (17), 1–17 DOI: 10.1002/aenm.201700127.

(43) Venugopal, G.; Moore, J.; Howard, J.; Pendalwar, S. Characterization of Microporous Separators for Lithium-Ion Batteries. **1999**, No. July 1998, 34–41.

(44) Ponrouch, A.; Palacín, M. R. Optimisation of Performance through Electrode Formulation in Conversion Materials for Lithium Ion Batteries: Co3O4as a Case Example. *J. Power Sources* **2012**, *212*, 233–246 DOI: 10.1016/j.jpowsour.2012.04.005.

(45) Ma, D.; Cao, Z.; Hu, A. Si-Based Anode Materials for Li-Ion Batteries: A Mini Review. *Nano-Micro Lett.* **2014**, *6* (4), 347–358 DOI: 10.1007/s40820-014-0008-2.

(46) Zhao, Y.; Li, X.; Yan, B.; Xiong, D.; Li, D.; Lawes, S.; Sun, X. L. Recent Developments and Understanding of Novel Mixed Transition-Metal Oxides as Anodes in Lithium Ion Batteries. *Advanced Energy Materials*. 2016.

(47) Zhang, L.; Wu, H. Bin; Lou, X. W. Iron-Oxide-Based Advanced Anode Materials for Lithium-Ion Batteries. *Adv. Energy Mater.* **2014**, *4* (4), 1–11 DOI: 10.1002/aenm.201300958.

(48) Krajewski, M.; Hamankiewicz, B.; Michalska, M.; Andrzejczuk, M.; Lipinska, L.; Czerwinski, A. Electrochemical Properties of Lithium-Titanium Oxide, Modified with Ag-Cu Particles, as a Negative Electrode for Lithium-Ion Batteries. *RSC Adv.* **2017**, *7* (82), 52151–52164 DOI: 10.1039/c7ra10608d.

(49) Chou, S. L.; Wang, J. Z.; Liu, H. K.; Dou, S. X. Rapid Synthesis of Li4Ti5O12

Microspheres as Anode Materials and Its Binder Effect for Lithium-Ion Battery. *J. Phys. Chem. C* **2011**, *115* (32), 16220–16227 DOI: 10.1021/jp2039256.

(50)   Reddy, M. V.; Mauger, A.; Julien, C. M.; Paolella, A.; Zaghib, K. Brief History of Early Lithium-Battery Development. *Materials (Basel).* **2020**, *13* (8), 1–9 DOI: 10.3390/MA13081884.

(51)   Lin, D.; Liu, Y.; Cui, Y. Reviving the Lithium Metal Anode for High-Energy Batteries. *Nat. Nanotechnol.* **2017**, *12* (3), 194–206 DOI: 10.1038/nnano.2017.16.

(52)   Naotoshi Nakashima. *"Nanocarbons for Energy Conversion: Supramolecular Approaches";* 2019; Vol. 63.

(53)   Antonopoulos, B. K.; Maglia, F.; Schmidt-Stein, F.; Schmidt, J. P.; Hoster, H. E. Formation of the Solid Electrolyte Interphase at Constant Potentials: A Model Study on Highly Oriented Pyrolytic Graphite. *Batter. Supercaps* **2018**, *1* (3), 110–121 DOI: 10.1002/batt.201800029.

(54)   An, S. J.; Li, J.; Daniel, C.; Mohanty, D.; Nagpure, S.; Wood, D. L. The State of Understanding of the Lithium-Ion-Battery Graphite Solid Electrolyte Interphase (SEI) and Its Relationship to Formation Cycling. *Carbon N. Y.* **2016**, *105*, 52–76 DOI: 10.1016/j.carbon.2016.04.008.

(55)   Steinhauer, M.; Risse, S.; Wagner, N.; Friedrich, K. A. Investigation of the Solid Electrolyte Interphase Formation at Graphite Anodes in Lithium-Ion Batteries with Electrochemical Impedance Spectroscopy. *Electrochim. Acta* **2017**, *228*, 652–658 DOI: 10.1016/j.electacta.2017.01.128.

(56)   Wang, L.; Han, J.; Kong, D.; Tao, Y.; Yang, Q. H. Enhanced Roles of Carbon Architectures in High-Performance Lithium-Ion Batteries. *Nano-Micro Lett.* **2019**, *11* (1), 1–23 DOI: 10.1007/s40820-018-0233-1.

(57)   Kang, C.; Cha, E.; Patel, M.; Wu, H.; Choi, W. Three-Dimensional Carbon Nanostructures for Advanced Lithium-Ion Batteries. *C* **2016**, *2* (4), 23 DOI: 10.3390/c2040023.

(58)   Lei, Y.; Huang, Z. H.; Yang, Y.; Shen, W.; Zheng, Y.; Sun, H.; Kang, F. Porous Mesocarbon Microbeads with Graphitic Shells: Constructing a High-Rate, High-Capacity

Cathode for Hybrid Supercapacitor. *Sci. Rep.* **2013**, *3*, 1–6 DOI: 10.1038/srep02477.

(59) Obrovac, M. N.; Chevrier, V. L. Alloy Negative Electrodes for Li-Ion Batteries. *Chem. Rev.* **2014**, *114* (23), 11444–11502 DOI: 10.1021/cr500207g.

(60) Sharova, V.; Moretti, A.; Giffin, G.; Carvalho, D.; Passerini, S. Evaluation of Carbon-Coated Graphite as a Negative Electrode Material for Li-Ion Batteries. *J. Carbon Res.* **2017**, *3* (22), 1–11 DOI: 10.3390/c3030022.

(61) Loeffler, N.; Bresser, D.; Passerini, S.; Copley, M. Secondary Lithium-Ion Battery Anodes: From First Commercial Batteries to Recent Research Activities. *Johnson Matthey Technol. Rev.* **2015**, *59* (1), 34–44 DOI: 10.1595/205651314X685824.

(62) Baby, T. T.; Marques, G. C.; Neuper, F.; Singaraju, S. A.; Garlapati, S.; von Seggern, F.; Kruk, R.; Dasgupta, S.; Sykora, B.; Breitung, B.; Sukkurji, P. A.; Bog, U.; Kumar, R.; Fuchs, H.; Reinheimer, T.; Mikolajek, M.; Binder, J. R.; Hirtz, M.; Ungerer, M.; Koker, L.; Gengenbach, U.; Mishra, N.; Gruber, P.; Tahoori, M.; Hagmann, J. A.; von Seggern, H.; Hahn, H. Printing Technologies for Integration of Electronic Devices and Sensors. In *NATO Science for Peace and Security Series C: Environmental Security*; Springer, 2020; pp 1–34.

(63) Zuo, X.; Zhu, J.; Müller-Buschbaum, P.; Cheng, Y. J. Silicon Based Lithium-Ion Battery Anodes: A Chronicle Perspective Review. *Nano Energy* **2017**, *31* (October 2016), 113–143 DOI: 10.1016/j.nanoen.2016.11.013.

(64) Sun, W.; Hu, R.; Zhang, H.; Wang, Y.; Yang, L.; Liu, J.; Zhu, M. A Long-Life Nano-Silicon Anode for Lithium Ion Batteries: Supporting of Graphene Nanosheets Exfoliated from Expanded Graphite by Plasma-Assisted Milling. *Electrochim. Acta* **2016**, *187*, 1–10 DOI: 10.1016/j.electacta.2015.11.020.

(65) Zhang, L.; Liu, X.; Zhao, Q.; Dou, S.; Liu, H.; Huang, Y.; Hu, X. Si-Containing Precursors for Si-Based Anode Materials of Li-Ion Batteries: A Review. *Energy Storage Mater.* **2016**, *4*, 92–102 DOI: 10.1016/j.ensm.2016.01.011.

(66) Chevrier, V. L.; Zwanziger, J. W.; Dahn, J. R. First Principles Study of Li-Si Crystalline Phases: Charge Transfer, Electronic Structure, and Lattice Vibrations. *J. Alloys Compd.* **2010**, *496* (1–2), 25–36 DOI: 10.1016/j.jallcom.2010.01.142.

(67)   Li, J.; Dahn, J. R. An In Situ X-Ray Diffraction Study of the Reaction of Li with Crystalline Si. *J. Electrochem. Soc.* **2007**, *154* (3), A156 DOI: 10.1149/1.2409862.

(68)   Kasavajjula, U.; Wang, C.; Appleby, A. J. Nano- and Bulk-Silicon-Based Insertion Anodes for Lithium-Ion Secondary Cells. *J. Power Sources* **2007**, *163* (2), 1003–1039 DOI: 10.1016/j.jpowsour.2006.09.084.

(69)   Wu, H.; Zheng, G.; Liu, N.; Carney, T. J.; Yang, Y.; Cui, Y. Engineering Empty Space between Si Nanoparticles for Lithium-Ion Battery Anodes. *Nano Lett.* **2012**, *12* (2), 904–909 DOI: 10.1021/nl203967r.

(70)   Liu, N.; Lu, Z.; Zhao, J.; Mcdowell, M. T.; Lee, H. W.; Zhao, W.; Cui, Y. A Pomegranate-Inspired Nanoscale Design for Large-Volume-Change Lithium Battery Anodes. *Nat. Nanotechnol.* **2014**, *9* (3), 187–192 DOI: 10.1038/nnano.2014.6.

(71)   Eom, K.; Joshi, T.; Bordes, A.; Do, I.; Fuller, T. F. The Design of a Li-Ion Full Cell Battery Using a Nano Silicon and Nano Multi-Layer Graphene Composite Anode. *J. Power Sources* **2014**, *249*, 118–124 DOI: 10.1016/j.jpowsour.2013.10.087.

(72)   Park, H. W.; Song, J.-H.; Choi, H.; Jin, J. S.; Lim, H.-T. Anode Performance of Lithium–Silicon Alloy Prepared by Mechanical Alloying for Use in All-Solid-State Lithium Secondary Batteries. *Jpn. J. Appl. Phys.* **2014**, *53* (8S3), 08NK02 DOI: 10.7567/JJAP.53.08NK02.

(73)   Shobukawa, H.; Alvarado, J.; Yang, Y.; Meng, Y. S. Electrochemical Performance and Interfacial Investigation on Si Composite Anode for Lithium Ion Batteries in Full Cell. *J. Power Sources* **2017**, *359*, 173–181 DOI: 10.1016/j.jpowsour.2017.05.044.

(74)   Erk, C.; Brezesinski, T.; Sommer, H.; Schneider, R.; Janek, J. Toward Silicon Anodes for Next-Generation Lithium Ion Batteries: A Comparative Performance Study of Various Polymer Binders and Silicon Nanopowders. *ACS Appl. Mater. Interfaces* **2013**, *5* (15), 7299–7307 DOI: 10.1021/am401642c.

(75)   Xun, S.; Song, X.; Wang, L.; Grass, M. E.; Liu, Z.; Battaglia, V. S.; Liu, G. The Effects of Native Oxide Surface Layer on the Electrochemical Performance of Si Nanoparticle-Based Electrodes. *J. Electrochem. Soc.* **2011**, *158* (12), A1260 DOI: 10.1149/2.007112jes.

(76)   Liu, G.; Xun, S.; Vukmirovic, N.; Song, X.; Olalde-Velasco, P.; Zheng, H.; Battaglia, V.

S.; Wang, L.; Yang, W. Polymers with Tailored Electronic Structure for High Capacity Lithium Battery Electrodes. *Adv. Mater.* **2011**, *23* (40), 4679–4683 DOI: 10.1002/adma.201102421.

(77) Yue, L.; Zhang, L.; Zhong, H. Carboxymethyl Chitosan: A New Water Soluble Binder for Si Anode of Li-Ion Batteries. *J. Power Sources* **2014**, *247*, 327–331 DOI: 10.1016/j.jpowsour.2013.08.073.

(78) Schiele, A.; Breitung, B.; Hatsukade, T.; Berkes, B. B.; Hartmann, P.; Janek, J.; Brezesinski, T. The Critical Role of Fluoroethylene Carbonate in the Gassing of Silicon Anodes for Lithium-Ion Batteries. *ACS Energy Lett.* **2017**, *2* (10), 2228–2233 DOI: 10.1021/acsenergylett.7b00619.

(79) Nguyen, C. C.; Lucht, B. L. Comparative Study of Fluoroethylene Carbonate and Vinylene Carbonate for Silicon Anodes in Lithium Ion Batteries. *J. Electrochem. Soc.* **2014**, *161* (12), A1933–A1938 DOI: 10.1149/2.0731412jes.

(80) Lindgren, F.; Xu, C.; Niedzicki, L.; Marcinek, M.; Gustafsson, T.; Björefors, F.; Edström, K.; Younesi, R. SEI Formation and Interfacial Stability of a Si Electrode in a LiTDI-Salt Based Electrolyte with FEC and VC Additives for Li-Ion Batteries. *ACS Appl. Mater. Interfaces* **2016**, *8* (24), 15758–15766 DOI: 10.1021/acsami.6b02650.

(81) Markevich, E.; Salitra, G.; Aurbach, D. Fluoroethylene Carbonate as an Important Component for the Formation of an Effective Solid Electrolyte Interphase on Anodes and Cathodes for Advanced Li-Ion Batteries. *ACS Energy Lett.* **2017**, *2* (6), 1337–1345 DOI: 10.1021/acsenergylett.7b00163.

(82) Breitung, B.; Aguiló-Aguayo, N.; Bechtold, T.; Hahn, H.; Janek, J.; Brezesinski, T. Embroidered Copper Microwire Current Collector for Improved Cycling Performance of Silicon Anodes in Lithium-Ion Batteries. *Sci. Rep.* **2017**, *7* (1), 3–8 DOI: 10.1038/s41598-017-13261-y.

(83) Boukamp, B. A.; Lesh, G. C.; Huggins, R. A.; Soc, J. E. All − Solid Lithium Electrodes with Mixed − Conductor Matrix Tetra Acknowledgment All-Solid Lithium Electrodes with Mixed-Conductor Matrix. *Joutnal Electrochem. Soc.* **1981**, *128* (4), 725–729.

(84) Liu, C.; Neale, Z. G.; Cao, G. Understanding Electrochemical Potentials of Cathode

Materials in Rechargeable Batteries. *Mater. Today* **2016**, *19* (2), 109–123 DOI: 10.1016/j.mattod.2015.10.009.

(85) Nitta, N.; Wu, F.; Lee, J. T.; Yushin, G. Li-Ion Battery Materials: Present and Future. *Mater. Today* **2015**, *18* (5), 252–264 DOI: 10.1016/j.mattod.2014.10.040.

(86) Takahashi, K.; Saitoh, M.; Asakura, N.; Hibino, T.; Sano, M.; Fujita, M.; Kifune, K. Electrochemical Properties of Lithium Manganese Oxides with Differnt Surface Areas for Lithium Ion Batteries. *J. Power Sources* **2004**, *136* (1), 115–121 DOI: 10.1016/j.jpowsour.2004.05.014.

(87) David, W. I. F.; Thackeray, M. M.; De Picciotto, L. A.; Goodenough, J. B. Structure Refinement of the Spinel-Related Phases Li2Mn2O4 and Li0.2Mn2O4. *J. Solid State Chem.* **1987**, *67* (2), 316–323 DOI: 10.1016/0022-4596(87)90369-0.

(88) Padhi, A. K.; Nanjundaswamy, K. S.; Masquelier, C.; Okada, S.; Goodenough, J. B. Effect of Structure on the Fe3 + / Fe2 + Redox Couple in Iron Phosphates. *J. Electrochem. Soc.* **1997**, *144* (5), 1609–1613 DOI: 10.1149/1.1837649.

(89) Toh, W. D.; Xu, B.; Jia, J.; Chin, C. S.; Chiew, J.; Gao, Z. Lithium Iron Phosphate (LiFePO4) Battery Power System for Deepwater Emergency Operation. *Energy Procedia* **2017**, *143*, 348–353 DOI: 10.1016/j.egypro.2017.12.695.

(90) Chi, Z. X.; Zhang, W.; Cheng, F. Q.; Chen, J. T.; Cao, A. M.; Wan, L. J. Optimizing the Carbon Coating on LiFePO4 for Improved Battery Performance. *RSC Adv.* **2014**, *4* (15), 7795–7798 DOI: 10.1039/c3ra47702a.

(91) Cui, Y.; Zhao, X.; Guo, R. Enhanced Electrochemical Properties of LiFePO4 Cathode Material by CuO and Carbon Co-Coating. *J. Alloys Compd.* **2010**, *490* (1–2), 236–240 DOI: 10.1016/j.jallcom.2009.09.165.

(92) Delacourt, C.; Laffont, L.; Bouchet, R.; Wurm, C.; Leriche, J.-B.; Morcrette, M.; Tarascon, J.-M.; Masquelier, C. Toward Understanding of Electrical Limitations (Electronic, Ionic) in LiMPO[Sub 4] (M=Fe, Mn) Electrode Materials. *J. Electrochem. Soc.* **2005**, *152* (5), A913 DOI: 10.1149/1.1884787.

(93) Recham, N.; Chotard, J. N.; Dupont, L.; Delacourt, C.; Walker, W.; Armand, M.; Tarascon, J. M. A 3.6 v Lithium-Based Fluorosulphate Insertion Positive Electrode for

Lithium-Ion Batteries. *Nat. Mater.* **2010**, *9* (1), 68–74 DOI: 10.1038/nmat2590.

(94)   Wang, R.; Li, X.; Liu, L.; Lee, J.; Seo, D. H.; Bo, S. H.; Urban, A.; Ceder, G. A Disordered Rock-Salt Li-Excess Cathode Material with High Capacity and Substantial Oxygen Redox Activity: Li1.25Nb0.25Mn0.5O2. *Electrochem. commun.* **2015**, *60*, 70–73 DOI: 10.1016/j.elecom.2015.08.003.

(95)   Yabuuchi, N.; Nakayama, M.; Takeuchi, M.; Komaba, S.; Hashimoto, Y.; Mukai, T.; Shiiba, H.; Sato, K.; Kobayashi, Y.; Nakao, A.; Yonemura, M.; Yamanaka, K.; Mitsuhara, K.; Ohta, T. Origin of Stabilization and Destabilization in Solid-State Redox Reaction of Oxide Ions for Lithium-Ion Batteries. *Nat. Commun.* **2016**, *7* (May), 1–10 DOI: 10.1038/ncomms13814.

(96)   Lee, J.; Seo, D. H.; Balasubramanian, M.; Twu, N.; Li, X.; Ceder, G. A New Class of High Capacity Cation-Disordered Oxides for Rechargeable Lithium Batteries: Li-Ni-Ti-Mo Oxides. *Energy Environ. Sci.* **2015**, *8* (11), 3255–3265 DOI: 10.1039/c5ee02329g.

(97)   House, R. A.; Jin, L.; Maitra, U.; Tsuruta, K.; Somerville, J. W.; Förstermann, D. P.; Massel, F.; Duda, L.; Roberts, M. R.; Bruce, P. G. Lithium Manganese Oxyfluoride as a New Cathode Material Exhibiting Oxygen Redox. *Energy Environ. Sci.* **2018**, *11* (4), 926–932 DOI: 10.1039/c7ee03195e.

(98)   Malini, R.; Uma, U.; Sheela, T.; Ganesan, M.; Renganathan, N. G. Conversion Reactions: A New Pathway to Realise Energy in Lithium-Ion Battery - Review. *Ionics (Kiel).* **2009**, *15* (3), 301–307 DOI: 10.1007/s11581-008-0236-x.

(99)   Park, M.; Zhang, X.; Chung, M.; Less, G. B.; Sastry, A. M. A Review of Conduction Phenomena in Li-Ion Batteries. *J. Power Sources* **2010**, *195* (24), 7904–7929 DOI: 10.1016/j.jpowsour.2010.06.060.

(100)   Yim, C.-H.; Niketic, S.; Salem, N.; Naboka, O.; Abu-Lebdeh, Y. Towards Improving the Practical Energy Density of Li-Ion Batteries: Optimization and Evaluation of Silicon:Graphite Composites in Full Cells. *J. Electrochem. Soc.* **2017**, *164* (1), A6294–A6302 DOI: 10.1149/2.0481701jes.

(101)   Jain, A.; Ong, S. P.; Hautier, G.; Chen, W.; Richards, W. D.; Dacek, S.; Cholia, S.; Gunter, D.; Skinner, D.; Ceder, G.; Persson, K. A. Commentary: The Materials Project: A

Materials Genome Approach to Accelerating Materials Innovation. *APL Mater.* **2013**, *1* (1) DOI: 10.1063/1.4812323.

(102) Yamada, S.; Fujiwara, M.; Kanda, M. Synthesis and Properties of LiNiO2 as Cathode Material for Secondary Batteries. *J. Power Sources* **1995**, *54* (2), 209–213 DOI: 10.1016/0378-7753(94)02068-E.

(103) Chen, R.; Whittingham, M. S. Cathodic Behavior of Alkali Manganese Oxides from Permanganate. *J. Electrochem. Soc.* **1997**, *144* (4), L64–L67 DOI: 10.1149/1.1837554.

(104) Whittingham, M. S. Lithium Batteries and Cathode Materials. *Chem. Rev.* **2004**, *104* (10), 4271–4302 DOI: 10.1021/cr020731c.

(105) Whittingham, M. S.; Savinell, R. F.; Zawodzinski, T. Introduction: Batteries and Fuel Cells. *Chem. Rev.* **2004**, *104* (10), 4243–4244 DOI: 10.1021/cr020705e.

(106) Liao, P. Y.; Duh, J. G.; Sheen, S. R. Effect of Mn Content on the Microstructure and Electrochemical Performance of LiNi0.75-XCo0.25MnxO2 Cathode Materials. *J. Electrochem. Soc.* **2005**, *152* (9), A1695 DOI: 10.1149/1.1952687.

(107) Noh, H. J.; Youn, S.; Yoon, C. S.; Sun, Y. K. Comparison of the Structural and Electrochemical Properties of Layered Li[NixCoyMnz]O2 (x = 1/3, 0.5, 0.6, 0.7, 0.8 and 0.85) Cathode Material for Lithium-Ion Batteries. *J. Power Sources* **2013**, *233*, 121–130 DOI: 10.1016/j.jpowsour.2013.01.063.

(108) Park, K. J.; Hwang, J. Y.; Ryu, H. H.; Maglia, F.; Kim, S. J.; Lamp, P.; Yoon, C. S.; Sun, Y. K. Degradation Mechanism of Ni-Enriched NCA Cathode for Lithium Batteries: Are Microcracks Really Critical? *ACS Energy Lett.* **2019**, *4* (6), 1394–1400 DOI: 10.1021/acsenergylett.9b00733.

(109) Kim, T.; Song, W.; Son, D. Y.; Ono, L. K.; Qi, Y. Lithium-Ion Batteries: Outlook on Present, Future, and Hybridized Technologies. *J. Mater. Chem. A* **2019**, *7* (7), 2942–2964 DOI: 10.1039/C8TA10513H.

(110) Julien, C.; Mauger, A.; Zaghib, K.; Groult, H. Optimization of Layered Cathode Materials for Lithium-Ion Batteries. *Materials (Basel).* **2016**, *9* (7) DOI: 10.3390/MA9070595.

(111) Kraytsberg, A.; Ein-Eli, Y. A Critical Review-Promises and Barriers of Conversion

Electrodes for Li-Ion Batteries. *J. Solid State Electrochem.* **2017**, *21* (7), 1907–1923 DOI: 10.1007/s10008-017-3580-9.

(112) Momma, K.; Izumi, F. VESTA 3 for Three-Dimensional Visualization of Crystal, Volumetric and Morphology Data. *J. Appl. Crystallogr.* **2011**, *44* (6), 1272–1276 DOI: 10.1107/S0021889811038970.

(113) Alcántara, R.; Jaraba, M.; Lavela, P.; Tirado, J. L. NiCo 2O 4 Spinel: First Report on a Transition Metal Oxide for the Negative Electrode of Sodium-Ion Batteries. *Chem. Mater.* **2002**, *14* (7), 2847–2848 DOI: 10.1021/cm025556v.

(114) Débart, A.; Dupont, L.; Poizot, P.; Leriche, J.-B.; Tarascon, J. M. A Transmission Electron Microscopy Study of the Reactivity Mechanism of Tailor-Made CuO Particles toward Lithium. *J. Electrochem. Soc.* **2001**, *148* (11), A1266 DOI: 10.1149/1.1409971.

(115) Wang, F.; Robert, R.; Chernova, N. A.; Pereira, N.; Omenya, F.; Badway, F.; Hua, X.; Ruotolo, M.; Zhang, R.; Wu, L.; Volkov, V.; Su, D.; Key, B.; Stanley Whittingham, M.; Grey, C. P.; Amatucci, G. G.; Zhu, Y.; Graetz, J. Conversion Reaction Mechanisms in Lithium Ion Batteries: Study of the Binary Metal Fluoride Electrodes. *J. Am. Chem. Soc.* **2011**, *133* (46), 18828–18836 DOI: 10.1021/ja206268a.

(116) Nishijima, M.; Gocheva, I. D.; Okada, S.; Doi, T.; Yamaki, J. ichi; Nishida, T. Cathode Properties of Metal Trifluorides in Li and Na Secondary Batteries. *J. Power Sources* **2009**, *190* (2), 558–562 DOI: 10.1016/j.jpowsour.2009.01.051.

(117) Arai, H.; Okada, S.; Sakurai, Y.; Yamaki, J. I. Cathode Performance and Voltage Estimation of Metal Trihalides. *J. Power Sources* **1997**, *68* (2), 716–719 DOI: 10.1016/S0378-7753(96)02580-3.

(118) Badway, F.; Cosandey, F.; Pereira, N.; Amatucci, G. G. Carbon Metal Fluoride Nanocomposites. *J. Electrochem. Soc.* **2003**, *150* (10), A1318 DOI: 10.1149/1.1602454.

(119) Badway, F.; Pereira, N.; Cosandey, F.; Amatucci, G. G. Carbon-Metal Fluoride Nanocomposites. *J. Electrochem. Soc.* **2003**, *150* (9), A1209 DOI: 10.1149/1.1596162.

(120) Huang, Q.; Turcheniuk, K.; Ren, X.; Magasinski, A.; Song, A. Y.; Xiao, Y.; Kim, D.; Yushin, G. Cycle Stability of Conversion-Type Iron Fluoride Lithium Battery Cathode at Elevated Temperatures in Polymer Electrolyte Composites. *Nat. Mater.* **2019**, *18* (12),

1343–1349 DOI: 10.1038/s41563-019-0472-7.

(121) Gordon, D.; Huang, Q.; Magasinski, A.; Ramanujapuram, A.; Bensalah, N.; Yushin, G. Mixed Metal Difluorides as High Capacity Conversion-Type Cathodes: Impact of Composition on Stability and Performance. *Adv. Energy Mater.* **2018**, *8* (19), 1–10 DOI: 10.1002/aenm.201800213.

(122) Wu, F.; Yushin, G. Conversion Cathodes for Rechargeable Lithium and Lithium-Ion Batteries. *Energy Environ. Sci.* **2017**, *10* (2), 435–459 DOI: 10.1039/c6ee02326f.

(123) Huang, Q.; Turcheniuk, K.; Ren, X.; Magasinski, A.; Song, A. Y.; Xiao, Y.; Kim, D.; Yushin, G. Cycle Stability of Conversion-Type Iron Fluoride Lithium Battery Cathode at Elevated Temperatures in Polymer Electrolyte Composites. *Nat. Mater.* **2019**, *18* (12), 1343–1349 DOI: 10.1038/s41563-019-0472-7.

(124) Guo, Y.-G.; Hu, J.-S.; Wan, L.-J. Nanostructured Materials for Electrochemical Energy Conversion and Storage Devices. *Adv. Mater.* **2008**, *20* (15), 2878–2887 DOI: 10.1002/adma.200800627.

(125) Yeh, J.; Chen, S.; Gan, J.; Lin, S.; Chin, T. Communications: Formation of Simple Crystal Structures in Cu-Co-Ni-Cr-Al-Fe-Ti-V Alloys with Multiprincipal Metallic Elements. **2010**, *35* (August 2004), 2533–2536.

(126) Cantor, B.; Chang, I. T. H.; Knight, P.; Vincent, A. J. B. Microstructural Development in Equiatomic Multicomponent Alloys. *Mater. Sci. Eng. A* **2004**, *375–377* (1-2 SPEC. ISS.), 213–218 DOI: 10.1016/j.msea.2003.10.257.

(127) Murty, B. S.; Ranganathan, S.; Yeh, J. W.; Bhattacharjee, P. P. *High-Entropy Alloys*; Elsevier, 2019.

(128) Djenadic, R.; Sarkar, A.; Clemens, O.; Loho, C.; Botros, M.; Chakravadhanula, V. S. K.; Kübel, C.; Bhattacharya, S. S.; Gandhi, A. S.; Hahn, H. Multicomponent Equiatomic Rare Earth Oxides. *Mater. Res. Lett.* **2017**, *5* (2), 102–109 DOI: 10.1080/21663831.2016.1220433.

(129) Liu, R.; Chen, H.; Zhao, K.; Qin, Y.; Jiang, B.; Zhang, T.; Sha, G.; Shi, X.; Uher, C.; Zhang, W.; Chen, L. Entropy as a Gene-Like Performance Indicator Promoting Thermoelectric Materials. *Adv. Mater.* **2017**, *29* (38), 1–7 DOI: 10.1002/adma.201702712.

(130) Gild, J.; Braun, J.; Kaufmann, K.; Marin, E.; Harrington, T.; Hopkins, P.; Vecchio, K.; Luo, J. A High-Entropy Silicide: (Mo0.2Nb0.2Ta0.2Ti0.2W0.2)Si2. *J. Mater.* **2019**, *5* (3), 337–343 DOI: 10.1016/j.jmat.2019.03.002.

(131) Jiang, S.; Hu, T.; Gild, J.; Zhou, N.; Nie, J.; Qin, M.; Harrington, T.; Vecchio, K.; Luo, J. A New Class of High-Entropy Perovskite Oxides. *Scr. Mater.* **2018**, *142*, 116–120 DOI: 10.1016/j.scriptamat.2017.08.040.

(132) Gild, J.; Samiee, M.; Braun, J. L.; Harrington, T.; Vega, H.; Hopkins, P. E.; Vecchio, K.; Luo, J. High-Entropy Fluorite Oxides. *J. Eur. Ceram. Soc.* **2018**, *38* (10), 3578–3584 DOI: 10.1016/j.jeurceramsoc.2018.04.010.

(133) Gild, J.; Zhang, Y.; Harrington, T.; Jiang, S.; Hu, T.; Quinn, M. C.; Mellor, W. M.; Zhou, N.; Vecchio, K.; Luo, J. High-Entropy Metal Diborides: A New Class of High-Entropy Materials and a New Type of Ultrahigh Temperature Ceramics. *Sci. Rep.* **2016**, *6* (July), 2–11 DOI: 10.1038/srep37946.

(134) Wang, Q.; Sarkar, A.; Wang, D.; Velasco, L.; Azmi, R.; Bhattacharya, S. S.; Bergfeldt, T.; Düvel, A.; Heitjans, P.; Brezesinski, T.; Hahn, H.; Breitung, B. Multi-Anionic and -Cationic Compounds: New High Entropy Materials for Advanced Li-Ion Batteries. *Energy Environ. Sci.* **2019**, No. 12, 2433–2442 DOI: 10.1039/c9ee00368a.

(135) Zhao, X.; Xue, Z.; Chen, W.; Wang, Y.; Mu, T. Eutectic Synthesis of High-Entropy Metal Phosphides for Electrocatalytic Water Splitting. *ChemSusChem* **2020**, *13* (8), 2038–2042 DOI: 10.1002/cssc.202000173.

(136) Wang, Q.; Sarkar, A.; Wang, D.; Velasco, L.; Azmi, R.; Bhattacharya, S. S.; Bergfeldt, T.; Düvel, A.; Heitjans, P.; Brezesinski, T.; Hahn, H.; Breitung, B. Multi-Anionic and -Cationic Compounds: New High Entropy Materials for Advanced Li-Ion Batteries. *Energy Environ. Sci.* **2019**, *12*, 2433–2442 DOI: 10.1039/c9ee00368a.

(137) Sarkar, A.; Wang, Q.; Schiele, A.; Chellali, M. R.; Bhattacharya, S. S.; Wang, D.; Brezesinski, T.; Hahn, H.; Velasco, L.; Breitung, B. High-Entropy Oxides: Fundamental Aspects and Electrochemical Properties. *Advanced Materials*. 2019.

(138) Sarkar, A.; Djenadic, R.; Usharani, N. J.; Sanghvi, K. P.; Chakravadhanula, V. S. K.; Gandhi, A. S.; Hahn, H.; Bhattacharya, S. S. Nanocrystalline Multicomponent Entropy

Stabilised Transition Metal Oxides. *J. Eur. Ceram. Soc.* **2017**, *37* (2), 747–754 DOI: 10.1016/j.jeurceramsoc.2016.09.018.

(139) Sarkar, A.; Loho, C.; Velasco, L.; Thomas, T.; Bhattacharya, S. S.; Hahn, H.; Djenadic, R. Multicomponent Equiatomic Rare Earth Oxides with a Narrow Band Gap and Associated Praseodymium Multivalency. *Dalt. Trans.* **2017**, *46* (36), 12167–12176 DOI: 10.1039/c7dt02077e.

(140) Zhang, Y.; Zuo, T. T.; Tang, Z.; Gao, M. C.; Dahmen, K. A.; Liaw, P. K.; Lu, Z. P. Microstructures and Properties of High-Entropy Alloys. *Prog. Mater. Sci.* **2014**, *61* (September 2013), 1–93 DOI: 10.1016/j.pmatsci.2013.10.001.

(141) Zhang, R. Z.; Reece, M. J. Review of High Entropy Ceramics: Design, Synthesis, Structure and Properties. *J. Mater. Chem. A* **2019**, *7* (39), 22148–22162 DOI: 10.1039/c9ta05698j.

(142) Sarkar, A.; Velasco, L.; Wang, D.; Wang, Q.; Talasila, G.; de Biasi, L.; Kübel, C.; Brezesinski, T.; Bhattacharya, S. S.; Hahn, H.; Breitung, B. High Entropy Oxides for Reversible Energy Storage. *Nat. Commun.* **2018**, *9* (3400), 1–9 DOI: 10.1038/s41467-018-05774-5.

(143) Murty, B. S.; Ranganathan, S.; Yeh, J. W.; Bhattacharjee, P. P. *High-Entropy Alloys*; Elsevier, 2019.

(144) Yeh, J. W.; Chen, Y. L.; Lin, S. J.; Chen, S. K. High-Entropy Alloys – A New Era of Exploitation. *Mater. Sci. Forum* **2007**, *560*, 1–9 DOI: 10.4028/www.scientific.net/msf.560.1.

(145) Yeh, J. W.; Chen, S. K.; Lin, S. J.; Gan, J. Y.; Chin, T. S.; Shun, T. T.; Tsau, C. H.; Chang, S. Y. Nanostructured High-Entropy Alloys with Multiple Principal Elements: Novel Alloy Design Concepts and Outcomes. *Adv. Eng. Mater.* **2004**, *6* (5), 299–303 DOI: 10.1002/adem.200300567.

(146) Amiri, A.; Shahbazian-Yassar, R. Recent Progress of High-Entropy Materials for Energy Storage and Conversion. *J. Mater. Chem. A* **2021**, *9*, 782–823 DOI: 10.1039/D0TA09578H.

(147) Bérardan, D.; Franger, S.; Meena, A. K.; Dragoe, N. Room Temperature Lithium

Superionic Conductivity in High Entropy Oxides. *J. Mater. Chem. A* **2016**, *4* (24), 9536–9541 DOI: 10.1039/c6ta03249d.

(148) Wang, Q.; Sarkar, A.; Li, Z.; Lu, Y.; Velasco, L.; Bhattacharya, S. S.; Brezesinski, T.; Hahn, H.; Breitung, B. High Entropy Oxides as Anode Material for Li-Ion Battery Applications: A Practical Approach. *Electrochem. commun.* **2019**, *100* (February), 121–125 DOI: 10.1016/j.elecom.2019.02.001.

(149) Wang, J.; Stenzel, D.; Azmi, R.; Najib, S.; Wang, K.; Jeong, J.; Sarkar, A.; Wang, Q.; Sukkurji, P. A.; Bergfeldt, T.; Botros, M.; Maibach, J.; Hahn, H.; Brezesinski, T.; Breitung, B. Spinel to Rock-Salt Transformation in High Entropy Oxides with Li Incorporation. *Electrochem* **2020**, *1* (1), 60–74 DOI: 10.3390/electrochem1010007.

(150) Wang, J.; Cui, Y.; Wang, Q.; Wang, K.; Huang, X.; Stenzel, D.; Sarkar, A.; Azmi, R.; Bergfeldt, T.; Bhattacharya, S. S.; Kruk, R.; Hahn, H.; Schweidler, S.; Brezesinski, T.; Breitung, B. Lithium Containing Layered High Entropy Oxide Structures. *Sci. Rep.* **2020**, *10* (1), 1–13 DOI: 10.1038/s41598-020-75134-1.

(151) Zhao, C.; Ding, F.; Lu, Y.; Chen, L.; Hu, Y. S. High-Entropy Layered Oxide Cathodes for Sodium-Ion Batteries. *Angew. Chemie - Int. Ed.* **2020**, *59* (1), 264–269 DOI: 10.1002/anie.201912171.

(152) Chen, X.; Wu, Y. High-Entropy Transparent Fluoride Laser Ceramics. *J. Am. Ceram. Soc.* **2019**, *103* (2), 750–756 DOI: 10.1111/jace.16842.

(153) Biswas, K.; Yeh, J. W.; Bhattacharjee, P. P.; DeHosson, J. T. M. High Entropy Alloys: Key Issues under Passionate Debate. *Scr. Mater.* **2020**, *188*, 54–58 DOI: 10.1016/j.scriptamat.2020.07.010.

(154) Thiébaut, B. Flame Spray Pyrolysis: A Unique Facility for the Production of Nanopowders. *Platin. Met. Rev.* **2011**, *55* (2), 149–151 DOI: 10.1595/147106711X567680.

(155) Witte, R.; Sarkar, A.; Kruk, R.; Eggert, B.; Brand, R. A.; Wende, H.; Hahn, H. High-Entropy Oxides: An Emerging Prospect for Magnetic Rare-Earth Transition Metal Perovskites. *Phys. Rev. Mater.* **2019**, *3* (3), 1–8 DOI: 10.1103/PhysRevMaterials.3.034406.

(156) Djenadic, R.; Sarkar, A.; Clemens, O.; Loho, C.; Botros, M.; Chakravadhanula, V. S. K.; Kübel, C.; Bhattacharya, S. S.; Gandhi, A. S.; Hahn, H. Multicomponent Equiatomic Rare Earth Oxides. *Mater. Res. Lett.* **2017**, *5* (2), 102–109 DOI: 10.1080/21663831.2016.1220433.

(157) Biesuz, M.; Spiridigliozzi, L.; Dell'Agli, G.; Bortolotti, M.; Sglavo, V. M. Synthesis and Sintering of (Mg, Co, Ni, Cu, Zn)O Entropy-Stabilized Oxides Obtained by Wet Chemical Methods. *J. Mater. Sci.* **2018**, *53* (11), 8074–8085 DOI: 10.1007/s10853-018-2168-9.

(158) Lin, L.; Wang, K.; Azmi, R.; Wang, J.; Sarkar, A.; Botros, M.; Najib, S.; Cui, Y.; Stenzel, D.; Anitha Sukkurji, P.; Wang, Q.; Hahn, H.; Schweidler, S.; Breitung, B. Mechanochemical Synthesis: Route to Novel Rock-Salt-Structured High-Entropy Oxides and Oxyfluorides. *J. Mater. Sci.* **2020**, *55* (36), 16879–16889 DOI: 10.1007/s10853-020-05183-4.

(159) Sharma, Y.; Musico, B. L.; Gao, X.; Hua, C.; May, A. F.; Herklotz, A.; Rastogi, A.; Mandrus, D.; Yan, J.; Lee, H. N.; Chisholm, M. F.; Keppens, V.; Ward, T. Z. Single-Crystal High Entropy Perovskite Oxide Epitaxial Films. *Phys. Rev. Mater.* **2018**, *2* (6), 1–6 DOI: 10.1103/PhysRevMaterials.2.060404.

(160) Kotsonis, G. N.; Rost, C. M.; Harris, D. T.; Maria, J. P. Epitaxial Entropy-Stabilized Oxides: Growth of Chemically Diverse Phases via Kinetic Bombardment. *MRS Commun.* **2018**, *8* (3), 1371–1377 DOI: 10.1557/mrc.2018.184.

(161) Nathan, A.; Ahnood, A.; Cole, M. T.; Lee, S.; Suzuki, Y.; Hiralal, P.; Bonaccorso, F.; Hasan, T.; Garcia-Gancedo, L.; Dyadyusha, A.; Haque, S.; Andrew, P.; Hofmann, S.; Moultrie, J.; Chu, D.; Flewitt, A. J.; Ferrari, A. C.; Kelly, M. J.; Robertson, J.; Amaratunga, G. A. J.; Milne, W. I. Flexible Electronics: The next Ubiquitous Platform. *Proc. IEEE* **2012**, *100* (SPL CONTENT), 1486–1517 DOI: 10.1109/JPROC.2012.2190168.

(162) Søndergaard, R. R.; Hösel, M.; Krebs, F. C. Roll-to-Roll Fabrication of Large Area Functional Organic Materials. *J. Polym. Sci. Part B Polym. Phys.* **2013**, *51* (1), 16–34 DOI: 10.1002/polb.23192.

(163) Parashkov, R.; Becker, E.; Riedl, T.; Johannes, H. H.; Kowalsky, W. Large Area

Electronics Using Printing Methods. *Proc. IEEE* **2005**, *93* (7), 1321–1329 DOI: 10.1109/JPROC.2005.850304.

(164) Teichler, A.; Perelaer, J.; Schubert, U. S. Inkjet Printing of Organic Electronics-Comparison of Deposition Techniques and State-of-the-Art Developments. *J. Mater. Chem. C* **2013**, *1* (10), 1910–1925 DOI: 10.1039/c2tc00255h.

(165) Khan, S.; Lorenzelli, L.; Dahiya, R. S. Technologies for Printing Sensors and Electronics over Large Flexible Substrates: A Review. *IEEE Sens. J.* **2015**, *15* (6), 3164–3185 DOI: 10.1109/JSEN.2014.2375203.

(166) Shimura, F. *Basic Semiconductor Physics*; 1989.

(167) Sze. *Physics of Semiconductor Devices Physics of Semiconductor Devices*; 1995; Vol. 10.

(168) Schmechel, R.; Hepp, A.; Heil, H.; Ahles, M.; Weise, W.; von Seggern, H. Light-Emitting Field-Effect Transistor: Simple Model and Underlying Functional Mechanisms. *Org. F. Eff. Transistors II* **2003**, *5217*, 101–111 DOI: 10.1117/12.508846.

(169) Xiao, H. *Introduction to Semiconductor Manufacturing Technology*; SPIE, 2012.

(170) Kim, S. H.; Hong, K.; Xie, W.; Lee, K. H.; Zhang, S.; Lodge, T. P.; Frisbie, C. D. Electrolyte-Gated Transistors for Organic and Printed Electronics. *Advanced Materials*. 2013, pp 1822–1846.

(171) H Helmholtz. Ueber Einige Gesetze Der Vertheilung Elektrischer Ströme in Körperlichen Leitern Mit Anwendung Auf Die Thierisch-Elektrischen Versuche. *Ann Phys. Chemie* **1853**, *89* (165), 211–233.

(172) Von Seggern, F.; Keskin, I.; Koos, E.; Kruk, R.; Hahn, H.; Dasgupta, S. Temperature-Dependent Performance of Printed Field-Effect Transistors with Solid Polymer Electrolyte Gating. *ACS Appl. Mater. Interfaces* **2016**, *8* (46), 31757–31763 DOI: 10.1021/acsami.6b10939.

(173) Dumitru, L. M.; Irimia-Vladu, M.; Sariciftci, N. S. Biocompatible Integration of Electronics Into Food Sensors. In *Comprehensive Analytical Chemistry*; 2016; Vol. 74, pp 247–271.

(174) Jeong, J.; Marques, G. C.; Feng, X.; Boll, D.; Singaraju, S. A.; Aghassi-Hagmann, J.;

Hahn, H.; Breitung, B. Ink-Jet Printable, Self-Assembled, and Chemically Crosslinked Ion-Gel as Electrolyte for Thin Film, Printable Transistors. *Adv. Mater. Interfaces* **2019**, *6* (21), 1–7 DOI: 10.1002/admi.201901074.

(175) Cadilha Marques, G.; Garlapati, S. K.; Dehm, S.; Dasgupta, S.; Hahn, H.; Tahoori, M.; Aghassi-Hagmann, J. Digital Power and Performance Analysis of Inkjet Printed Ring Oscillators Based on Electrolyte-Gated Oxide Electronics. *Appl. Phys. Lett.* **2017**, *111* (10) DOI: 10.1063/1.4991919.

(176) Marques, G. C.; Garlapati, S. K.; Chatterjee, D.; Dehm, S.; Dasgupta, S.; Aghassi, J.; Tahoori, M. B. Electrolyte-Gated FETs Based on Oxide Semiconductors: Fabrication and Modeling. *IEEE Trans. Electron Devices* **2017**, *64* (1), 279–285 DOI: 10.1109/TED.2016.2621777.

(177) Nasr, B.; Wang, D.; Kruk, R.; Rösner, H.; Hahn, H.; Dasgupta, S. High-Speed, Low-Voltage, and Environmentally Stable Operation of Electrochemically Gated Zinc Oxide Nanowire Field-Effect Transistors. *Adv. Funct. Mater.* **2013**, *23* (14), 1750–1758 DOI: 10.1002/adfm.201202500.

(178) Liu, C. Te; Lee, W. H.; Shih, T. L. Synthesis of ZnO Nanoparticles to Fabricate a Mask-Free Thin-Film Transistor by Inkjet Printing. *J. Nanotechnol.* **2012**, *2012* (710908), 1–8 DOI: 10.1155/2012/710908.

(179) Kang, B. J.; Lee, C. K.; Oh, J. H. All-Inkjet-Printed Electrical Components and Circuit Fabrication on a Plastic Substrate. *Microelectron. Eng.* **2012**, *97* (4023), 251–254 DOI: 10.1016/j.mee.2012.03.032.

(180) Yan, H.; Chen, Z.; Zheng, Y.; Newman, C.; Quinn, J. R.; Dötz, F.; Kastler, M.; Facchetti, A. A High-Mobility Electron-Transporting Polymer for Printed Transistors. *Nature* **2009**, *457* (7230), 679–686 DOI: 10.1038/nature07727.

(181) Madej, E.; Espig, M.; Baumann, R. R.; Schuhmann, W.; La Mantia, F. Optimization of Primary Printed Batteries Based on Zn/MnO2. *J. Power Sources* **2014**, *261*, 356–362 DOI: 10.1016/j.jpowsour.2014.03.103.

(182) Gaikwad, A. M.; Arias, A. C. Understanding the Effects of Electrode Formulation on the Mechanical Strength of Composite Electrodes for Flexible Batteries. *ACS Appl. Mater.*

Interfaces **2017**, *9* (7), 6390–6400 DOI: 10.1021/acsami.6b14719.

(183) Hu, L.; Cui, Y. Energy and Environmental Nanotechnology in Conductive Paper and Textiles. *Energy Environ. Sci.* **2012**, *5* (4), 6423–6435 DOI: 10.1039/c2ee02414d.

(184) Kuang, M.; Wang, L.; Song, Y. Controllable Printing Droplets for High-Resolution Patterns. *Adv. Mater.* **2014**, *26* (40), 6950–6958 DOI: 10.1002/adma.201305416.

(185) Lessing, J.; Glavan, A. C.; Walker, S. B.; Keplinger, C.; Lewis, J. A.; Whitesides, G. M. Inkjet Printing of Conductive Inks with High Lateral Resolution on Omniphobic "RF Paper" for Paper-Based Electronics and MEMS. *Adv. Mater.* **2014**, *26* (27), 4677–4682 DOI: 10.1002/adma.201401053.

(186) Kil, E. H.; Choi, K. H.; Ha, H. J.; Xu, S.; Rogers, J. A.; Kim, M. R.; Lee, Y. G.; Kim, K. M.; Cho, K. Y.; Lee, S. Y. Imprintable, Bendable, and Shape-Conformable Polymer Electrolytes for Versatile-Shaped Lithium-Ion Batteries. *Adv. Mater.* **2013**, *25* (10), 1395–1400 DOI: 10.1002/adma.201204182.

(187) Singh, N.; Galande, C.; Miranda, A.; Mathkar, A.; Gao, W.; Reddy, A. L. M.; Vlad, A.; Ajayan, P. M. Paintable Battery. *Sci. Rep.* **2012**, *2*, 6–10 DOI: 10.1038/srep00481.

(188) Braam, K.; Subramanian, V. A Stencil Printed, High Energy Density Silver Oxide Battery Using a Novel Photopolymerizable Poly(Acrylic Acid) Separator. *Adv. Mater.* **2015**, *27* (4), 689–694 DOI: 10.1002/adma.201404149.

(189) Roberts, M.; Johns, P.; Owen, J.; Brandell, D.; Edstrom, K.; El Enany, G.; Guery, C.; Golodnitsky, D.; Lacey, M.; Lecoeur, C.; Mazor, H.; Peled, E.; Perre, E.; Shaijumon, M. M.; Simon, P.; Taberna, P. L. 3D Lithium Ion Batteries - From Fundamentals to Fabrication. *J. Mater. Chem.* **2011**, *21* (27), 9876–9890 DOI: 10.1039/c0jm04396f.

(190) Tang, Y.; Zhang, Y.; Rui, X.; Qi, D.; Luo, Y.; Leow, W. R.; Chen, S.; Guo, J.; Wei, J.; Li, W.; Deng, J.; Lai, Y.; Ma, B.; Chen, X. Conductive Inks Based on a Lithium Titanate Nanotube Gel for High-Rate Lithium-Ion Batteries with Customized Configuration. *Adv. Mater.* **2016**, *28* (8), 1567–1576 DOI: 10.1002/adma.201505161.

(191) Liangbing Hua, Jang Wook Choia, Yuan Yanga, Sangmoo Jeongb, Fabio La Mantiaa, Li-Feng Cuia, Y. C. Highly Conductive Paper for Energy-Storage Devices. *Proc. Natl. Acad. Sci. U. S. A.* **2007**, *106* (51), 21490–21494.

(192) Iwakura, C.; Fukumoto, Y.; Inoue, H.; Ohashi, S.; Kobayashi, S.; Tada, H.; Abe, M. Electrochemical Characterization of Various Metal Foils as a Current Collector of Positive Electrode for Rechargeable Lithium Batteries. *J. Power Sources* **1997**, *68* (2), 301–303 DOI: 10.1016/S0378-7753(97)02538-X.

(193) Gaikwad, A. M.; Whiting, G. L.; Steingart, D. A.; Arias, A. C. Highly Flexible, Printed Alkaline Batteries Based on Mesh-Embedded Electrodes. *Adv. Mater.* **2011**, *23* (29), 3251–3255 DOI: 10.1002/adma.201100894.

(194) Delannoy, P. E.; Riou, B.; Lestriez, B.; Guyomard, D.; Brousse, T.; Le Bideau, J. Toward Fast and Cost-Effective Ink-Jet Printing of Solid Electrolyte for Lithium Microbatteries. *J. Power Sources* **2015**, *274*, 1085–1090 DOI: 10.1016/j.jpowsour.2014.10.164.

(195) Ho, C. C.; Murata, K.; Steingart, D. A.; Evans, J. W.; Wright, P. K. A Super Ink Jet Printed Zinc-Silver 3D Microbattery. *J. Micromechanics Microengineering* **2009**, *19* (094013), 1–15 DOI: 10.1088/0960-1317/19/9/094013.

(196) Prosini, P. P.; Mancini, R.; Petrucci, L.; Contini, V.; Villano, P. Li4Ti5O12 as Anode in All-Solid-State, Plastic, Lithium-Ion Batteries for Low-Power Applications. *Solid State Ionics* **2001**, *144* (1–2), 185–192 DOI: 10.1016/S0167-2738(01)00891-8.

(197) Choi, M. G.; Kim, K. M.; Lee, Y. G. Design of 1.5V Thin and Flexible Primary Batteries for Battery-Assisted Passive (BAP) Radio Frequency Identification (RFID) Tag. *Curr. Appl. Phys.* **2010**, *10*, 92–96 DOI: 10.1016/j.cap.2010.03.010.

(198) Gören, A.; Mendes, J.; Rodrigues, H. M.; Sousa, R. E.; Oliveira, J.; Hilliou, L.; Costa, C. M.; Silva, M. M.; Lanceros-Méndez, S. High Performance Screen-Printed Electrodes Prepared by a Green Solvent Approach for Lithium-Ion Batteries. *J. Power Sources* **2016**, *334*, 65–77 DOI: 10.1016/j.jpowsour.2016.10.019.

(199) Sousa, R. E.; Oliveira, J.; Gören, A.; Miranda, D.; Silva, M. M.; Hilliou, L.; Costa, C. M.; Lanceros-Mendez, S. High Performance Screen Printable Lithium-Ion Battery Cathode Ink Based on C-LiFePO4. *Electrochim. Acta* **2016**, *196*, 92–100 DOI: 10.1016/j.electacta.2016.02.189.

(200) Lee, J. H.; Wee, S. B.; Kwon, M. S.; Kim, H. H.; Choi, J. M.; Song, M. S.; Park, H. B.; Kim, H.; Paik, U. Strategic Dispersion of Carbon Black and Its Application to Ink-Jet-

Printed Lithium Cobalt Oxide Electrodes for Lithium Ion Batteries. *J. Power Sources* **2011**, *196* (15), 6449–6455 DOI: 10.1016/j.jpowsour.2011.03.041.

(201) Shi, Y.; Zhou, X.; Yu, G. Material and Structural Design of Novel Binder Systems for High-Energy, High-Power Lithium-Ion Batteries. *Acc. Chem. Res.* **2017**, *50* (11), 2642–2652 DOI: 10.1021/acs.accounts.7b00402.

(202) Kammoun, M.; Berg, S.; Ardebili, H. Flexible Thin-Film Battery Based on Graphene-Oxide Embedded in Solid Polymer Electrolyte. *Nanoscale* **2015**, *7* (41), 17516–17522 DOI: 10.1039/c5nr04339e.

(203) Braam, K. T.; Volkman, S. K.; Subramanian, V. Characterization and Optimization of a Printed, Primary Silver-Zinc Battery. *J. Power Sources* **2012**, *199*, 367–372 DOI: 10.1016/j.jpowsour.2011.09.076.

(204) Takeuchi, E. S.; Leising, R. A. Lithium Batteries for Biomedical Applications. *MRS Bull.* **2002**, *27* (8), 624–627 DOI: 10.1557/mrs2002.199.

(205) Delannoy, P. E.; Riou, B.; Brousse, T.; Le Bideau, J.; Guyomard, D.; Lestriez, B. Ink-Jet Printed Porous Composite LiFePO4 Electrode from Aqueous Suspension for Microbatteries. *J. Power Sources* **2015**, *287*, 261–268 DOI: 10.1016/j.jpowsour.2015.04.067.

(206) Gaikwad, A. M.; Steingart, D. A.; Ng, T. N.; Schwartz, D. E.; Whiting, G. L. A Flexible High Potential Printed Battery for Powering Printed Electronics A Flexible High Potential Printed Battery for Powering Printed Electronics. **2013**, *233302* (2013), 1–6 DOI: 10.1063/1.4810974.

(207) Kumar, R.; Shin, J.; Yin, L.; You, J.; Meng, Y. S.; Wang, J. All-Printed , Stretchable Zn-Ag 2 O Rechargeable Battery via Hyperelastic Binder for Self-Powering Wearable Electronics. *Adv. Energy Mater.* **2017**, *7* (1602096), 1–8 DOI: 10.1002/aenm.201602096.

(208) Massa, W. *Kristallstrukturbestimmung*; Vieweg+Teubner Verlag, 2011.

(209) Dinnebier, R. E.; Billinge, S. J. L. *Powder Diffraction - Theory and Practice*; The Royal Society of Chemistry, 2008.

(210) Kang, J.; Wen, J.; Jayaram, S. H.; Yu, A.; Wang, X. Development of an Equivalent

Circuit Model for Electrochemical Double Layer Capacitors (EDLCs) with Distinct Electrolytes. *Electrochim. Acta* **2014**, *115*, 587–598 DOI: 10.1016/j.electacta.2013.11.002.

(211) Colliex, C. Seeing and Measuring with Electrons: Transmission Electron Microscopy Today and Tomorrow - An Introduction. *Comptes Rendus Phys.* **2014**, *15* (2–3), 101–109 DOI: 10.1016/j.crhy.2014.02.001.

(212) Suenaga, K. Elemental Analysis down to the Single Atom with Electron Beams. *Comptes Rendus Phys.* **2014**, *15* (2–3), 151–157 DOI: 10.1016/j.crhy.2013.12.003.

(213) Wang, Z. L. New Developments in Transmission Electron Microscopy for Nanotechnology. *Adv. Mater.* **2003**, *15* (18), 1497–1514 DOI: 10.1002/adma.200300384.

(214) Kogure, T. *Electron Microscopy*, 2nd ed.; Elsevier Ltd., 2013; Vol. 5.

(215) Singha, A.; Dhar, P.; Roy, A. A Nondestructive Tool for Nanomaterials: Raman and Photoluminescence Spectroscopy. *Am. J. Phys.* **2005**, *73* (3), 224–233 DOI: 10.1119/1.1819933.

(216) Dornhaus, R. *Surface Enhanced Raman Spectroscopy.*; 2016.

(217) Stevie, F. A.; Donley, C. L. Introduction to X-Ray Photoelectron Spectroscopy. *J. Vac. Sci. Technol. A* **2020**, *38* (6), 063204 DOI: 10.1116/6.0000412.

(218) Steinhardt, R. G.; Serfass, E. J. X-Ray Photoelectron Spectrometer for Chemical Analysis. *Anal. Chem.* **1951**, *23* (11), 1585–1590 DOI: 10.1021/ac60059a019.

(219) Zambonin, P. G.; Desimoni, E. X-Ray Photoelectron Spectroscopy: Principles, Instrumentation, Data Processing and Molten Salt Applications. In *Molten Salt Chemistry*; Springer Netherlands, 1987; pp 425–445.

(220) Oswald, S. *X-Ray Photoelectron Spectroscopy in Analysis of Surfaces*; 2013.

(221) Parry, K. L.; Shard, A. G.; Short, R. D.; White, R. G.; Whittle, J. D.; Wright, A. ARXPS Characterisation of Plasma Polymerised Surface Chemical Gradients. *Surf. Interface Anal.* **2006**, *38* (11), 1497–1504 DOI: 10.1002/sia.2400.

(222) Scofield, J. H. Hartree-Slater Subshell Photoionization Cross-Sections at 1254 and 1487 EV. *J. Electron Spectros. Relat. Phenomena* **1976**, *8* (2), 129–137 DOI: 10.1016/0368-

2048(76)80015-1.

(223) Shinotsuka, H.; Tanuma, S.; Powell, C. J.; Penn, D. R. Calculations of Electron Inelastic Mean Free Paths. X. Data for 41 Elemental Solids over the 50eV to 200keV Range with the Relativistic Full Penn Algorithm. *Surf. Interface Anal.* **2015**, *47* (9), 871–888 DOI: 10.1002/sia.5789.

(224) Guenter, H. *NMR Spectroscopy: Basic Principles, Concepts and Applications in Chemistry, 3rd Edition*; 2013.

(225) Harlow, J. E.; Ma, X.; Li, J.; Logan, E.; Liu, Y.; Zhang, N.; Ma, L.; Glazier, S. L.; Cormier, M. M. E.; Genovese, M.; Buteau, S.; Cameron, A.; Stark, J. E.; Dahn, J. R. A Wide Range of Testing Results on an Excellent Lithium-Ion Cell Chemistry to Be Used as Benchmarks for New Battery Technologies. *J. Electrochem. Soc.* **2019**, *166* (13), A3031–A3044 DOI: 10.1149/2.0981913jes.

(226) Elgrishi, N.; Rountree, K. J.; McCarthy, B. D.; Rountree, E. S.; Eisenhart, T. T.; Dempsey, J. L. A Practical Beginner's Guide to Cyclic Voltammetry. *J. Chem. Educ.* **2018**, *95* (2), 197–206 DOI: 10.1021/acs.jchemed.7b00361.

(227) Liu, C.; Neale, Z. G.; Cao, G. Understanding Electrochemical Potentials of Cathode Materials in Rechargeable Batteries. *Mater. Today* **2016**, *19* (2), 109–123 DOI: 10.1016/j.mattod.2015.10.009.

(228) Silva, V. *Impedance Spectroscopy*; 2015.

(229) Orazem, M. E.; Tribollet, B. *Electrochemical Impedance Spectroscopy*; 2008.

(230) Franco, A. A. *Physical Multiscale Modeling and Numerical Simulation of Electrochemical Devices for Energy Conversion and Storage - From Theory to Engineering to Practice*; 2015.

(231) Abe, Y.; Hori, N.; Kumagai, S. Electrochemical Impedance Spectroscopy on the Performance Degradation of LiFePO4/Graphite Lithium-Ion Battery Due to Charge-Discharge Cycling under Different C-Rates. *Energies MDPI* **2019**, *12* (4507), 1–14.

(232) Fassel, V. A. Analytical Inductively Coupled Plasma Spectroscopies - Past, Present, and Future. *Fresenius' Zeitschrift für Anal. Chemie* **1986**, *324* (6), 511–518 DOI:

10.1007/BF00470406.

(233) Titus, D.; James Jebaseelan Samuel, E.; Roopan, S. M. Nanoparticle Characterization Techniques. In *Green Synthesis, Characterization and Applications of Nanoparticles*; Elsevier, 2019; pp 303–319.

(234) Caruso, F.; Mantellato, S.; Palacios, M.; Flatt, R. J. ICP-OES Method for the Characterization of Cement Pore Solutions and Their Modification by Polycarboxylate-Based Superplasticizers. *Cem. Concr. Res.* **2017**, *91*, 52–60 DOI: 10.1016/j.cemconres.2016.10.007.

(235) Schiele, A.; Breitung, B.; Mazilkin, A.; Schweidler, S.; Janek, J.; Gumbel, S.; Fleischmann, S.; Burakowska-Meise, E.; Sommer, H.; Brezesinski, T. Silicon Nanoparticles with a Polymer-Derived Carbon Shell for Improved Lithium-Ion Batteries: Investigation into Volume Expansion, Gas Evolution, and Particle Fracture. *ACS Omega* **2018**, *3* (12), 16706–16713 DOI: 10.1021/acsomega.8b02541.

(236) I. Kovalenko, B. Zdyrko, A. Magasinski, B. Hertzberg, Z. Milicev, R. Burtovyy, I. Luzinov, G. Y. A Major Constituent of Brown Algae For. *Science (80-.).* **2011**, *334* (October), 75–79.

(237) MacKin, C.; Palacios, T. Large-Scale Sensor Systems Based on Graphene Electrolyte-Gated Field-Effect Transistors. *Analyst* **2016**, *141* (9), 2704–2711 DOI: 10.1039/c5an02328a.

(238) Tekin, E.; Smith, P. J.; Schubert, U. S. Inkjet Printing as a Deposition and Patterning Tool for Polymers and Inorganic Particles. *Soft Matter* **2008**, *4* (4), 703–713 DOI: 10.1039/b711984d.

(239) Neuvo, Y.; Ylönen, S. *Bit Bang Rays to the Future*.

(240) McKinley, G. H.; Renardy, M. Wolfgang von Ohnesorge. *Phys. Fluids* **2011**, *23* (12) DOI: 10.1063/1.3663616.

(241) Yunker, P. J.; Still, T.; Lohr, M. A.; Yodh, A. G. Suppression of the Coffee-Ring Effect by Shape-Dependent Capillary Interactions. *Nature* **2011**, *476* (7360), 308–311 DOI: 10.1038/nature10344.

(242) Garlapati, S. K.; Marques, G. C.; Gebauer, J. S.; Dehm, S.; Bruns, M.; Winterer, M.; Tahoori, M. B.; Aghassi-Hagmann, J.; Hahn, H.; Dasgupta, S. High Performance Printed Oxide Field-Effect Transistors Processed Using Photonic Curing. *Nanotechnology* **2018**, *29* (235205), 1–7 DOI: 10.1088/1361-6528/aab7a2.

(243) Singaraju, S. A.; Baby, T. T.; Neuper, F.; Kruk, R.; Hagmann, J. A.; Hahn, H.; Breitung, B. Development of Fully Printed Electrolyte-Gated Oxide Transistors Using Graphene Passive Structures. *ACS Appl. Electron. Mater.* **2019** DOI: 10.1021/acsaelm.9b00313.

(244) Sukkurji, P. A.; Issac, I.; Singaraju, S. A.; Velasco, L.; Hagmann, J. A.; Bessler, W.; Hahn, H.; Botros, M.; Breitung, B. Tailored Silicon/Carbon Compounds for Printed Li–Ion Anodes. *Batter. Supercaps* **2020**, *3* (8), 713–720 DOI: 10.1002/batt.202000052.

(245) Kayser, L. V.; Lipomi, D. J. Stretchable Conductive Polymers and Composites Based on PEDOT and PEDOT:PSS. *Adv. Mater.* **2019**, *31* (10), 1–13 DOI: 10.1002/adma.201806133.

(246) Chan, C. K.; Peng, H.; Liu, G.; McIlwrath, K.; Zhang, X. F.; Huggins, R. A.; Cui, Y. High-Performance Lithium Battery Anodes Using Silicon Nanowires. *Nat. Nanotechnol.* **2008**, *3* (1), 31–35 DOI: 10.1038/nnano.2007.411.

(247) Feng, K.; Li, M.; Liu, W.; Kashkooli, A. G.; Xiao, X.; Cai, M.; Chen, Z. Silicon-Based Anodes for Lithium-Ion Batteries: From Fundamentals to Practical Applications. *Small* **2018**, *14* (8) DOI: 10.1002/smll.201702737.

(248) Kim, H.; Yun, Y.; Lee, Y. C.; Lee, M. H.; Saito, N.; Kang, J. Synthesis of Silicon-Carbon Black Composite as Anode Material for Lithium Ion Battery. *Jpn. J. Appl. Phys.* **2018**, *57* (1), 1–4 DOI: 10.7567/JJAP.57.0102B2.

(249) Yi, R.; Dai, F.; Gordin, M. L.; Chen, S.; Wang, D. Micro-Sized Si-c Composite with Interconnected Nanoscale Building Blocks as High-Performance Anodes for Practical Application in Lithium-Ion Batteries. *Adv. Energy Mater.* **2013**, *3* (3), 295–300 DOI: 10.1002/aenm.201200857.

(250) Park, C. M.; Kim, J. H.; Kim, H.; Sohn, H. J. Li-Alloy Based Anode Materials for Li Secondary Batteries. *Chem. Soc. Rev.* **2010**, *39* (8), 3115–3141 DOI: 10.1039/b919877f.

(251) Cadilha Marques, G.; Garlapati, S. K.; Dehm, S.; Dasgupta, S.; Hahn, H.; Tahoori, M.;

Aghassi-Hagmann, J. Digital Power and Performance Analysis of Inkjet Printed Ring Oscillators Based on Electrolyte-Gated Oxide Electronics. *Appl. Phys. Lett.* **2017**, *111* (10) DOI: 10.1063/1.4991919.

(252) Gaikwad, A. M.; Steingart, D. A.; Nga Ng, T.; Schwartz, D. E.; Whiting, G. L. A Flexible High Potential Printed Battery for Powering Printed Electronics. *Appl. Phys. Lett.* **2013**, *102* (23) DOI: 10.1063/1.4810974.

(253) Weller, D.; Cadilha Marques, G.; Aghassi-Hagmann, J.; Tahoori, M. B. An Inkjet-Printed Low-Voltage Latch Based on Inorganic Electrolyte-Gated Transistors. *IEEE Electron Device Lett.* **2018**, *39* (6), 831–834 DOI: 10.1109/LED.2018.2826361.

(254) Jung, R.; Metzger, M.; Haering, D.; Solchenbach, S.; Marino, C.; Tsiouvaras, N.; Stinner, C.; Gasteiger, H. A. Consumption of Fluoroethylene Carbonate (FEC) on Si-C Composite Electrodes for Li-Ion Batteries. *J. Electrochem. Soc.* **2016**, *163* (8), A1705–A1716 DOI: 10.1149/2.0951608jes.

(255) Li, Y.; Lin, Z.; Xu, G.; Yao, Y.; Zhang, S.; Toprakci, O.; Alcoutlabi, M.; Zhang, X. Electrochemical Performance of Carbon Nanofibers Containing an Enhanced Dispersion of Silicon Nanoparticles for Lithium-Ion Batteries by Employing Surfactants. *ECS Electrochem. Lett.* **2012**, *1* (2), A31–A33 DOI: 10.1149/2.002202eel.

(256) Qu, F.; She, G.; Wang, J.; Qi, X.; Li, S.; Zhang, S.; Mu, L.; Shi, W. Journal of Physics and Chemistry of Solids Coating Nanoparticle-Assembled Si Microspheres with Carbon for Anode Material in Lithium-Ion Battery. *J. Phys. Chem. Solids* **2019**, *124* (September 2018), 312–317 DOI: 10.1016/j.jpcs.2018.09.037.

(257) Yi, R.; Dai, F.; Gordin, M. L.; Sohn, H.; Wang, D. Influence of Silicon Nanoscale Building Blocks Size and Carbon Coating on the Performance of Micro-Sized Si-c Composite Li-Ion Anodes. *Adv. Energy Mater.* **2013**, *3* (11), 1507–1515 DOI: 10.1002/aenm.201300496.

(258) Ferrari, A. C.; Robertson, J. Raman Spectroscopy of Amorphous, Nanostructured, Diamond-like Carbon, and Nanodiamond. *Philos. Trans. R. Soc. A Math. Phys. Eng. Sci.* **2004**, *362* (1824), 2477–2512 DOI: 10.1098/rsta.2004.1452.

(259) Kim, S.-G.; Park, O.-K.; Lee, J. H.; Ku, B.-C. Layer-by-Layer Assembled Graphene

Oxide Films and Barrier Properties of Thermally Reduced Graphene Oxide Membranes. *Carbon Lett.* **2013**, *14* (4), 247–250 DOI: 10.5714/cl.2013.14.4.247.

(260) Wang, W.; Favors, Z.; Li, C.; Liu, C.; Ye, R.; Fu, C.; Bozhilov, K.; Guo, J.; Ozkan, M.; Ozkan, C. S. Silicon and Carbon Nanocomposite Spheres with Enhanced Electrochemical Performance for Full Cell Lithium Ion Batteries. *Sci. Rep.* **2017**, *7* (March), 1–9 DOI: 10.1038/srep44838.

(261) Momma, T.; Yokoshima, T.; Nara, H.; Gima, Y.; Osaka, T. Distinction of Impedance Responses of Li-Ion Batteries for Individual Electrodes Using Symmetric Cells. *Electrochim. Acta* **2014**, *131*, 195–201 DOI: 10.1016/j.electacta.2014.01.091.

(262) Schmidt, J. P.; Chrobak, T.; Ender, M.; Illig, J.; Klotz, D.; Ivers-Tiffée, E. Studies on LiFePO4 as Cathode Material Using Impedance Spectroscopy. *J. Power Sources* **2011**, *196* (12), 5342–5348 DOI: 10.1016/j.jpowsour.2010.09.121.

(263) Ovejas, V. J.; Cuadras, A. Impedance Characterization of an LCO-NMC/Graphite Cell: Ohmic Conduction, Sei Transport and Charge-Transfer Phenomenon. *Batteries* **2018**, *4* (3) DOI: 10.3390/batteries4030043.

(264) Tatara, R.; Karayaylali, P.; Yu, Y.; Zhang, Y.; Giordano, L.; Maglia, F.; Jung, R.; Schmidt, J. P.; Lund, I.; Shao-Horn, Y. The Effect of Electrode-Electrolyte Interface on the Electrochemical Impedance Spectra for Positive Electrode in Li-Ion Battery. *J. Electrochem. Soc.* **2019**, *166* (3), A5090–A5098 DOI: 10.1149/2.0121903jes.

(265) Sukkurji, P. A.; Cui, Y.; Lee, S.; Wang, K.; Azmi, R.; Sarkar, A.; Indris, S.; Bhattacharya, S. S.; Kruk, R.; Hahn, H.; Wang, Q.; Botros, M.; Breitung, B. Mechanochemical Synthesis of Novel Rutile-Type High Entropy Fluorides for Electrocatalysis. *J. Mater. Chem. A* **2021** DOI: 10.1039/d0ta10209a.

(266) Yeh, J. W.; Lin, S. J. Breakthrough Applications of High-Entropy Materials. *J. Mater. Res.* **2018**, *33* (19), 3129–3137 DOI: 10.1557/jmr.2018.283.

(267) Oses, C.; Toher, C.; Curtarolo, S. High-Entropy Ceramics. *Nat. Rev. Mater.* **2020**, *7936* (5), 295–309 DOI: 10.1038/s41578-019-0170-8.

(268) Gwalani, B.; Pohan, R. M.; Lee, J.; Lee, B.; Banerjee, R.; Ryu, H. J.; Hong, S. H. High-Entropy Alloy Strengthened by in Situ Formation of Entropy-Stabilized Nano-

Dispersoids. *Sci. Rep.* **2018**, *8* (1), 1–9 DOI: 10.1038/s41598-018-32552-6.

(269) Sarkar, A.; Breitung, B.; Hahn, H. High Entropy Oxides: The Role of Entropy, Enthalpy and Synergy. *Scr. Mater.* **2020**, *187*, 43–48 DOI: 10.1016/j.scriptamat.2020.05.019.

(270) Bérardan, D.; Franger, S.; Dragoe, D.; Meena, A. K.; Dragoe, N. Colossal Dielectric Constant in High Entropy Oxides. *Phys. Status Solidi - Rapid Res. Lett.* **2016**, *10* (4), 328–333 DOI: 10.1002/pssr.201600043.

(271) Qin, Y.; Liu, J. X.; Li, F.; Wei, X.; Wu, H.; Zhang, G. J. A High Entropy Silicide by Reactive Spark Plasma Sintering. *J. Adv. Ceram.* **2019**, *8* (1), 148–152 DOI: 10.1007/s40145-019-0319-3.

(272) Jin, T.; Sang, X.; Unocic, R. R.; Kinch, R. T.; Liu, X.; Hu, J.; Liu, H.; Dai, S. Mechanochemical-Assisted Synthesis of High-Entropy Metal Nitride via a Soft Urea Strategy. *Advanced Materials*. 2018.

(273) Sedegov, A.; Vorotilo, S.; Tsybulin, V.; Kuskov, K.; Moscovskikh, D. Synthesis and Study of High-Entropy Ceramics Based on the Carbides of Refractory Metals. *IOP Conf. Ser. Mater. Sci. Eng.* **2019**, *558* (12043), 1–7 DOI: 10.1088/1757-899X/558/1/012043.

(274) Zhang, K.; Li, W.; Zeng, J.; Deng, T.; Luo, B.; Zhang, H.; Huang, X. Preparation of (La0.2Nd0.2Sm0.2Gd0.2Yb0.2)2Zr2O7 High-Entropy Transparent Ceramic Using Combustion Synthesized Nanopowder. *J. Alloys Compd.* **2020**, *817*, 153328 DOI: 10.1016/j.jallcom.2019.153328.

(275) Wang, T.; Chen, H.; Yang, Z.; Liang, J.; Dai, S. High-Entropy Perovskite Fluorides: A New Platform for Oxygen Evolution Catalysis. *J. Am. Chem. Soc.* **2020**, *142* (10), 4550–4554 DOI: 10.1021/jacs.9b12377.

(276) Hua, X.; Robert, R.; Du, L. S.; Wiaderek, K. M.; Leskes, M.; Chapman, K. W.; Chupas, P. J.; Grey, C. P. Comprehensive Study of the CuF2 Conversion Reaction Mechanism in a Lithium Ion Battery. *J. Phys. Chem. C* **2014**, *118* (28), 15169–15184 DOI: 10.1021/jp503902z.

(277) Cottam, M. G.; Lockwood, D. J. Spin-Phonon Interaction in Transition-Metal Difluoride Antiferromagnets: Theory and Experiment. *Low Temp. Phys.* **2019**, *45* (1) DOI: 10.1063/1.5082316.

(278) Waltz, F.; Swider, M. A.; Hoyer, P.; Hassel, T.; Erne, M.; Möhwald, K.; Adlung, M.; Feldhoff, A.; Wickleder, C.; Bach, F. W.; Behrens, P. Synthesis of Highly Stable Magnesium Fluoride Suspensions and Their Application in the Corrosion Protection of a Magnesium Alloy. *J. Mater. Sci.* **2012**, *47* (1), 176–183 DOI: 10.1007/s10853-011-5785-0.

(279) Rehmer, A.; Scheurell, K.; Scholz, G.; Kemnitz, E. Sol-Gel-Synthesis of Nanoscopic Complex Metal Fluorides. *Nanomaterials* **2017**, *7* (11), 1–13 DOI: 10.3390/nano7110362.

(280) Tong, W.; Amatucci, G. G. Silver Copper Fluoride: A Novel Perovskite Cathode for Lithium Batteries. *J. Power Sources* **2017**, *362*, 86–91 DOI: 10.1016/j.jpowsour.2017.07.008.

(281) Kohl, J.; Wiedemann, D.; Nakhal, S.; Bottke, P.; Ferro, N.; Bredow, T.; Kemnitz, E.; Wilkening, M.; Heitjans, P.; Lerch, M. Synthesis of Ternary Transition Metal Fluorides Li 3MF 6via a Sol-Gel Route as Candidates for Cathode Materials in Lithium-Ion Batteries. *J. Mater. Chem.* **2012**, *22* (31), 15819–15827 DOI: 10.1039/c2jm32133e.

(282) Li, J.; Xu, L.; Wei, K.; Ma, S.; Liu, X.; Zhao, Y.; Cui, Y. In Situ Forming of Ternary Metal Fluoride Thin Films with Excellent Li Storage Performance by Pulsed Laser Deposition. *Ionics (Kiel).* **2020**, *26*, 3367–3375 DOI: 10.1007/s11581-020-03528-2.

(283) Chen, H.; Fu, J.; Zhang, P.; Peng, H.; Abney, C. W.; Jie, K.; Liu, X.; Chi, M.; Dai, S. Entropy-Stabilized Metal Oxide Solid Solutions as CO Oxidation Catalysts with High-Temperature Stability. *J. Mater. Chem. A* **2018**, *6* (24), 11129–11133 DOI: 10.1039/c8ta01772g.

(284) O'Mullane, A. P.; Escudero-Escribano, M.; Stephens, I. E. L.; Krischer, K. The Role of Electrocatalysis in a Sustainable Future: From Renewable Energy Conversion and Storage to Emerging Reactions. *ChemPhysChem* **2019**, *20* (22), 2900–2903 DOI: 10.1002/cphc.201901058.

(285) Cui, X.; Zhang, B.; Zeng, C.; Guo, S. Electrocatalytic Activity of High-Entropy Alloys toward Oxygen Evolution Reaction. *MRS Commun.* **2018**, *8* (3), 1230–1235 DOI: 10.1557/mrc.2018.111.

(286) Ramasamy, S.; Jiang, J.; Gleiter, H.; Birringer, R.; Gonser, U. Investigation of

Nanocrystalline FeF2 by Mössbauer Spectroscopy. *Solid State Commun.* **1990**, *74* (8), 851–855 DOI: 10.1016/0038-1098(90)90949-C.

(287) Troparevsky, M. C.; Morris, J. R.; Daene, M.; Wang, Y.; Lupini, A. R.; Stocks, G. M. Beyond Atomic Sizes and Hume-Rothery Rules: Understanding and Predicting High-Entropy Alloys. *Jom* **2015**, *67* (10), 2350–2363 DOI: 10.1007/s11837-015-1594-2.

(288) Stout, J. W.; Reed, S. A. The Crystal Structure of MnF2, FeF2, CoF2, NiF2 and ZnF2. *J. Am. Chem. Soc.* **1954**, *76* (21), 5279–5281 DOI: 10.1021/ja01650a005.

(289) Armstrong, M. J.; Panneerselvam, A.; O'Regan, C.; Morris, M. A.; Holmes, J. D. Supercritical-Fluid Synthesis of FeF2 and CoF2 Li-Ion Conversion Materials. *J. Mater. Chem. A* **2013**, *1* (36), 10667–10676 DOI: 10.1039/c3ta12436c.

(290) Shannon, R. D. Revised Effective Ionic Radii and Systematic Studies of Interatomic Distances in Halides and Chalcogenides. *Acta Crystallogr. Sect. A* **1976**, *32* (5), 751–767 DOI: 10.1023/A:1018927109487.

(291) Šepelák, V.; Feldhoff, A.; Heitjans, P.; Krumeich, F.; Menzel, D.; Litterst, F. J.; Bergmann, I.; Becker, K. D. Nonequilibrium Cation Distribution, Canted Spin Arrangement, and Enhanced Magnetization in Nanosized MgFe2O4 Prepared by a One-Step Mechanochemical Route. *Chem. Mater.* **2006**, *18* (13), 3057–3067 DOI: 10.1021/cm0514894.

(292) Wagner, C. D. Auger Parameter in Electron Spectroscopy for the Identification of Chemical Species. *Anal. Chem.* **1975**, *47* (7), 1201–1203 DOI: 10.1021/ac60357a021.

(293) Biesinger, M. C. Advanced Analysis of Copper X-Ray Photoelectron Spectra. *Surf. Interface Anal.* **2017**, *49* (13), 1325–1334 DOI: 10.1002/sia.6239.

(294) Da-Ming, S.; Zhao-Qi, S.; Ai-Xia, L.; Zhi-Yuan, X. XPS Analysis of the Oxidation of Ag-MgF2 Cermet Film. *Vacuum* **1999**, *52* (4), 383–386 DOI: 10.1016/S0042-207X(98)00196-1.

(295) Quesnel, E.; Dumas, L.; Jacob, D.; Peiró, F. Optical and Microstructural Properties of MgF2 UV Coatings Grown by Ion Beam Sputtering Process. *J. Vac. Sci. Technol. A Vacuum, Surfaces, Film.* **2000**, *18* (6), 2869–2876 DOI: 10.1116/1.1290374.

(296) Azmi, R.; Masoumi, M.; Ehrenberg, H.; Trouillet, V.; Bruns, M. Surface Analytical Characterization of LiNi0.8-YMnyCo0.2O2 (0 ≤ y ≤ 0.4) Compounds for Lithium-Ion Battery Electrodes. *Surf. Interface Anal.* **2018**, *50* (11), 1132–1137 DOI: 10.1002/sia.6415.

(297) Mariappan, C. R.; Kumar, V.; Azmi, R.; Esmezjan, L.; Indris, S.; Bruns, M.; Ehrenberg, H. High Electrochemical Performance of 3D Highly Porous Zn0.2Ni0.8Co2O4 Microspheres as an Electrode Material for Electrochemical Energy Storage. *CrystEngComm* **2018**, *20* (15), 2159–2168 DOI: 10.1039/c7ce02161e.

(298) Azmi, R.; Trouillet, V.; Strafela, M.; Ulrich, S.; Ehrenberg, H.; Bruns, M. Surface Analytical Approaches to Reliably Characterize Lithium Ion Battery Electrodes. *Surf. Interface Anal.* **2018**, *50* (1), 43–51 DOI: 10.1002/sia.6330.

(299) Kumar, V.; Mariappan, C. R.; Azmi, R.; Moock, D.; Indris, S.; Bruns, M.; Ehrenberg, H.; Vijaya Prakash, G. Pseudocapacitance of Mesoporous Spinel-Type MCo 2 O 4 (M = Co, Zn, and Ni) Rods Fabricated by a Facile Solvothermal Route. *ACS Omega* **2017**, *2* (9), 6003–6013 DOI: 10.1021/acsomega.7b00709.

(300) Mori, S.; Cong, P.; Shinden, Y.; Nanao, H. Tribochemical Reactions and Lubricating Effects of Fluorinated Methanes for Al2O3 Ceramic. *Tribol. Lett.* **2004**, *17* (1), 83–89 DOI: 10.1023/B:TRIL.0000017422.55135.78.

(301) Scholz, G.; Breitfeld, S.; Krahl, T.; Düvel, A.; Heitjans, P.; Kemnitz, E. Mechanochemical Synthesis of MgF2 - MF2 Composite Systems (M Combining Double Low Line Ca, Sr, Ba). *Solid State Sci.* **2015**, *50*, 32–41 DOI: 10.1016/j.solidstatesciences.2015.10.004.

(302) Sadoc, A.; Body, M.; Legein, C.; Biswal, M.; Fayon, F.; Rocquefelte, X.; Boucher, F. NMR Parameters in Alkali, Alkaline Earth and Rare Earth Fluorides from First Principle Calculations. *Phys. Chem. Chem. Phys.* **2011**, *13* (41), 18539–18550 DOI: 10.1039/c1cp21253b.

(303) Guo, Y.; Wuttke, S.; Vimont, A.; Daturi, M.; Lavalley, J. C.; Teinz, K.; Kemnitz, E. Novel Sol-Gel Prepared Zinc Fluoride: Synthesis, Characterisation and Acid-Base Sites Analysis. *J. Mater. Chem.* **2012**, *22* (29), 14587–14593 DOI: 10.1039/c2jm31357j.

(304) Matwiyoff, N. A.; Asprey, L. B.; Wageman, W. E.; Reisfeld, M. J.; Fukushima, E.

Fluorine-19 Nuclear Magnetic Resonance Studies of Diamagnetic Fluoride Complexes of Nickel(IV), Palladium(IV), and Platinum(IV) in Anhydrous Hydrogen Fluoride Solutions. *Inorg. Chem.* **1969**, *8* (4), 750–753 DOI: 10.1021/ic50074a009.

(305) Armand, M. Nature Lithium Battery. *Nature* **2001**, *414* (November), 359–367 DOI: 10.1038/35104644.

(306) Cabana, J.; Monconduit, L.; Larcher, D.; Palacín, M. R. Beyond Intercalation-Based Li-Ion Batteries: The State of the Art and Challenges of Electrode Materials Reacting through Conversion Reactions. *Adv. Mater.* **2010**, *22* (35), 170–192 DOI: 10.1002/adma.201000717.

(307) Wang, L.; Wu, Z.; Zou, J.; Gao, P.; Niu, X.; Li, H.; Chen, L. Li-Free Cathode Materials for High Energy Density Lithium Batteries. *Joule* **2019**, 1–17 DOI: 10.1016/j.joule.2019.07.011.

(308) Yu, S. H.; Feng, X.; Zhang, N.; Seok, J.; Abruña, H. D. Understanding Conversion-Type Electrodes for Lithium Rechargeable Batteries. *Acc. Chem. Res.* **2018**, *51* (2), 273–281 DOI: 10.1021/acs.accounts.7b00487.

(309) Ko, J. K.; Wiaderek, K. M.; Pereira, N.; Kinnibrugh, T. L.; Kim, J. R.; Chupas, P. J.; Chapman, K. W.; Amatucci, G. G. Transport, Phase Reactions, and Hysteresis of Iron Fluoride and Oxyfluoride Conversion Electrode Materials for Lithium Batteries. *ACS Appl. Mater. Interfaces* **2014**, *6* (14), 10858–10869 DOI: 10.1021/am500538b.

(310) Villa, C.; Kim, S.; Lu, Y.; Dravid, V. P.; Wu, J. Cu-Substituted NiF 2 as a Cathode Material for Li-Ion Batteries. *ACS Appl. Mater. Interfaces* **2019**, *11* (1), 647–654 DOI: 10.1021/acsami.8b15791.

(311) Qiu, N.; Chen, H.; Yang, Z.; Sun, S.; Wang, Y.; Cui, Y. A High Entropy Oxide (Mg0.2Co0.2Ni0.2Cu0.2Zn0.2O) with Superior Lithium Storage Performance. *J. Alloys Compd.* **2019**, *777*, 767–774 DOI: 10.1016/j.jallcom.2018.11.049.

(312) Castle, E.; Csanádi, T.; Grasso, S.; Dusza, J.; Reece, M. Processing and Properties of High-Entropy Ultra-High Temperature Carbides. *Sci. Rep.* **2018**, *8* (1), 1–12 DOI: 10.1038/s41598-018-26827-1.

(313) Tsai, C. W.; Lai, S. W.; Cheng, K. H.; Tsai, M. H.; Davison, A.; Tsau, C. H.; Yeh, J. W.

Strong Amorphization of High-Entropy AlBCrSiTi Nitride Film. *Thin Solid Films* **2012**, *520* (7), 2613–2618 DOI: 10.1016/j.tsf.2011.11.025.

(314) Zhang, R. Z.; Gucci, F.; Zhu, H.; Chen, K.; Reece, M. J. Data-Driven Design of Ecofriendly Thermoelectric High-Entropy Sulfides. *Inorg. Chem.* **2018**, *57* (20), 13027–13033 DOI: 10.1021/acs.inorgchem.8b02379.

(315) Huang, Q.; Pollard, T. P.; Ren, X.; Kim, D.; Magasinski, A. Fading Mechanisms and Voltage Hysteresis in FeF 2 – NiF 2 Solid Solution Cathodes for Lithium and Lithium-Ion Batteries. **2019**, *1804670*, 1–11 DOI: 10.1002/smll.201804670.

(316) Thorpe, R.; Rangan, S.; Whitcomb, R.; Basaran, A. C.; Saerbeck, T.; Schuller, I. K.; Bartynski, R. A. The Solid State Conversion Reaction of Epitaxial FeF2(110) Thin Films with Lithium Studied by Angle-Resolved X-Ray Photoelectron Spectroscopy. *Phys. Chem. Chem. Phys.* **2015**, *17* (23), 15218–15225 DOI: 10.1039/c5cp01150g.

(317) Pereira, N.; Badway, F.; Wartelsky, M.; Gunn, S.; Amatucci, G. G. Iron Oxyfluorides as High Capacity Cathode Materials for Lithium Batteries. *J. Electrochem. Soc.* **2009**, *156* (6), A407 DOI: 10.1149/1.3106132.

(318) Yang, K.; Niu, B.; Liu, Y.; Zhong, J.; Li, J. Understanding the Mechanism of MgF 2 Modification on the Electrochemical Performance of Lithium-Rich Layered Oxides. *Int. J. Electrochem. Sci.* **2019**, *14* (4), 3139–3152 DOI: 10.20964/2019.04.14.

(319) Xu, Q.; Yang, X.; Rao, M.; Lin, D.; Yan, K.; Du, R. A.; Xu, J.; Zhang, Y.; Ye, D.; Yang, S.; Zhou, G.; Lu, Y.; Qiu, Y. High Energy Density Lithium Metal Batteries Enabled by a Porous Graphene/MgF2 Framework. *Energy Storage Mater.* **2020**, *26*, 73–82 DOI: 10.1016/j.ensm.2019.12.028.

(320) Reddy, M. A.; Fichtner, M. *Fluoride Cathodes for Secondary Batteries*; Elsevier, 2015.

(321) Hwang, I.; Jung, S. K.; Jeong, E. S.; Kim, H.; Cho, S. P.; Ku, K.; Kim, H.; Yoon, W. S.; Kang, K. NaF–FeF2 Nanocomposite: New Type of Na-Ion Battery Cathode Material. *Nano Res.* **2017**, *10* (12), 4388–4397 DOI: 10.1007/s12274-017-1538-y.

(322) Mao, O.; Turner, R. L.; Courtney, I. A.; Fredericksen, B. D.; Buckett, M. I.; Krause, L. J.; Dahn, J. R. Active/Inactive Nanocomposites as Anodes for Li-Ion Batteries. *Electrochem. Solid-State Lett.* **1999**, *2* (1), 3–5 DOI: 10.1149/1.1390715.

(323) Fan, X.; Zhu, Y.; Luo, C.; Suo, L.; Lin, Y.; Gao, T.; Xu, K.; Wang, C. Pomegranate-Structured Conversion-Reaction Cathode with a Built-in Li Source for High-Energy Li-Ion Batteries. *ACS Nano* **2016**, *10* (5), 5567–5577 DOI: 10.1021/acsnano.6b02309.

(324) Wang, J.; Wang, L.; Eng, C.; Wang, J. Elucidating the Irreversible Mechanism and Voltage Hysteresis in Conversion Reaction for High-Energy Sodium–Metal Sulfide Batteries. *Adv. Energy Mater.* **2017**, *7* (14), 1–8 DOI: 10.1002/aenm.201602706.

(325) Li, C.; Chen, K.; Zhou, X.; Maier, J. Electrochemically Driven Conversion Reaction in Fluoride Electrodes for Energy Storage Devices. *npj Comput. Mater.* **2018**, *4* (22), 1–15 DOI: 10.1038/s41524-018-0079-6.

(326) Reddy, M. A.; Breitung, B.; Chakravadhanula, V. S. K.; Wall, C.; Engel, M.; Kübel, C.; Powell, A. K.; Hahn, H.; Fichtner, M. CFx Derived Carbon-FeF2nanocomposites for Reversible Lithium Storage. *Adv. Energy Mater.* **2013**, *3* (3), 308–313 DOI: 10.1002/aenm.201200788.

(327) Dees, D.; Gunen, E.; Abraham, D.; Jansen, A.; Prakash, J. Alternating Current Impedance Electrochemical Modeling of Lithium-Ion Positive Electrodes. *J. Electrochem. Soc.* **2005**, *152* (7), A1409 DOI: 10.1149/1.1928169.

(328) Chen, Y. S.; Kang, J. F.; Chen, B.; Gao, B.; Liu, L. F.; Liu, X. Y.; Wang, Y. Y.; Wu, L.; Yu, H. Y.; Wang, J. Y.; Chen, Q.; Wang, E. G. Microscopic Mechanism for Unipolar Resistive Switching Behaviour of Nickel Oxides. *J. Phys. D. Appl. Phys.* **2012**, *45* (6) DOI: 10.1088/0022-3727/45/6/065303.

(329) Chhetri, M.; Sultan, S.; Rao, C. N. R. Electrocatalytic Hydrogen Evolution Reaction Activity Comparable to Platinum Exhibited by the Ni/Ni(OH)2/Graphite Electrode. *Proc. Natl. Acad. Sci. U. S. A.* **2017**, *114* (34), 8986–8990 DOI: 10.1073/pnas.1710443114.

(330) Jenks, C. J.; Chang, S.-L.; Anderegg, J. W.; Thiel, P. A.; Lynch, D. W. Photoelectron Spectra of an Al70 Pd21 Mn9 Quasicrystal and the Cubic Alloy Al60 Pd25 Mn15 . *Phys. Rev. B* **1996**, *54* (9), 6301–6306 DOI: 10.1103/physrevb.54.6301.

(331) Rui, K.; Wen, Z.; Lu, Y.; Jin, J.; Shen, C. One-Step Solvothermal Synthesis of Nanostructured Manganese Fluoride as an Anode for Rechargeable Lithium-Ion Batteries and Insights into the Conversion Mechanism. *Adv. Energy Mater.* **2015**, *5* (7), 1–11 DOI:

10.1002/aenm.201401716.

(332) Huang, Y.; Ding, R.; Ying, D.; Shi, W.; Huang, Y.; Tan, C.; Sun, X.; Gao, P.; Liu, E. Engineering Doping-Vacancy Double Defects and Insights into the Conversion Mechanisms of an Mn-O-F Ultrafine Nanowire Anode for Enhanced Li/Na-Ion Storage and Hybrid Capacitors. *Nanoscale Adv.* **2019**, *1* (12), 4669–4678 DOI: 10.1039/c9na00521h.

(333) Fu, Z.-W.; Li, C.-L.; Liu, W.-Y.; Ma, J.; Wang, Y.; Qin, Q.-Z. Electrochemical Reaction of Lithium with Cobalt Fluoride Thin Film Electrode. *J. Electrochem. Soc.* **2005**, *152* (2), E50 DOI: 10.1149/1.1839512.

(334) Yamakawa, N.; Jiang, M.; Key, B.; Grey, C. P. Identifying the Local Structures Formed during Lithiation of the Conversion Material, Iron Fluoride, in a Li Ion Battery: A Solid-State NMR, X-Ray Diffraction, and Pair Distribution Function Analysis Study. *J. Am. Chem. Soc.* **2009**, *131* (30), 10525–10536 DOI: 10.1021/ja902639w.

(335) Hua, X.; Eggeman, A. S.; Castillo-Martínez, E.; Robert, R.; Geddes, H. S.; Lu, Z.; Pickard, C. J.; Meng, W.; Wiaderek, K. M.; Pereira, N.; Amatucci, G. G.; Midgley, P. A.; Chapman, K. W.; Steiner, U.; Goodwin, A. L.; Grey, C. P. Revisiting Metal Fluorides as Lithium-Ion Battery Cathodes. *Nat. Mater.* **2021** DOI: 10.1038/s41563-020-00893-1.

(336) Xiao, A. W.; Lee, H. J.; Capone, I.; Robertson, A.; Wi, T. U.; Fawdon, J.; Wheeler, S.; Lee, H. W.; Grobert, N.; Pasta, M. Understanding the Conversion Mechanism and Performance of Monodisperse FeF2 Nanocrystal Cathodes. *Nat. Mater.* **2020**, *19* (6), 644–654 DOI: 10.1038/s41563-020-0621-z.

(337) Zhang, S. S.; Jow, T. R. Study of Poly(Acrylonitrile-Methyl Methacrylate) as Binder for Graphite Anode and LiMn2O4 Cathode of Li-Ion Batteries. *J. Power Sources* **2002**, *109* (2), 422–426 DOI: 10.1016/S0378-7753(02)00107-6.